LBNL-44714

ERNEST ORLANDO LAWRENCE
BERKELEY NATIONAL LABORATORY

Photodissociation and Charge Transfer Dynamics of Negative Ions Studied with Femtosecond Photoelectron Spectroscopy

Martin Thomas Zanni

Chemical Sciences Division

December 1999

Ph.D. Thesis

DISCLAIMER

Portions of this document may be illegible in electronic image products. Images are produced from the best available original document.

LBNL-44714

Photodissociation and Charge Transfer Dynamics of Negative Ions Studied with Femtosecond Photoelectron Spectroscopy

Martin Thomas Zanni
Ph.D. Thesis

Department of Chemistry
University of California, Berkeley

and

Chemical Sciences Division
Ernest Orlando Lawrence Berkeley National Laboratory
University of California
Berkeley, CA 94720

December 1999

This work was supported in part by the Director, Office of Science, Office of Basic Energy Sciences, Chemical Sciences Division, of the U.S. Department of Energy under Contract No. DE-AC03-76SF00098, the National Science Foundation under Grant No. CHE-9710243, and the Defense University Research Instrumentation Program under Grant No. F49620-95-1-0078.

LBNL-44714

Photodissociation and charge transfer dynamics of negative ions studied with femtosecond photoelectron spectroscopy

by

Martin Thomas Zanni

B.S. (University of Rochester) 1994
B.A. (University of Rochester) 1994

A dissertation submitted in partial satisfaction of the

requirements for the degree of

Doctor of Philosophy

in

Chemistry

in the

GRADUATE DIVISION

of the

UNIVERSITY OF CALIFORNIA, BERKELEY

Committee in charge:

Professor Daniel M. Neumark, Chair
Professor Richard J. Saykally
Professor Jeffrey Bokor

Fall 1999

This work was supported in part by the Director, Office of Science, Office of Basic Energy Sciences, Chemical Sciences Division, of the U.S. Department of Energy under contract No. DE-AC03-76SF00098, by the National Science Foundation under Grant No. CHE-9710243, and by the Defense University Research Instrumentation Program under Grant No. F49620-95-1-0078.

Abstract

Photodissociation and charge transfer dynamics of negative ions studied with femtosecond photoelectron spectroscopy

by

Martin Thomas Zanni

Doctor of Philosophy in Chemistry

University of California, Berkeley

Professor Daniel M. Neumark, Chair

This dissertation presents studies aimed at understanding the potential energy surfaces and dynamics of isolated negative ions, and the effects of solvent on each. Although negative ions play important roles in atmospheric and solution phase chemistry, to a large extent the ground and excited state potential energy surfaces of gas phase negative ions are poorly characterized, and solvent effects even less well understood. In an effort to fill this gap, my coworkers and I have developed a new technique, anion femtosecond photoelectron spectroscopy, and applied it to gas phase photodissociation and charge transfer processes. Studies are presented that 1) characterize the ground and excited states of isolated and clustered anions, 2) monitor the photodissociation dynamics of isolated and clustered anions, and 3) explore the charge-transfer-to-solvent states of atomic iodide clustered with polar and non-polar solvents.

Dedicated to my

Mother and Father

and

Christie

Table of Contents

Acknowledgements

Far from trying to claim all the work presented in this dissertation as my own, I would like to thank and recognize the contributions of many friends and coworkers.

When I first came to Berkeley in 1994, I had no intention of working for Dan Neumark – that is, until he told me about the FPES project. I have been excited about our research ever since. Dan has been an excellent advisor, and in the early years of building the FPES spectrometer encouraged my enthusiasm with near-hourly visits to the lab. From his visits and advice, I have become better at judging when to ignore details and press on with the work, and when to pay closer attention. My paper writing has steadily improved because of his critiques, but I had always hoped that one day I would write an introduction that met his approval. It never happened, even with the introduction of this dissertation.

My largest recognition and warmest thanks go to Jeff Greenblatt. Jeff and I worked on the project together for three years at a furious pace. At one point, we pledged to arrive at work by 8 am each day, and most often we stayed very late. I had a hard time keeping up with him. He was an excellent partner: inventive, insightful, methodical, and a brilliant programmer. If it were not for his programming abilities, the project would still be in its infancy. But the best part of our partnership is that we complemented each other well. My research style tends to be energetic and spontaneous, but not always well thought out. Jeff kept me in check, and prevented me from making grievous errors on more than one occasion.

Alison Davis and Christian Frischkorn have both made excellent contributions to the project. Christian's contributions to the CTTS work (Chapters 9 & 10) was of

tremendous help. Alison and I worked together on the Sn2 systems (not reported in this dissertation) during which I was looking over her shoulder and correcting her mistakes. Now she is looking over mine, which is rather unnerving. She also deserves equal credit for our first SEP paper (Chapter 5).

We have also had many collaborators on the project in the last four years. Our work with Leo Lehr and Rainer Weinkauf turned out well (Chapter 10), and they were excellent fun to work with. Benoit Soep and Mohamed Elhanine were valuable sources of knowledge during their stay. Special thanks go to Gustav Gerber for helpful conversations, but also for rescuing me during my talk at the 1998 Atomic Clusters conference in Seattle.

Theoreticians Victor Batista, Jim Faeder, and Robert Parson have provided much insight into our work on the I_2^- cluster systems. In particular, Victor and I collaborated on several topics and published two papers together, one of which appears in this thesis (Chapter 4). Jim Faeder and I have yet to meet, but we have exchanged numerous emails.

Special thanks goes to Yongqin Chen. Yong provided essential laser expertise to Jeff and me during our first year while we were still femto-rookies. He also helped with my formal education through lengthy discussions while I was a teaching assistant for him in spectroscopy and quantum mechanics.

I have also had a good group to work with these last 5.5 years. Cangshan Xu taught me much of what I know about circuits. Thanks go to Travis Taylor who is responsible for a large portion of my first paper (Chapter 3). Mike Furlanetto and Ryan

Bise have been good friends. I could always count on Mike to stay late at my parties, and to Ryan I am indebted one skateboard.

Kim Hamad and Niels Damrauer have been my best friends through graduate school and roommates for the past two years. I have been lucky to have friends with diverse interests, and they have helped broaden my scientific and personal knowledge, often through late-night, scotch drinking conversations on the porch.

Although not directly involved in my graduate work, I would also like to acknowledge Jim Farrar and Franck Wolfs, my undergraduate advisors. They are the people who helped form my research habits while I was still impressionable.

My thanks go to my Mom and Dad for their encouragement and financial support through college and graduate school. I dedicate this dissertation to them for the sacrifices they have made for me.

I would also like to thank Christie Olsen, my wife of four months, for her love, understanding, and encouragement over the last 3.5 years. I knew that she was the right person for me when she showed genuine interest in my work with iodine. I dedicate this thesis to her as well, both in gratitude and as a promise to be as supportive of her interests as she has been of mine.

Chapter 1. Introduction

Numerous techniques have been developed in the preceding decades to probe chemical reactions in the gas phase.[1] High-resolution frequency measurements have led to detailed characterization of product state distributions from which the nature of the reactive process has been deduced,[2-4] and femtosecond pump-probe experiments have allowed the short time transition state dynamics to be monitored directly.[5] To date, most experiments have focused on monitoring the dynamics and characterizing the surfaces of neutral species. Relatively little is known about the gas phase dynamics and potential energy surfaces of negative ions. To a large degree, this is because the majority of the techniques, such as laser-induced fluorescence and multiphoton ionization, cannot be applied to negative ions due to their extremely low gas phase number density. As a consequence, the majority of photodissociation studies on gas phase, negative ions have consisted of measuring photodissociation cross sections, and in some cases, product branching ratios.[6,7]

In light of this, it is not surprising that most information on the solvent effects of negative ions comes from femtosecond, condensed phase experiments.[8,9] However, it is often difficult to distinguish between solvent effects and solute dynamics in these experiments, in part because the potentials and dynamics of the isolated anion are most often not well understood. An alternative method for studying solvent/solute effects is the initiation of reactions in gas phase clusters.[6,7] Using this approach, the dynamics and potential energy surfaces of the isolated chromophore can be characterized, and then the solvent added in a stepwise fashion. In this way, the solvent effects on the bare chromophore are studied in a systematic manner, and the reduced number of degrees of

freedom allows the microscopic solvent/solute effects to be rigorously modeled. Indeed, this method of study often provides insight into typical condensed phase processes, such as caging, vibrational relaxation, solvent induced non-adiabatic curve crossing, and electron solvation.[6,7] When these processes are studied with time-resolved techniques, direct comparison is readily made to the bulk condensed phase experiments.

In this dissertation, a number of studies are presented, aimed at better understanding anion dynamics themselves, as well as solvent effects on the photodissociation and charge-transfer processes involving anions. To this end, my coworkers and I have developed a new technique, anion femtosecond photoelectron spectroscopy (FPES).[10] FPES is a technique where a photodissociation, bimolecular chemical reaction, or charge-transfer process is initiated with a femtosecond pump pulse. The ensuing dynamics are monitored by photodetachment with a femtosecond probe pulse and the resulting photoelectron spectrum is recorded. Dynamics occurring on both the ground and excited states are monitored with FPES. Hence, we can observe depletion of the ground state, monitor excited state dynamics from the Franck-Condon region to asymptotic products, and determine the internal energy distributions of the anion products. Unlike many studies on neutral species where time-domain experiments complement already existing frequency measurements, the negative ion FPES experiments reported here reveal dynamics that cannot be obtained in any other way.

Three broad categories of experiments are presented in this dissertation. First, FPES is used to monitor the photodissociation dynamics of isolated I_2^-, and determine accurate ground and excited state potentials. These experiments have helped us develop our technique, and the improved potentials will aid in interpreting already existing cluster and condensed phase experiments. In a similar manner, the photodissociation dynamics

of bare I_3^- are studied to help provide insight into the condensed phase experiments. Second, the solvent effects on the ground potential energy surface of I_2^- is monitored for varying size $I_2^-(Ar)_n$ and $I_2^-(CO_2)_n$ clusters, and the effects of increasing solvation on the dissociation dynamics in $I_2^-(Ar)_n$ are studied. Finally, the origin and dynamics of the charge-transfer-to-solvent bands that lead to electron solvation are studied in $I^-(Xe)_n$ and $I^-(H_2O)_n$.

The experiments are presented in the latter chapters of this dissertation. The following sections of this chapter describe the methodology of our technique in more detail, provides background on the experiments that motivated this research, and summarizes the experiments contained in this thesis.

1. Anion femtosecond photoelectron spectroscopy

In order to characterize the potentials and dynamics of gas phase anions and their clusters, we have developed a new technique: anion femtosecond photoelectron spectroscopy (FPES).[10] Prior to the work presented here, femtosecond photoelectron spectroscopy had been applied to the study of neutrals,[11,12] as had the related technique of femtosecond zero electron kinetic energy spectroscopy.[13,14] Since our original publication, the field has grown to include other groups studying neutrals and anions.[15-20]

Anion FPES is a pump-probe technique where a femtosecond pump pulse triggers a photodissociation, bimolecular chemical reaction, or charge transfer event. After some time delay, a femtosecond probe pulse interrogates the sample by detaching the excess electron, and a photoelectron spectrum (PES) is measured. This yields a "snapshot" of the reaction, and by measuring the photoelectron spectrum as a function of time delay, the dynamics can be followed from initial excitation to asymptotic products. It is an

elegant method for studying negative ions and clusters because of three distinct advantages over techniques used to study neutral species. One advantage inherent to charged systems is that they are readily mass selected, a particularly important advantage when studying clusters since there is no ambiguity concerning the identity of the species under study. A second is that negative ions have low electron binding energies, and in most cases can be detached by a single near UV photon. This eliminates the need for intermediate electronic states typical in multiphoton ionization schemes, and significantly simplifies interpretation of the experiments. The final advantage is that the entire wavepacket is monitored at each time delay with a single probe pulse. Hence, dynamics can be studied at all points along the reaction coordinate, whereas absorption experiments are often limited by the tunability of the probe pulse. A disadvantage of negative ion experiments is their low gas phase densities. Thus, the experiments presented in this dissertation have only become possible with the advent of high repetition rate, high power, femtosecond laser systems.

Figure 1 illustrates the methodology of the technique in more detail, using the photodissociation of a generic AB^- diatomic as an example. In this example, the anion is created in its ground electronic state, excited with a femtosecond pump pulse to a dissociative electronic state, and monitored with a femtosecond probe pulse at various delay times. Unlike the pump pulse, the probe pulse has enough energy to detach the excess electron and project the evolving wavefunction onto the low-lying neutral states. The energies of the detached electrons are measured to give a time-dependent photoelectron spectrum. In the example of Fig. 1, detachment at early delay times will produce a complicated photoelectron spectrum because detachment occurs to all the neutral vibrational states. But at long delay times, when the wavepacket represents

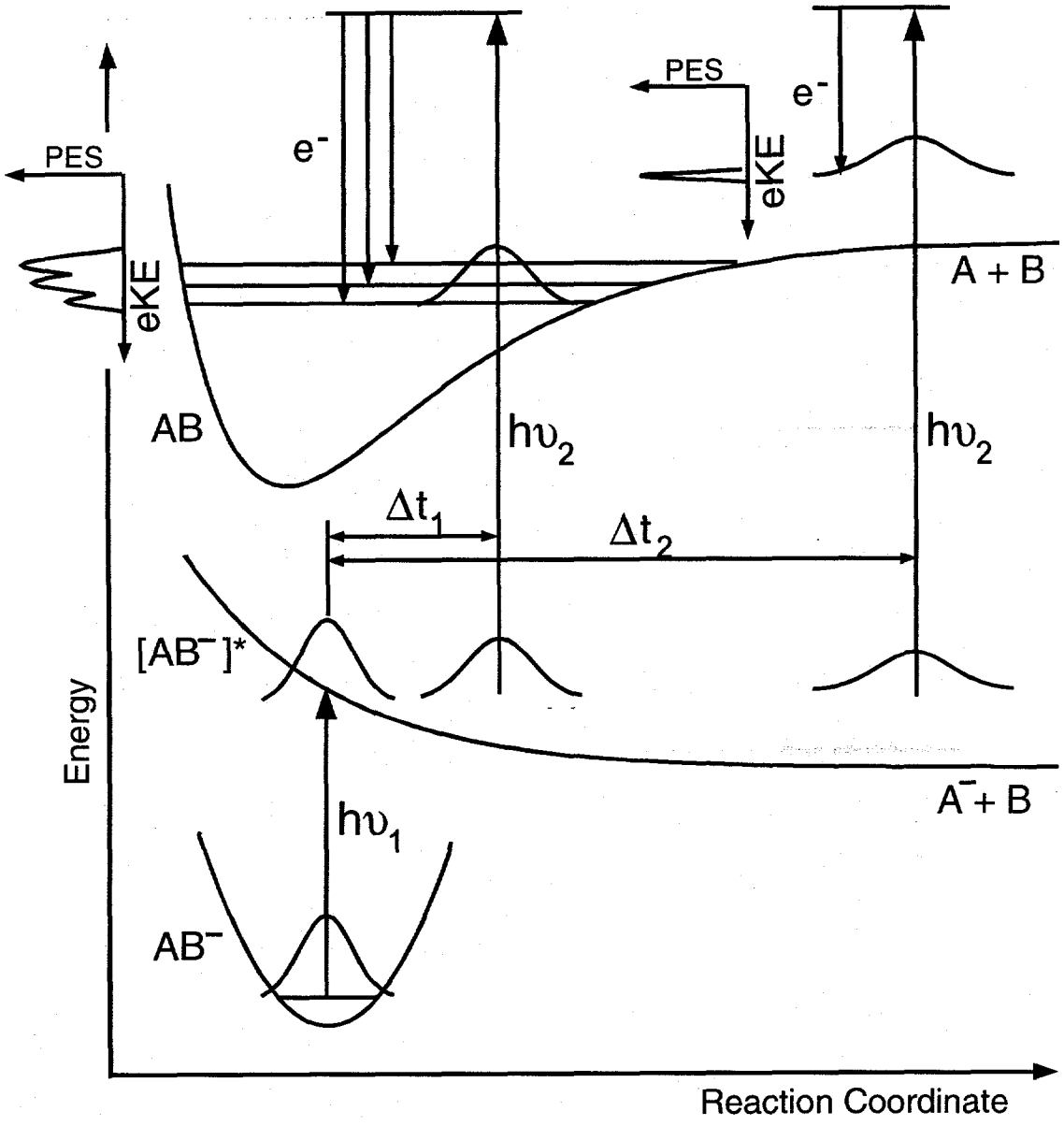

Figure 1. Methodology of femtosecond photoelectron spectroscopy.

dissociated A^- + B products, the spectrum will only consist of a single peak due to detachment of the atomic A^- species. By varying the pump-probe delay times, the dynamics can be monitored throughout the dissociation process. We demonstrate in Chapter 4 that when the neutral states are well characterized, as is often the case, the FPE spectra can be simulated to determine quantitative anion excited states.

If the probe pulse has sufficient energy to detach the ground state, FPES can monitor ground state dynamics as well. Ground state dynamics can be a result of both solvent and laser induced effects. For example, in addition to the excited state processes initiated by the pump pulse, higher order interactions often create a ground state wavepacket by resonance impulsive stimulated Raman scattering (RISRS).[21] When this process is active, oscillations are observed in the time-dependent photoelectron spectra with a period inversely proportional to the υ=0-1 ground state frequency (Chapter 3). We have also demonstrated that stimulated emission pumping (SEP) can be used to selectively populate higher vibrational states by using an additional laser pulse that coherently transfers excited state population back to the ground state. In such experiments, frequencies lower than that of the fundamental are observed due to the anharmonicity of the potential. We demonstrate in Chapter 5 that by measuring the frequency as a function of vibrational energy, a quantitative ground state potential for I_2^- can be determined. Finally, cluster experiments often involve recombination and relaxation on the ground state, and these processes can be monitored with photoelectron spectroscopy as well (Chapter 7).

Hence, FPES applied to anions is a very powerful tool for determining quantitative potential energy surfaces and studying cluster solvation processes. Not only does it incorporate the inherent mass resolution associated with anion experiments, but

also its probe technique, photoelectron spectroscopy, is particularly sensitive to the local environment of the excess electron in the cluster. As we show in later chapters of this dissertation, it is not limited to studies on diatomics, as presented in the above example. We have also used it to study the photodissociation of a polyatomic (Chapter 8), initiate and probe bimolecular reactions,[22] and study the charge transfer processes associated with detachment of I^- in size-selected clusters (Chapters 9 & 10). In the latter experiments, the photoelectron spectra monitor the excess electron as it becomes trapped and solvated by cluster rearrangement.

2. Solvent/solute effects on photodissociation dynamics

Our interest in the solvent effects associated with photodissociation dynamics has been spurred by a number of insightful experiments on neutral and negative ion systems in both the gas and condensed phases. A landmark system that has led to a detailed understanding of many solvent/solute effects is the photolysis of I_2, carried out in the gas phase,[23-26] clusters,[27-30] liquids,[31-33] and matrices.[34-36] From the gas phase experiments, extremely accurate potentials have been derived,[23-25] and a dissociation time of several hundred femtoseconds has been measured.[26] In non-polar solvents, dissociation is followed by caging and curve crossing to the ground electronic state within 2 ps;[31] vibrational relaxation then occurs over the next 50 to 900 ps,[32] depending on the solvent. Insight into the condensed phase processes has been provided by photolysis studies of I_2 in clusters,[27,28] and it has been shown that even the weak interaction of a single argon atom can cause caging by inducing non-adiabatic interactions that lead to a curve crossing onto a bound potential.[29,30,37,38]

Despite the solvent induced dynamics described above, the solvent/solute coupling for I_2 is relatively weak, and the electronic structure of I_2 is largely decoupled from the solvent.[35,39] Systems that undergo a change in charge distribution upon dissociation will be affected more strongly. For example, the potential energy surfaces of HgBr fragments formed from dissociation of $HgBr_2$ are modified during the course of the reaction by solvent reorganization, leading to chirped wavepacket dynamics.[40] Anions also have strong solvent/solute interactions which have been explored in cluster experiments, for example, on $Br_2^-(CO_2)_n$,[41] $I_2^-(CO_2)_n$,[42,43] $I_2^-(Ar)_n$,[44,45] $ICl^-(CO_2)_n$,[46] and in liquid phase studies on I_2^-,[47-49] I_3^-,[50-53] O_3^-,[54] N_3^-,[55] and ClO^-.[56] In these systems, vibrational relaxation rates are an order of magnitude faster, and the potentials more strongly affected by solvent, than those of their respective neutral counterparts.[8]

Much of the work presented in this thesis has been motivated by a small number of time-resolved photodissociation experiments on negative ions in clusters and solution. In one set of experiments, Lineberger and coworkers have studied the photodissociation of I_2^- in CO_2 and Ar clusters,[42-44,57,58] which is illustrated in Fig. 2. In their work, a single laser pulse excited I_2^- from the $\tilde{X}\ ^2\Sigma_u^+$ ground state to the $\tilde{A}'\ ^2\Pi_{g,1/2}$ excited state, and the resulting photofragments were measured using mass spectrometry.[42,58] This allowed the branching ratio between caged and uncaged products to be monitored as a function of cluster size and type. They found that a single solvent shell was sufficient to produce complete caging of the chromophore. In the case of Ar solvation, inconclusive evidence was also found for recombination on the first excited state. In a second set of experiments, but using a probe laser to time resolve any recombined products, they determined that the time required for recombination and vibrational relaxation is 130 ps for $I_2^-(Ar)_{20}$ and 1.3 ps for $I_2^-(CO_2)_{16}$.

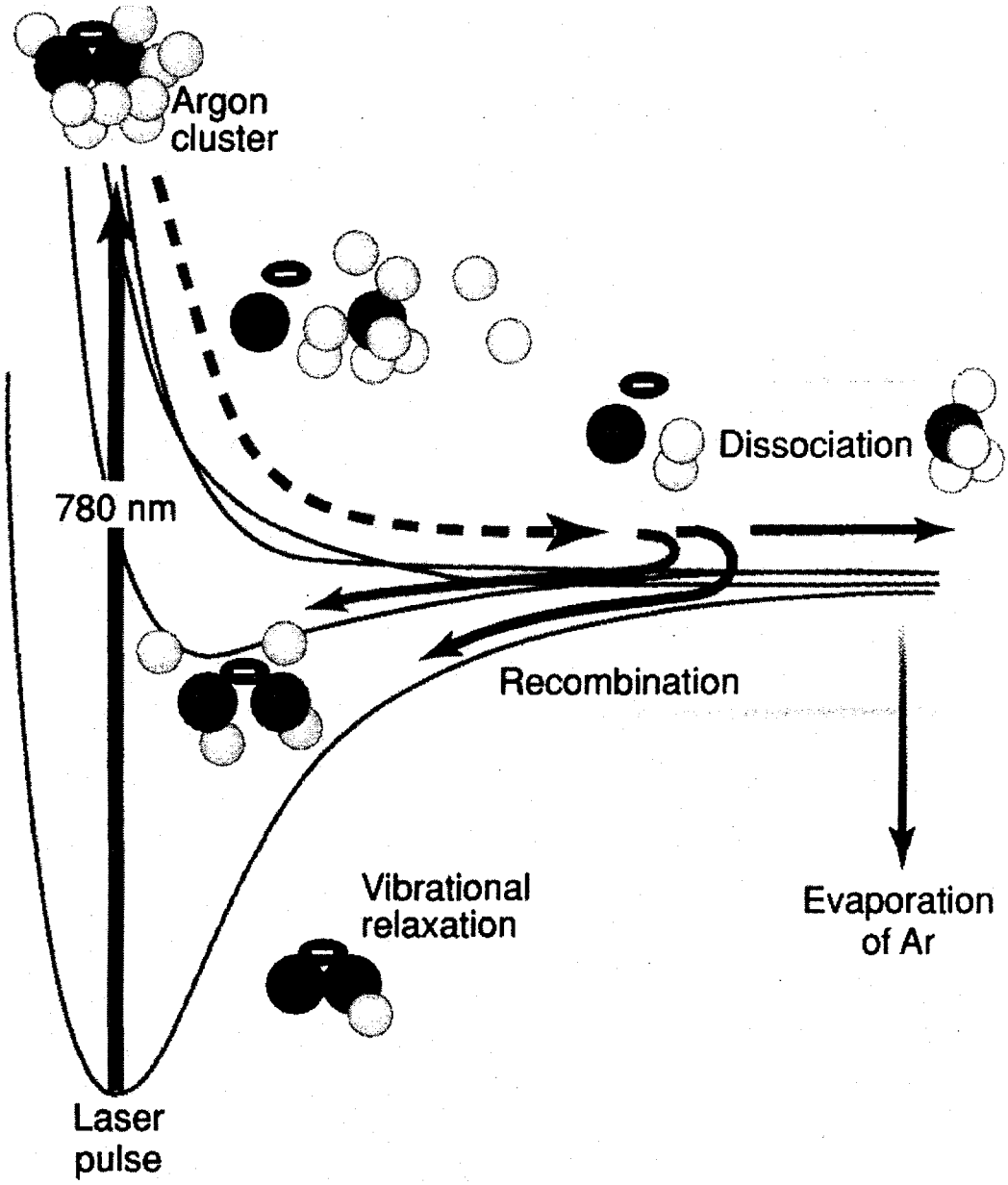

Figure 1.1 Schematic of $I_2^-(Ar)_{20}$ cluster dynamics. Courtesy of Faeder and Parson, Science, 276, 1660 (1997).

The relaxation rates measured by Lineberger and coworkers for $I_2^-(CO_2)_n$ clusters are comparable to rates measured in liquid phase experiments. In polar and non-polar solvents, Barbara and coworkers[47-49] used infrared probe wavelengths to monitor the relaxation time of vibrational states below υ=15. They found that internal conversion, geminate recombination, and vibrational relaxation in the top 70% of the ground state occur within 300 fs, and the remaining vibrational relaxation takes place with a time constant of 3 ps. Banin *et al.* found a similar time constant for vibrational relaxation of I_2^- generated by photolysis of I_3^- in ethanol.[59] However, in the I_3^- experiments, the photolysis reaction directly produces I_2^- products that exhibit coherent vibrational motion.[50,60] At the earliest observation time (~500 fs) the products are in an average vibrational state of υ=12, and pure dephasing irreversibly destroys the coherent motion within 4 ps. The dynamics before 500 fs are less well understood.

Insight into the nature of the geometries, electronic structure, and dissociation dynamics of the $I_2^-(solvent)_n$ systems has been made through theoretical models and simulations. Amar and Perrera were the first to focus on initial cluster geometries, time scales for vibrational relaxation, and solvent evaporation on the ground electronic state.[61] Their model relied on partial charges associated with each iodine atom, although the solvent itself could not polarize the solute. The work of Parson and coworkers,[57,62-65] and Coker and coworkers[66-68] refined and extended these calculations. Both groups calculated cluster geometries similar to those of Amar and Perrera, but also considered the importance and time-scale of non-adiabatic transitions that may occur after photodissociation. In the model developed by Parson and coworkers, the polarization of both the solvent and solute is included, and a two-dimensional charge-switching function allows the solute's electronic structure to be directly influenced by the solvent. Their

treatment has revealed the importance of "anomalous charge switching" in the dynamics that occur on the $\tilde{A}'\,^2\Pi_{g,1/2}$ excited state; the negative charge that is primarily located on the most solvated iodine atom switches to the less solvated atom upon excitation.

3. Charge-transfer-to-solvent bands and the solvated electron

A dramatic example of a system with strong solvent/solute interactions is that of the solvated electron.[69] The solvated electron is formed in polar solvents, most notably water, that rearrange to trap and stabilize the electron, giving rise to ground and excited electronic states separated by ~1.5 eV.[70] Since the electronic states are formed by solvent/solute interactions, the solvent is very sensitive to excitation between the ground and excited states. This has spurred numerous experimental and theoretical studies exploring solvent dynamics.[71-78] Furthermore, cluster studies have been undertaken to determine the minimum number of solvent molecules needed to create stable ground and excited electronic surfaces; because a single water molecule does not bind an electron, the stability must arise from cooperative and multibodied interactions requiring some finite number of solvent molecules. Haberland and coworkers were the first to observe finite sized water cluster anions using mass spectroscopy,[79,80] and it is generally believed that a minimum of six water molecules are needed to localize the electron into a partially solvated state.[81,82] However, Johnson and coworkers may have found experimental evidence for linear chain isomers.[83]

The bulk studies require a method for generating excess electrons. One such method is photodetachment of a halide anion, a typical choice being the iodide ion. In isolation, iodide has no electronic states below the detachment threshold. However, in polar solvents, absorption bands appear in the ultraviolet below the vacuum detachment

energy,[84] and excitation into these states gives rise to solvated electrons.[85-88] Hence, they are termed charge-transfer-to-solvent (CTTS) bands. Theoretical studies predict that the lower CTTS orbital is centered on the iodine atom, but delocalized over the first solvent shell oriented around the ion in its ground state.[89,90] Non-adiabatic transitions and solvent rearrangement lead to its decay and the appearance of solvated electrons.[91,92]

The utility of photodetaching dissolved anions to produce solvated electrons has prompted related studies in gas phase clusters. Johnson and coworkers have measured the photoelectron yield as a function of detachment energy for $I^-(H_2O)_{n\leq 4}$ clusters, and found quasi-bound excited states lying just below the vertical detachment energies.[93] The states are thought to be precursors to the bulk CTTS bands, because they are diffuse and appear to be evolving towards the bulk absorption spectrum. However, it is unclear whether they are due to partially solvated or dipole bound electrons. In the latter case, the excess electron resides in diffuse orbitals located predominantly outside the cluster, bound by the large dipole moment of the solvent network.[94]

In bulk and clustered water, the solvated electron is stabilized by the charge-dipole interaction, but electrons can also be stabilized in bulk xenon by the charge-induced dipole interaction.[95,96] In this case, the electronic state takes on a much different character, and the electron is predicted to reside in narrow channels between the xenon atoms.[97-99] Similar to the water studies, xenon cluster studies have been performed; negatively charged xenon clusters have been observed,[100] and so have CTTS bands in $I^-(Xe)_n$ clusters.[101,102]

4. Thesis overview

The studies presented in the remainder of this thesis have been motivated by the work outlined in Sections 2 and 3. Our studies provide insight into these systems, and serve to develop our technique and explore its merits. In Chapters 3, 4, and 5, the sensitivity of our technique to ground and excited state dynamics is examined for isolated I_2^-. In Chapters 3 and 4, potential energy curves for the I_2^- $\tilde{X}\ ^2\Sigma_u^+$ ground and $\tilde{A}'\ ^2\Pi_{g,1/2}$ second excited states have been constructed. To accomplish this, resonance impulsive stimulated Raman spectroscopy (RISRS) was used to determine the ground υ=0-1 vibrational frequency in Chapter 3, and the FPE spectra of the dissociation dynamics were modeled to determine an accurate excited state potential in Chapter 4. In Chapter 5 we revisit the ground state to better characterize the potential near the dissociation limit using stimulated emission pumping (SEP). Prior to our work, these states were poorly characterized, although reliable surfaces are critical for accurate analysis and modeling of the cluster and solution experiments.

In Chapters 6 and 7, solvent effects are explored in experiments probing the static effects of Ar and CO_2 on the ground electronic state of I_2^- and the dynamics of I_2^- photodissociation, respectively. For the ground state, the vibrational frequency of I_2^- embedded in differing size Ar and CO_2 clusters was measured. We found that the I_2^- frequency blueshifts, and that the degree of blueshifting depends on the number of solvent molecules, strength of attraction to the solute, and geometry of the solvent with respect to the I_2^- chromophore. In Chapter 7, the photodissociation studies on $I_2^-(Ar)_n$ clusters originally performed by Lineberger and coworkers were repeated using FPES. In contrast to their mass spectrometric work, our experiments give detailed information on

clusters in which neither caging nor recombination occurs. When recombination does occur, we are able to determine the electronic state of the solute at each delay time and the approximate amount of solute vibrational energy and number of solvent molecules remaining in the cluster. The major findings here are the observation of recombination on the $\tilde{A}\ ^2\Pi_{g,3/2}$ 1st excited state, and an estimate of the vibrational relaxation rate as a function of quantum state (instead of the overall relaxation rate).

Chapter 8 presents the first study on the photodissociation dynamics of the isolated I_3^- anion. As discussed above, the dynamics of the I_3^- chromophore in solution have received much attention. However, the effects of solvent on the dissociation process and vibrational distribution of I_2^- products is vague, although there is evidence for solvent induced symmetry breaking. Our gas phase measurements determined that the I_2^- vibrational distribution is much higher than in solution and that the lack of solvent allows equal amounts of two and three body dissociation to occur, suggesting that solvent induced symmetry breaking is indeed active in the condensed phase.

Finally, Chapters 9 and 10 present studies on the CTTS states associated with I^- in H_2O and Xe clusters, respectively. For the $I^-(Xe)_n$ work, lifetimes for both the $^2P_{1/2}$ and $^2P_{3/2}$ CTTS states were measured. The $^2P_{1/2}$ lifetimes are on the order of several picoseconds, and increase slowly with cluster size. On the other hand, the $^2P_{3/2}$ states show no loss of population up to the longest times measured, 200 ps. Neither system displays cluster reorganization. In comparison, the dynamics associated with the $I^-(H_2O)_n$ clusters are much more complex. For $n \leq 4$, simple decay kinetics are observed. However, for $n \geq 5$, non-adiabatic dynamics and solvent reorganization is observed. We attribute this to formation of a partially solvated electron, making the smallest cluster analog of electron solvation five water molecules.

5. References

[1] For example, see the centennial issue of J. Phys. Chem. **100,** 12691 (1996).

[2] F. F. Crim, J. Phys. Chem. **100,** 12725 (1996).

[3] P. Houston, J. Phys. Chem. **100,** 12757 (1996).

[4] L. J. Butler and D. M. Neumark, J. Phys. Chem. **100,** 12801 (1996).

[5] A. H. Zewail, J. Phys. Chem. **100,** 12701 (1996).

[6] J. Castleman, A. W. and J. Bowen, K. H., J. Phys. Chem. **100,** 12911 (1996).

[7] Z. Bacic and R. E. Miller, J. Phys. Chem. **100,** 12945 (1996).

[8] R. M. Stratt and M. Maroncelli, J. Phys. Chem. **100,** 12981 (1996).

[9] G. A. Voth and R. M. Hochstrasser, J. Phys. Chem. **100,** 13034 (1996).

[10] B. J. Greenblatt, M. T. Zanni, and D. M. Neumark, Chem. Phys. Lett. **258,** 523 (1996).

[11] B. Kim, C. P. Schick, and P. M. Weber, J. Chem. Phys. **103,** 6903 (1995).

[12] D. R. Cyr and C. C. Hayden, J. Chem. Phys. **104,** 771 (1996).

[13] T. Baumert, R. Thalweiser, and G. Gerber, Chem. Phys. Lett. **209,** 29 (1993).

[14] I. Fischer, D. M. Villeneuve, M. J. J. Vrakking, and A. Stolow, J. Chem. Phys. **102,** 5566 (1995).

[15] P. Ludowise, M. Blackwell, and Y. Chen, Chem. Phys. Lett. **258,** 530 (1996).

[16] A. Assion, M. Geisler, J. Helbing, V. Seyfried, and T. Baumert, Phys. Rev. A **54,** R4605 (1996).

[17] G. Gantefor, S. Kraus, and W. Eberhardt, J. Elect. Spect. Rel. Phen. **88,** 35 (1998).

[18] Y. Arasaki, K. Takatsuka, K. Wang, and V. McKoy, Chem. Phys. Lett. **302,** 363 (1999).

[19] P. Farmanara, W. Radloff, V. Stert, H.-H. Ritze, and I. V. Hertel, J. Chem. Phys. **111,** 633 (1999).

[20] T. Suzuki, L. Wang, and H. Kohguchi, J. Chem. Phys. **111,** 4859 (1999).

[21] U. Banin, A. Bartana, S. Ruhman, and R. Kosloff, J. Chem. Phys. **101,** 8461 (1994).

[22] Not reported in this dissertation.

[23] F. Martin, R. Bacis, S. Churassy, and J. Verges, J. Mol. Spectrosc. **116,** 71 (1986).

[24] J. Tellinghuisen, S. Fei, X. Zheng, and M. C. Heaven, Chem. Phys. Lett. **176,** 373 (1991).

[25] D. R. T. Appadoo, R. J. Leroy, P. F. Bernath, S. Gerstenkorn, P. Luc, J. Verges, J. Sinzelle, J. Chevillard, and Y. Daignaux, J. Chem. Phys. **104,** 903 (1996).

[26] R. M. Bowman, M. Dantus, and A. H. Zewail, Chem. Phys. Lett. **161,** 297 (1989).

[27] Q. L. Liu, J. K. Wang, and A. H. Zewail, Nature **364,** 427 (1993).

[28] J.-K. Wang, Q. L. Liu, and A. H. Zewail, J. Phys. Chem. **99,** 11309 (1995).

[29] K. L. Sanger, G. M. McClelland, and D. R. Herschbach, J. Phys. Chem. **85,** 3333 (1981).

[30] J. Valentini and J. Cross, J. Chem. Phys. **77,** 572 (1982).

[31] T. J. Chuang, G. W. Hoffman, and K. B. Eisenthal, Chem. Phys. Lett. **25,** 201 (1974).

[32] D. J. Nesbitt and J. T. Hynes, J. Chem. Phys. **77,** 2130 (1982).

[33] A. L. Harris, J. K. Brown, and C. B. Harris, Annu. Rev. Phys. Chem. **39,** 341 (1988).

[34] R. Zadoyan, Z. Li, P. Ashjian, C. C. Martens, and V. A. Apkarian, Chem. Phys. Lett. **218,** 504 (1994).

[35] Z. Li, R. Zadoyan, V. A. Apkarian, and C. C. Martens, J. Phys. Chem. **99,** 7453 (1995).

[36] R. Zadoyan, Z. Li, C. C. Martens, and V. A. Apkarian, J. Chem. Phys. **101,** 6648 (1994).

[37] M. L. Burke and W. Klemperer, J. Chem. Phys. **98,** 1797 (1993).

[38] A. A. Buchachenko and N. F. Stepanov, J. Chem. Phys. **104,** 9913 (1996).

[39] Q. Liu, J.-K. Wong, and A. H. Zewail, J. Phys. Chem. **99,** 11321 (1995).

[40] M. Lim, M. F. Wolford, P. Hamm, and R. H. Hochstrasser, Chem. Phys. Lett. **290,** 355 (1998).

[41] M. L. Alexander, N. E. Levinger, M. A. Johnson, D. Ray, and W. C. Lineberger, J. Chem. Phys. **88,** 6200 (1988).

[42] J. M. Papanikolas, J. R. Gord, N. E. Levinger, D. Ray, V. Vorsa, and W. C. Lineberger, J. Phys. Chem. **95,** 8028 (1991).

[43] J. M. Papanikolas, V. Vorsa, M. E. Nadal, P. J. Campagnola, H. K. Buchenau, and W. C. Lineberger, J. Chem. Phys. **99,** 8733 (1993).

[44] V. Vorsa, S. Nandi, P. J. Campagnola, M. Larsson, and W. C. Lineberger, J. Chem. Phys. **106,** 1402 (1997).

[45] A. Sanov, T. Sanford, S. Nandi, and W. C. Lineberger, J. Chem. Phys. **111,** 664 (1999).

[46] M. E. Nadal, P. D. Kleiber, and W. C. Lineberger, J. Chem. Phys. **105,** 504 (1996).

[47] A. E. Johnson, N. E. Levinger, and P. F. Barbara, J. Phys. Chem. **96,** 7841 (1992).

[48] J. C. Alfano, Y. Kimura, P. K. Walhout, and P. F. Barbara, Chem. Phys. **175,** 147 (1993).

[49] P. K. Walhout, J. C. Alfano, K. A. M. Thakur, and P. F. Barbara, J. Phys. Chem. **99,** 7568 (1995).

[50] U. Banin, A. Waldman, and S. Ruhman, J. Chem. Phys. **96,** 2416 (1992).

[51] U. Banin and S. Ruhman, J. Chem. Phys. **98,** 4391 (1993).

[52] T. Kühne and P. Vöhringer, J. Chem. Phys. **105,** 10788 (1996).

[53] T. Kühne, R. Küster, and P. Vöhringer, Chem. Phys. **233,** 161 (1998).

[54] P. K. Walhout, C. Silva, and P. F. Barbara, J. Phys. Chem. **100,** 5188 (1996).

[55] J. C. Owrutsky, D. Raftery, and R. M. Hochstrasser, Annu. Rev. Phys. Chem. **45,** 519 (1994).

[56] M. H. Lim, S. Gnanakaran, and R. M. Hochstrasser, J. Chem. Phys. **106,** 3485 (1997).

[57] J. M. Papanikolas, P. E. Maslen, and R. Parson, J. Chem. Phys. **102,** 2452 (1995).

[58] V. Vorsa, P. J. Campagnola, S. Nandi, M. Larsson, and W. C. Lineberger, J. Chem. Phys. **105,** 2298 (1996).

[59] U. Banin, R. Kosloff, and S. Ruhman, Chem. Phys. **183,** 289 (1994).

[60] U. Banin and S. Ruhman, J. Chem. Phys. **99,** 9318 (1993).

[61] F. G. Amar and L. Perera, Z. Phys. D **20,** 173 (1991).

[62] J. Faeder, N. Delaney, P. E. Maslen, and R. Parson, Chem. Phys. Lett. **270,** 196 (1997).

[63] J. Faeder and R. Parson, J. Chem. Phys. **108,** 3909 (1998).

[64] N. Delaney, J. Faeder, and R. Parson, J. Chem. Phys. **111,** 452 (1999).

[65] N. Delaney, J. Faeder, and R. Parson, J. Chem. Phys. **111,** 651 (1999).

[66] V. S. Batista and D. F. Coker, J. Chem. Phys. **106,** 7102 (1997).

[67] V. S. Batista and D. F. Coker, J. Chem. Phys. **110,** 6583 (1999).

[68] C. J. Margulis and D. F. Coker, J. Chem. Phys. **110,** 5677 (1999).

[69] W. Weyl, Poyg. Ann. **123,** 350 (1864).

[70] E. J. Hart and J. W. Boag, J. Am. Chem. Soc. **84,** 4090 (1962).

[71] A. Migus, Y. Gauduel, J. L. Martin, and A. Antonetti, Phys. Rev. Lett. **58,** 1559 (1987).

[72] M. U. Sander, K. Luther, and J. Troe, J. Phys. Chem. **97,** 11489 (1993).

[73] A. Staib and D. Borgis, J. Chem. Phys. **103,** 2642 (1995).

[74] X. Shi, F. H. Long, H. Lu, and K. B. Eisenthal, J. Phys. Chem. **100,** 11903 (1996).

[75] P. Graf, A. Nitzan, and G. H. F. Diercksen, J. Phys. Chem. **100,** 18916 (1996).

[76] L. Turi, P. Holpar, E. Keszei, C. Pepin, and D. Houde, J. Phys. Chem. A **101,** 5469 (1997).

[77] L. Turi, A. Mosyak, and P. J. Rossky, J. Chem. Phys. **107,** 1970 (1997).

[78] C. Silva, P. K. Walhout, P. J. Reid, and P. F. Barbara, J. Phys. Chem. A **102,** 5701 (1998).

[79] M. Armbruster, H. Haberland, and H.-G. Schindler, Phys. Rev. Lett. **47,** 323 (1981).

[80] H. Haberland, C. Ludewigt, H.-G. Schindler, and D. R. Worsnop, J. Chem. Phys. **81,** 3742 (1984).

[81] N. R. Kestner and J. Jortner, J. Phys. Chem. **88,** 3818 (1984).

[82] S. Lee, J. Kim, S. J. Lee, and K. S. Kim, Phys. Rev. Lett. **79,** 2038 (1997).

[83] P. Ayotte, G. H. Weddle, C. G. Bailey, M. A. Johnson, F. Vila, and K. D. Jordan, J. Chem. Phys. **110,** 6268 (1999).

[84] J. Franck and G. Scheibe, Z. Phys. Chem. A **139,** 22 (1928).

[85] J. Jortner, M. Ottolenghi, and G. Stein, J. Phys. Chem. **68,** 247 (1964).

[86] F. H. Long, X. Shi, H. Lu, and K. B. Eisenthal, J. Phys. Chem. **98,** 7252 (1994).

[87] Y. Gaudeul, H. Gelabert, and M. Ashokkumar, Chem. Phys. **197,** 167 (1995).

[88] J. A. Kloepfer, V. H. Vilchiz, V. A. Lenchenkov, and S. E. Bradforth, Chem. Phys. Lett. **298,** 120 (1998).

[89] W.-S. Sheu and P. J. Rossky, J. Am. Chem. Soc. **115,** 7729 (1993).

[90] W.-S. Sheu and P. J. Rossky, J. Phys. Chem. **100,** 1295 (1996).

[91] W.-S. Sheu and P. J. Rossky, Chem. Phys. Lett. **213,** 233 (1993).

[92] A. Staib and D. Borgis, J. Chem. Phys. **104,** 9027 (1996).

[93] D. Serxner, C. E. H. Dessent, and M. A. Johnson, J. Chem. Phys. **105,** 7231 (1996).

[94] C. Desfrancois, Phys. Rev. Lett. **73,** 2436 (1994).

[95] L. Kevan, J. Phys. Chem. **76,** 3830 (1972).

[96] B. Baron, D. Hoover, and F. Williams, J. Chem. Phys. **68,** 1997 (1978).

[97] D. F. Coker, B. J. Berne, and D. Thirumalai, J. Chem. Phys. **86,** 5689 (1987).

[98] G. J. Martyna and B. J. Berne, J. Chem. Phys. **88,** 4516 (1988).

[99] G. J. Martyna and B. J. Berne, J. Chem. Phys. **90,** 3744 (1989).

[100] H. Haberland, T. Kolar, and T. Reiners, Phys. Rev. Lett. **63,** 1219 (1989).

[101] I. Becker, G. Markovich, and O. Cheshnovsky, Phys. Rev. Lett. **79,** 3391 (1997).

[102] I. Becker and O. Cheshnovsky, J. Chem. Phys. **110,** 6288 (1999).

Chapter 2. Experimental Apparatus

The experimental apparatus consists of two major components: a "magnetic bottle" negative ion photoelectron spectrometer, and a high (1 kHz) repetition rate, sub-100 fs laser. The spectrometer shares several features with spectrometers currently operating in our group laboratories,[1] as well as others,[2-4] but is optimized to be compatible with the high laser repetition rate and low photoelectron yield expected for a two-color pump-probe experiment. Many aspects of the spectrometer and laser have been detailed in B. Jefferys Greenblatt's thesis.[5] In this thesis, a general overview of the instrument will be given, followed by items not covered by Greenblatt, including the circuit designs for the interlock system, deflectors, pulsed valve, extraction and acceleration plates, and the push-pull MOSFET circuit configurations used in the mass gate and decelerator ion optics. A brief comparison between push-pull configurations triggered using optoisolators versus ferrite coils, and powered by homemade versus commercial supplies is also given.

1. General Overview

A schematic of the photoelectron spectrometer is shown in Fig. 1. It consists of an ion source region, time-of-flight (TOF) mass spectrometer, photofragment analyzer, and magnetic bottle TOF photoelectron spectrometer, divided into five differentially pumped chambers. The source chamber, 0^{th} differential, and 1^{st} differential chambers comprise the low vacuum side of the instrument and are pumped with diffusion pumps. The remaining 2^{nd} differential and detector chambers constitute the high vacuum side of the spectrometer. A pneumatic gate valve separates the high and low vacuum regions.

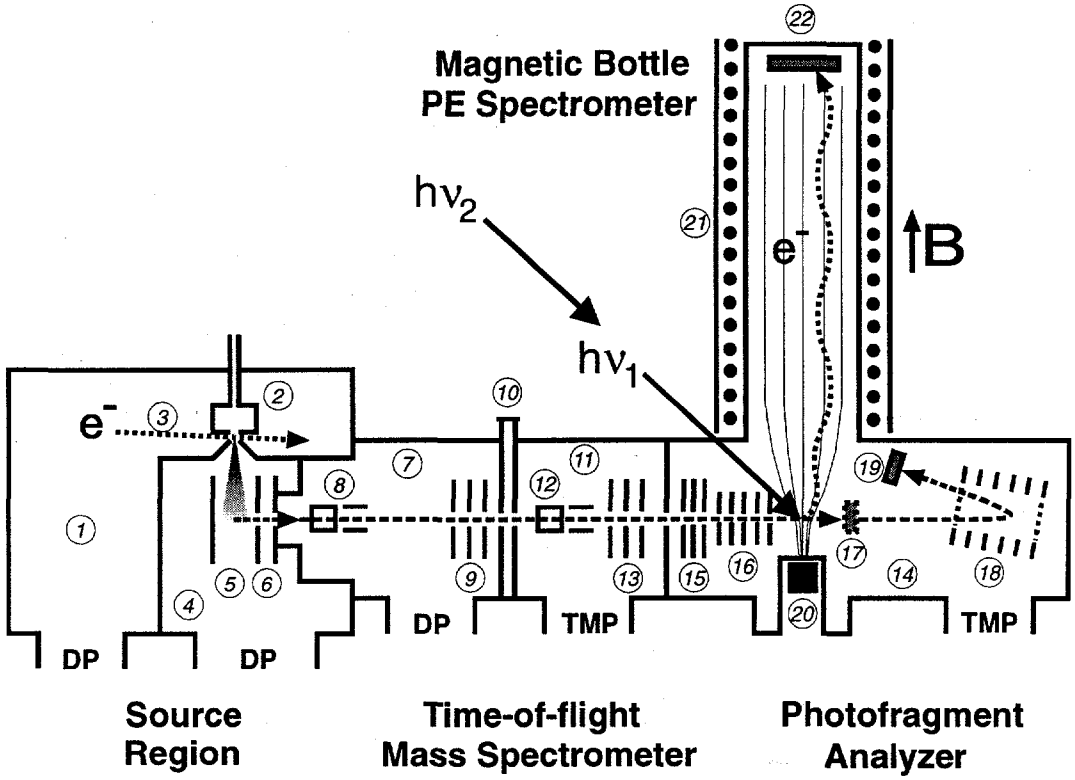

1. Source Region Chamber
2. Pulsed Valve
3. Electron Beam
4. 0^{th} Differential Chamber
5. Extraction Plate
6. Acceleration Plate
7. 1^{st} Differential Chamber
8. Ion Deflectors
9. Einzel Lense
10. Gate Valve
11. 2^{nd} Differential Chamber
12. Ion Deflectors
13. Einzel Lense
14. Detector Chamber
15. Mass Gate
16. Deceleration Stack
17. Retractable Ion MCP
18. Reflectron
19. Photofragment Ion MCP
20. Permanent Magnet
21. Solenoid
22. Electron MCP

Figure 1. Femtosecond Photoelectron Spectrometer

Because photoelectron spectroscopy requires low pressure conditions (<$1x10^{-8}$ Torr), the high vacuum region is pumped by turbo molecular pumps and is baked out for several days at ~100°C after being exposed to atmosphere.

Anions and cluster anions are generated by passing 10-40 psig of backing gas, seeded with the species under study, through the piezoelectric pulsed valve and into the source chamber. To match the laser repetition rate (typically 500 Hz), the pulsed valve is triggered by a delay generator (Stanford Research Systems DG535) that is in turn triggered by the laser's pockels cell driver (DT-505) (for an overview of the timing mechanism, see Greenblatt). The method of seeding the backing gas varies with experiment (see Chapters 3, 6, 9, 10). For example, to make I_2^-, we pass argon carrier gas over crystalline iodine; to make $I^-(D_2O)_n$ clusters, N_2 is passed over a reservoir of CH_3I and a separate reservoir of D_2O. The mixture supersonically expands through a 200 μm orifice in the pulsed valve, and the resulting free jet is crossed with a 1.5 keV electron beam just downstream of the nozzle.

The resulting plasma cools to produce negative ions and their clusters, and the center portion of the beam passes through a 5 mm skimmer into the zeroeth differential chamber. The delay generator triggers the extraction and acceleration plates approximately 500 μs after the pulsed valve is opened, injecting the negative ions into the Wiley-McLaren TOF mass spectrometer[6] consisting of three differentially pumped regions. In the first differential region, the ions are guided by a pair of deflectors through an einzel lense and into the second differential chamber. A second set of deflectors steers the ions through a second einzel lens kept grounded (voltage on the 2nd einzel lense increases the signal at the ion multichannel plate (MCP), but decreases the photoelectron

yield), and into the detector differential region. Since the lighter ions travel faster than the heavier ones, they separate out by mass and discrete peaks are observed on the ion MCP as a function of time. Only the cluster of interest will be intercepted by the pump and probe laser pulses (at the center of the magnetic bottle interaction region) by properly timing the extraction plates trigger relative to the laser.

The magnetic bottle[4,7,8] produces a highly diverging magnetic field in the vicinity where the ions are detached that guides most of the electrons up to the electron MCP, regardless of their original direction, without changing their energies. It consists of a strong, rare earth (8000 G surface flux) permanent magnet located ~3/8" below and a long solenoid ~6" above (creating a field of ~10 G) the interaction region. The electron MCP signal is boosted with a 10x fast preamplifier (Ortec 9301) and recorded by a multichannel scaler (Stanford Research Systems SR430). Although the magnetic bottle collection efficiency is greater than 50%, the velocity of the ions degrades the energy resolution.[4] To minimize this effect, deceleration optics are present to slow the ions just prior to detachment.[5,8] Typical resolution for I_2^- without deceleration is 250 meV for electrons with 1.7 eV of kinetic energy, but resolution down to 75 meV has been obtained by deceleration.[9] A mass gate is also installed so that only the ions of interest are decelerated.

Instead of collecting photoelectrons, photofragments can be monitored by retracting the co-linear ion MCP and allowing the ions to enter the reflectron mass analyzer.[10] The reflectron has a static voltage applied to it, and redirects the ions to a second, off-axis ion MCP. Thus, any daughter ions created by photodissociation of the parent molecules will enter the reflectron as the same time and with the same velocity as

their parents ions. However, the daughter fragments have less mass and will not travel as deep into the reflectron. Hence, they arrive at the second MCP earlier. The reflectron was used to determine the branching ratio between I^- and I_2^- photoproducts from the dissociation of I_3^- (Chapter 8).

The laser pulses are generated from a commercial femtosecond laser system. A Coherent Innova-90 Ar^+ laser pumps a Clark-MXR NJA-5 Ti:Sapphire oscillator. Selected pulses are amplified using a Clark-MXR regenerative amplifier that includes a pulse stretcher and compressor, and is pumped by a Nd:YAG laser. At 790 nm the pulses are typically 80 fs FWHM ($sech^2$) and 1 mJ. The fundamental beam is split into several portions, depending on the experiment. For I_2^- dissociation, ~20% of the fundamental is used as the pump pulse while the remaining 80% is used to generate 3ω at 263 nm using a CSK harmonic generator to act as the probe pulse. Of course the harmonic generator also doubles the fundamental, which, for example, was used as the pump pulse in the I_3^- experiments (Chapter 8). A portion of the fundamental can also be used to pump the Light Conversion TOPAS (Travelling-wave Optical Parametric Amplifier of Superflourescence) to create tunable infrared pulses (which were used as Stokes pulses in Chapter 5) that can be doubled or summed with the fundamental to create tunable visible pulses (to dissociate O_3^-, not reported), or can be quadrupled yielding tunable ultraviolet light (used to in the $I^-(Xe)_n$ experiments, Chapter 10). The relative timing between the pulses used in the experiment are computer controlled with either a Newport motion controller (MM3000) and translation stage (UTM150CC.5HA) and/or an Aerotech controller (U100M-A-40-F1) with one or more translation stages (ATS-100-150). All beams are collinearly recombined and focused into the vacuum chamber. To accurately

determine the temporal overlap of laser pulses inside the machine, two-color above threshold detachment on I^- is used,[11] although cross-correlations before the chamber are routinely used to approximate the time delays.

Oftentimes the pump or probe pulse can independently detach electrons from the negative ion being studied. In this case the spectra are not background free. Background subtraction is typically performed during the experiment using an optical chopper (New Focus 3501) that blocks the pump pulse every other shot. The photoelectron signal is alternately added and subtracted from the multichannel scaler. Background spectra are also simultaneously collected on a digital oscilloscope (Tektronics TDS744A) at an 80 Hz repetition rate and are used for longer-time normalization of the spectra.

2. Interlock Circuit

The most fundamental circuit to the operation of the vacuum system is the interlock circuit. It allows the user to operate the valves that isolate the pumps and differential chambers, provides power to the electronics, and automatically protects the instrument in case of power failure, equipment failure, and pressure bursts by closing valves, shutting off pumps and electronics, and venting the chamber. The interlock vacumm system is roughly divided into two halves: the high and low vacuum sides, which are separated by a pneumatic gate valve. Each side has its own criteria for safe operation and operates independently of the other. In case of an emergency on the low vacuum side, the gate valve closes to isolate the high and low vacuum regions, the source and detector electronics shut off to prevent short circuits, and a warning bell rings. The power to the diffusion pumps may or may not be cut, depending on the origin of the

emergency. On the high vacuum side, in addition to closing the gate valve, cutting the power to the electronics, and ringing the bell, the turbo pumps are turned off and isolated from their mechanical roughing pumps by closing their respective pneumatic valves. After a six second delay, two pneumatic vent valves are opened and the chamber is brought to atmospheric pressure. The extra precautions taken on the high vacuum side are needed to insure that oil from the mechanical pumps does not contaminate the chamber. An interlocked ion gauge on the 1st differential and detector chambers monitors the pressure in the low and high vacuum sides, respectively. If either gauge reads an abnormally high pressure, the emergency effects described above are enacted for the respective vacuum chambers.

A schematic of the interlock circuit is shown in Figs. 2(a) and (b). The power to each pump, valve, and electronic unit is regulated through a relay (#1-11) that is normally open (when no power is present). To close the relay, the respective manual switch and safety switches must all be closed. Upon equipment failure, one or more of the safety switches (e.g. thermocouple, thermal switch, etc.) will open and cut power to the relay, which in turn opens and cuts power to its respective unit. In addition, power is also cut to relays 12A and 12B that regulate the source and detector electronics, emergency bell, and gate valve. If the emergency occurs on the high vacuum side, relay 11 is also opened, and power to the turbo pumps, pneumatic foreline valves, and vent valves is cut, which vents the high vacuum side of the spectrometer as discussed above.

The safety switches differ depending on the type of pump they are monitoring. In the case of the diffusion pumps, a thermal switch and a thermocouple monitor the pump temperature and foreline pressures, respectively. If the pump overheats or the foreline

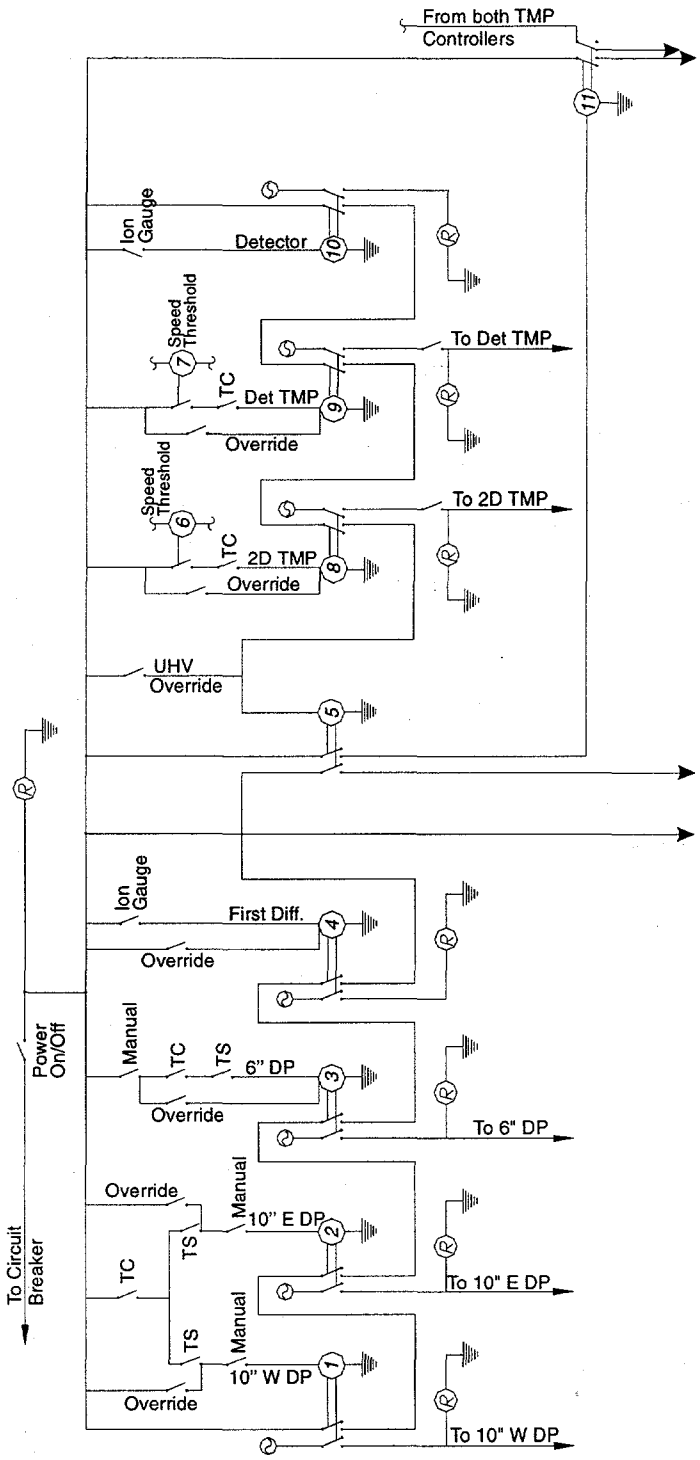

Figure 2a. Interlock box circuit diagram

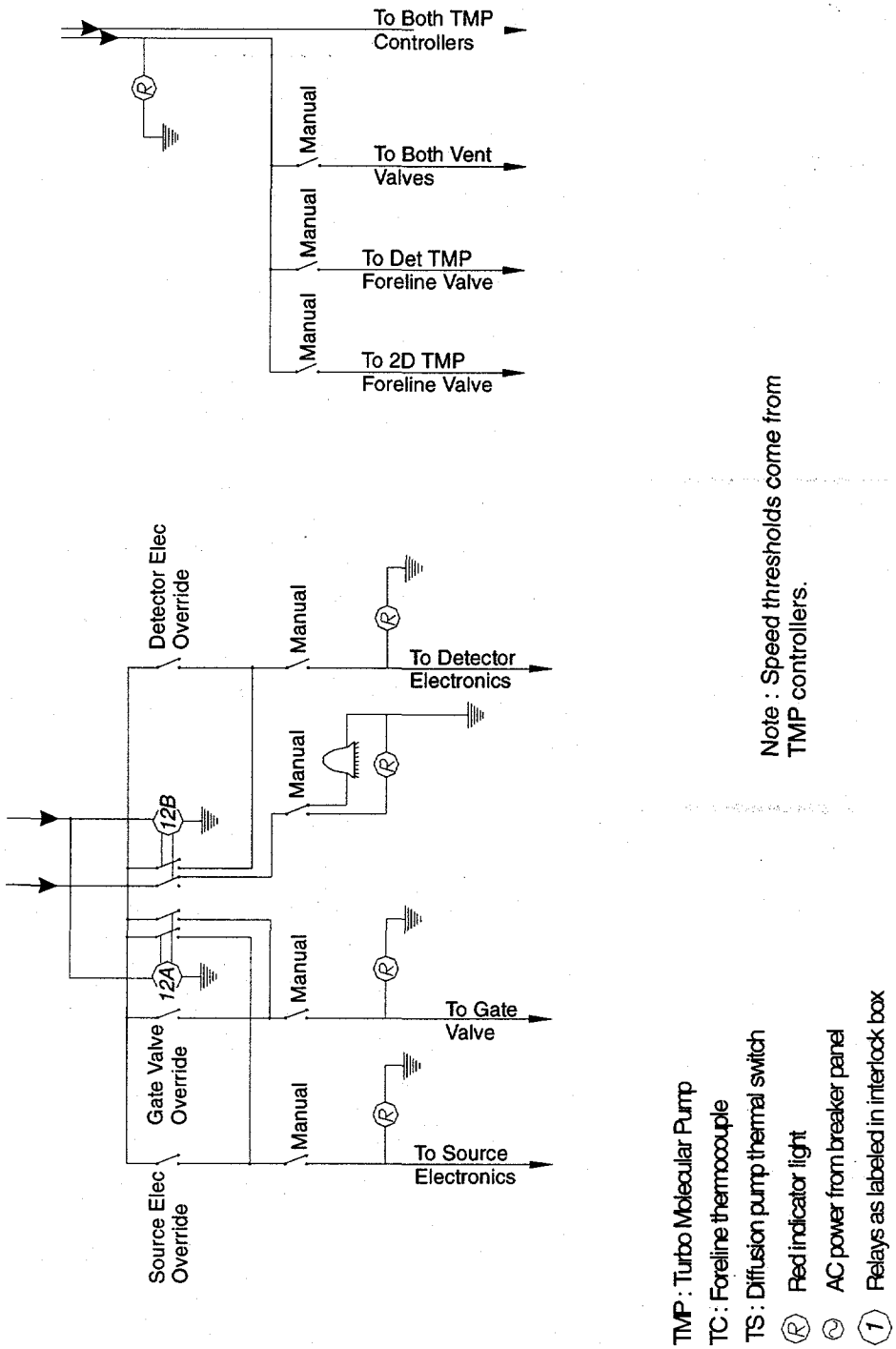

Figure 2b. Interlock box circuit diagram

pressure rises above 0.15 Torr, the appropriate switch opens. Each turbo pump has a thermocouple switch that monitors the foreline pressure and a switch controlled by an extra relay (6 & 7) connected to the turbo pump controllers. The turbo relay switch is opened when the turbo pump speed becomes low, high temperatures are detected, or excess power is being drawn. For pumping down, the controllers are set to close these relays for a limited time, although other controller options are available. All of the safety switches can be manually overridden, which is often necessary when venting the chambers or changing pump oil. The high vacuum side also has a main override that allows the foreline valves and vents valves to be controlled irrespective of the turbo pump conditions.

An ion gauge on each side of the vacuum system also acts as a safety switch. For the low vacuum side, the safety switch is connected to the 1st differential chambers ion gauge and is opened when the pressure reaches above $1x10^{-3}$ Torr. The high vacuum safety switch is connected to the 2nd differential chamber's ion gauge, and is set to $5x10^{-8}$ Torr. Each ion gauge can be overridden; the 1D ion gauge has a manual override while the main override for the high vacuum side serves to override the 2D ion gauge.

Under normal operating conditions red indicators are lit when current is flowing to the respective units. If a circuit breaker or relay is open, the respective light is off. Although not shown in Fig. 2, the override switches also have indicator lights attached that are lit when closed. Hence, in normal operating conditions, all indicators are lit except the override indicators.

3. Fast Pulsing Circuits

Time-of-flight mass spectroscopy is inherently pulsed, and in our setup requires many circuits capable of delivering high voltage electric pulses in short time intervals. The fast switching circuits currently in use operate the pulsed valve, acceleration and extraction plates, mass gate, and deceleration stack. All the circuits utilize fast switching MOSFET transistors (RFP4N100) capable of holding 1 kV of potential and delivering 4.3 A of current in less than 50 ns. By stacking the MOSFETs in series, many kVs of potential can be delivered quickly, and a fast leading edge can be produced (Fig. 3). Or, by using a push-pull configuration, fast leading and falling edges can be obtained (Fig. 4). In this section we introduce the common features shared among the fast switching circuits, followed by diagrams and explanations of each circuit individually.

The MOSFET configuration used to create a fast, high voltage, leading edge (such as is used in the acceleration and extraction circuits) is shown in Fig. 3. It consists of a series of MOSFETs; one transistor for each 1 kV of potential the circuit is to deliver. Each transistor has three inputs: the drain, source, and gate, and is triggered by the rising edge at its gate. When the gate reaches a potential higher than the source, the connection between the drain and source is opened. Because "n" type MOSFETs are used here, the drain must always be at higher potential than the source ("p" type transistors are also available, but cannot hold as much potential). Placed in parallel with each MOSFET is a Zener diode (ZNR 20K102U) to protect against burn out. Several publications also suggest placing resistors and capacitors in parallel to control the current flow,[12-16] but these recommendations have not been explored in the Neumark group.

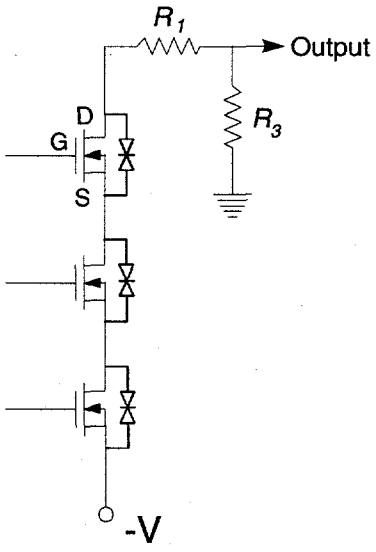

Figure 3 Fast leading edge circuit design

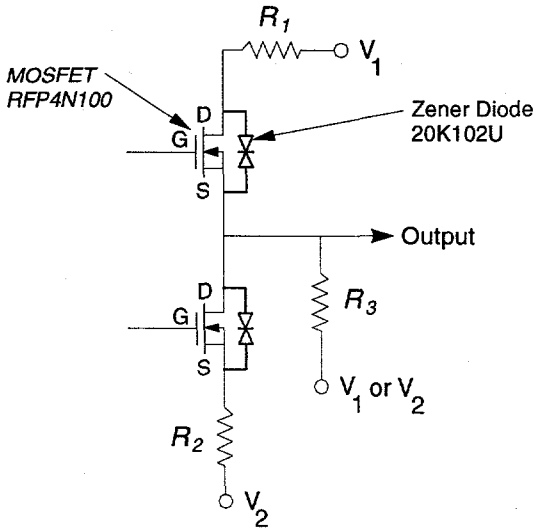

$V_1 > V_2$

Figure 4. Fast leading and falling edge circuit design utilizing a push-pull MOSFET configuration.

A TTL based circuit connected to the MOSFETs gate provides the trigger to open the transistors. Because several kVs of potential are delivered in ~25 ns, a substantial amount of ringing occurs at the output. To damp the ringing, a resistor is placed in series (labeled R_1 in Fig. 3) to slow the current flow through the MOSFETs. However, it also slows the risetime. In the circuits presented below, R_1 has been carefully selected to minimize the ringing and risetime. In addition, a resistor is wired in parallel (labeled R_3 in Fig. 3) to return the voltage back to baseline. Its resistance is typically several kΩ so that minimal current is lost while the MOSFETs are open.

As mentioned above, the trigger pulse applied to the gate must be at higher potential than the source in order to open the transistor, and thus must float on the potential V_2. This can be accomplished using either a transformer or an optoisolator. Both methods are used in the circuits described below and are briefly compared in Section 3.4.

The MOSFET configuration described above produces a leading edge with a risetime of ~100 ns and a falltime that is typically many μs long. This is suitable for the acceleration and extraction plates, as discussed in the following section. However, the pulsed valve, mass gate, and decelerator circuits need fast rising and falling edges (Section 3.2 and 3.3). In order to create such pulses, two sets of MOSFETs are arranged in a push-pull configuration[17] as shown in Fig. 4. In this configuration, one set of MOSFETs produces a fast leading edge, while the second set quickly resets the output voltage. Delaying the triggers between the sets of MOSFETs controls the duration, and either set of stages can be triggered first, allowing the voltage pulse to rise from V_1 to V_2 or fall from V_2 to V_1. Two resistors placed in series with the MOSFETs, R_1 and R_2,

damp the ringing associated with the fast edges; R_1 damps the ringing created by the output voltage rising to V_1, and R_2 damps the ringing created by voltage falling to V_2. Because the MOSFETs tend to bleed current slightly, the resistor R_3 is used to maintain the baseline during the ms long intervals between laser shots. It should be noted that the set of stages associated with V_1 floats on top of V_2. The added capacitance associated with these stages tends to slow the V_2 edge.

3.1 Acceleration and extraction circuit

The acceleration plate needs to switch from ground to between –700 V and –1500 V as quickly as possible, while the extraction plate simultaneously switches to approximately –400 V beyond the acceleration plate voltage. Because only a single, fast leading edge is needed to inject the ions into the TOF mass spectrometer, the circuit design follows the example discussed in Fig. 3, and is shown in Fig. 5.1. It is modeled after the circuits built by Xu,[18] Osborn,[19] and Cyr,[20] and consists of two MOSFET stacks, one to switch the acceleration plate and one to switch the extraction plate. Each MOSFET is soldered onto a removable circuit board that can be easy replaced in case of failure.[19] Currently two MOSFET boards are used in each assembly, allowing voltages down to –2 kV, with room for a third.

Because both plates need to switch simultaneously, a single circuit triggers both stacks. It consists of a SN74121 one-shot chip, a SN137 (same as a 2601) optoisolator, and a MOSFET driver (TC4422), all of which are powered by a 5 V commercial power supply (International Power). The SN74121 is triggered by the delay generator, and outputs a pulse variable up to 10 μs. The optoisolator serves as a safety and

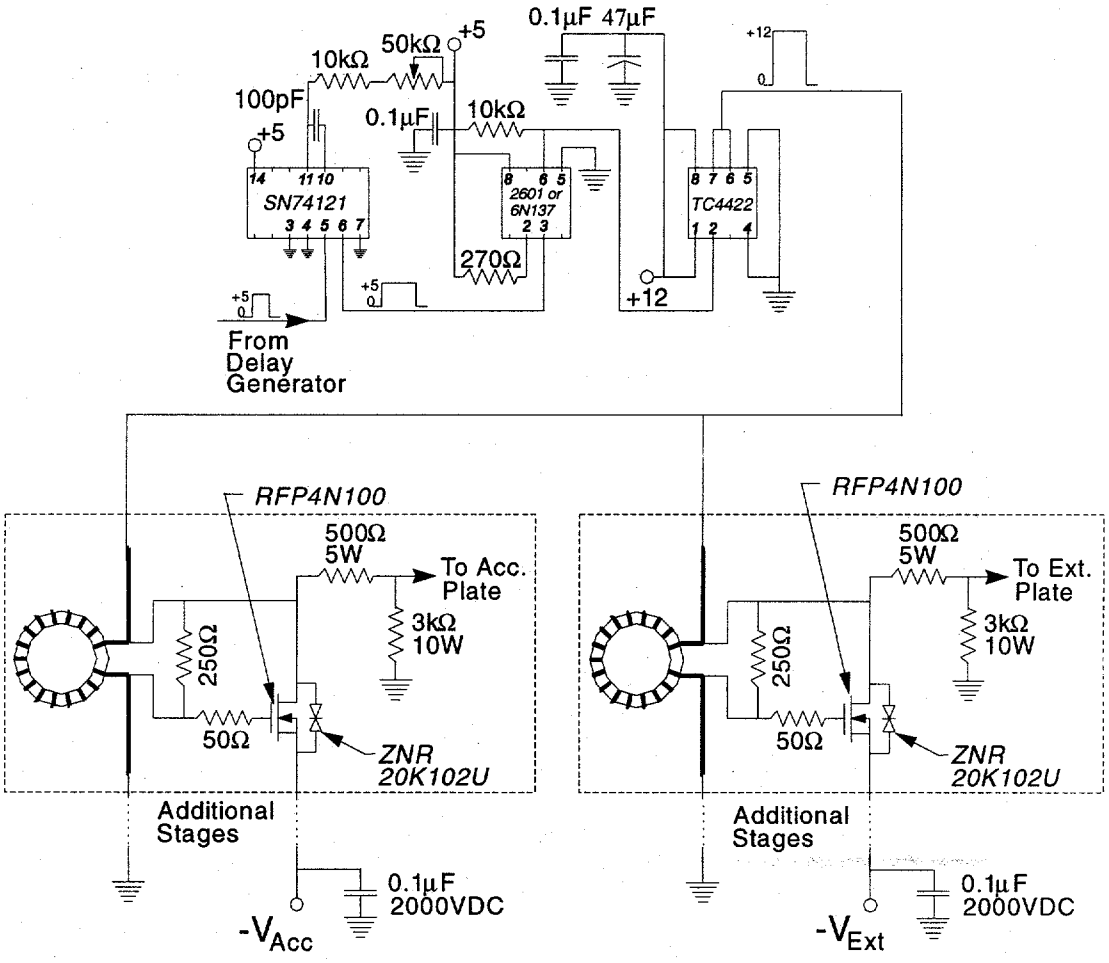

Figure 5.1 Acceleration and extraction circuit diagram

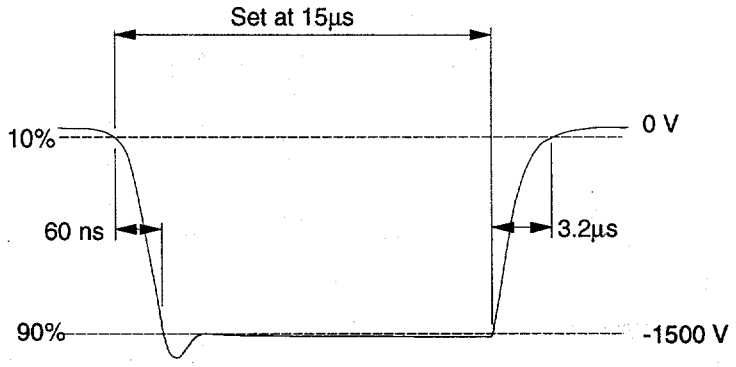

Figure 5.2 Acceleration and extraction circuit output

prevents any possible feedback from reaching the delay generator. Finally, the TC4422 serves to amplify the TTL pulse to +12 V, which has a higher efficiency for triggering the MOSFETs. As mentioned above, the trigger pulse needs to float on top of the applied voltage. In this circuit, homemade ferrite coil transformers are used to isolate the trigger pulse from the applied voltage.[21]

The circuit output is shown in Fig. 5.1, for a typical extraction and acceleration voltage drop from 0 to –1500 V. The falltime is 62 ns, with a slight overshoot. The overshoot is due to ringing that would normally occur, but a 500 Ω, 5W resistor damps the oscillations. The one-shot chip has been adjusted to give a 15 μs pulse, and R_3 is a 3 kΩ, 10 W resistor that brings the pulse back to baseline in 3.2 μs. In addition, a 0.1 μF, 2000 VDC capacitor is placed in parallel with the $-V_{Acc}$ and $-V_{Ext}$ power supply. This helps to reduce the fall time by providing extra current when the MOSFET is initially opened.

3.2 Pulsed valve circuit

Unlike the acceleration and extraction plate circuits, the pulsed valve circuit delivers a voltage pulse with fast rising and falling edges to open the pulsed valve for a discrete and controllable amount of time. It is capable of delivering a 0 to –1 kV pulse, variable from 0 to 250 μs in duration, and follows the design from Hanna Reisler's group at the University of Southern California. The circuit diagram is shown in Figs. 6.1 through 6.4, and uses a push-pull MOSFET configuration similar in concept to that presented in Fig. 4. It consists of two MOSFET stages (Fig. 6.4), one each to provide the leading and falling edges, a trigger circuit (Fig. 6.1), and three homemade power

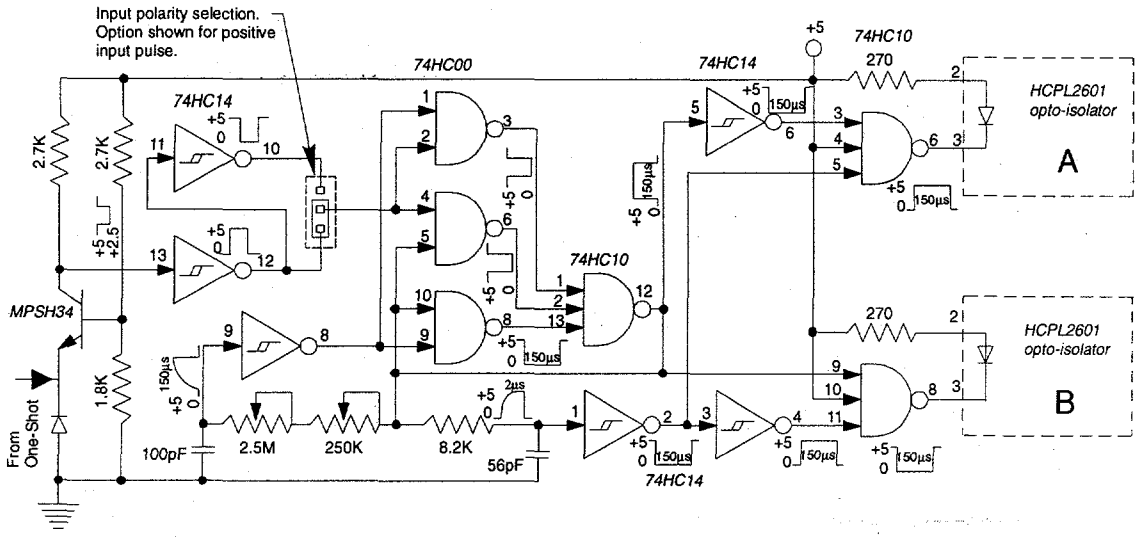

Figure 6.1 Pulsed valve trigger circuit

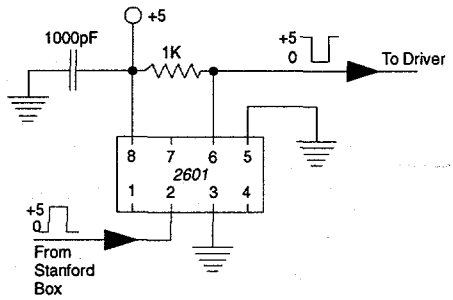

Figure 6.2 Safety optoisolator

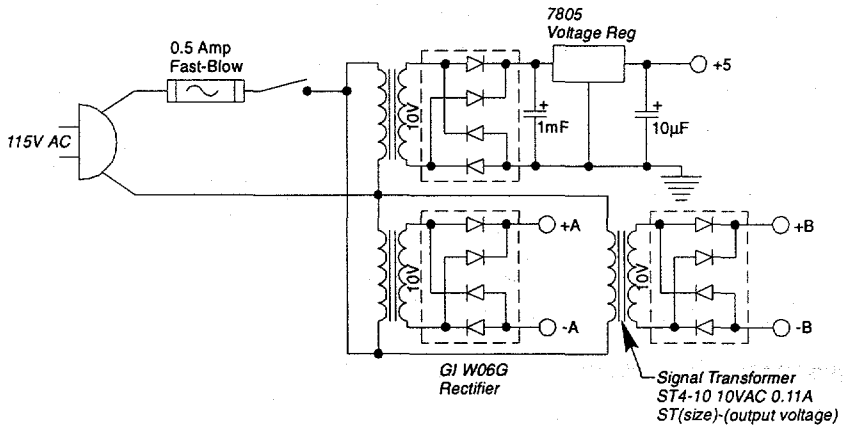

Figure 6.3 Three homemade power supplies

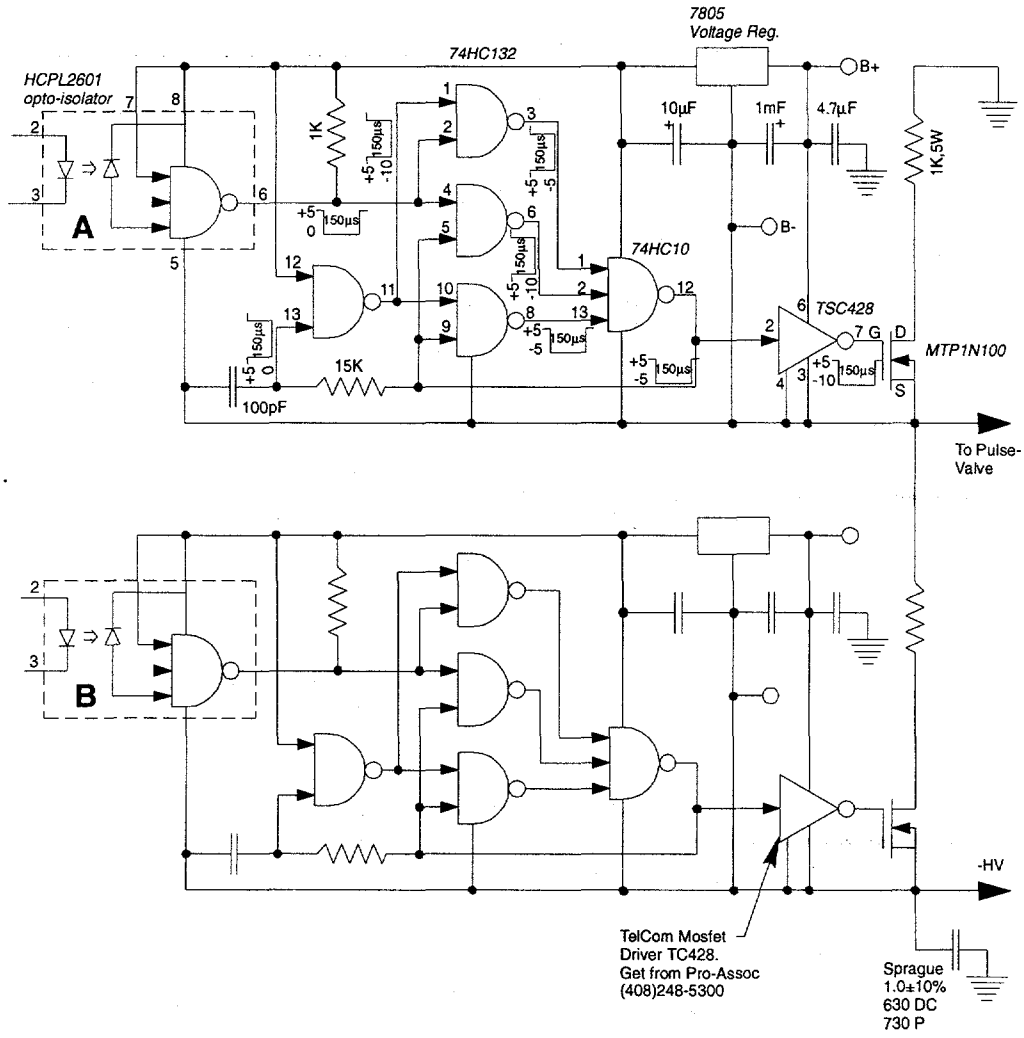

Figure 6.4 Pulsed valve driver circuit

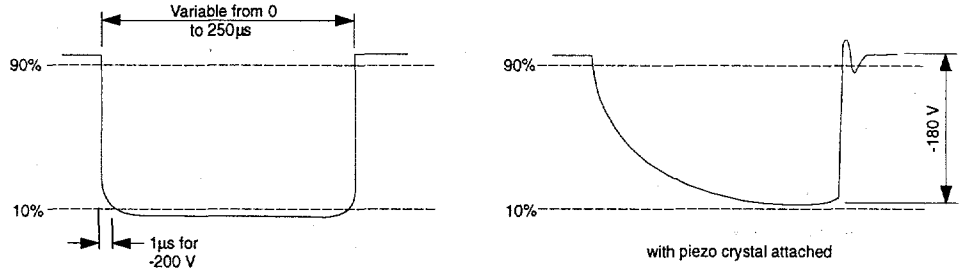

Figure 6.5 Pulsed valve circuit output

supplies (Fig. 6.3). The trigger circuit is itself triggered from the delay generator that is electro-optically isolated with a 2601 chip to prevent feedback (Fig. 6.2). Its power is provided by one of the homemade power supplies, consisting of a 10 VAC transformer, a bridge rectifier, and a 5 V voltage regulator. Following a number of chips used to produce a variable length TTL pulse and its inverse, the trigger pulse is passed to the MOSFET stages using 2601 optoisolators.

Each MOSFET stage uses a number of chips to amplify the TTL pulse to a 12 V signal that finally triggers the MOSFET. Because the TTL triggers are inverses of each other, and the chips are triggered by the rising edges, one MOSFET will open at the beginning of the TTL trigger, while the other will open at the end. This provides the fast rising and falling edges. Because all of the chips need to float on top of the input voltages, the power for the chips comes from an additional homemade power supply with a transformer that uncouples the voltages from ground.

Shown in Fig. 5 is the circuit output with and without the piezocrystal attached. Without the crystal connected, 1 μs rise and fall times are produced. 1 kΩ, 5 W resistors suppress the ringing. The output with the piezocrystal attached resembles an inverted shark fin due to the large load of the crystal. Because the response time of the crystal is slow, the relatively slow rise and fall times (as compared to the acceleration and extraction circuit) are adequate to operate the pulsed valve. And, similar to the acceleration and extraction circuit, a 630 VDC capacitor is wired in parallel to the power supply to help offset the current requirements upon switching.

3.3 Mass gate and decelerator circuits

As discussed above, the ion velocity degrades the electron kinetic energy resolution,[4] and therefore the ions are often decelerated prior to detachment by the laser. This requires two sets of ion optics: a mass gate and a deceleration stack each controlled with a fast pulsing circuit described in this section. The mass gate is typically kept several hundred volts lower potential than the extraction voltage, which inhibits the ions from entering the detector chamber and the deceleration stack.[8] However, by quickly pulsing the mass gate to ground potential and back again, the ion packet being studied is allowed to pass. Hence, a pulsing circuit that produces a fast rising and falling edge is required. Following the mass gate, the selected ions enter the deceleration stack while it is at ground potential. After entering, a positive potential of several kV is applied to retard the ion velocity. Fast rising and falling edges are required so that the ions are only affected while in the deceleration stack itself, and the pulse ranges in duration from 500 ns to 2-3 μs. Because both the mass gate and the deceleration circuits pulse up to a more positive potential, the two circuits are very similar in design, as described below.

In principle, the circuits resemble the pulsed valve circuit described in Section 3.2. However, the timing electronics and method of triggering the MOSFETs are significantly different. The circuits described in this section are modeled after the designs of Bernius and Chutjian,[12,13] and are detailed in Figs. 7.1 through 7.6. The timing circuit, driving circuit, power supply, and circuit board template are the same for both circuits (Figs. 7.1 to 7.4). The differences in circuit design and output are made evident by comparison of Figs. 7.5 and 7.6.

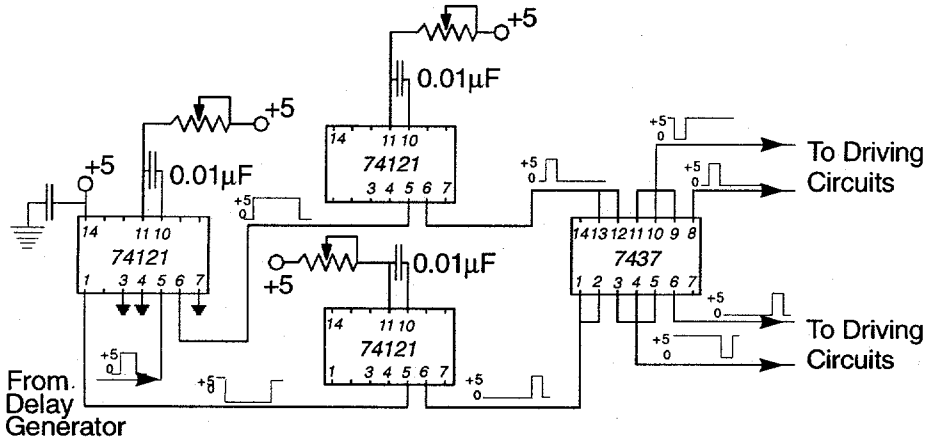

Figure 7.1 Mass gate and decelerator timing circuit

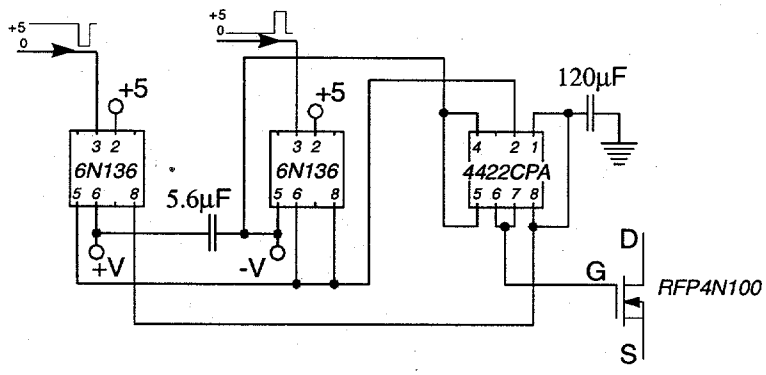

Figure 7.2 Mass gate and decelerator driving circuit

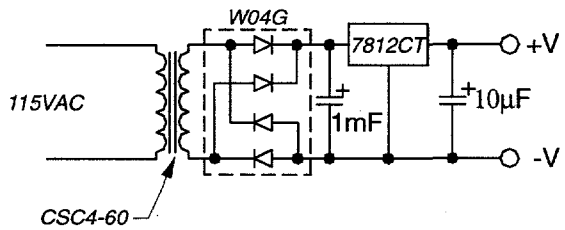

Figure 7.3 Mass gate and decelerator homemade power supply

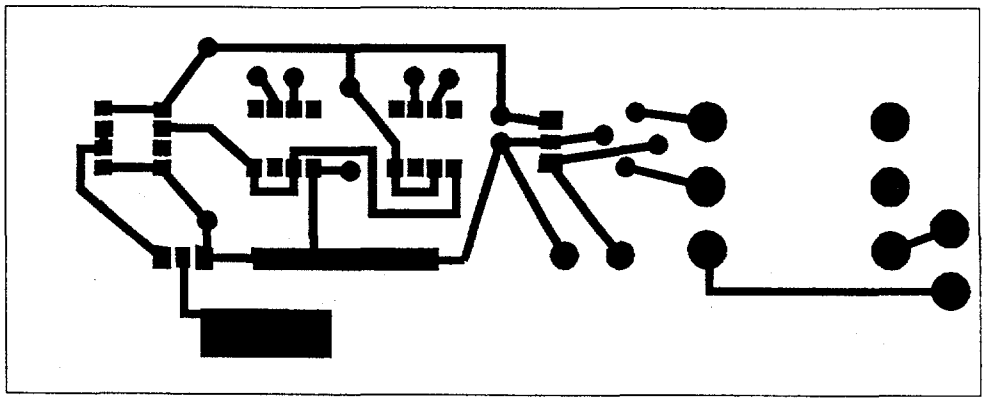

Figure 7.4 Mass gate and decelerator circuit board for driving circuit

Each circuit operates in the push-pull MOSFET configuration described above. Thus two trigger pulses are needed, one for each set of MOSFET stages, with a variable delay time between them. This is accomplished using three one-shot chips (74121) shown in Fig. 7.1. The first 74121 is triggered from the delay generator and produces both a variable length pulse and its inverse that are directed to two additional one-shot chips. Because TTL chips are triggered from rising edges, one 74121 will trigger off the leading edge of the TTL pulse and the other will trigger off the following edge, producing two more variable length pulses separated by the length of the initial 74121 pulse. The outputs from the second and third one-shot chips are sent to a 7437 quad 2-input NAND buffer. Normal TTL chips only deliver enough current to drive 10 other TTL chips. Buffers drive up to 30 chips. Although only 8 chips are used in the circuit, substantial current is still required, and the 7437 has burned out on occasion. Future designs should perhaps incorporate a second 7437.

The negative and positive ouputs of the 7437 are sent to the driving circuits, which are housed in a separate box located near the ion optics feed throughs. It is important to use shielded cable, because the circuits are sensitive to stray radio frequency noise that can falsely trigger the circuits. Each driver consists of two 6N136 optoisolators, one triggered by the negative input pulse and the other the positive. The outputs of these produce a rising RC time constant that is used to trigger a TC4422CPA. The TC4422CPA serves the same purpose as the 427 used in the pulsed valve circuit, but delivers a faster pulse to drive its respective MOSFET chip.

The 6N136 are equivalent to the 4502, have a risetime of 250 to 800 ns, and can isolate up to 2500 V. There are also faster optoisolators; the HCPL-4661 is 10 times

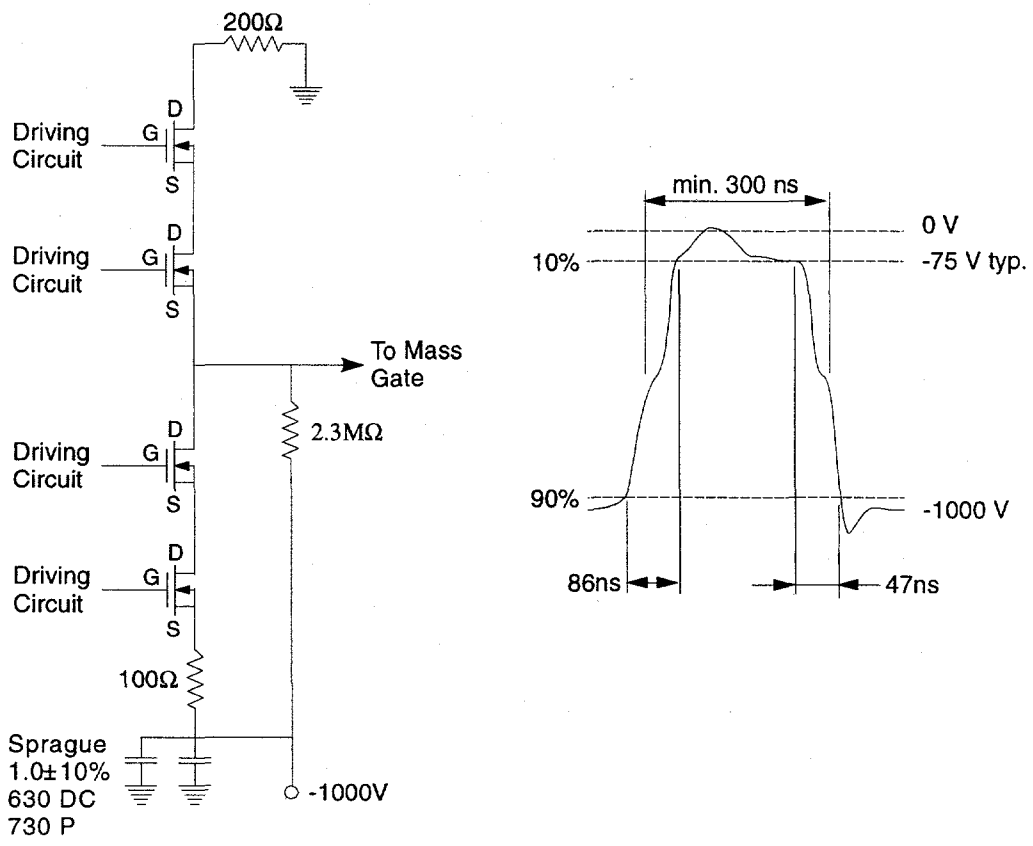

Figure 7.5 Mass gate circuit and output

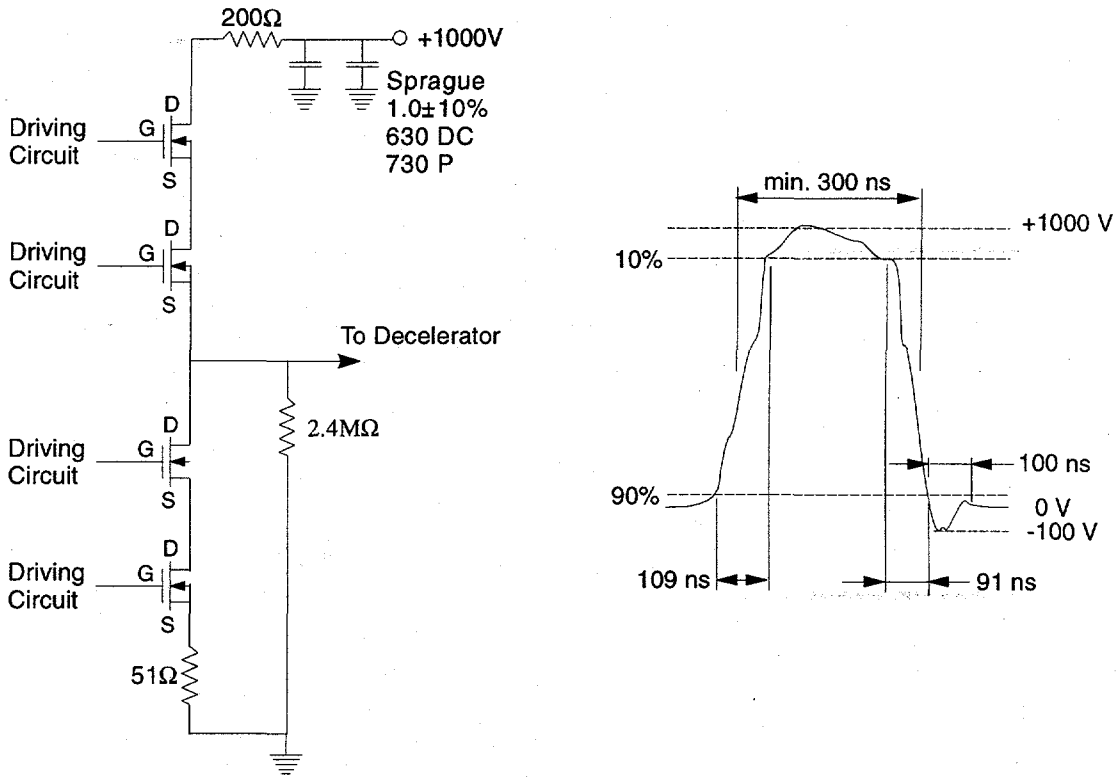

Figure 7.6 Decelerator circuit and output

faster, and there is also a new chip that isolates up to 10 kV (manufacturers number not known, order from Newark).

Because the driving circuit chips need 12 V to operate, but still must be isolated in order to float at several kV potential, homemade power supplies are used similar to those in the pulsed valve circuit (Fig. 6.3). However, 7812CT voltage regulators produce the necessary 12 V. Both the driving circuit chips and the homemade power supplies are soldered onto a specially designed circuit board (Fig. 7.4). Each of these circuit boards triggers one MOSFET, and hence is capable of pulsing up to a 1000 V. Both the mass gate and decelerator circuits must operate up to 2000 V, and hence require four such boards apiece: two for the fast rising and two for the fast falling edge, as shown in Figs. 7.5 and 7.6.

To create as fast a rise and fall time as possible, each pair of MOSFETs must open at the same time, although each chip in the circuit has a slightly different response time. The largest discrepancies arise from differing risetimes of the 6N136 chips and varying trigger voltages of the TC4422CPA chips. To help match the pairs of driving circuits, the MOSFET chips are disconnected, and the output of the TC4422CPA drivers are monitored while changing the 6N136 and 4422 chips. The final matched set of drivers should have rise and fall times within 50 ns of each other.

Figs. 7.5 and 7.6 show typical outputs for the circuits when a 1000 V potential is applied. The rise and fall times for the mass gate are 86 and 47 ns, respectively, and are a bit shorter then the decelerator times of 109 and 91 ns. This is probably because the MOSFETs and high voltage power supply operate differently at positive and negative potentials. 300 ns is the shortest pulse duration possible with these circuits, and is easy to

achieve with the decelerator pulsing circuit, because the decelerator stack has a large load associated with it that damps out much of the spurious ringing caused by the fast rising and falling edges. The mass gate on the other hand has essentially no load, and the radio frequency noise sometimes re-triggers the driving circuits. To minimize this, the duration of the trigger that controls the falling edge is maximized to leave the MOSFETs open for as long as possible, and the trigger from the delay generator is set shorter than the desired high voltage pulse. For both circuits, the rising edge trigger must be made as short as possible.

3.4 Comparison of push-pull configurations

As a final note on push-pull MOSFET configurations, a brief comparison is made in this section between circuits using optoisolators and those using ferrite coils, and between homemade and commercial power supplies. Fig. 8 shows the circuit diagram and output for a push-pull configuration using ferrite coils to trigger the MOSFETs (as was used in the extraction and acceleration circuit, Sec. 3.1, Fig. 5.1), and is to be compared to the decelerator output (Fig. 7.6) that uses optoisolators. Although the ferrite coils are simpler to implement than the optoisolators, their output is not sufficient for use with either the decelerator or mass gate. The output has much slower risetimes, on the order of several microseconds, and significant ringing associated with the falling edge. The ringing can be damped out, but is replaced by an 800 ns falltime.

The power supply that provides the 12 V potential also dramatically effects the rise and fall times. Using a commercial power supply (International Power)

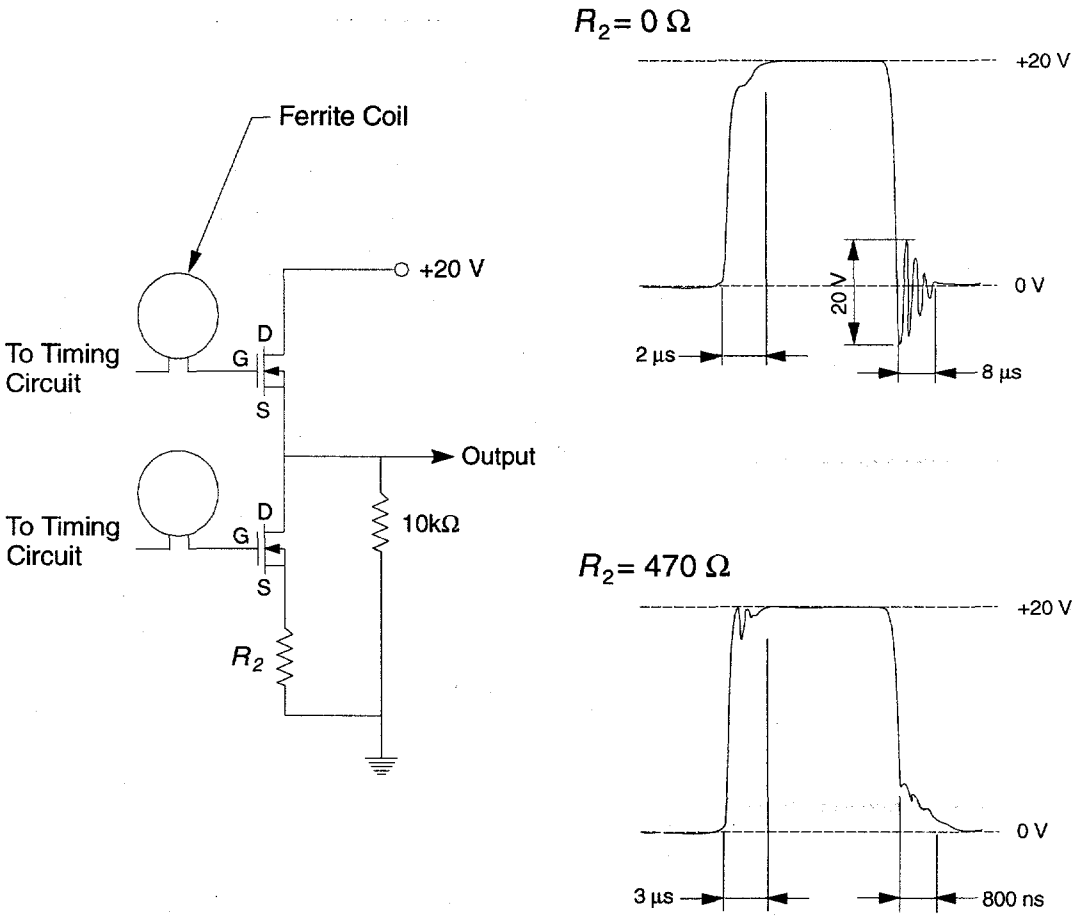

Figure 8 Push-pull MOSFET circuit and output using ferrite coils

instead of the homemade power supplies (Fig. 7.3) increases the risetime by a factor of three, and the falltime by a factor of two. Because half of the circuit must ride on top of the high voltage pulse, an increase in capacitance or inductance could alter the rise and fall times, and may account for the differences between the push-pull configuration using optoisolators versus ferrite coils, and homemade versus commercial power supplies.

4. Ion and electron gun deflector circuits

The final circuits needed to guide the ions are variable voltage supplies that control the ion deflectors. The ion deflectors consist of parallel plates separated by about 1 cm, and are kept at opposite polarity to create an electric field with zero potential at their center point. Previous circuits built in the Neumark group have instead held one plate at ground and varied the voltage on the other plate,[22] but because the ions are referenced to ground potential, zero potential directly along their flight path is more desirable. Previous circuits have also required either double potentiometers or switches to change polarities. The deflector circuits outlined in this chapter are designed to allow a single potentiometer to swing from negative to positive voltages. Originally this circuit design was used for the electron gun deflectors as well. However, it was found that stray current from the electron beam made the voltages vary. The circuits were replaced with constant current power supplies and are described in Greenblatt's thesis.[5]

Two circuit designs are shown in Figs. 9.1 and 9.2. The first produces a variable voltage output between 0 and –100 V, but cannot switch polarities. This can be used as the first vertical deflector after the extraction and acceleration plates since the ions necessarily have downward momentum from the pulsed valve and will only need to be

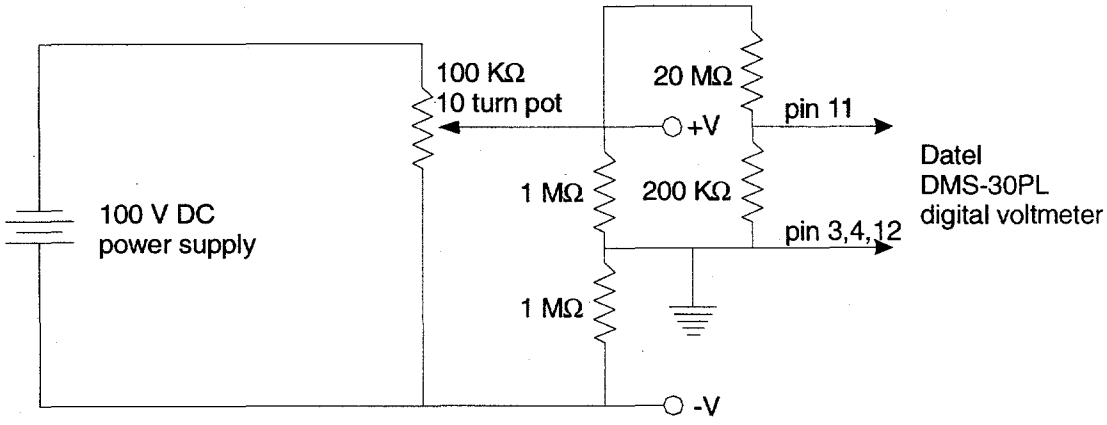

Figure 9.1 Ion deflector circuit, variable from 0 to –100 V

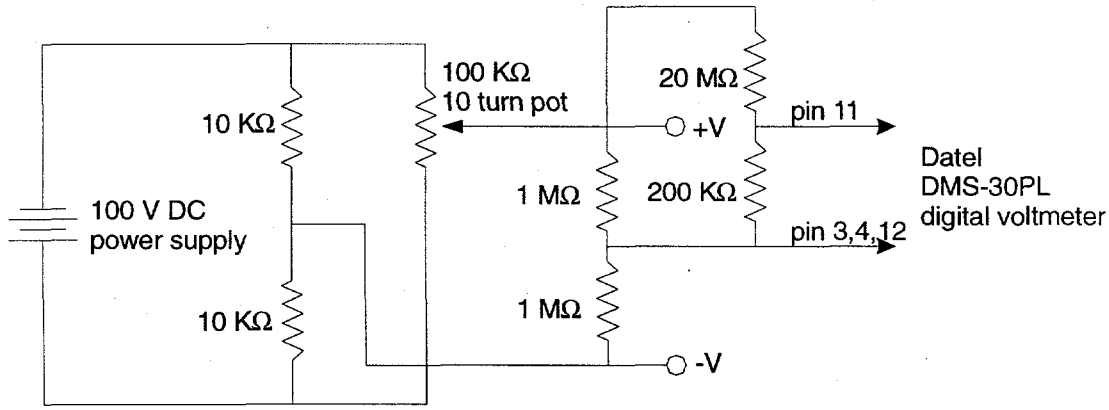

Figure 9.2 Ion deflector circuit, variable from –50 to +50 V

deflected upwards. Each deflector requires a 100 V power supply (International Power), and a 100 KΩ, 10 turn potentiometer. A simple voltage divider produces the positive and negative voltages, and is monitored with a second voltage divider that leads to a digital display. It is important that each set of dividers is uncoupled from the others by choosing resistances that differ by an order of magnitude.

The second deflector design is similar to the first, except that it incorporates an additional voltage divider to create a reference potential that the potentiometer divider can swing above or below. Because of the additional divider, this circuit operates between –50 and +50 Volts. Currently this type of circuit is used for all the ion deflectors.

5. References

[1] R. B. Metz, A. Weaver, S. E. Bradforth, T. N. Kitsopoulos, and D. M. Neumark, J. Phys. Chem. **94,** 1377 (1990).

[2] L. A. Posey, M. J. DeLuca, and M. A. Johnson, Chem. Phys. Lett. **131,** 170 (1986).

[3] C.-Y. Cha, G. Gantefor, and W. Eberhardt, Rev. Sci. Instrum. **63,** 5661 (1992).

[4] O. Cheshnovsky, S. H. Yang, C. L. Pettiette, M. J. Craycraft, and R. E. Smalley, Rev. Sci. Instrum. **58,** 2131 (1987).

[5] B. J. Greenblatt, Ph.D. Thesis, University of California, 1999.

[6] W. C. Wiley and I. H. McLaren, Rev. Sci. Instrum. **26,** 1150 (1955).

[7] J. M. Alford, P. E. Williams, D. J. Trevor, and R. E. Smalley, Intl. J. Mass.Spec. Ion Proc. **72,** 33 (1986).

[8] L.-S. Wang, H.-S. Cheng, and J. Fan, J. Chem. Phys. **102,** 9480 (1995).

[9] M. T. Zanni, V. S. Batista, B. J. Greenblatt, W. H. Miller, and D. M. Neumark, J. Chem. Phys. **110,** 3748 (1998).

[10] M. L. Alexander, N. E. Levinger, M. A. Johnson, D. Ray, and W. C. Lineberger, J. Chem. Phys. **88,** 6200 (1988).

[11] M. D. Davidson, B. Broers, H. G. Muller, and H. B. v. L. v. d. Heuvell, J. Phys. B **25,** 3093 (1992).

[12] M. T. Bernius and A. Chutjian, Rev. Sci. Instrum. **60,** 779 (1989).

[13] M. T. Bernius and A. Chutjian, Rev. Sci. Instrum. **61,** 925 (1990).

[14] R. J. Baker and B. P. Johnson, Rev. Sci. Instrum. **63,** 5799 (1992).

[15] R. J. Baker and B. P. Johnson, Rev. Sci. Instrum. **64,** 1655 (1993).

[16] V. N. Rai and M. Shukla, Rev. Sci. Instrum. **65,** 2134 (1994).

[17] P. Horowitz and W. Hill, *The Art of Electronics* (Cambridge U. P., Cambridge, 1980).

[18] C. Xu, Ph.D. Thesis, University of California, 1997.

[19] D. L. Osborn, Ph.D. Thesis, University of California, 1996.

[20] D. R. Cyr, Ph.D. Thesis, University of California, 1993.

[21] R. E. Continetti, D. R. Cyr, and D. M. Neumark, Rev. Sci. Instrum. **63,** 1840 (1992).

[22] A. Weaver, Ph.D. Thesis, University of California, 1991.

Chapter 3. Characterization of the I_2^- anion ground state using conventional and femtosecond photoelectron spectroscopy[†]

The $\tilde{X}\ ^2\Sigma_u^+$ state of the I_2^- anion has been fit to a Morse potential using data from two techniques: conventional and femtosecond photoelectron spectroscopy (FPES). Conventional photoelectron spectroscopy is used to determine the adiabatic electron affinity of I_2 as well as the well depth and equilibrium nuclear geometry of I_2^-. In the FPES experiment, the pump pulse induces coherent nuclear motion on the ground state of I_2^- by resonant impulsive stimulated Raman scattering (RISRS), and the vibrational frequency of the anion is determined from the resulting oscillatory structure in the time-dependent photoelectron spectra. We find the electron affinity (EA) of I_2 to be 2.524 ± 0.005 eV, the well depth (D_e) for I_2^- to be 1.014 ± 0.005 eV, the equilibrium internuclear separation (R_e) to be 3.205 ± 0.005 Å, and the vibrational frequency to be 110 ± 2 cm^{-1}. These values for the I_2^- potential parameters differ significantly from previous results.

1. Introduction

In recent years, the role of solute/solvent interactions on chemical dynamics has been explored in experiments that probe the photodissociation of anions in liquids and size-selected clusters. The I_2^- anion has been a particularly attractive target for this type of investigation; its photodissociation dynamics have been studied in size-selected $I_2^-(CO_2)_n$[1-3] and $I_2^-(Ar)_n$[3,4] clusters and in several polar solvents.[5-7] The interpretation of these experiments relies at least in part on the potential energy curves for the ground and

[†] Originally published in J. Chem. Phys. **107**, 7613 (1997).

low-lying excited states of I_2^-, but the potential energy curves available in the literature are at best approximately correct. In this study we have constructed an improved potential for the ground state of I_2^- using a combination of conventional (~10 meV resolution) and femtosecond photoelectron spectroscopy. As part of this study, we have demonstrated a new method for determining vibrational frequencies in gas phase negative ions using femtosecond photoelectron spectroscopy.

The most widely referenced potential curves for the I_2^- ground and excited states are the Morse potentials constructed by Chen and Wentworth,[8] of which the ground and second excited states are shown in Figure 1. These are based on an assortment of experimental data including Raman spectroscopy in matrices, electronic spectroscopy in crystals, and gas-phase dissociative attachment experiments. However, there remains a large degree of uncertainty in these semi-empirical curves as each is constructed from, at most, four experimental parameters. In addition, the parameters taken from matrices and crystals are likely to be perturbed from the gas phase values. Recently, Chen and co-workers[9] published new potentials for I_2^- in which the equilibrium internuclear distance of the ground state was taken to be the sum of the ionic and covalent radii of I^- and I, respectively. This resulted in a significant increase in the bond length, from 3.23 to 3.385 Å and a decrease in the well depth from 1.10 to 1.055 eV, with even larger changes in the excited states. In the most recent paper from this group,[10] the proposed equilibrium bond length was further increased by 0.015 Å and the well depth was again increased by 0.051 eV, based on correlations with the Morse parameters for the isoelectronic rare gas positive ion, Xe_2^+. The parameters for the three potentials are listed in Table I.

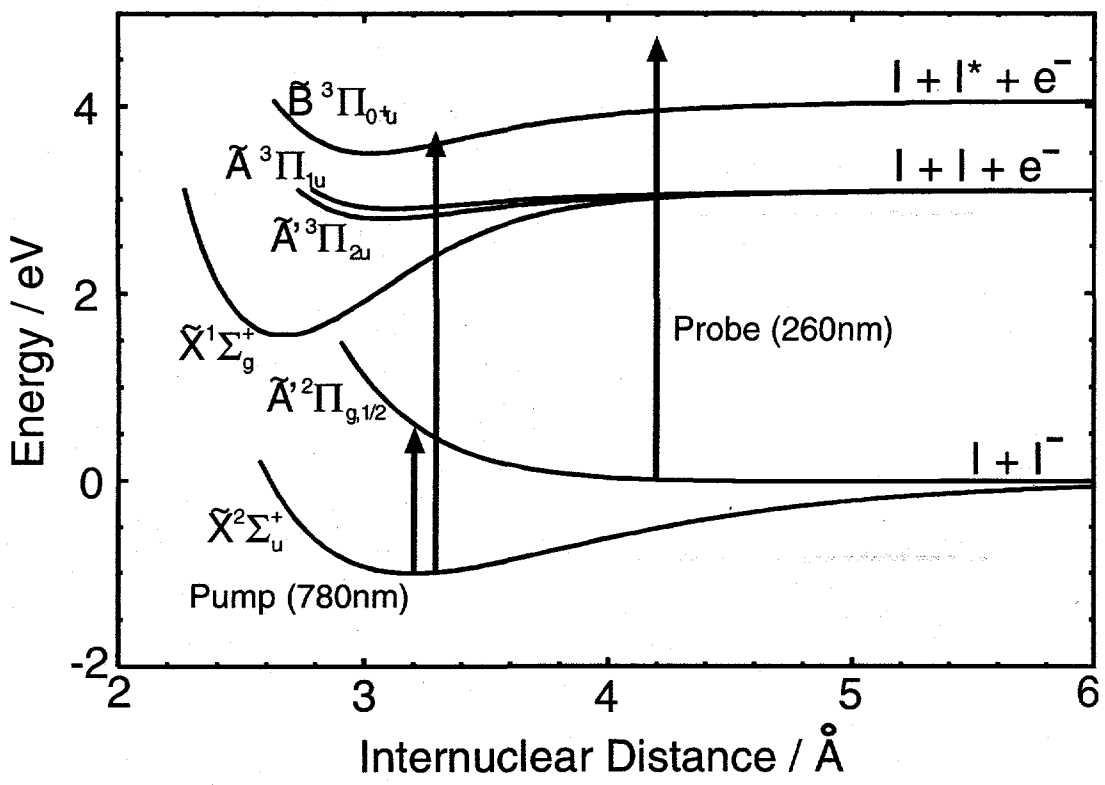

Figure 1 Potential energy curves for the relevant electronic states of I_2^- and I_2 taken from Refs. 15-18. The pump and probe wavelengths are shown for the FPES experiment, probing the ground and excited state potentials.

The I_2^- electronic states have also been investigated by *ab initio* methods, but these studies are complicated by the large number of electrons and strong spin-orbit coupling. The few calculations performed have been limited to valence bond methods by Tasker *et al.*,[11] self-consistent field (SCF) calculations by Bowmaker *et. al.*,[12] and relativistic core potential calculations by Shaik and coworkers.[13] Maslen *et al.*,[14] using a multireference configuration interaction (MRCI) calculation for the ground and excited states, have recently incorporated spin-orbit effects for the first time. Compared to the three semiempirical potentials proposed by Chen and coworkers, Maslen *et al.* predict a shallower anion ground state potential, 0.905 eV, and a bond length of 3.33 Å that lies between the various values proposed by Chen and coworkers.[8-10] The considerable variation in the potential parameters for I_2^-, particularly the bond length, is in stark contrast to the precisely known neutral state curves, generated using the RKR inversion technique with vibrational energies and rotational constants derived from fluorescence data.[15-18]

Table I Spectroscopic constants for the ground state of I_2^-

	Current Work	Ab Initio[a]	Chen & Wentworth[a]	Dojahn *et al.*[a]	Chen *et al.*[a]
R_e (Å)	3.205 ± 0.005	3.33	3.23	3.385	3.40
D_e (eV)	1.014 ± 0.005	0.905	1.10	1.055	1.106[a]
ω_e (cm^{-1})	110 ± 2	99.9	113	115	116

[a] Ref. 14
[a] Ref. 8
[a] Ref. 9
[a] Ref. 10
[a] Reported value is D_0=1.099 eV. D_e determined by adding 0.007 eV zero point energy.

In this paper, we use a combination of conventional and femtosecond photoelectron spectroscopy (FPES) techniques to characterize the I_2^- ground state. The conventional photoelectron spectrum obtained at 10 meV resolution yields vibrationally resolved bands representing transitions from I_2^- to the $\tilde{X}\,^1\Sigma_g^+$, $\tilde{A}'\,^3\Pi_{2u}$, and $\tilde{A}\,^3\Pi_{1u}$ states of I_2. Because the three I_2 electronic states are well-characterized, our photoelectron spectrum yields an accurate adiabatic electron affinity of I_2. In addition, we determine the I_2^- well depth, equilibrium internuclear separation, and vibrational temperature.

Anion FPES is a relatively new femtosecond pump-probe technique which we have used recently to investigate the excited state dynamics of both I_2^- and $I_2^-Ar_n$ clusters.[4,19] In this experiment, I_2^- is excited to the $\tilde{A}'\,^2\Pi_{1/2,g}$ state by a femtosecond pump pulse, and the photoelectron spectrum of the evolving system is measured at a series of delay times by photodetachment with a second femtosecond probe pulse. Here we demonstrate that the pump pulse induces vibrational coherences on the I_2^- ground state that can be readily detected as oscillatory structure in the time-dependent photoelectron spectra. The process by which the coherences are induced is analogous to that seen in condensed phase studies of I_3^- by Ruhman and co-workers.[20] We obtain the gas phase I_2^- vibrational frequency from the oscillations in our spectra. This frequency along with the information obtained from the conventional photoelectron spectrum leads to a much-improved potential for the I_2^- ground state.

2. Experimental

The conventional and femtosecond photoelectron spectroscopy experiments are carried out on two different time-of-flight photoelectron spectrometers. Each has been described previously,[19,21,22] but a brief summary will be given here and the differences between the instruments outlined.

In both experiments, argon carrier gas (15 psig) is passed over crystalline I_2 and supersonically expanded through a pulsed piezo electric valve.[23] Anions are generated by a 1 keV electron beam which crosses the expansion just downstream of the nozzle, and are injected into a Wiley-McLaren time-of-flight mass spectrometer[24] by applying pulsed extraction and acceleration fields perpendicular to the molecular beam axis. An additional reflectron stage in the conventional photoelectron spectrometer provides higher mass resolution, although this is not needed for the work presented here. After passing through several differentially pumped regions, the ions enter the detector chamber where they interact with one or more laser pulses. An in-line microchannel plate detector is used to monitor the ion beam.

In the conventional spectrometer, the ions are photodetached with a pulsed Nd:YAG laser operating at a repetition rate of 20 Hz. The photodetachment photon energy of 4.141 eV (299 nm) is obtained by Raman-shifting the fourth harmonic (266 nm) of the Nd:YAG fundamental in high pressure H_2. The electron kinetic energies are measured by time-of-flight through a 100 cm long field-free region. The instrumental resolution is 8-10 meV for an electron kinetic energy (eKE) of 0.65 eV and degrades as $(eKE)^{3/2}$.

The femtosecond photoelectron spectrometer has been optimized to be compatible with the high laser repetition rate, 500 Hz in these experiments, and the low photoelectron signal expected for a two-photon pump-and-probe experiment. The pulsed piezoelectric valve operates at the laser repetition rate, and the resulting large gas load is handled with two diffusion pumps totaling 8,800 l/s of pumping speed on the ion source chamber. In addition, a "magnetic bottle" time-of-flight analyzer[25] is used to yield a considerably higher photoelectron collection efficiency, >50% *vs.* <0.1% for the field-free design. In the work reported here, the resolution of the femtosecond spectrometer is approximately 200 meV for 1 eV electrons.

The FPES experiment uses a commercial laser system to generate the femtosecond pump and probe pulses. A Coherent Innova-90 Ar^+ laser pumps a Clark-MXR NJA-5 Ti:Sapphire oscillator. Selected pulses are amplified using a Clark-MXR regenerative amplifier that includes a pulse stretcher, Ti:Sapphire regenerative amplifier pumped by a Nd:YAG laser running at a repetition rate of 500 Hz, and a pulse compressor. At 780 nm the resulting pulse widths and energies were 75 fs at FWHM ($sech^2$) and 1 mJ, respectively. Seventy percent of this beam is split and tripled, resulting in a probe pulse at 260 nm, 105 fs wide and with 20 μJ of energy, characterized by difference frequency cross-correlation in a 200 μm thick KDP crystal. The remaining 30% of the 780 nm pulse passes through a computer controlled delay line and acts as the pump pulse.

3. Results

3.1 Conventional Photoelectron Spectrum

The photoelectron spectra of I_2^- at hν=4.141 eV is presented in Figure 2. This spectrum was taken with the laser polarized at 54.7° with respect to the direction of electron detection (the "magic" angle), and is plotted as a function of electron kinetic energy (eKE). The eKE is related to the internal energy of the neutral molecule by the expression

$$eKE = h\nu - EA - (T_0 + E_v^0) + E_v^- \qquad (1)$$

where $h\nu$ is the photon energy and EA is the adiabatic electron affinity corresponding to the difference in energy between the lowest vibrational state of the anion to the lowest vibrational state of the neutral. E_v^0 and E_v^- are the vibrational energies above the zero point energy of the anion and neutral, respectively, and T_0 is the term value for the electronic state of the neutral. A simulated spectrum (dashed line) is superimposed on the experimental spectrum and discussed in Section 4.2.

The spectrum shows three bands corresponding to transitions from the anion ground state to the lowest three electronic states of I_2: the $\tilde{X}\ ^1\Sigma_g^+$, $\tilde{A}'\ ^3\Pi_{2u}$, and $\tilde{A}\ ^3\Pi_{1u}$ states. All three bands exhibit resolved vibrational structure. The band due to the $\tilde{X}$ state is quite broad, indicating a large geometry change upon photodetachment. Vibrational structure with a typical peak spacing of 0.021 eV is apparent near the center of the band around eKE=0.92 eV, but becomes unresolved at the wings. The $\tilde{A}$ and $\tilde{A}'$ bands are considerably narrower. Both bands show resolved vibrational structure with characteristic spacing of 0.011 eV. Although this frequency is considerably lower than in

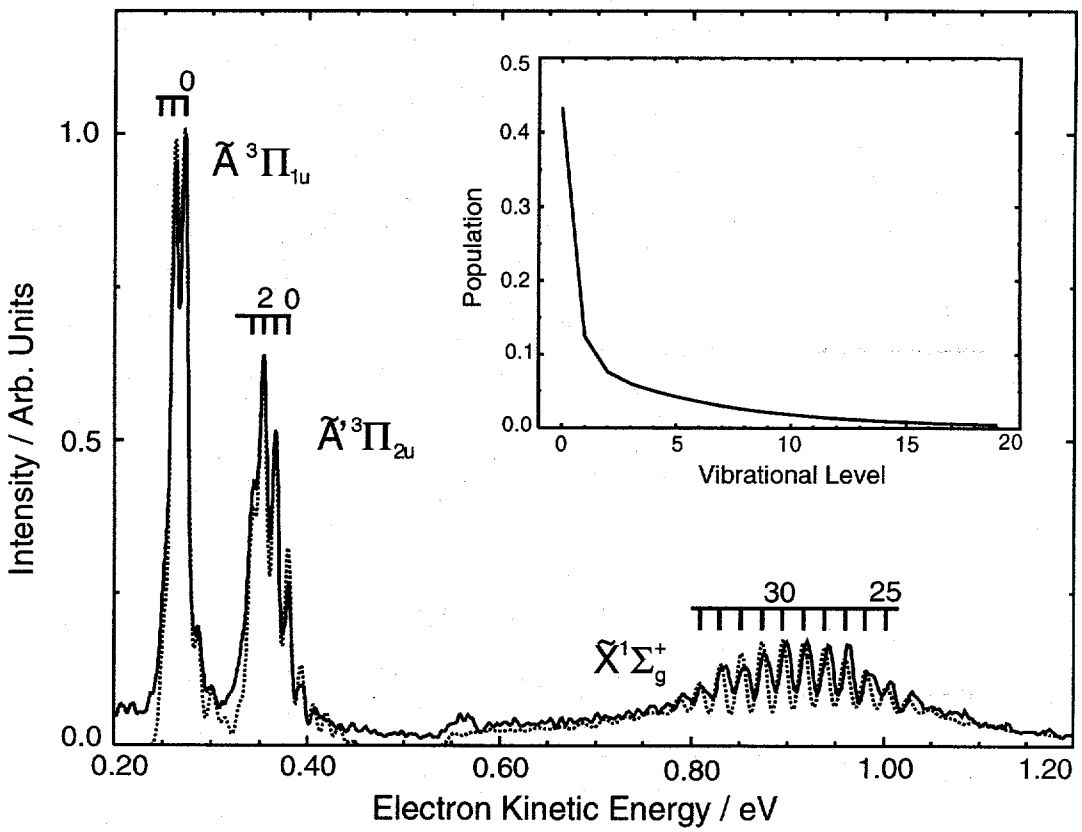

Figure 2 Conventional photoelectron spectrum taken at 299 nm. Experimental spectrum is shown solid and simulations dashed. Transitions to neutral electronic states are labeled and vibrational progressions marked for transitions from υ=0 of the anion. The inset shows the anion vibrational population used in the simulation.

the $\tilde{X}$ band, the vibrational structure in the $\tilde{A}'$ and $\tilde{A}$ bands is well-resolved because of their low electron kinetic energy.

The vibrational origin of the $\tilde{A}$ band is clearly at 0.272 eV; the very weak transitions at higher electron kinetic energy are from hot band transitions originating from vibrationally excited levels of the anion. Since the well depths of all three I_2 states are well-known, it is straightforward to assign the somewhat less obvious origin of the $\tilde{A}'$ band (see Fig. 2) and to assign the vibrational structure in the center of the $\tilde{X}$ band to transitions to highly excited vibrational levels of I_2. The vibrational structure and assignments are discussed in more detail in Section 4.2.

3.2 Femtosecond Photoelectron Spectroscopy

Figure 3 shows successive femtosecond photoelectron spectra starting at a pump-probe delay of 500 fs and stepping every 25 fs up to 1500 fs. Note that I_2^- can be detached by the probe pulse; this background signal from the probe pulse alone has been subtracted from the spectra in Figure 3. As shown in our previous work[19] on I_2^-, dissociation to I^- + I is complete by 200 fs, so these spectra at later delay times are dominated by two peaks at 0.77 eV and 1.70 eV that correspond to transitions from the I^- photo-product to the $^2P_{1/2}$ and $^2P_{3/2}$ states of iodine, respectively. The additional feature of interest in Figure 3 is the time-varying oscillatory structure superimposed on the spectrum. This is most noticeable around eKE = 1.45 eV, near the base of the $I(^2P_{3/2}) \leftarrow I^-$ transition, but it is apparent over other ranges of electron kinetic energy as well.

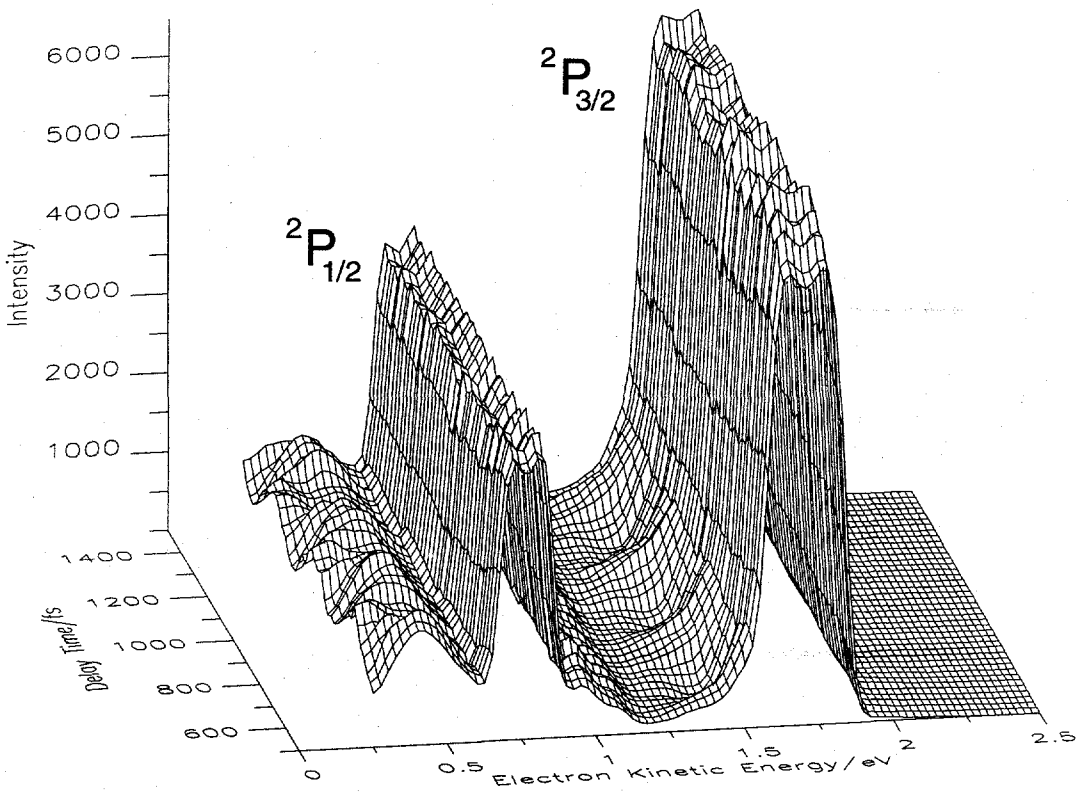

Figure 3. Experimental FPES spectra of I_2^-. Spectra at delay times ranging from 500 to 1500 fs in 25 fs steps. Assignments of atomic iodine features are indicated.

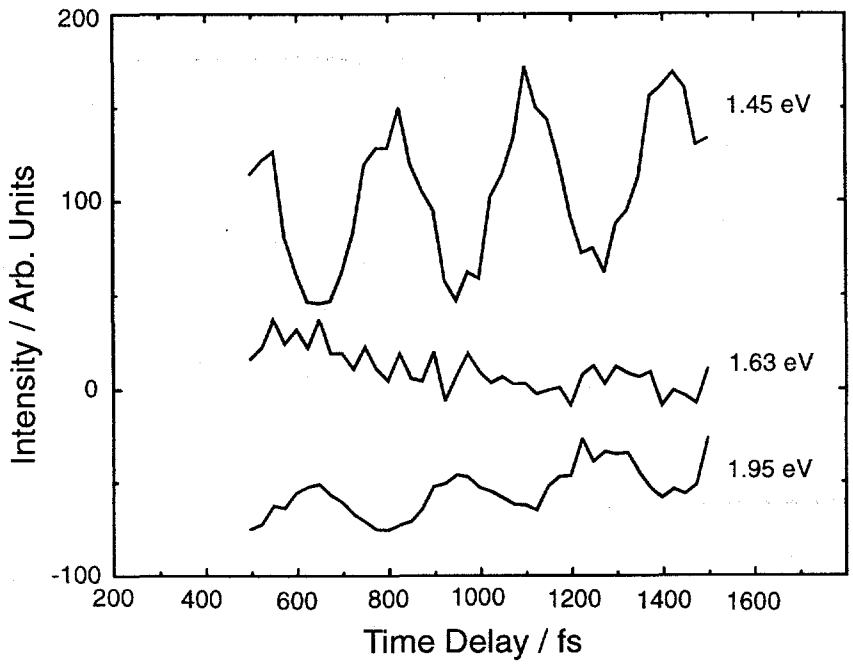

Figure 4 Slices through FPES spectra of Figure 3 at 1.45, 1.63, and 1.95 eV.

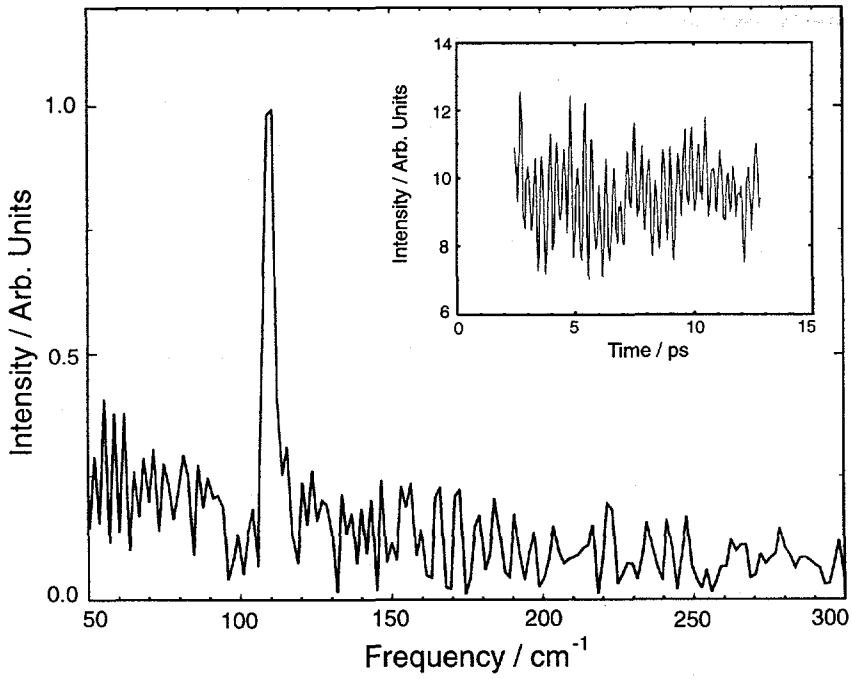

Figure 5 Solid graph is the Fourier transform at 1.45 eV of long-time FPES experiment, shown in the inset, consisting of 265 spectra stepping every 40 fs from 2000 to 12,580 fs.

The oscillations are seen more clearly in Figure 4, which shows cuts through the photoelectron spectra at three different electron kinetic energies, 1.45, 1.63 and 1.95 eV. The period of the oscillation at 1.45 and 1.95 eV is approximately 300 fs, but there is a phase shift of 180° between the two data sets. The oscillatory structure is largely absent at 1.63 eV. Shown in the inset of Figure 5 is the time-slice at 1.45 eV for a much longer experiment, consisting of approximately 30 oscillations over 12 ps. The solid line in Figure 5 is the Fourier transform of this spectrum; this is dominated by a single frequency at 110 ± 2 cm^{-1}.

4 Analysis and Discussion

4.1 Origin and significance of the coherences

In the FPES experiment, the pump pulse excites I_2^- to the repulsive $\tilde{A}'\,^2\Pi_{g,1/2}$ state. The photoelectron spectrum obtained by photodetachment with the probe pulse follows the evolution to products on this excited state, but the closed-shell atomic I^- product resulting from dissociation on the $\tilde{A}'\,^2\Pi_{g,1/2}$ state cannot be the origin of the oscillations in Figures 3 to 5. However, as mentioned above, the probe pulse does have sufficient energy to photodetach I_2^- from its ground electronic state. This suggests that the oscillatory structure in the photoelectron spectrum is associated with coherent vibrational motion induced by the pump pulse on the ground electronic state of I_2^-.

These vibrational coherences are readily understood in the context of previous femtosecond experiments. It is well known that laser pulses shorter than molecular vibrational periods and resonant with an electronic transition can excite coherences in

both the ground and excited electronic states.[26-39] If the upper electronic state is bound, excited state coherences can arise from excitation of a coherent superposition of vibrational levels lying within the laser bandwidth. The concurrent generation of coherences in the ground electronic state is a somewhat more subtle effect, because if one is starting in the ground vibration-electronic state of a molecule, then the observation of ground state oscillations signifies vibrational excitation. This process is due to resonant impulsive stimulated Raman scattering (RISRS), in which resonant Raman scattering from an ultrafast pump pulse induces vibrational excitation into nearby eigenstates[40-44]. The resonance enhancement of this process distinguishes it from the non-resonant impulsive SRS process discussed by Nelson and co-workers.[45,46] The extent to which RISRS occurs and the nature of the resulting wavepacket will depend on the pulse energy and bandwidth as well as the shape of the resonant excited state potential. Alternatively, the excitation induced by the pump can be described as "dynamical hole-burning" resulting from non-uniform excitation of the initial vibrational wavefunction.[44,47]

When the RISRS process is active, the probe pulse will typically detect vibrational coherences arising from both the ground and excited states. However, when the excited state is dissociative,[48,49] as was the case in the transient absorption experiments on I_3^- by Ruhman and co-workers,[20] the only modulations attributed to I_3^- arise from a coherent superposition of vibrational levels on its ground electronic state.

Our experiment represents another example of resonant excitation with a dissociative upper state. We therefore attribute the oscillations in our spectra to coherences on the ground electronic state of I_2^- created by the RISRS process. Figure 6 illustrates how a non-stationary wavepacket on the ground state results in oscillations in

the photoelectron spectrum. As the wavepacket evolves, its Franck-Condon overlap with the I_2 vibrational levels changes. Thus, for example, one expects photodetachment to the I_2 ground state when the anion wavepacket is at its inner turning point to produce faster electrons than at its outer turning point, because the vertical detachment energy is less at the inner turning point (compare solid and dotted lines in Figure 6). This is the origin of the phase shift in the oscillations shown in Figure 4; electron kinetic energies of 1.45 and 1.95 eV correspond to detachment at internuclear distances larger and smaller than the equilibrium bond length, respectively.

Fourier transforms were taken at 25 meV slices over the entire range of kinetic energies. Each slice is analogous to a single transient absorption experiment with a fixed probe frequency. In each case, the Fourier transform is dominated at most by a single peak, which is most prominent at eKE = 1.45 eV as shown in Figure 5. The frequency of this peak, 110 ± 2 cm^{-1}, is the fundamental vibrational frequency in I_2^-; this is the first accurate gas phase measurement of this value, and it is 5 cm^{-1} lower than the frequency obtained using Raman spectroscopy in a matrix.

As will be shown in the next section, there is some vibrationally excited I_2^- produced in our ion beam, although most of the population is in the υ=0 level. The peak in the Fourier transform is therefore primarily a result of a coherent superposition of the υ=0 and 1 levels resulting from vibrational excitation of the υ=0 level via the RISRS process. (The pump laser linewidth, 140 cm^{-1}, is larger than the 110 cm^{-1} spacing of these levels.) Coherences between adjacent levels resulting from RISRS excitation of the vibrationally excited levels of the anion are also expected, but the analysis in the next section shows that the anharmonicity $\omega_e x_e$ is only 0.370 cm^{-1}. This means that the $\upsilon_{0\text{-}1}$

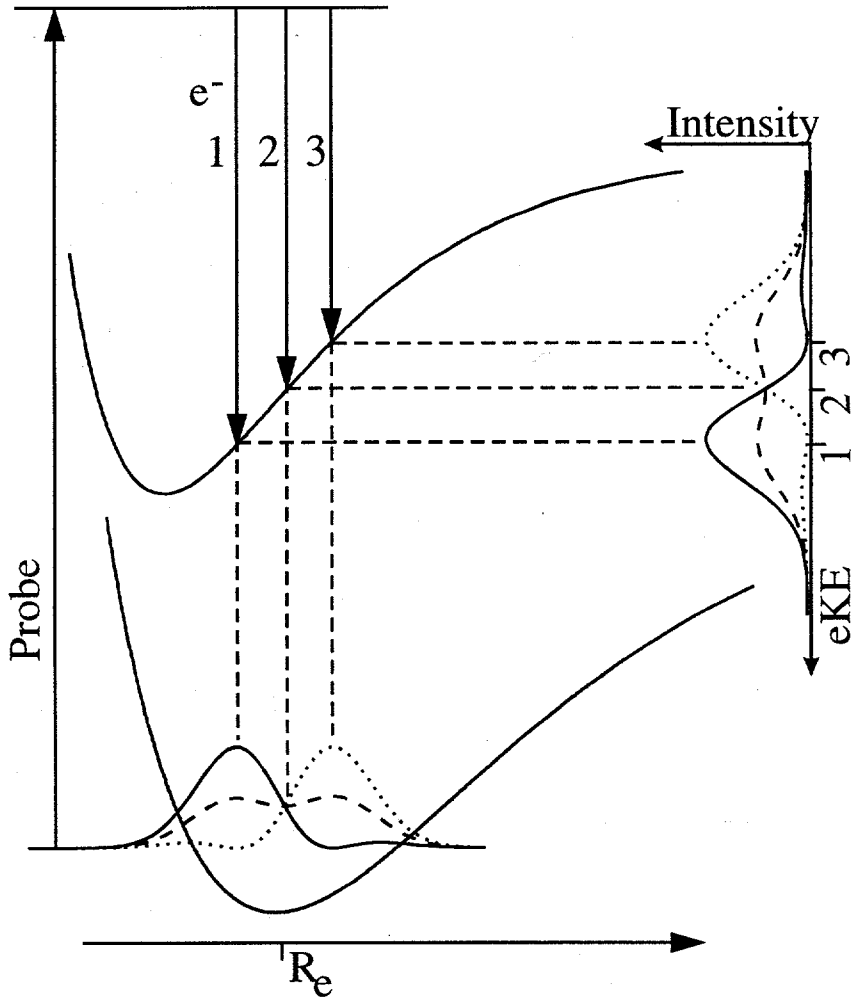

Figure 6. Effect of wavepacket motion on photoelectron spectrum. Time-evolution of coherent superposition of υ=0 and 1 vibrational eigenstates (with equal amplitude) is shown on anion potential at bottom of figure. Photoelectron signal at the three electron kinetic energies indicated are most sensitive to the wavepacket intensity at (1) $R<R_e$, (2) $R=R_e$, and (3) $R>R_e$. Right: Photoelectron spectra taken at three delay times corresponding to the three wavefunctions shown on the anion potential. The signals at energies (1) and (3) are out of phase by 180°, while the signal at (2) remains constant.

and $\upsilon_{1\text{-}2}$ frequencies differ by less than a wavenumber, and this small splitting is apparently not detectable in our experiment. Some of the Fourier transforms at eKE < 1.45 eV show evidence for a peak at twice the fundamental frequency, as expected for a coherence between vibrational levels differing by two quanta. However, this peak is at best barely above the noise level, so these coherences are either very weak or non-existent in our experiment.

One final point of interest is that when the wavepacket is only composed of adjacent vibrational levels (υ=0 and 1, υ=1 and 2, etc.), the probability density as a function of time is approximately constant at the equilibrium bond length (exactly constant for a harmonic oscillator). This is shown explicitly in Figure 6. As a result, there should be very little oscillatory structure at eKE values that correspond to vertical detachment near the equilibrium bond length. This is the reason for the absence of oscillations in the energy slice at 1.63 eV in Figure 4.

4.2 I_2^- ground state potential

In this section a Morse potential for the ground state of I_2^- is constructed by fitting the conventional photoelectron spectrum in Figure 2 with the harmonic vibrational frequency, ω_e, constrained to equal the fundamental vibrational frequency $\upsilon_{0\text{-}1}$ determined in the previous section(see below). Since the Morse potential only has three parameters

$$V(r) = D_e[1 - e^{-\beta(R-R_e)}]^2 \qquad (2)$$

where

$$\beta = \omega_e\left(\frac{2\pi^2\mu}{D_e}\right)^{1/2} \qquad (3)$$

and μ is the reduced mass, the analysis in this section is aimed at determining the well depth, D_e, and equilibrium internuclear separation, R_e. This information can be extracted from the photoelectron spectrum in Figure 2 because (a) the neutral states of I_2 are very well characterized from fluorescence measurements,[15-18] and (b) the origin of the band corresponding to photodetachment to the $\tilde{A}\ ^3\Pi_{1u}$ state of I_2 at eKE($\tilde{A}$)=0.272 ± 0.005 eV can be assigned by inspection.

The adiabatic electron affinity of I_2 is then given by

$$EA(I_2) = h\nu - eKE(\tilde{A}) - T_0(\tilde{A}), \qquad (4)$$

where $T_0(\tilde{A})$=1.345 eV is the electronic term value for the $\tilde{A}\ ^3\Pi_{1u}$ state of I_2.[15] This yields 2.524 ± 0.005 eV for the electron affinity of I_2, in contrast to the previous, averaged literature value of 2.55 eV.[8] The well depth $D_0(I_2^-)$ is then determined from

$$D_0(I_2^-) = EA(I_2) + D_0(I_2) - EA(I) \qquad (5)$$

Using D_0 (I_2)=1.542 eV and EA(I)=3.059 eV (Ref. 18 and 50), we find D_0 (I_2^-)=1.007 eV. The well depth, D_e = 1.014 eV is determined by adding the anion zero point vibrational energy (assumed to be $\omega_e/2$) of 0.007 eV. The anharmonicity $\omega_e x_e$ can then be from obtained from

$$\omega_e x_e = \frac{\omega_e^2}{4D_e} \qquad (6)$$

yielding $\omega_e x_e$=0.370 cm^{-1}. This small value justifies setting $\omega_e = \upsilon_{01}$.

With the well depth and vibrational frequency of I_2^- determined, R_e can be obtained through simulations of the conventional photoelectron spectrum within the Franck-Condon approximation. The Discrete Variable Representation (DVR) with a

Morse oscillator basis set[51] was used to calculate anion and neutral vibrational wavefunctions and the Franck-Condon factors between the anion and the three neutral states. The anion R_e and vibrational populations were varied, and the simulation was convoluted with an instrument response function to accurately reproduce the neutral state vibrational progressions. The final Morse parameters are given in Table I, and the simulated spectrum and assumed vibrational distribution for the I_2^- are shown in Figure 2.

The effects of hot bands on the spectrum are quite pronounced. Peaks solely due to hot bands are seen on the high electron kinetic energy side of the origin transitions for the $\tilde{A}$ and $\tilde{A}'$ bands. They also add intensity to transitions originating from the $I_2^-(\upsilon=0)$ level. The effects of hot bands can also be seen in the $\tilde{X}$ band. Because of the large geometry change upon photodetachment to the $\tilde{X}$ state, the spatial extent and nodal structure of the anion vibrational wavefunctions are reflected in the intensity profile in the photoelectron spectrum. Thus, transitions originating from the $I_2^-(\upsilon=0)$ level have an approximately Gaussian intensity profile, while those from $I_2^-(\upsilon=1)$ have a bimodal intensity profile extending to higher and lower final vibrational levels than the $\upsilon=0$ transitions, but with relatively little intensity at the center of the $\upsilon=0$ profile. The net effect is that vibrational structure is resolved in the center of the $\tilde{X}$ band, as these are primarily transitions from the anion $\upsilon=0$ level, while transitions from multiple anion vibrational levels contribute to the wings of the $\tilde{X}$ band, resulting in overlapped transitions that cannot be resolved by our spectrometer. Although there is some range in the anion population within which the spectrum can be successfully simulated, R_e did not change by more than 0.005 Å over this range.

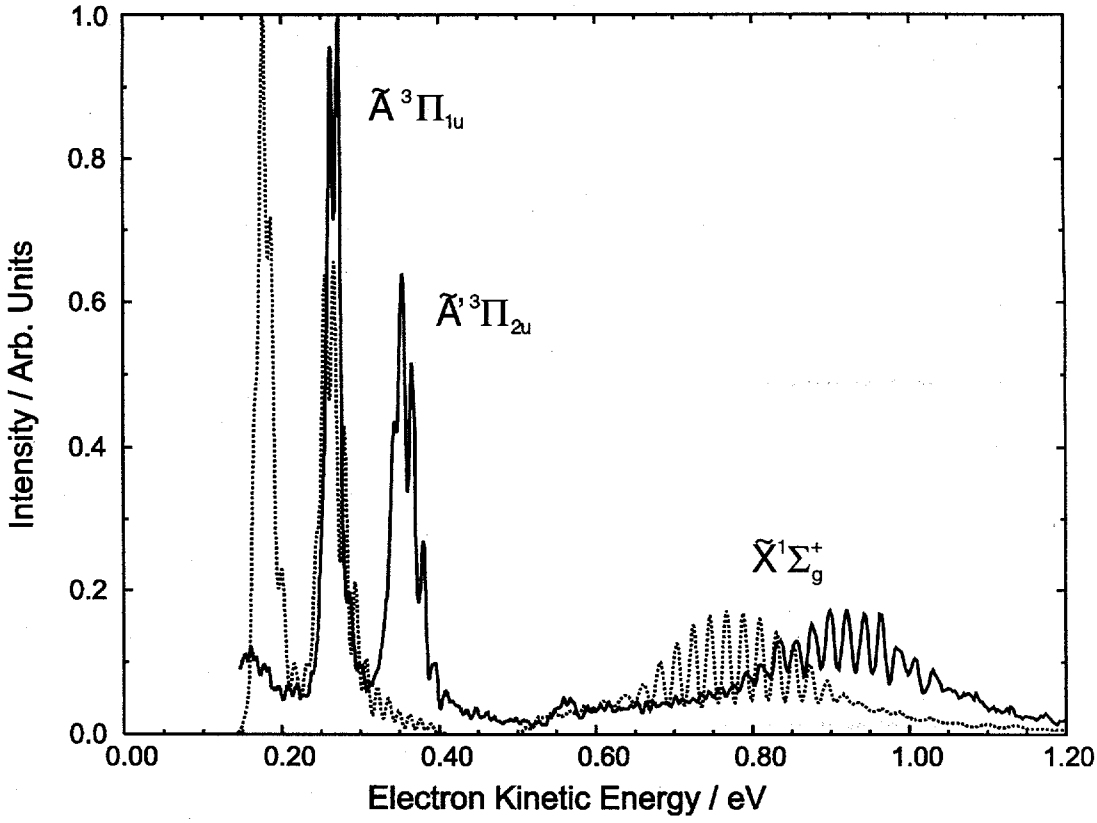

Figure 7. Experimental (solid) and simulated (dashed) photoelectron spectrum of I_2^- using the Chen and Wentworth potential.[8]

Table I compares our Morse parameters with four other potentials proposed for the I_2^- ground state: the empirical potentials of Chen and Wentworth,[8] Dojahn *et al.*,[9] and Chen *et al.*,[10] and the *ab initio* potential of Maslen *et al.*[14] The original Chen and Wentworth potential is closest to ours, although our potential well is not as deep (1.014 *vs.* 1.10 eV), and our value for R_e is smaller (3.205 *vs.* 3.23 Å). As an indication of the sensitivity of the photoelectron spectrum to the potential parameters, Figure 7 shows simulations using the Chen and Wentworth potential (dashed), superimposed on the experimental spectrum (solid). The simulated $\tilde{A}'$ and $\tilde{A}$ bands occur at about 0.1 eV lower eKE than the experimental bands, indicating that the anion potential well is too deep. The even larger shift of 0.2 eV in the center of the simulated $\tilde{X}$ band and the differences in the Franck-Condon profiles for all three bands result from the overly large bond length in the anion potential. Note that the more recent potentials by Dojahn *et al.* and Chen *et al.* are progressively moving away from our parameters, implying that the assumptions made about the bond length and the correlation between the anions and positive ion dimers are not reliable for the case of I_2^-.

5. Conclusion

The ground state of I_2^- has been fit to a Morse function. The vibrational frequency is obtained from a femtosecond photoelectron spectroscopy experiment, in which resonant impulsive stimulated Raman scattering (RISRS) induced by the pump pulse leads to oscillatory structure in the time-dependent photoelectron spectra. The well depth and equilibrium bond length are derived from a Franck-Condon analysis of the high resolution photoelectron spectrum of I_2^- which consists of vibrationally resolved

transitions to the three lowest electronic states of I_2. Our results yield a shallower well depth and a shorter bond length than the previously published semiempirical potentials.

The results presented here show FPES and conventional photoelectron spectroscopy to be a complementary and powerful set of techniques to probe anion potential energy features. The demonstration of the RISRS process on gas-phase anions and the resulting determination of the I_2^- vibrational frequency suggests that the FPES experiment will be useful in measuring vibrational frequencies of other molecular and cluster anions.

6. Acknowledgments

This research is supported by the National Science Foundation under Grant No. CHE-9404735. Support from the Defense University Research Instrumentation Program and Air Force Office of Scientific Research under Grant No. F49620-95-1-0078 is also gratefully acknowledged. The authors also thank Robert J. Le Roy for providing the RKR algorithm and Joel Tellinghuisen for insight into the $\tilde{A}'$ neutral state.

7. References

[1] J. M. Papanikolas, J. R. Gord, N. E. Levinger, D. Ray, V. Vorsa, and W. C. Lineberger, J. Phys. Chem. **95,** 8028 (1991).

[2] J. M. Papanikolas, V. Vorsa, M. E. Nadal, P. J. Campagnola, H. K. Buchenau, and W. C. Lineberger, J. Chem. Phys. **99,** 8733 (1993).

[3] V. Vorsa, S. Nandi, P. J. Campagnola, M. Larsson, and W. C. Lineberger, J. Chem. Phys. **106,** 1402 (1997).

[4] B. J. Greenblatt, M. T. Zanni, and D. M. Neumark, Science **276,** 1675 (1997).

[5] I. Benjamin, P. F. Barbara, B. J. Gertner, and J. T. Hynes, J. Phys. Chem. **99,** 7557 (1995).

[6] A. E. Johnson, N. E. Levinger, and P. F. Barbara, J. Phys. Chem. **96,** 7841 (1992).

[7] P. K. Walhout, J. C. Alfano, K. A. M. Thakur, and P. F. Barbara, J. Phys. Chem. **99,** 7568 (1995).

[8] E. C. M. Chen and W. E. Wentworth, J. Phys. Chem. **89,** 4099 (1985).

[9] J. G. Dojahn, E. C. M. Chen, and W. E. Wentworth, J. Phys. Chem. **100,** 9649 (1996).

[10] E. C. M. Chen, J. G. Dojahn, and W. E. Wentworth, J. Phys. Chem. A **101,** 3088 (1997).

[11] P. W. Tasker, G. G. Balint-Kurti, and R. N. Dixon, Mol. Phys. **32,** 1651 (1976).

[12] G. A. Bowmaker, P. Schwerdfeger, and L. v. Szentpaly, J. Mol. Struct. THEOCHEM **53,** 87 (1989).

[13] D. Danonvich, J. Hrusak, and S. Shaik, Chem. Phys. Lett. **233,** 249 (1995).

[14] P. E. Maslen, J. Faeder, and R. Parson, Chem. Phys. Lett. **263,** 63 (1996).

[15] D. R. T. Appadoo, R. J. Leroy, P. F. Bernath, S. Gerstenkorn, P. Luc, J. Verges, J. Sinzelle, J. Chevillard, and Y. Daignaux, J. Chem. Phys. **104,** 903 (1996).

[16] X. N. Zheng, S. L. Fei, M. C. Heaven, and J. Tellinghuisen, J. Chem. Phys. **96,** 4877 (1992).

[17] J. W. Tromp and R. J. Le Roy, Journal of Molecular Spectroscopy **109,** 352 (1985).

[18] F. Martin, R. Bacis, S. Churassy, and J. Verges, Journal of Molecular Spectroscopy **116,** 71 (1986).

[19] B. J. Greenblatt, M. T. Zanni, and D. M. Neumark, Chem. Phys. Lett. **258,** 523 (1996).

[20] U. Banin and S. Ruhman, J. Chem. Phys. **98,** 4391 (1993).

[21] C. Xu, G. R. Burton, T. R. Taylor, and D. M. Neumark, J. Chem. Phys., in press (1997).

[22] R. B. Metz, A. Weaver, S. E. Bradforth, T. N. Kitsopoulos, and D. M. Neumark, J. Phys. Chem. **94,** 1377 (1990).

[23] R. Prosch and T. Trickl, Rev. Sci. Instrum. **60,** 713 (1989).

[24] W. C. Wiley and I. H. McLaren, Rev. Sci. Instrum. **26,** 1150 (1955).

[25] O. Cheshnovsky, S. H. Yang, C. L. Pettiette, M. J. Craycraft, and R. E. Smalley, Rev. Sci. Instrum. **58,** 2131 (1987).

[26] M. J. Rosker, F. W. Wise, and C. L. Tang, Phys. Rev. Lett. **57,** 321 (1986).

[27] J. M. Y. Ha, H. J. Maris, W. M. Risen, Jr., J. Tauc, C. Thomsen, and Z. Vardeny, Phys. Rev. Lett. **57,** 3302 (1986).

[28] K. A. Nelson and L. R. Williams, Phys. Rev. Lett. **58,** 745 (1987).

[29] B. Hartke, R. Kosloff, and S. Ruhman, Chem. Phys. Lett. **158,** 238 (1989).

[30] R. M. Bowman, M. Dantus, and A. H. Zewail, Chem. Phys. Lett. **161,** 297 (1989).

[31] M. Gruebele, G. Roberts, M. Dantus, R. M. Bowman, and A. H. Zewail, Chem. Phys. Lett. **166,** 459 (1990).

[32] T. Baumert, V. Engel, C. Meier, and G. Gerber, Chem. Phys. Lett. **200,** 488 (1992).

[33] S. Rutz, S. Greschik, E. Schreiber, and L. Woste, Chem. Phys. Lett. **200,** 488 (1992).

[34] T. Baumert, V. Engel, C. Rottgermann, W. T. Strunz, and G. Gerber, Chem. Phys. Lett. **191,** 639 (1992).

[35] M. Gruebele and A. H. Zewail, J. Chem. Phys. **98,** 883 (1993).

[36] G. Rodriguez and J. G. Eden, Chem. Phys. Lett. **205,** 371 (1993).

[37] H. Ruppe, S. Rutz, E. Schrieber, and L. Woste, Chem. Phys. Lett. **257,** 356 (1996).

[38] R. de Vivie-Riedle, K. Kobe, J. Manz, W. Meyer, B. Reischl, S. Rutz, E. Schreiber, and L. Woste, J. Phys. Chem. **100,** 7789 (1996).

[39] A. Assion, M. Geisler, J. Helbing, V. Seyfried, and T. Baumert, Phys. Rev. A **54,** R4605 (1996).

[40] A. Mokhtari and J. Chesnoy, Europhys. Lett. **5,** 523 (1988).

[41] J. Chesnoy and A. Mokhtari, Phys. Rev. A **38,** 3566 (1988).

[42] S. L. Dexheimer, Q. Wang, L. A. Peteanu, W. T. Pollard, R. A. Mathies, and C. V. Shank, Chem. Phys. Lett. **188,** 61 (1992).

[43] W. T. Pollard and R. A. Mathies, Annu. Rev. Phys. Chem. **43,** 497 (1992).

[44] U. Banin, A. Bartana, S. Ruhman, and R. Kosloff, J. Chem. Phys. **101,** 8461 (1994).

[45] S. de Silvestri, J. G. Fujimoto, E. P. Ippen, E. B. Gamble, Jr., L. R. Williams, and K. A. Nelson, Chem. Phys. Lett. **116,** 146 (1985).

[46] Y. Yong-Xin, E. B. Gamble, Jr., and K. A. Nelson, J. Chem. Phys. **83,** 5391 (1985).

[47] D. M. Jonas, S. E. Bradforth, S. A. Passino, and G. R. Fleming, J. Phys. Chem. **99,** 2594 (1995).

[48] N. F. Scherer, L. D. Ziegler, and G. R. Fleming, J. Chem. Phys. **97,** 5544 (1992).

[49] N. F. Scherer, D. M. Jonas, and G. R. Fleming, J. Chem. Phys. **99,** 153 (1993).

[50] H. Hotop and W. C. Lineberger, J. Phys. Chem. Ref. Data **14,** 731 (1985).

[51] E. M. Greenawalt and A. S. Dickinson, J. Mol. Spec. **30,** 427 (1969).

Chapter 4. Femtosecond photoelectron spectroscopy of the I_2^- anion: characterization of the $\tilde{A}'\,^2\Pi_{g,1/2}$ excited state[†]

A potential energy curve for the $\tilde{A}'\,^2\Pi_{g,1/2}$ state of I_2^- is constructed based on femtosecond photoelectron spectroscopy of the I_2^- $\tilde{A}'\,^2\Pi_{g,1/2} \leftarrow \tilde{X}\,^2\Sigma_u^+$ transition at 780 nm. The experiment is sensitive to the slope of the repulsive potential wall, the well depth, equilibrium bond length, and the long-range attractive portion of the upper state potential. The $\tilde{A}'\,^2\Pi_{g,1/2}$ potential is fit to a piecewise potential, which is flexible in each of these regions. Simulations of the spectrum using a previously determined Morse potential for the $\tilde{X}\,^2\Sigma_u^+$ state of I_2^- [J. Chem. Phys. **107,** 7613 (1997)] yields a well depth (D_e) of 0.017 ± 0.010 eV for the $\tilde{A}'\,^2\Pi_{g,1/2}$ state with an equilibrium bond length (R_e) of 6.2 ± 0.6 Å. These values differ significantly from previous semi-empirical results.

1. Introduction

Photodissociation of iodine in clusters,[1,2] liquids,[3-10] and matrices[11,12] has for many years been a model system for the study of caging, recombination, and vibrational relaxation. In I_2^-, the analogous negative ion system, the effect of much stronger solvent/solute interactions on these processes has been explored in size-selected clusters of $I_2^-(Ar)_n$,[13,14] $I_2^-(CO_2)_n$,[13,15-17] $I_2^-(OCS)_n$[18] and in several polar solvents.[19-21] The vibrational relaxation of I_2^- photofragments created by the photodissociation of I_3^- has also been studied in liquids.[22-24] The interpretation and theoretical modeling of all of

[†] Originally published in J. Chem. Phys. **110**, 3748 (1999).

these experiments, however, relies at least in part on accurate ground and excited state potential energy curves for I_2^-. We have recently reported an accurate ground state potential for I_2^-,[25] but the available empirical excited state potentials are at best approximately correct.[26-28] In this study, we apply femtosecond photoelectron spectroscopy (FPES) to the photodissociation of I_2^-, and simulate our experimental results using an improved quantum mechanical simulation method. The experimental results are of considerably higher quality than those reported by us previously.[29] The new results in conjuction with the simulations enables us to generate the first quantitative potential for the $I_2^-(\tilde{A}'\,^2\Pi_{g,1/2})$ excited state.

The FPES experiment involves photoexcitation of I_2^- from its ground $\tilde{X}\,^2\Sigma_u^+$ state to the dissociative $\tilde{A}'\,^2\Pi_{g,1/2}$ state with a femtosecond pump pulse at 780 nm. The photoelectron spectrum of the dissociating molecule is measured at a series of delay times by photodetachment with a femtosecond probe pulse. The variation of the photoelectron spectrum with delay time monitors the dissociating anion from the initial Franck-Condon region of excitation out to the asymptotic product channel of I^- + I. Hence one can, in principle, probe the excited state potential over the entire reaction coordinate.

The anion and neutral states potentials relevant to our experiment are shown in Fig. 1. Most of the neutral I_2 states which correlate to $I(^2P_{3/2})$ + $I(^2P_{3/2})$ products are well characterized,[30-36] as is the ground state of the anion,[25] leaving the excited anion surface the most uncertain. There exist several previously reported empirical and *ab initio* potentials for the excited states of I_2^-. Chen and Wentworth have published semi-

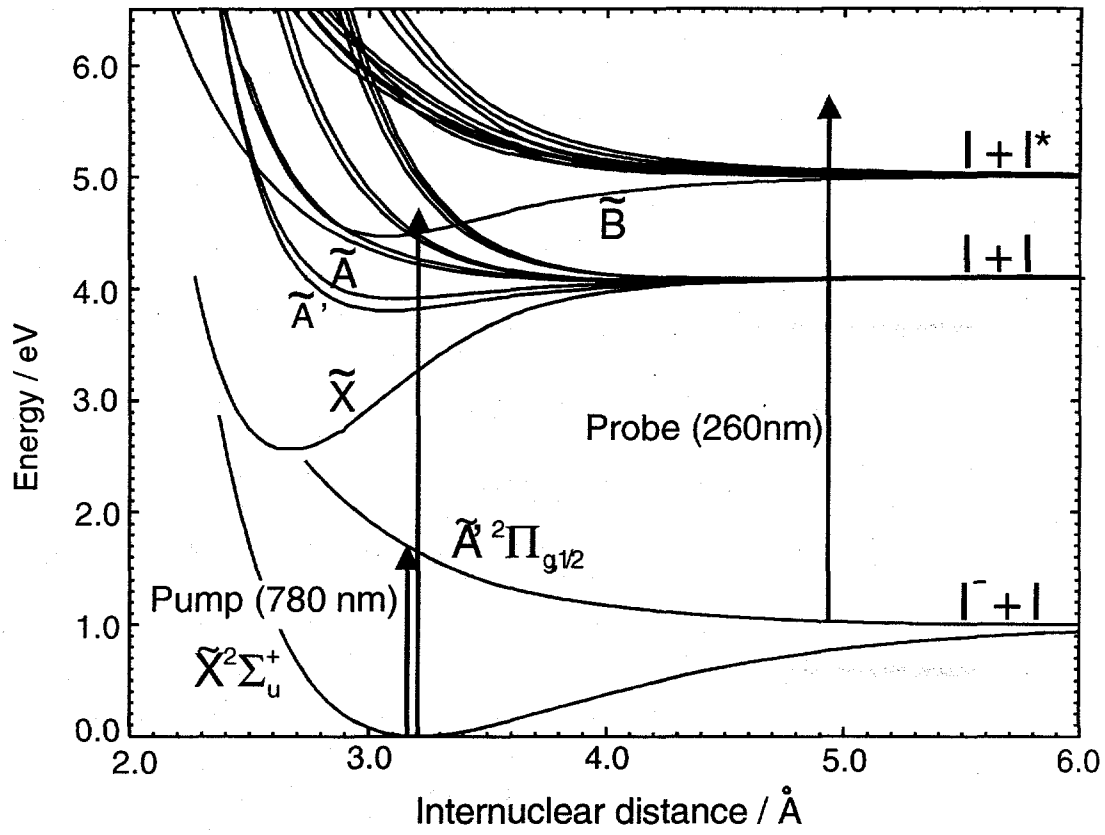

Figure 1. Potential energy curves for the I_2 and I_2^- electronic states relevant to the discussion.[25,30-36,53] Only the $\tilde{X}\ ^1\Sigma_g^+$, $\tilde{A}'^3\Pi_{2u}$, $\tilde{A}^3\Pi_{1u}$, and $\tilde{B}^3\Pi_{0^+u}$ states of I_2 are labelled. The 260 nm probe is shown detaching the ground and excited state potentials of I_2^-.

empirical potentials based on a wide range of experimental data including electronic spectroscopy in crystals and gas phase dissociative attachment experiments.[26] *Since their* original publication in 1985, they have twice updated the potentials for these states using more recent experimental data.[27,28] The potentials remain largely uncertain, however, since they are composed of at most four experimental parameters.

Several *ab initio* studies have also been performed on I_2^-. These include valence bond methods by Tasker *et al.*,[37] self-consistent field (SCF) calculations by Bowmaker *et al.*,[38] and relativistic core potentials by Shaik and co-workers.[39] These studies are complicated, however, because of the large number of electrons and strong spin-orbit coupling in I_2^-. Spin-orbit effects were explicitly included in a multirerence configuration interaction calculation of the I_2^- potentials by Maslen *et al.*[40] These potentials have been recently improved[41,42] by scaling the *ab initio* curves to reproduce the experimental equilibrium bond length and well depth for the $\tilde{X}\ ^2\Sigma_u^+$ state,[25] while maintaining the *ab initio* energy spacings. The resulting potential for the $I_2^-(\tilde{A}'\ ^2\Pi_{g,1/2})$ state has a shallow well at long internuclear distance: D_e = 19.5 meV and R_e = 6.8 Å. Simulations[43] on the scaled potentials yield reasonable agreement with our original FPES study of I_2^-,[29] particularly at early time delays.

We have previously reported on the $I_2^-\ \tilde{A}'\ ^2\Pi_{g,1/2} \leftarrow \tilde{X}\ ^2\Sigma_u^+$ photodissociation at 780 nm studied with FPES.[29] Since then, the experimental resolution has been improved by more than a factor of three. In addition, our ability to simulate the spectra has improved significantly for several reasons. First, we now have a more accurate potential[25] for the ground state of I_2^- than was available at the time of the original study. Secondly, the quantum mechanical simulation method originally used was extremely

time-consuming, and the simulations performed included photodetachment transitions to only three of the 20 neutral I_2 electronic states that correlate to $I(^2P_{3/2})+ I(^2P_{3/2})$ and $I(^2P_{3/2})+I^*(^2P_{1/2})$ products, namely the $\tilde{A}'\,^3\Pi_{2u}$, $\tilde{A}\,^3\Pi_{1u}$, and $\tilde{B}'\,^3\Pi_{0^-_u}$ states. The improved quantum mechanical simulation method described in our accompanying paper[44] is considerably more efficient, and the simulations reported here incorporate photodetachment to all 20 relevant states of I_2. Finally, we have developed an empirical functional form to reproduce our experimental resolution, and thus more faithfully convolute our simulations for comparison with experiment. These improvements in the experiment and analysis result in a definitive characterization of the $I_2^-(\tilde{A}'\,^2\Pi_{g,1/2})$ state.

2. Experimental

The FPES experiment consists of two major components: a negative ion photoelectron spectrometer and a high repetition rate femtosecond laser. Each has been described in detail elsewhere and will be discussed only briefly below.[17,25]

The photoelectron spectrometer has been optimized to be compatible with the high laser repetition rate (500 Hz in these experiments) and the low photoelectron signal expected for a two-photon pump-and-probe experiment. Argon carrier gas (10 psig) is passed over crystalline I_2 and supersonically expanded through a pulsed piezo electric valve operating at a repetition rate of 500 Hz.[45] Anions are generated by a 1 keV electron beam which crosses the expansion just downstream of the nozzle, and are injected into a Wiley-McLaren time-of-flight mass spectrometer[46] by applying pulsed extraction and acceleration fields perpendicular to the molecular beam axis. After passing through several differentially pumped regions, the ions enter the detector chamber where they are

dissociated with the pump laser pulse and detached with the probe laser pulse. The ions are monitored with a retractable, in-line microchannel plate detector. High electron collection efficiency is achieved with a "magnetic bottle" time-of-flight analyzer[47] whose energy resolution has been optimized using a pulsed decelerator[48,49] applied to the ions just prior to photodetachment. The instrument resolution is determined by photodetachment of I^- with 390 and 260 nm light. This produces three atomic peaks at 0.12, 0.77, and 1.71 eV whose widths increase with electron kinetic energy. Their widths are 20, 50, and 76 meV, respectively. These three peaks are used to convolute the simulated FPES spectra as described in Section 4.2.

The pump and probe laser pulses are obtained from a Clark-MXR regeneratively amplified Ti:Sapphire laser system, which generates pulses at 780 nm (1.59 eV) with 1 mJ energy and 80 fs ($sech^2$) width. About 150 μJ of this is used as the pump pulse. The probe pulse is generated by frequency-tripling the remainder of the 780 nm fundamental, producing pulses at 260 nm (4.77 eV), with 20 μJ energy, and 130 fs width (the latter measured by difference frequency mixing with the fundamental light). The relative delay between the pump and probe pulses is adjusted with a computer controlled translation stage, and the beams are collinearly recombined prior to entering the vacuum chamber. The probe pulse has enough energy to detach the I^- products as well as ground state I_2^-, which produces a background spectrum. By passing the pump beam through a 250 Hz chopper (New Focus, 3501), shot-to-shot subtraction of the background photoelectron signal is performed. The background signal is also integrated and used to normalize different scans.

The vacuum chamber window affects the individual pulse widths and the relative delay between the pump and probe pulses. To characterize the pulses and determine the zero-of-time inside the chamber, two-color above-threshold detachment of I^- is used.[50] The probe pulse alone produces a photoelectron spectrum with two peaks at 0.77 and 1.71 eV. When the pump and probe pulses are temporally overlapped, additional peaks are observed that correspond to shifting the I^- peaks by 1.59 eV towards higher eKE; i.e. the photon energy of the pump pulse. From the intensity of this two-color signal as a function of pump-probe delay, we determine the zero-delay time and the cross-correlation of the pump and probe pulses inside the vacuum chamber. This yields a convoluted FWHM of 175 fs.

3. Results

Fig. 2 (solid) shows successive femtosecond photoelectron spectra, plotted as a function of electron kinetic energy, and taken at increasingly larger pump-probe delay times. Also included in Fig. 2 (dotted and dashed) are the simulated spectra, which will be discussed in Section 4. At the bottom of the figure, the experimental background spectrum arising from detachment of ground state I_2^- by the probe pulse is shown, and the peaks labelled A, B, and C in the background spectrum are due to transitions to the $\tilde{A}\ ^3\Pi_{1u}$, $\tilde{A}'\ ^3\Pi_{2u}$, and $\tilde{X}\ ^1\Sigma_g^+$ states of neutral I_2, respectively.[25] This spectrum has been suitably scaled and subtracted from each of the two-photon spectra to remove the effects of ground state depletion by the pump pulse. Hence, these spectra reflect only the dynamics induced by the pump pulse.

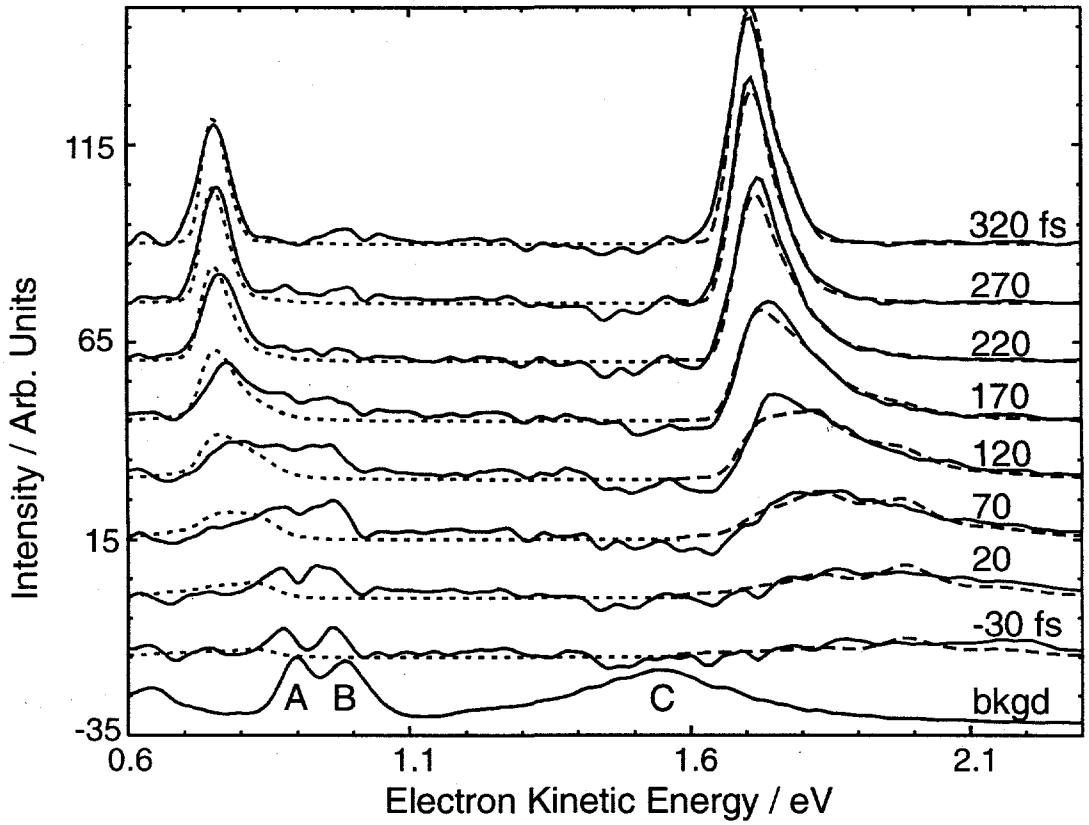

Figure 2. Experimental femtosecond photoelectron spectrum taken at various pump-probe delay times (solid). The background spectrum from detachment of ground state I_2^- by the 260 nm probe pulse is also shown (bottom). The peaks labelled A, B, and C result from detachment to the $\tilde{A}^3\Pi_{1u}$, $\tilde{A}'^3\Pi_{2u}$, and $\tilde{X}\ ^1\Sigma_g^+$ states of I_2, respectively. Simulated spectra used to characterize the $I_2^-(\tilde{A}'\ ^2\Pi_{g,1/2})$ state (dashed), and simulations used to evaluate the *ab initio* potentials (dotted) are also shown.

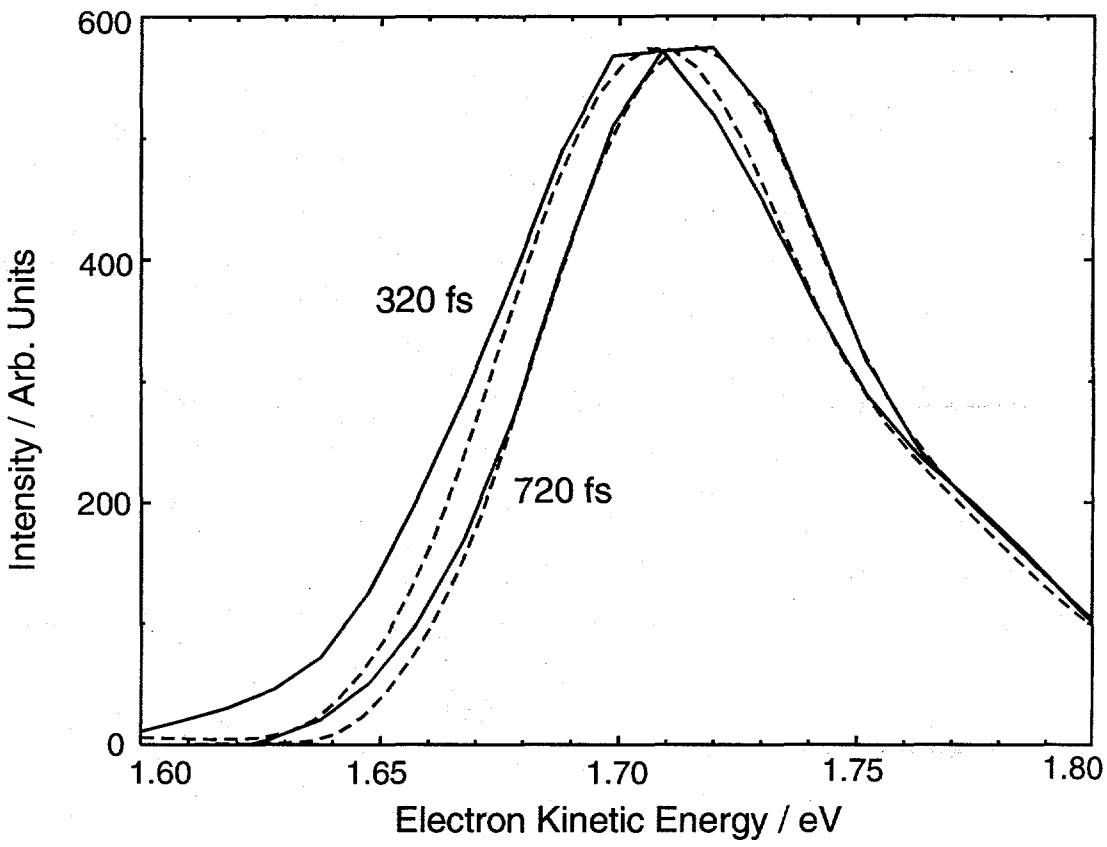

Figure 3. Expanded view of the atomic $I(^2P_{3/2}) \leftarrow I^-(^1S)$ feature at 1.71 eV. The experimental spectra (solid) shifts ~10 meV to higher energies from 320 to 720 fs. The simulated spectra (dashed) closely follows this trend.

The spectra in Fig. 2 are qualitatively similar to lower energy resolution spectra reported previously. In Fig. 2, one observes two broad features shifting toward lower energy as the delay time increases and evolving by 320 fs into two narrow peaks centered at 0.76 and 1.70 eV. Previously, the two narrow features were assigned to transitions from the I^- photoproduct to the $^2P_{1/2}$ and $^2P_{3/2}$ states of iodine, respectively, and the broad transients at earlier times were assigned to detachment of the dissociating wavepacket on the $I_2^-(\tilde{A}'\,^2\Pi_{g,1/2})$ potential energy curve.

However, while the atomic features reach their maximum height by 320 fs, they undergo a 10 meV shift to higher kinetic energies over the next 400 fs, which actually brings them into better agreement with the atomic transitions for free I^- (which appear at 0.77 and 1.71 eV). This shift is shown in Fig. 3, where higher energy atomic features are expanded and compared at 320 fs and 720 fs. The energy shift is continuous and smooth over this time interval, and was not observed before in our earlier study on I_2^-, most likely due to our poorer electron energy resolution. As will be discussed below, the shift arises from the excited state wavepacket traversing the long-range attractive portion of the I_2^- potential.

Since 1.71 eV corresponds to photodetachment of I^- products, a cut through the FPES spectra at this energy provides a measure of I^- production as a function of time. This is shown in Fig. 4 (solid). The half-maximum height is reached by 180 fs, and the full height at 320 fs. Repeated measurements of the experiment give a risetime which is reproduceable to within ±10 fs, and is considered our experimental error. The half-maximum height observed here is approximately 50 fs longer than our previously

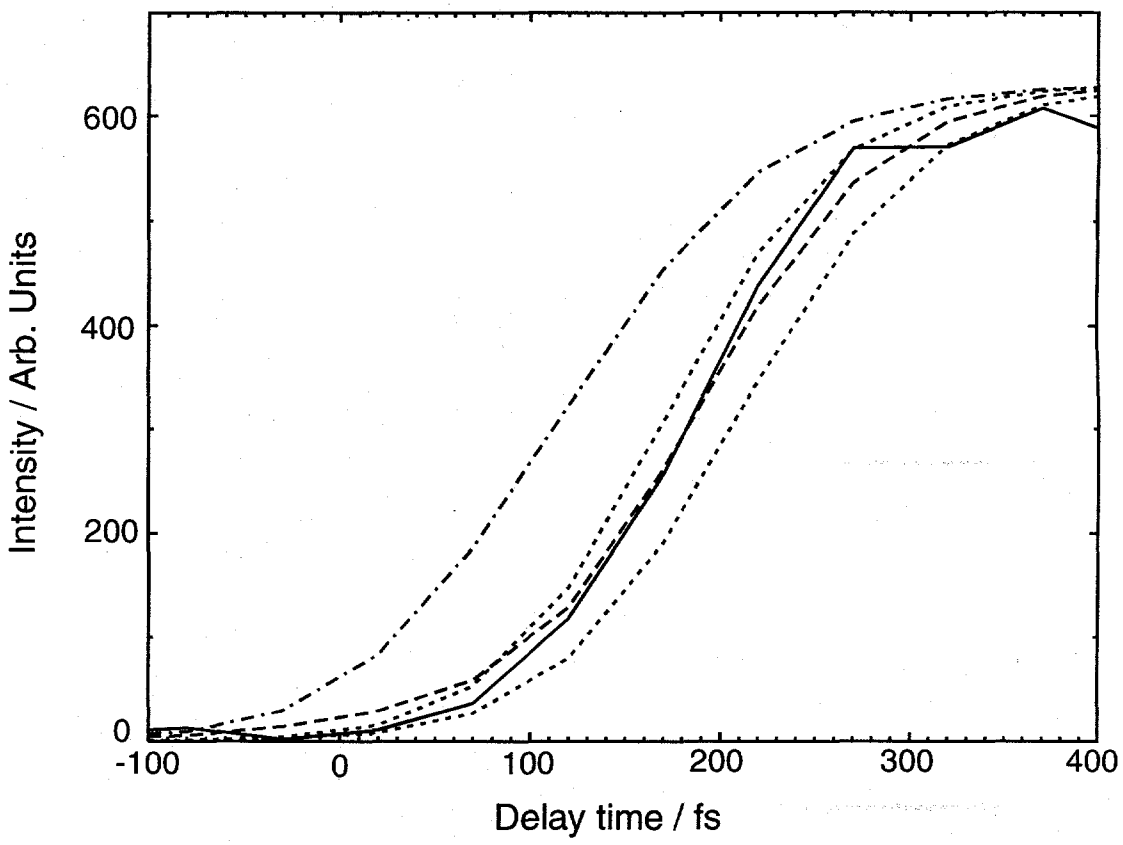

Figure 4. Intensity at 1.71 eV plotted as a function of delay time, monitoring the appearance of I^- products. The experimental intensity (solid) reaches its half-maximum height by 180 fs and its full height by 320 fs. Risetimes for the best-fit potential (dashed), error-limit potentials (dotted), and the Chen and Wentworth potential[26] (dot-dashed) are also shown.

reported results.[29] This is again a result of our improved energy resolution which enables us to separate better the atomic and transient contributions to the spectra.

4. Analysis and Discussion

In this section we develop a $I_2^-(\tilde{A}'\,^2\Pi_{g,1/2})$ excited state potential that is accurate to within our experimental error by simulating the FPES spectra above 1.6 eV. To this end, we first explain the analytical potential used in the simulations, and our method of convoluting the simulated spectra. The simulations are then compared to experiment, error bars on the potential are estimated, and a comparison is made to previously reported potentials. Finally, the complete FPES spectra are simulated using all 20 neutral potentials, and the accuracy of current I_2 *ab initio* potentials is commented on.

4.1 Analytical Form of the $I_2^-(\tilde{A}'\,^2\Pi_{g,1/2})$ state

The FPES spectra are sensitive to three parts of the potential, listed in order of increasing internuclear distance: (1) the FC region, where the potential is repulsive, (2) the region in the vicinity of the attractive well, the existence of which is supported by the results in Fig. 3, and (3) the long-range attractive region. To effectively simulate the FPES spectra, a potential is needed which can be easily modified in these three areas. We have chosen Morse potentials to represent the first two regions, while the long-range attractive region is represented by a function which includes the charge-induced dipole (r^{-4}) and charge-induced quadrupole and dispersion (r^{-6}) terms. Two switching functions are used for transitions between regions. The analytical form for the entire potential is given in Eqns. 1 & 2,

$$
\begin{aligned}
V(\mathrm{r}) &= 2D_e^1 \exp[-\beta^1(r-r_e^1)] + D_e^1 \exp[-2\beta^1(r-r_e^1)] \equiv v_1(r), && 0<r\le r_1 \\
&= sf_1(r)v_1(r) + [1-sf_1(r)]v_2(r), && r_1<r\le r_2 \\
&= 2D_e^2 \exp[-\beta^2(r-r_e^2)] + D_e^2 \exp[-2\beta^2(r-r_e^2)] \equiv v_2(r), && r_2<r\le r_3 \qquad (1) \\
&= sf_2(r)v_2(r) + [1-sf_2(r)]v_3(r), && r_3<r\le r_4 \\
&= -B_4/(D_e^2 r^4) - B_6/(D_e^2 r^6) \equiv v_3(r), && r_4<r<\infty
\end{aligned}
$$

where

$$
sf_n(r) = \frac{1}{2}\left(\cos\frac{\pi(r-r_n)}{r_{n+1}-r_n}+1\right). \qquad (2)
$$

$sf_n(r)$ are the switching functions connecting the three functions $v_n(r)$. D_e^n, r_e^n, and β^n are the well depth, equilibrium bond length, and beta parameter for each of the two Morse potentials. B_4 and B_6 are the charge-induced dipole and charge-induced quadrupole and dispersion terms, respectively, approximated with the parameters for XeI$^-$.[51] The parameters r_n in the two switching functions are chosen so that $v_1(r)$, $v_2(r)$, and $v_3(r)$ describe the three regions of the potential defined above.

The FC region is centered around R=3.205 Å, i.e. R_e for the I_2^- $\tilde{X}\ ^2\Sigma_u^+$ state.[25] The potential in this region, along with the ground state wavefunction and photon energy, determines the initial wavefunction created on the excited state potential. To fit the potential in the FC region, we have simulated the photodissociation cross-section measurement carried out by Papanikolas *et al.*[15] on gas phase I_2^-. Their results are shown by the solid line in Fig. 5. Using a wavepacket propagation code described earlier,[52] and assuming a temperature of 100 K for the I_2^-,[25] the cross section was simulated. Only the three parameters which determine $v_1(r)$ were adjusted to reproduce the maximum and

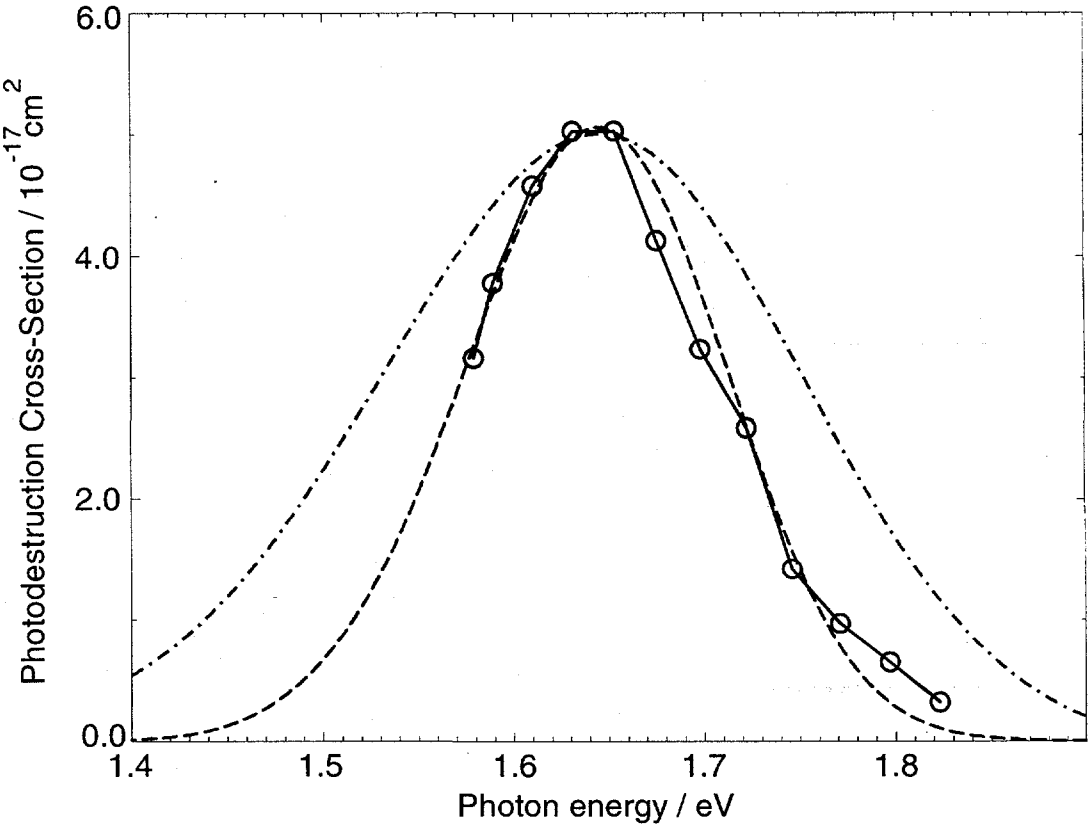

Figure 5. Photodestruction cross-section measurement[15] (solid-circles) and simulations using the best-fit potential (dashed) and the Chen and Wentworth potential[26] (dot-dashed).

width of the cross section, and the results are presented in Fig. 5 (dashed). This produces a reliable excited state potential in the FC region. In the simulations presented throughout the rest of this report, these three parameters are held fixed and only the remaining parameters are varied to fit the FPES spectra.

4.2 Convolution routine

Because we have found that the risetime of the $I(^2P_{3/2})$ spectra at 1.71 eV (Fig. 4) is very sensitive to the resolution of our spectrometer,[29] it is important to perform accurate convolutions of the simulated spectrum with the experimental resolution function. Previously an analytical form for the convolution function was used which had been derived based on the expected energy resolution of the magnetic bottle analyzer and the angular distribution of ejected electrons.[29] Here an improved procedure is employed, in which the simulations are convoluted with an empirical resolution function derived from the photoelectron spectrum of I^-.

The standard convolution formula is used,

$$g_{conv}(\varepsilon) = \int_{-\infty}^{\infty} f(E) \cdot g(\varepsilon - E)\, dE \qquad (2)$$

where $g(\varepsilon)$ is the simulated spectrum and $f(E)$ is the convolution function. In our routine, $f(E)$ assumes the experimental I^- features at their respective electron energies of 0.12, 0.77 and 1.71 eV; the first peak is obtained at a detachment wavelength of 390 nm, and the second two at 260 nm. At other electron energies, the convolution function is computed by interpolation (or extrapolation) of the two nearest experimental I^- features. This guarantees that at long times, when the experimental spectrum only consists of atomic features, the simulated and experimental spectra will match. It also

helps ensure that the risetime of the I^- feature at 1.71 eV is accurately modeled with the current experimental resolution. However, the procedure implicitly assumes that at *all* time delays the angular distribution is the same as for I^- photodetachment. The effect of the angular distribution on the photoelectron spectra diminishes when the ion beam is slowed down, as was the case here,[29,47] and plays a much smaller role in this report than in our original study.

4.3 Simulated FPES spectra above 1.7 eV

With the first three parameters fixed to reproduce the photodestruction cross section, the other ten parameters were varied and the FPES spectra simulated. In our companion paper,[44] we discuss the exact method for simulating the spectra. In this paper, we concentrate only on the results of these simulations. In addition, for the purpose of determining an accurate $I_2^-(\tilde{A}'\,^2\Pi_{g,1/2})$ excited state potential, only the spectrum from 1.6 eV and above was modeled (Fig. 2, solid). This region of the spectrum corresponds to detachment to the neutral potentials which correlate to $I(^2P_{3/2}) + I(^2P_{3/2})$ products. These potentials are considerably better characterized than the potentials correlating to $I(^2P_{3/2}) + I^*(^2P_{1/2})$ products.

Simulations from the optimized $I_2^-(\tilde{A}'\,^2\Pi_{g,1/2})$ potential are shown in Fig. 2 (dashed), superimposed on the experimental spectrum. The potential itself is shown in Fig. 6 (dashed), and its parameters are given in Table I. For the purpose of determining the $I_2^-(\tilde{A}'\,^2\Pi_{g,1/2})$ excited state, the simulations include photodetachment to the lowest 10 states of neutral I_2 which correlate to $I(^2P_{3/2}) + I(^2P_{3/2})$ products, seven of which have been characterized experimentally: the $\tilde{X}\,^1\Sigma_g^+$, $\tilde{A}'^3\Pi_{2u}$, $\tilde{A}^3\Pi_{1u}$, $\tilde{B}'^3\Pi_{0^-u}$, $\tilde{B}''^1\Pi_u$, $\tilde{a}\,^3\Pi_{1g}$, and

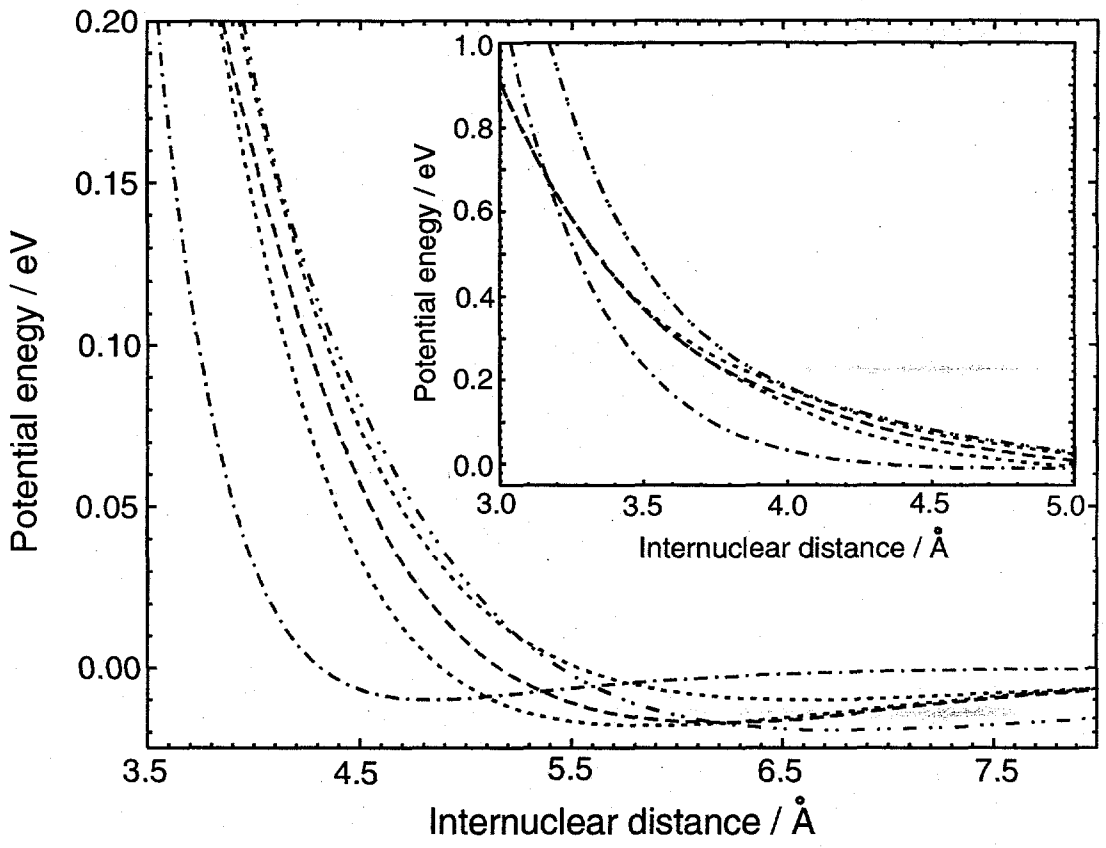

Figure 6. Comparison of our potential (dashed) with estimated error limits (dotted) to the Chen and Wentworth potential[26] (dot-dashed), and *ab initio* potential[40-42] (double dot-dashed). Inset shows FC region of the potentials.

Table I. Spectroscopic constants for the $I_2^-(\tilde{A}'\,^2\Pi_{g,1/2})$ potential in Eqs. 1 & 2.

$v_1(r)$	$r_e^1 = 0.01$ Å	$sf_1(r)$	$r_1 = 3.4$ Å
	$D_e^1 = 6.000$ eV		$r_2 = 4.2$ Å
	$\beta^1 = 0.787$ Å^{-1}		
$v_2(r)$	$r_e^2 = 0.017$ Å	$sf_2(r)$	$r_3 = 8.4$ Å
	$D_e^2 = 6.20$ eV		$r_4 = 9.0$ Å
	$\beta^2 = 0.663$ Å^{-1}		
$v_3(r)$	$B_4 = 28.977$ eV Å^4 (Ref. 51)		
	$B_6 = 365.448$ eV Å^6 (Ref. 51)		

the $\tilde{a}'\,^3\Sigma^-_{g(0^+)}$ states.[30-36] From *ab initio* work,[53,54] the $^3\Pi_{2g}$ and $\tilde{a}^3\Pi_{1g}$ states are predicted to be nearly degenerate, as are the $^3\Sigma^-_{u(0^-)}$ and $^3\Delta_{3u}$ states with the $\tilde{a}'\,^3\Sigma^-_{g(0^+)}$ state. Hence, we approximate these three experimentally undetermined states by their degenerate counterparts.

Several of these neutral states are not accessible by one-electron detachment from the $I_2^-(\tilde{A}'\,^2\Pi_{g,1/2})$ excited state. However, as discussed by Faeder and Parson,[43] the large spin-orbit coupling of iodine mixes the electronic configurations to such an extent that only transitions to the I_2 $\tilde{X}\,^1\Sigma_g^+$ state are predicted to be forbidden. Thus, equal weightings are assumed for transitions to all neutral states except the $\tilde{X}\,^1\Sigma_g^+$ state, for which the detachment cross section is set to zero.

Comparison of the simulated and experimental data in Fig. 2 (dashed) shows excellent agreement. The high energy features from 1.8 to 2.3 eV match the experiment well, and the rise of the Γ feature at 1.70 eV is followed closely. The intensity at 1.75 eV

is slightly underrepresented at delay times of 170, 220, and 270 fs. Comparison of the simulated risetime to experiment shows that the half-maximum height is reproduced at 180 fs, although the slope is not as steep (Fig. 4, dashed). This may be due to the simulated pulse widths being slightly too long in duration. Finally, a comparison of the energy shift observed between 420 to 700 fs is shown in Fig. 3 (dashed). At 420 fs the simulated spectra is approximately 2 meV higher in energy than experiment, and smoothly shifts to 1.71 eV over the next 300 fs.

These results represent a significant improvement over our previous study of I_2^- photodissociation.[29] As has been found by Faeder and Parson,[43] inclusion of the additional neutral potentials helps improve the fit to the transient intensities. We find that this does indeed improve the agreement, especially at energies above 1.8 eV, although modification of the $I_2^-(\tilde{A}'\ ^2\Pi_{g,1/2})$ potential itself was the largest factor in improving the fits.

Several assumptions are implicit in our calculations. First, the oscillator strengths for transitions from the $I_2^-(\tilde{A}'\ ^2\Pi_{g,1/2})$ anion to the neutral states are unknown. From the study of Asmis *et al.*,[55] it was found that detachment from the *ground* $\tilde{X}^2\Sigma_u^+$ state of I_2^- to the $\tilde{B}'^3\Pi_{0^-u}$ and $\tilde{B}''^1\Pi_u$ states of I_2 is only 1/3 as intense as detachment to the $\tilde{A}'^3\Pi_{2u}$ and $\tilde{A}^3\Pi_{1u}$ states. When using their weights for photodetachment from the $I_2^-(\tilde{A}'\ ^2\Pi_{g,1/2})$ state, however, the transient intensities are not as well represented as when all oscillator strengths are assumed to be the same. In fact, for a proper fit of the photoelectron spectra, transitions to the $\tilde{a}^3\Pi_{1g}$ and $^3\Pi_{2g}$ states must be included, even though these states are normally forbidden, lending support to the conclusion of Faeder and Parson[55]

that the one-electron transition rule is relaxed by the strong spin-orbit coupling. We have also individually varied the relative weightings of all the states, and found that the risetime (Fig. 4) is insensitive to the individual weights. In fact, except for the $\tilde{a}'^{3}\Sigma^{-}_{g(0^{+})}$ state, the individual risetimes of all the neutral states lie within ±10 fs of one another. Thus, the risetime is almost solely determined by the anion potential, at least for reasonably well characterized neutral states.

The second important assumption is that the photodetachment transition dipole moments are independent of nuclear coordinates. This is certainly not correct, although we have no means for calculating these moments. However, this approximation should only affect the relative intensity between the transient features above 1.8 eV and the I^{-} feature at 1.71 eV; the risetime should again remain unaffected.

Further insight into the photoelectron spectra can be gained by examining the time-dependence of the excited state anion wavefunction, which is also calculated as part of the quantum mechanical propagation method.[44] Shown in Fig. 7 are the wavefunctions at the experimental delay times superimposed on the anion and neutral potential energy surfaces. At 20 fs pump-probe delay, the wavepacket mostly resides in the FC region. At this time delay, detachment of the wavepacket produces a broad spectrum because of the large splittings between the neutral potential energy curves. The spectrum is also centered at higher electron energies than at longer times because the vertical detachment energies are lower, on the average. At 170 fs, the breadth of the spectra is almost entirely due to the slope of the anion potential since the neutral potentials have nearly reached their asymptotic values. The transient intensity in the simulated spectra does not disappear, however, until about 270 fs at which point the wavepacket resides in the

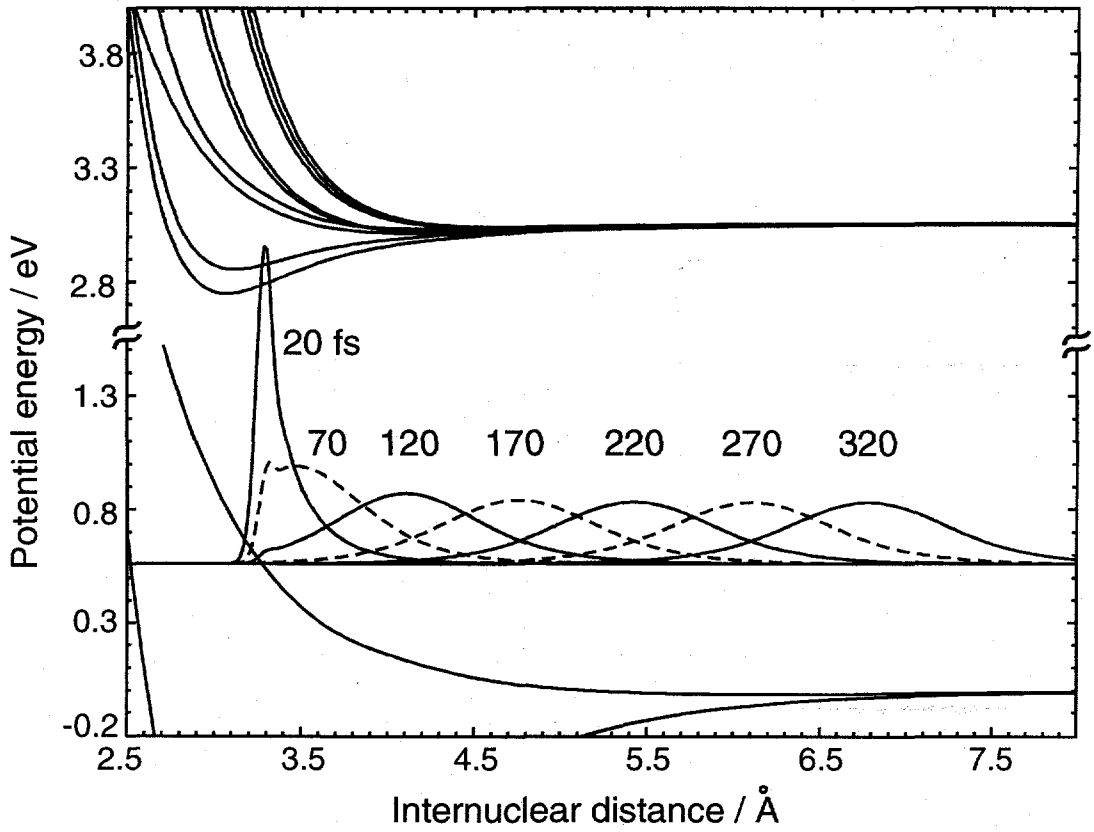

Figure 7. Simulated wavefunctions corresponding to the experimental spectra delay times. The wavefunction does not fully reach the bottom of the $I_2^-(\tilde{A}'\,^2\Pi_{g,1/2})$ well until 270 fs.

region of the shallow anion potential well. At this internuclear distance the neutral potentials are all within 4 meV of their asymptotic energies. The anion potential, however, is 17 meV lower than its asymptotic energy. Thus, the shift to higher energies over the next 400 femtoseconds is due to the wavepacket moving out of the anion potential well. By 700 fs, the experimental spectrum no longer shifts with time, and the effect of attractive interactions on the anion potential has become insignificant. From the simulations, this corresponds to an internuclear distance of about 11 Å.

In order to estimate the error in our potential, the FPES spectra were simulated for two additional potential surfaces with slightly more repulsive and attractive potentials. These potentials are shown in Fig. 6 (dotted), along with the best-fit potential described above (dashed). All three potentials are identical in the FC region of the potential (Fig. 6, inset). The simulated FPES spectra are not shown, but the risetimes at 1.71 eV are compared in Fig. 4 (dotted) to the best-fit (dashed) and experimental risetimes (solid). The potential with the steeper slope for $R< R_e$ produces a faster risetime because the wavepacket reaches the asympotic region more rapidly. Conversely, the potential with the shallower slope results in slower dissociation and a slower risetime. Although these two potentials do not fit the experimental risetimes as well, they are not necessarily bad fits. We believe they represent reasonable error limits in our determination of the $I_2^-(\tilde{A}'\,^2\Pi_{g,1/2})$ state, and are used to estimate error bars for the parameters listed in Table II.

4.4 Comparison with previous potentials

Table II compares our well depth and equilibrium bond length to the three semi-empirical potentials proposed by Chen and Wentworth,[26-28] and the *ab initio* potential by Maslen *et al.*.[40] As was the case in our previous determination of the $I_2^-(\tilde{X}^2\Sigma_u^+)$ ground state potential,[25] the original $I_2^-(\tilde{A}'\,^2\Pi_{g,1/2})$ semiempirical potential published[26] in 1985 matches our parameters more closely than the later two potentials.[27,28] As is seen in Fig. 6 (dot-dashed), however, even the original potential lies well outside our limits of error. It has a comparable well depth, but the well itself is located at much smaller internuclear distances, which produces a repulsive wall that is considerably steeper than predicted by our simulations.

As an indication of the sensitivity of our spectra to the shape of the excited state potential, we have simulated the spectra using our $I_2^-(\tilde{X}^2\Sigma_u^+)$ ground state and Chen and Wentworth's $I_2^-(\tilde{A}'\,^2\Pi_{g,1/2})$ excited state potential from 1985.[26] Fig. 8 compares the

Table II : Comparison of D_e and R_e with previously reported potentials

	Current Work	*ab initio*[a]	Chen & Wentworth[b]	Dojahn *et al.*[c]	Chen *et al.*[d]
R_e (Å)	6.2 ± 0.6	6.8	4.83	4.626	4.70
D_e (eV)	0.017 ± 0.010	0.0195	0.01	0.08	0.057[e]

[a]References 40-42.
[b]Reference 26.
[c]Reference 27.
[d]Reference 28.

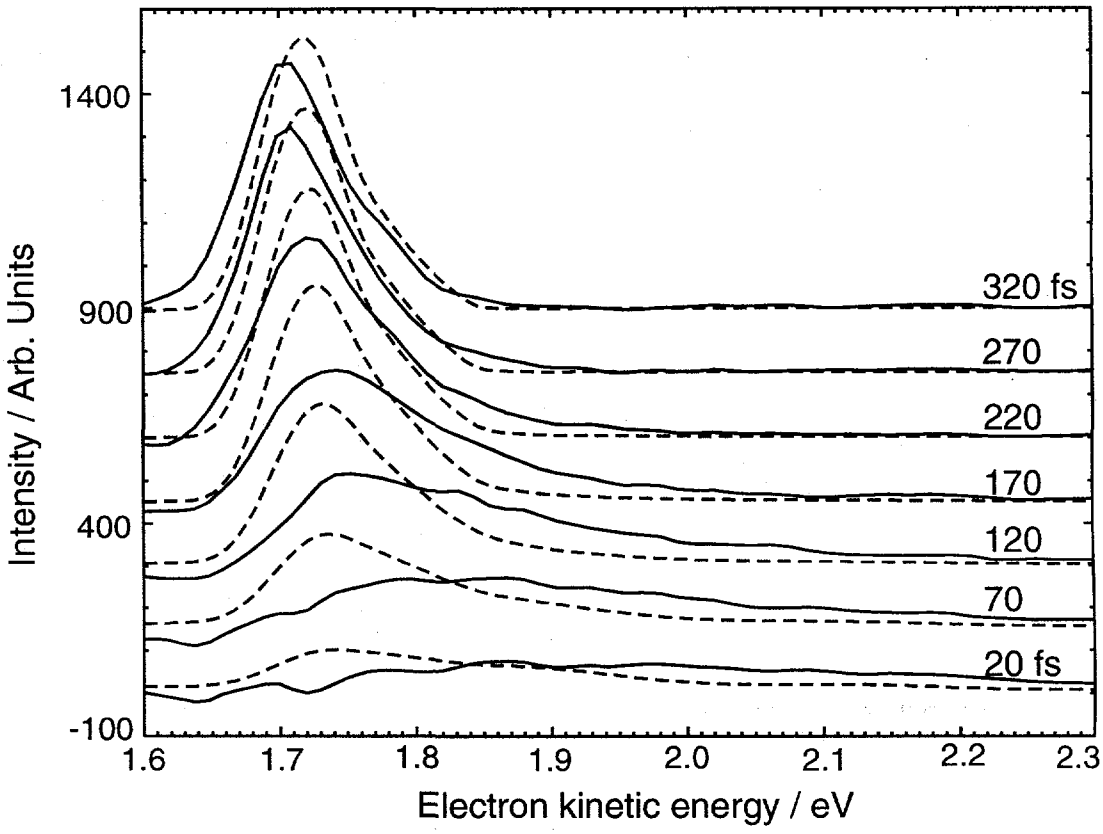

Figure 8. Comparison of the experimental spectra (solid) to simulations (dashed) using the Chen and Wentworth potential.[26]

simulations (dashed) to experiment (solid). Note that the transient intensity above 1.8 eV is almost completely missing, even at 20 fs delay time, and the atomic feature forms much too early. Indeed, the simulated risetime occurs 70 fs faster than the experiment (Fig. 4, dot-dashed), and the atomic feature rises directly at 1.71 eV with no energy shift. These discrepancies indicate that this potential is too repulsive at short internuclear distances and not attractive enough at long internuclear distances, both consequences of R_e being too small. We have also calculated the photodestruction cross-section using this potential and find it to be much too wide (Fig. 5, dot-dashed), showing that the potential is too steep in the FC region. It seems unlikely that a single Morse potential for the $I_2^-(\tilde{A}'\,^2\Pi_{g,1/2})$ state will suffice to fit all the experimental data now available.

The well depth and internuclear distance for the *ab initio* potential[40-42] are in remarkably good agreement with our results (Fig. 6, double dot-dashed). Its well depth D_e=19.5 meV and equilibrium internuclear distance R_e=6.8 Å lie within our estimated error bars. At smaller internuclear distances, however, the *ab initio* potential diverges from ours, and is ~300 meV too high in energy at the FC region (Fig. 6, inset). This seems to indicate that the *ab initio* methods are reliable in predicting long-range electrostatic interactions, and may be expected to accurately represent the excited state wells of other diatomic anions.

4.5 Simulation of the entire FPES spectrum

With the determination of a reliable $I_2^-(\tilde{A}'\,^2\Pi_{g,1/2})$ state, the entire FPES spectra can now be simulated by including the remaining 10 neutral states correlating to $I(^2P_{3/2})$ + $I^*(^2P_{1/2})$ products. Very little is known about these states; only the $\tilde{B}^3\Pi_{0^-_u}$ has been

spectroscopically determined.[32] Information on the other states comes from relativistic *ab initio* calculations by Li *et al.*,[56] Teichteil *et al.*,[53] and de Jong *et al.*[54] By simulating the region of the FPES spectra corresponding to these states (i.e. at electron energies below 1.6 eV) and comparing with experiment, the accuracy of the *ab initio* potentials can be evaluated.

Following the procedure described above, the entire photoelectron spectrum was simulated using the potentials calculated by de Jong *et al.*[54] (Fig. 2, dotted) and those used above (Fig. 2, dashed). Transitions to all states in the $I(^2P_{3/2}) + I^*(^2P_{1/2})$ manifold have been equally weighted, although their integrated intensity has been reduced by a factor of ~2 to reproduce the intensity of the $I(^2P_{1/2}) \leftarrow I^-$ transition at 0.77 eV. The agreement is far from perfect, however, for the formation of the $I^*(^2P_{1/2})$ peak. Except for the contribution of the $\tilde{B}^3\Pi_{0^-_u}$ state (which extends up to 1.5 eV, but at intensities too low to observe in Fig. 2), the simulations produce transient features from 0.6 to 0.9 eV, with no dominant features. The experiment, however, has intensity up to 1.0 eV, which indicates that the neutral states are at least 100 meV too high in energy at the FC region. In addition, sharp features at 0.85 and 0.95 eV are seen in the experiment at –30 fs; although similar in appearance to the background peaks labelled A and B in Fig. 2, these features are true transients and not artifacts of background subtraction. Each sharp feature arises from detachment to one or more neutral states, largely separated from adjacent states. The absence of these features in the simulations indicates that the *ab initio* potential energy curves are too evenly spaced in the FC region. Finally, the rise of the $I^*(^2P_{1/2})$ feature is much faster than experiment, and the transient intensity is too small, both suggesting that the I_2 states are "too parallel" to the $I_2^-(\tilde{A}'\ ^2\Pi_{g,1/2})$ state.

5. Conclusion

The feasibility of using femtosecond photoelectron spectroscopy to determine excited anion state potentials is demonstrated. The first quantitative excited state potential for the $I_2^-(\tilde{A}'\,^2\Pi_{g,1/2})$ excited state of I_2^- is reported, which has been fit to a piecewise potential by simulation of the spectra. Careful consideration has been given to the accuracy of our fit, and reasonable error limits have been assigned. We find the potential contains a shallow well located at large internuclear distances, in qualitative agreement with a recent *ab initio* calculation but not with previously proposed semi-empirical potentials. Comparison of the spectra to calculated wavefunctions reveals FPES to be sensitive to the repulsive wall, the potential well, and the long-range attractive portions of the potential. The accuracy of current *ab initio* potentials for the $I(^2P_{3/2}) + I^*(^2P_{1/2})$ manifold is also assessed. The extension of this type of analysis to higher dimensional systems, and to systems with a larger excited state wells are being investigated.

6. Acknowledgments

D.M.N. acknowledges support from the National Science Foundation under Grant No. CHE-9710243 and from the Defense University Research Instrumentation Program under Grant No. F49620-95-0078. W.H.M. acknowledges support from the National Science Foundation under Grant No. CHE-9732758, from the Director, Office of Energy Research, Office of Basic Energy Sciences, Chemical Sciences Division of the U.S. Department of Energy under Contract No. DE-AC03-76SF00098, and from the

Laboratory Directed Research and Development (LDRD) project from the National Energy Research Scientific Computing Center (NERSC), Lawrence Berkeley National Laboratory. The authors also thank Jim Faeder for helpful suggestions and Robert J. LeRoy for providing the RKRI algorithm for use in calculating the I_2 states.

7. References

[1] Q. L. Liu, J. K. Wang, and A. H. Zewail, Nature **364,** 427 (1993).

[2] J. K. Wang, Q. L. Liu, and A. H. Zewail, J. Phys. Chem. **99,** 11309 (1995).

[3] T. J. Chung, G. W. Hoffman, and K. B. Eisenthal, Chem. Phys. Lett. **25,** 201 (1974).

[4] P. Bado, C. Dupuy, D. Magde, K. R. Wilson, and M. M. Malley, J. Chem. Phys. **80,** 5531 (1984).

[5] P. Bado and K. R. Wilson, J. Phys. Chem. **88,** 655 (1984).

[6] D. F. Kelly, N. A. Abul-Haj, and D. J. Jang, J. Chem. Phys. **80,** 4105 (1984).

[7] D. E. Smith and C. B. Harris, J. Chem. Phys. **87,** 2709 (1987).

[8] A. L. Harris, J. K. Brown, and C. B. Harris, Annu. Rev. Phys. Chem. **39,** 341 (1988).

[9] N. F. Scherer, L. D. Ziegler, and G. R. Fleming, J. Chem. Phys. **97,** 5544 (1992).

[10] N. F. Scherer, D. M. Jonas, and G. R. Fleming, J. Chem. Phys. **99,** 153 (1993).

[11] R. Zadoyan, Z. Li, P. Ashjian, C. C. Martens, and V. A. Apkarian, Chem. Phys. Lett. **218,** 504 (1994).

[12] R. Zadoyan, Z. Li, C. C. Martens, and V. A. Apkarian, J. Chem. Phys. **101,** 6648 (1994).

[13] V. Vorsa, S. Nandi, P. J. Campagnola, M. Larsson, and W. C. Lineberger, J. Chem. Phys. **106,** 1402 (1997).

[14] B. J. Greenblatt, M. T. Zanni, and D. M. Neumark, Science **276,** 1675 (1997).

[15] J. M. Papanikolas, J. R. Gord, N. E. Levinger, D. Ray, V. Vorsa, and W. C. Lineberger, J. Phys. Chem. **95,** 8028 (1991).

[16] J. M. Papanikolas, V. Vorsa, M. E. Nadal, P. J. Campagnola, H. K. Buchenau, and W. C. Lineberger, J. Chem. Phys. **99,** 8733 (1993).

[17] B. J. Greenblatt, M. T. Zanni, and D. M. Neumark, Faraday Discuss. **108,** 101 (1998).

[18] A. Sanov, S. Nandi, and W. C. Lineberger, J. Chem. Phys. **108,** 5155 (1998).

[19] A. E. Johnson, N. E. Levinger, and P. F. Barbara, J. Phys. Chem. **96,** 7841 (1992).

[20] I. Benjamin, P. F. Barbara, B. J. Gertner, and J. T. Hynes, J. Phys. Chem. **99,** 7557 (1995).

[21] P. K. Walhout, J. C. Alfano, K. A. M. Thakur, and P. F. Barbara, J. Phys. Chem. **99,** 7568 (1995).

[22] U. Banin and S. Ruhman, J. Chem. Phys. **99,** 9318 (1993).

[23] U. Banin and S. Ruhman, J. Chem. Phys. **98,** 4391 (1993).

[24] T. Kuhne and P. Vohringer, J. Chem. Phys. **105,** 10788 (1996).

[25] M. T. Zanni, T. R. Taylor, B. J. Greenblatt, B. Soep, and D. M. Neumark, J. Chem. Phys. **107,** 7613 (1997).

[26] E. C. M. Chen and W. E. Wentworth, J. Phys. Chem. **89,** 4099 (1985).

[27] J. G. Dojahn, E. C. M. Chen, and W. E. Wentworth, J. Phys. Chem. **100,** 9649 (1996).

[28] E. C. M. Chen, J. G. Dojahn, and W. E. Wentworth, J. Phys. Chem. A **101,** 3088 (1997).

[29] B. J. Greenblatt, M. T. Zanni, and D. M. Neumark, Chem. Phys. Lett. **258,** 523 (1996).

[30] S. Churassy, F. Martin, R. Bacis, J. Verges, and R. W. Field, J. Chem. Phys. **75,** 4863 (1981).

[31] K. S. Viswanathan and J. Tellinghuisen, J. Mol. Spectrosc. **101,** 285 (1983).

[32] J. W. Tromp and R. J. Le Roy, J. Mol. Spectrosc. **109,** 352 (1985).

[33] J. Tellinghuisen, J. Chem. Phys. **82,** 4012 (1985).

[34] F. Martin, R. Bacis, S. Churassy, and J. Verges, J. Mol. Spectrosc. **116,** 71 (1986).

[35] X. N. Zheng, S. L. Fei, M. C. Heaven, and J. Tellinghuisen, J. Chem. Phys. **96,** 4877 (1992).

[36] D. R. T. Appadoo, R. J. Leroy, P. F. Bernath, S. Gerstenkorn, P. Luc, J. Verges, J. Sinzelle, J. Chevillard, and Y. Daignaux, J. Chem. Phys. **104,** 903 (1996).

[37] P. W. Tasker, G. G. Balint-Kurti, and R. N. Dixon, Mol. Phys. **32,** 1651 (1976).

[38] G. A. Bowmaker, P. Schwerdfeger, and L. v. Szentpaly, J. Mol. Struct. THEOCHEM **53,** 87 (1989).

[39] D. Danovich, J. Hrusak, and S. Shaik, Chem. Phys. Lett. **233,** 249 (1995).

[40] P. E. Maslen, J. Faeder, and R. Parson, Chem. Phys. Lett. **263,** 63 (1996).

[41] J. Faeder, N. Delaney, P. E. Maslen, and R. Parson, Chem. Phys. Lett. **270,** 196 (1997).

[42] J. Faeder, N. Delaney, P. E. Maslen, and R. Parson, Chem. Phys. , In Press (1998).

[43] J. Faeder and R. Parson, J. Chem. Phys. **108,** 3909 (1998).

[44] V. S. Batista, M. T. Zanni, B. J. Greenblatt, D. M. Neumark, and W. H. Miller, J. Chem. Phys. (1998).

[45] R. Prosch and T. Trickl, Rev. Sci. Instrum. **60,** 713 (1989).

[46] W. C. Wiley and I. H. McLaren, Rev. Sci. Instrum. **26,** 1150 (1955).

[47] O. Cheshnovsky, S. H. Yang, C. L. Pettiette, M. J. Craycraft, and R. E. Smalley, Rev. Sci. Instrum. **58,** 2131 (1987).

[48] H. Handschuh, G. Gantefor, and W. Eberhardt, Rev. Sci. Instrum. **66,** 3838 (1995).

[49] L.-S. Wang, H.-S. Cheng, and J. Fan, J. Chem. Phys. **102,** 9480 (1995).

[50] M. D. Davidson, B. Broers, H. G. Muller, and H. B. v. L. v. d. Heuvell, J. Phys. B **25,** 3093 (1992).

[51] T. Lenzer, M. R. Furlanetto, K. R. Asmis, and D. M. Neumark, J. Chem. Phys. , In press (1998).

[52] S. E. Bradforth, A. Weaver, D. W. Arnold, R. B. Metz, and D. M. Neumark, J. Chem. Phys. **92,** 7205 (1990).

[53] C. Teichteil and M. Pelissier, Chem. Phys. **180,** 1 (1994).

[54] W. A. de Jong, L. Visscher, and W. C. Nieuwpoort, J. Chem. Phys. **107,** 9046 (1997).

[55] K. R. Asmis, T. R. Taylor, C. Xu, and D. M. Neumark, J. Chem. Phys. **109,** 4389 (1998).

[56] Q. Li and K. Balasubramanian, J. Mol. Spectrosc. **138,** 162 (1989).

Chapter 5. Femtosecond stimulated emission pumping: characterization of the I_2^- ground state[†]

Femtosecond stimulated emission pumping in combination with femtosecond photoelectron spectroscopy is used to characterize the potential energy function of the $I_2^-(\tilde{X}\ ^2\Sigma_u^+)$ ground state up to vibrational energies to within 2% of the dissociation limit. The frequency and anharmonicity of this state is measured at several vibrational energies up to 0.993 eV by coherently populating a superposition of ground state vibrational levels using femtosecond stimulated emission pumping, and monitoring the resulting wavepacket oscillations with femtosecond photoelectron spectroscopy. The dissociative $I_2^-(\tilde{A}'\ ^2\Pi_{g,1/2})$ state is used for intermediate population transfer, allowing efficient population transfer to all ground state levels. Using the measured frequencies and anharmonicities, the $\tilde{X}\ ^2\Sigma_u^+$ state has been fit to a modified Morse potential with the β-parameter expanded in a Taylor series, and the bond length, well depth, and υ=0-1 fundamental frequency set equal to our previously determined Morse potential [J. Chem. Phys. **107**, 7613 (1997)]. At high vibrational energies, the modified potential deviates significantly from the previously determined potential.

1. Introduction

The photodissociation of I_2^- in size selected $I_2^-(CO_2)_n$, $I_2^-(Ar)_n$ clusters[1-9] and bulk polar solvents[10-13] has become a model system for the study of caging, recombination, and vibrational relaxation. In these systems, the strong solvent/solute

[†] Submitted for publication to J. Chem. Phys.

effects inherent to negatively charged species induce rapid energy transfer that depends sensitively on the shape of the ground and excited state potentials.[14,15] This is especially true for the ground state potential near the dissociation limit where energy transfer is much more rapid than at low vibrational quanta. For instance, Barbara and coworkers[10,12,13] have shown that within 300 fs of photodissociation, the I_2^- chromophore recombines and relaxes to the lower 25% of the ground state potential in liquid water and ethanol. The remaining relaxation occurs over ~2 ps. Hence, interpretation of the data and quantitative theoretical modeling requires accurate excited and ground state potentials to account for the dissociation and vibrational relaxation processes, respectively. We have previously reported ground and excited state potentials based on a series of frequency and time domain negative ion photoelectron spectroscopy (PES) experiments.[16-18] However, the ground state potential was only characterized near the bottom of the well. In this paper, we use femtosecond photoelectron spectroscopy (FPES) in conjunction with stimulated emission pumping (SEP) to characterize the I_2^- ground state potential to within 2% of the dissociation limit.

Our previous report[16] on the ground state of I_2^- relied on conventional, high-resolution photoelectron spectra to determine the equilibrium bond length (3.205 Å) and well depth (1.014 eV) of I_2^-. To determine the υ=0-1 vibrational frequency, resonance impulsive stimulated Raman scattering (RISRS) was used to create ground state motion near the bottom of the well. The Fourier transform of the oscillations observed in the FPE spectra gave the fundamental frequency with wavenumber accuracy (110 ± 2 cm^{-1}), and from these three parameters, a Morse potential was determined. Our results differed substantially from previous semi-empirical[19-21] and *ab initio* determinations[22-25] of the

ground state. The *ab initio* potential by Maslen *et al.*[14,15] has been brought into closer agreement with ours by scaling the potential to reproduce our experimental well depth. However, the ground state potential remains experimentally uncharacterized at energies much above the minimum.

In order to characterize the potential at higher energies, we utilize gas phase, femtosecond SEP to coherently populate vibrational levels to within 2% of the dissociation limit. Our method is an extension of conventional SEP[26,27] in which a narrow band pump laser populates a single vibrational eigenstate in an excited electronic state. A second, dump pulse then transfers population back to the ground state and into eigenstates resonant with the dump frequency. Hence, by scanning the dump laser wavelength and monitoring, for example, fluorescence depletion, the energies of the ground state levels can be measured and an accurate potential determined. In contrast to conventional SEP, our implementation of SEP utilizes femtosecond pump and dump pulses to coherently populate multiple excited and ground state levels of I_2^-, respectively. In this case, the pump pulse creates an excited state wavepacket for which the Franck-Condon overlap with the ground state vibrational levels constantly evolves with time. With proper timing of the dump pulse, population is coherently transferred back to the ground state, creating a wavepacket that oscillates with the frequencies determined by the populated vibrational levels. By following the wavepacket motion in real time, we determine the I_2^- ground state vibrational frequency and anharmonicity as a function of pump and dump wavelengths.

The technique we use to monitor the SEP signal is femtosecond photoelectron spectroscopy (FPES),[17,28] and our approach to create and monitor ground state

vibrational motion is illustrated in Fig. 1. In these experiments, a femtosecond pump pulse, centered at ~795 nm, excites I_2^- from its ground $\tilde{X}\ ^2\Sigma_u^+$ state to the dissociative $\tilde{A}'\ ^2\Pi_{g,1/2}$ potential. After a delay time of 50 to 150 fs, a second, femtosecond dump pulse transfers a fraction of the evolving excited state wavefunction back to the ground state, resulting in a coherent superposition of vibrational levels centered at the difference between the pump and dump laser pulse energies (hereafter referred to as the excitation energy). The vibrationally excited ground state wavepacket then oscillates with frequencies characteristic of the energy level spacings that comprise this vibrational distribution. The ensuing dynamics of the depleted υ=0 ground state, excited state dynamics, and dump induced ground state motion are all monitored by photodetachment with a femtosecond probe pulse at a series of delay times resulting in time-dependent photoelectron spectra. The dynamics of the depleted υ=0 ground state and evolving excited state wavefunctions have been reported previously.[16,17] In this article we focus on the dynamics induced by the dump pulse (dashed wavepackets).

Our technique is similar in some respects to femtosecond four wave mixing (FWM) techniques[29-31] including femtosecond coherent anti-Raman scattering (CARS)[32,33] and two dimensional time delayed femtosecond CARS.[34] In these experiments two resonant laser pulses, similar to the pump and dump pulses used in our experiment, create a population grating in the ground electronic state. Instead of monitoring the ground state motion by photodetachment, a third pulse is resonantly scattered from the oscillating polarization. Such methods are suitable for studying species that can be created with high number densities. The method described here is far

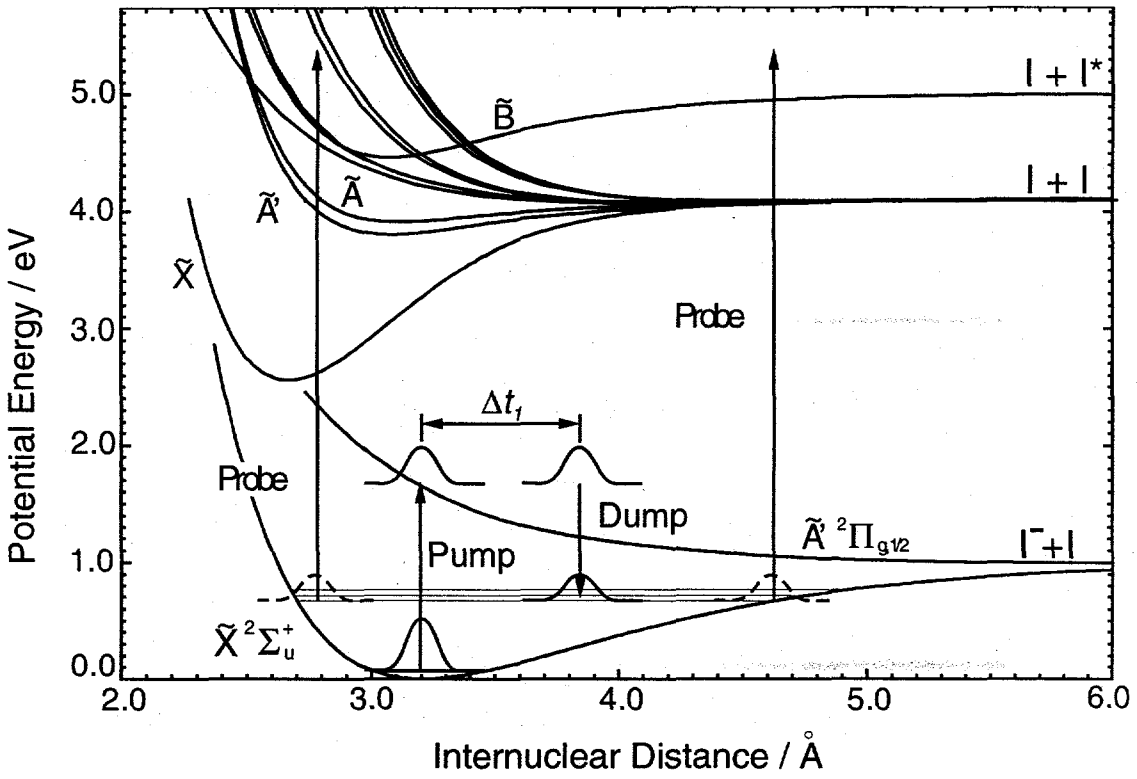

Figure 1. Schematic of the SEP-FPES technique and relevant I_2^- & I_2 potential energy curves. The SEP process is illustrated using solid curves to represent the excited and ground state wavepackets created by the pump and dump pulses, respectively, delayed Δt_1 with respect to each other. Detachment by the probe pulse is shown for two arbitrary delay times, when the ground state wavepacket (dashed) is located at the inner and outer turning points.

more sensitive, and can be used to study size-selected molecular anions, as we demonstrate in this report.

In this paper, we coherently populate vibrational states up to 0.993 eV on the $I_2^-(\tilde{X}\ ^2\Sigma_u^+)$ ground state (D_e= 1.014 eV) and use FPES to monitor the resulting oscillatory motion. In this manner, we determine the potential frequency and anharmonicity as a function of vibrational energy, and by modeling our results at successively higher vibrational energies, we have developed a quantitative ground state potential. We also demonstrate that the use of the dissociative $I_2^-(\tilde{A}'\ ^2\Pi_{g,1/2})$ electronic state for intermediate population transfer allows for efficient pumping to all ground state levels.

2. Experimental

The FPES negative ion photoelectron spectrometer and high-repetition rate femtosecond laser have been described in detail elsewhere.[17,35] A brief summary follows, highlighting the modifications made to incorporate an addition dump pulse.

The photoelectron spectrometer consists of an ion source region, time-of-flight (TOF) mass spectrometer, and a high collection efficiency TOF photoelectron spectrometer. I_2^- is produced when argon carrier gas (10 psig) is passed over crystalline iodine, supersonically expanded into the source chamber through a pulsed nozzle operating at 500 Hz, and crossed with a 1 keV electron beam. The I_2^- is isolated from the other anions and clusters formed in the expansion by injection into a Wiley-McLaren TOF mass spectrometer[36] using pulsed extraction and acceleration fields perpendicular to the molecular beam axis. After passing through several differentially pumped chambers, the ions enter the photoelectron spectrometer and interact with the pump, dump, and

probe laser pulses. The detached electrons are collected with high efficiency using a magnetic bottle,[37] and the 500 Hz repetition rate allows for rapid data collection. Although we often decelerate the ions prior to detachment to improve the photoelectron energy resolution,[17,38,39] in these experiments this is not necessary, and we have a resolution of approximately 300 meV at 1.7 eV electron kinetic energy (eKE) that degrades approximately as $(eKE)^{1/2}$.

The pump, dump, and probe pulses are obtained from the fundamental of a Clark-MXR regeneratively amplified Ti:sapphire laser system that generates pulses at ~795 nm (1.56 eV) with 1 mJ of energy and 80 fs ($sech^2$) width. About 40 μJ of this is used as the pump pulse and 500 μJ is used to pump a Light Conversion optical parametric amplifier (OPA) that generates infrared dump pulses from 950 to 2150 nm with an average of 40 μJ energy and 80 fs width. The remaining fundamental is frequency tripled to make 265 nm (4.68 eV), 20 μJ, and 130 fs probe pulses. In order to determine the exact excitation energy, the bandwidths of the pump and dump pulses are measured with a monochromator prior to each experiment. The relative timing between the three pulses is controlled by two translation stages, and the beams are collinearly recombined prior to entering the vacuum chamber. Because the entrance window affects the timing between the three pulses, above threshold detachment of I^- is used to determine the absolute zero-of-time inside the spectrometer; when any two pulses are temporally overlapped in the chamber, additional peaks are observed in the photoelectron spectrum for which the time-dependent intensity gives the cross-correlation of the respective pulses.[28,40]

Two procedures were used to normalize the spectra of different pump-dump-probe delay times. When the SEP signal is large, a phase-locked chopper is used to

perform shot-to-shot background subtraction by alternately collecting signal with and without the dump pulse to create a difference spectrum. The total background signal is also recorded (pump-probe only), which is constant after 300 fs since the excited state dynamics are complete, and thus can be used to normalize the difference spectra. When the signal is low, as it is for dump frequencies near 1067 nm due to low OPA conversion efficiency, shot-to-shot background is inefficient because the data collection rate is effectively halved. In this case, all spectra are collected with the dump pulse active, and the spectra are normalized by their integrated intensities at each delay time. This is a reliable normalization method because the SEP signal is less than 10% of the total intensity. Although shot-to-shot background subtraction is preferable, the pump-probe background spectra can be subtracted at a later time.

3. Results

Fig. 2a presents femtosecond photoelectron spectra of I_2^- taken with the probe only (solid), pump and probe (dashed), and pump, dump, and probe pulses active (dotted). The dump wavelength in this figure is 1450 nm (0.86 eV), resulting in an excitation energy of $h\nu_{pu} - h\nu_{pr} = 0.70$ eV, the pump-dump delay time, Δt_1, is 150 fs, and the pump-probe delay time, Δt_2, is 2200 fs. These spectra have not been background subtracted. In the probe-only spectra, peaks are observed at 0.3, 0.9 and 1.45 eV (labeled B, A, and X), primarily due to detachment to the $\tilde{B}\ ^3\Pi_{0^+u}$, $\tilde{A}\ ^3\Pi_{1u}$ & $\tilde{A}'\ ^3\Pi_{2u}$, and $\tilde{X}\ ^1\Sigma_g^+$ states of I_2, respectively.[16,41] With inclusion of the pump pulse, a portion of the I_2^- υ=0 ground state population is transferred to the $\tilde{A}'\ ^2\Pi_{g,1/2}$ excited state (see Fig. 1), resulting in a bleach of the probe-only spectra that is typically 40%. Additional peaks at 0.70 and

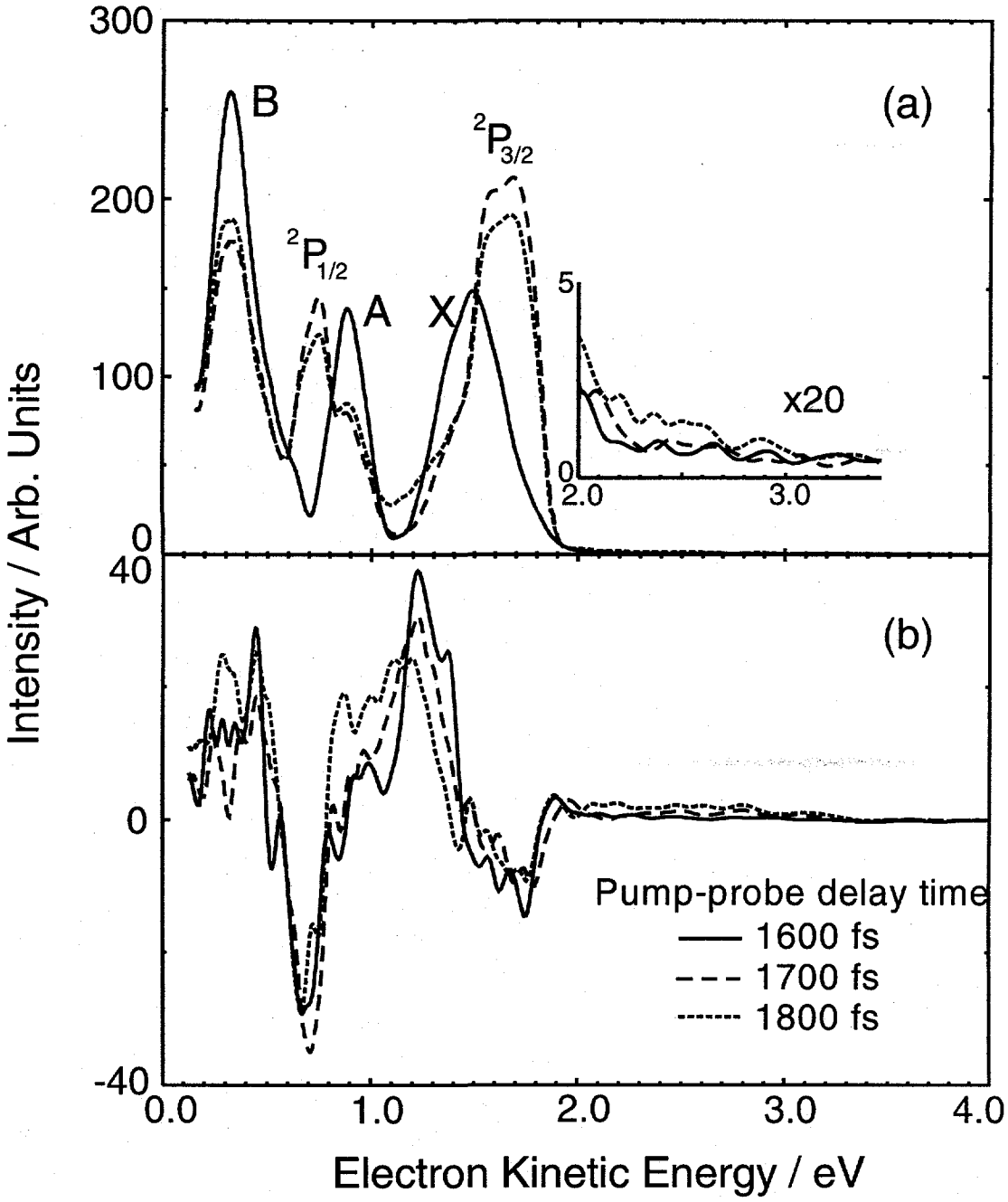

Figure 2. (a) FPE spectra using solely the probe (solid), pump and probe (dashed), and pump, dump, and probe pulses (dotted), with a dump wavelength of 1450 nm. (b) Spectra taken with shot-to-shot background subtraction active (Section 2) at three pump-probe delay times.

1.75 eV also appear due to detachment of the I^- products to the $I^*(^2P_{1/2})$ and $I(^2P_{3/2})$ spin-orbit states, respectively. Dissociation of I_2^- on the $\tilde{A}'\,^2\Pi_{g,1/2}$ takes on the order of 250 fs,[17,28] and in the spectra of Fig. 2a this process is already complete. With the addition of the dump pulse (dotted), the atomic I^- features decrease about 10% in intensity due to the transfer of population back to the ground state before dissociation occurs. However, the probe-only features do not increase in intensity. Rather, intensity appears between the I^- features at 1.1 eV as well as at high eKE up to ~3.1 eV. These features are due to photodetachment from high vibrational levels of I_2^-.[6,8] As the excitation energy is increased, the high eKE region of the spectra extend even further.

The pump and dump efficiencies can be determined by comparison of the ground and excited state bleach, respectively, to give an overall efficiency for population transfer to high vibrational levels of the ground state. From the bleach of the probe-only spectra, 42% of the ground state population is transferred to the excited state. With addition of the dump pulse, 10% of the excited state wavepacket is transferred back to the ground state, as determined from the bleach of the I^- product. Hence, we achieve 4 to 5% SEP efficiency. This is typical for all dump wavelengths used in this report.

The dump pulse induced features are more readily apparent in the shot-to-shot background subtracted mode (Section 2). In this mode, only features resulting from the interaction with the dump pulse are recorded. Fig. 2b show three spectra taken in this mode at different pump-probe delay times. Depletion of the I^- features now shows up as negative peaks, and the intensity due to detachment of the vibrationally excited levels is easily observable. At most eKEs, the photoelectron spectrum is rather complex; between 0.8 and 1.4 eV the photoelectron spectra (Fig. 2b) arises from detachment at both the

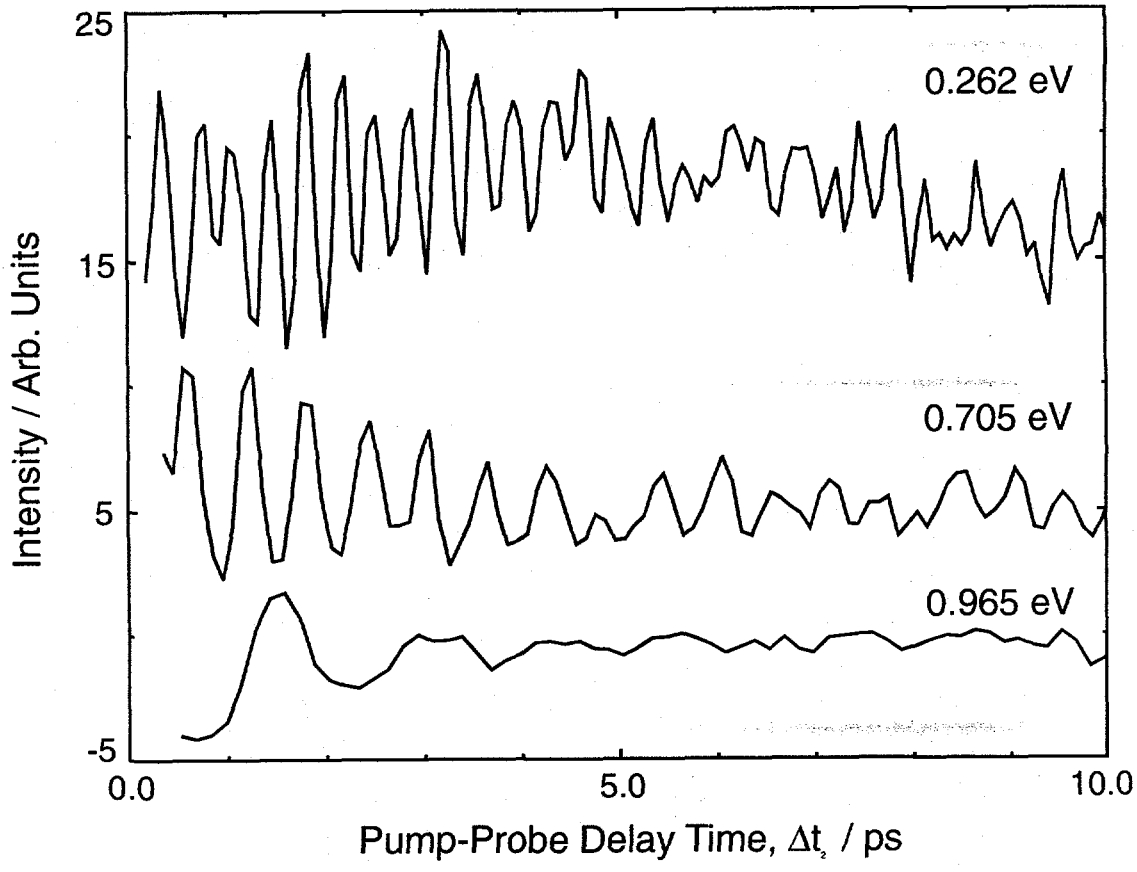

Figure 3. Slices through the SEP signal for three typical excitation energies. The period of the oscillations increase with excitation energy, and dephasing occurs by ~8 ps.

outer and inner turning points of the I_2^- ground state potential, and includes detachment to at least 10 energetically accessible I_2 potentials.[17,42] However, the signal extending to high eKE (>2.0 eV) is only due to detachment to the I_2 $\tilde{X}\ ^1\Sigma_g^+$ state at the inner turning point of the I_2^- vibrational distribution (Fig. 1).[42] This region of the photoelectron spectrum has previously been used to determine the vibrational distribution of I_2^- products in photodissociation and cluster recombination experiments.[6,8]

The features associated with the dump pulse exhibit oscillatory time-dependent dynamics. For example, above 2.0 eV and at 1.1 eV the signal clearly increases between 1600 and 1800 fs, while a corresponding decrease in intensity is observed at 1.4 eV eKE (Fig. 2b). As established above, the signal above 2.0 eV monitors the ground state population near the inner turning point. Hence, the time-evolution of the spectra in Fig. 2b indicate that the ground state wavepacket is moving towards the inner turning point during this 300 fs time interval. Since the oscillations at 1.1 and 2.0 eV have similar phases, the inner turning point is also monitored at 1.1 eV, albeit by detachment to I_2 states other than the ground state. On the other hand, the oscillations at 1.4 eV must reflect wavepacket motion at the outer turning point, since they are 180° out-of-phase with those at 2.0 eV. In principle the wavepacket can be monitored at all internuclear distances. However, the large number of neutral states that contribute to the signal below 2.0 eV make quantitative analysis of the spectra difficult. Hence, in this report, we focus on the portion of the signal above 2.0 eV eKE that solely monitors wavepacket motion near the inner turning point.

Fig. 3 shows slices through the intensity above eKE = 2.0 eV as a function of delay time for three different excitation energies: 0.262, 0.705, and 0.965 eV. The

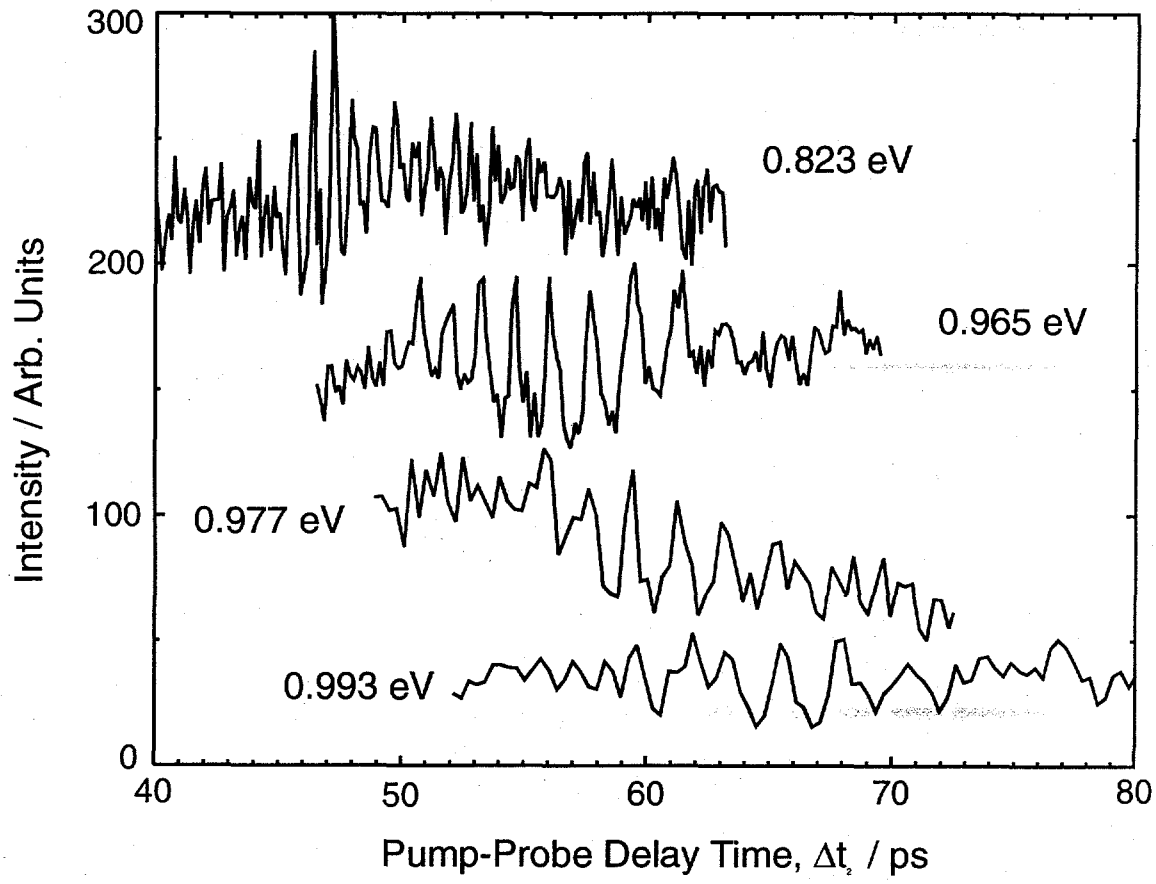

Figure 4. Recurrences of the four highest excitation energies. The recurrences appear at increasingly longer delay times, indicating the anharmonicity decreases with excitation energy.

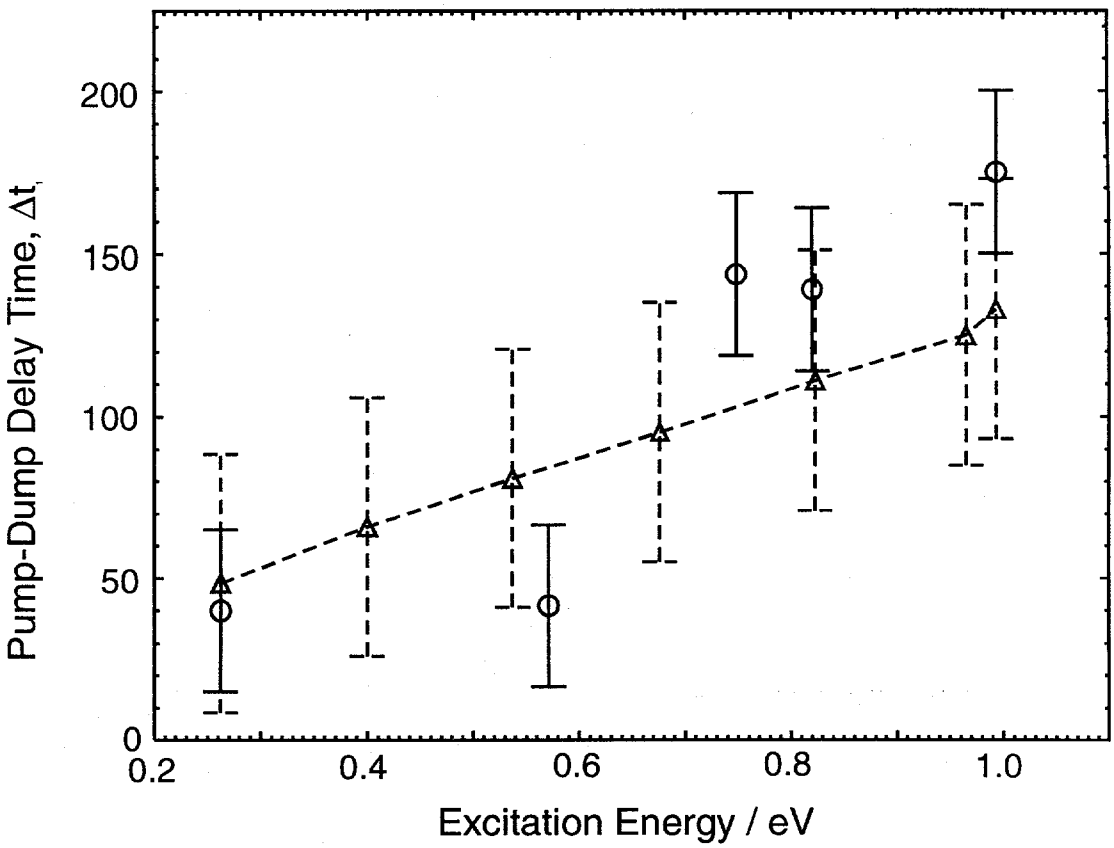

Figure 5. Experimental (circles, solid) and simulated (triangles, dashed) pump-dump delay times for optimal SEP transfer.

oscillatory behavior of the signal in this eKE range is apparent. The oscillations have frequencies of ~350, 650, and 1500 fs, respectively, showing a clear decrease in frequency with increasing excitation energy, and all disappear by roughly 8 ps. However, the oscillations reappear for approximately twice the duration between 40 and 70 ps, depending on the excitation energy; the recurrence time is 45 ps at or below 0.676 eV, and becomes increasingly longer for higher excitation energies. This is illustrated in Fig. 4. For the highest excitation energy used in our experiments (0.993 eV), the oscillations re-appear near 67 ps and have a period of ~2500 fs.

The time delay, Δt_1, between pump and dump pulses also affects the SEP efficiency. To maximize this, the SEP signal above 2.0 eV was monitored while scanning Δt_1 in 25 fs steps; the optimal delay times are plotted in Fig. 5 (circles) as a function of excitation energy. The general trend is to longer pump-dump delay times with increasing excitation energy. In fact, for excitation energies above 0.6 eV, Δt_1 must be at least 100 fs to observe SEP signal.

4. Analysis and Discussion

In this section we develop an $I_2^-(\tilde{X}\ ^2\Sigma_u^+)$ potential that is accurate to within our experimental error. To this end, we first determine the frequency and anharmonicity of the potential at a series of excitation energies. We then discuss the analytical potential and the procedure for fitting the measured frequencies and anharmonicities. The fit potential is then compared to previous ground state potentials. Finally, full quantum mechanical simulations of the SEP signal and photoelectron spectra are performed to

better understand the SEP-induced dynamics and demonstrate the effectiveness of our fitting procedure.

4.1. Determination of frequencies and anharmonicities

The first step in determining an accurate potential is to extract the frequencies and anharmonicities from the experimental results for each excitation energy. For excitation energies ≤0.823 eV, Fourier transforms of the oscillations, shown in Fig. 6, are sufficient to determine the frequencies.[16] However, the transforms are obtained from the recurrences rather than the initial oscillations, because these provide more intense and well-defined transforms. This is demonstrated in Fig. 6 for 0.823 eV of excitation energy, where the Fourier transforms of the initial oscillations (dashed) and recurrences (solid) are compared. Both are centered at the same frequency, but the transform of the recurrences is much more prominent, because the time-envelope in which the recurrences rephase and dephase is twice as long as the envelope that only includes the initial dephasing. Thus, the frequencies used in this report are the Fourier transforms in Fig. 6, which are listed in Table I with the error bars estimated as the FWHM of the transforms.

For excitation energies ≥0.965 eV, the Fourier transforms become less reliable for two reasons. First, even though the SEP efficiency is similar for all excitation energies, the signal to noise ratio decreases with excitation energy, because the photoelectron spectra are spread out over an increasingly larger range of eKEs (Section 3). Second, the wavepacket frequencies begin to merge with low frequency noise present in our experiments below 20 cm^{-1}, primarily caused by long-term drift in our laser beams. At 0.965 eV, the wavepacket frequency can still be extracted from the transform by comparison with transforms lacking the ground state oscillations, but above 0.965 eV this

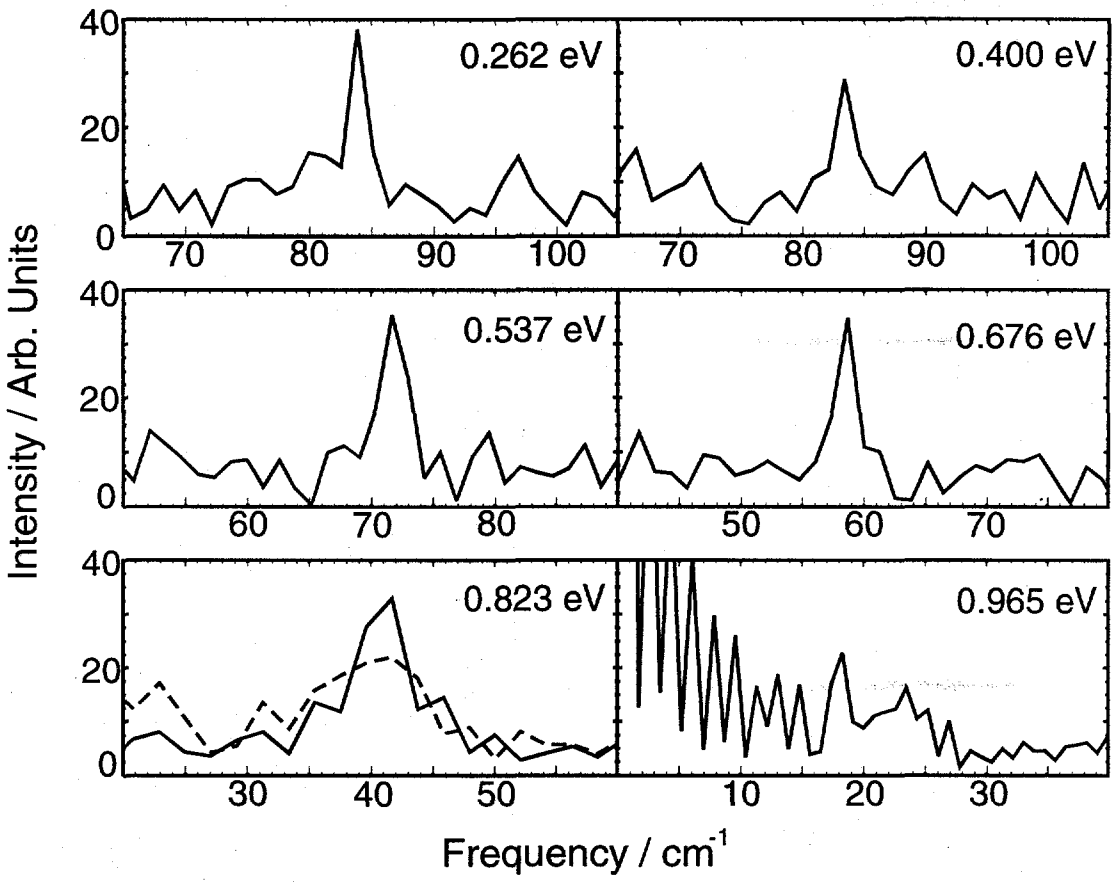

Figure 6. Fourier transforms of the SEP recurrences used to determine the potential's frequency as a function of excitation energy (Table I). At 0.823 eV, the Fourier transform of the initial oscillations (dashed) is compared to that of the recurrences (solid). At 0.965 eV, the low frequency noise is apparent below 20 cm^{-1}.

is no longer the case. Instead, the predominant frequency was obtained from the spectra in Fig. 4 using a least-squares fitting routine in which three sine waves of adjustable frequencies and intensities were fit to each of the rephased oscillations. The average of the three frequencies is listed in Table I. The accuracy of this method was tested for excitation energies of 0.823 and 0.965 eV and found to agree reasonably well with the Fourier transforms. In Table 1, somewhat larger error bars are assigned to the frequencies for excitation energies ≥0.965 eV to account for their less accurate determination.

Table I. Experimental and fit frequencies and anharmonicities.

	Experimental Data		Fit Potential	
Excitation Energy / eV	Freq / cm^{-1}	Anhar / cm^{-1}	Freq / cm^{-1}	Anhar / cm^{-1}
0.014[a]	110 ± 2		109.9	
0.262	94 ± 1		93.3	
0.400	83.5 ± 1		83.6	
0.537	72 ± 1.5		72.7	
0.676	58 ± 1		59.1	
0.823	41 ± 2.5	0.354 ± 0.016	42.7	0.345
0.965	22 ± 4	0.296 ± 0.015	19.0	0.292
0.977	17 ± 4	0.278 ± 0.014	15.6	0.277
0.993	13 ± 4	0.249 ± 0.011	10.8	0.249

[a] Taken from Ref. 16

Even though the frequency of the oscillations becomes harder to determine with excitation energy, the anharmonicity can still be accurately established, because it is directly proportion to the rephasing time. The rephasing time, τ, is determined by the change in frequency between any three adjacent vibrational levels, i.e. $\tau = \Delta\omega = \omega_{v+1} - \omega_v$.[43] For a Morse potential, $\Delta\omega = 2\omega_e\chi_e$ for any three adjacent vibrational levels. In this case, rephasing will occur at the same time for all excitation energies. For the previously determined $I_2^-(\tilde{X}\ ^2\Sigma_u^+)$ Morse potential, the anharmonicity is 0.37 cm^{-1}, which gives a rephasing time of $\tau = 2\omega_e\chi_e = 0.740\ cm^{-1} = 45$ ps.[16,43] In our experiment, the rephasing times ≥0.823 eV become longer with excitation energy (Fig. 4). Hence, the anharmonicity decreases with excitation energy, indicating a deviation from a Morse potential. For these excitation energies, the four highest in Table 1, the anharmonicity is determined from the center of the rephasing time and error bars assigned that encompass the approximate FWHM of the recurrences.

4.2. I_2^- ground state potential

In the previous section we determined the vibrational frequencies and anharmonicities for excitation energies up to 0.993 eV. In this section, an I_2^- ground state is constructed by an iterative fit to the data points (Table I). This is done using a Morse potential with the β-parameter expanded in a Taylor series, and with the bond length held constant:[44]

$$V(r) = D_e[1 - e^{-\beta(r-r_e)}]^2 \qquad (2)$$

$$\beta = \beta_0 + \beta_1(r - r_e) + \beta_2(r - r_e)^2 + \ldots \qquad (3)$$

where D_e and r_e are the previously determined well depth (1.014 eV) and equilibrium internuclear distance (3.205 Å), respectively.[16] Equations 2 and 3 allow sufficient flexibility to adequately fit the data, but only require the equilibrium internuclear distance. Up to an 8th order expansion of the β-parameter was used (Eq. 3), although it was found that inclusion of orders above the 4th did not significantly improve the fit.

Our procedure for determining the potential is as follows. First, a reasonable potential is generated with an appropriate choice of β-parameters using Eqs. 2 & 3. The vibrational eigenstates are then calculated using a discrete variable representation (DVR) code with a Morse oscillator basis set,[45] and the frequency and anharmonicity are determined for each excitation energy. A statistical analysis is performed with the calculated values and experimental data (Table I), and χ^2 is determined. The method is then repeated with different β-parameters. The entire procedure is automated using a downhill simplex method to iteratively improve the β-parameters and minimize χ^2.[46] The parameters of the fit potential are listed in Table II, and the fit frequencies and anharmonicities are compared to experiment in Table I and in Figs. 7 and 8. The agreement is remarkably good; all the calculated frequencies and anharmonicities fall within the experimental error bars. The potential itself is shown in Fig. 9.

Table II. β-parameters for the fit potential

$\beta_0 = 1.188497$ Å^{-1}	$\beta_1 = -6.810537 \times 10^{-2}$ Å^{-2}
$\beta_2 = 1.305919 \times 10^{-2}$ Å^{-3}	$\beta_3 = -2.957611 \times 10^{-3}$ Å^{-4}
$\beta_4 = 1.941355 \times 10^{-4}$ Å^{-5}	

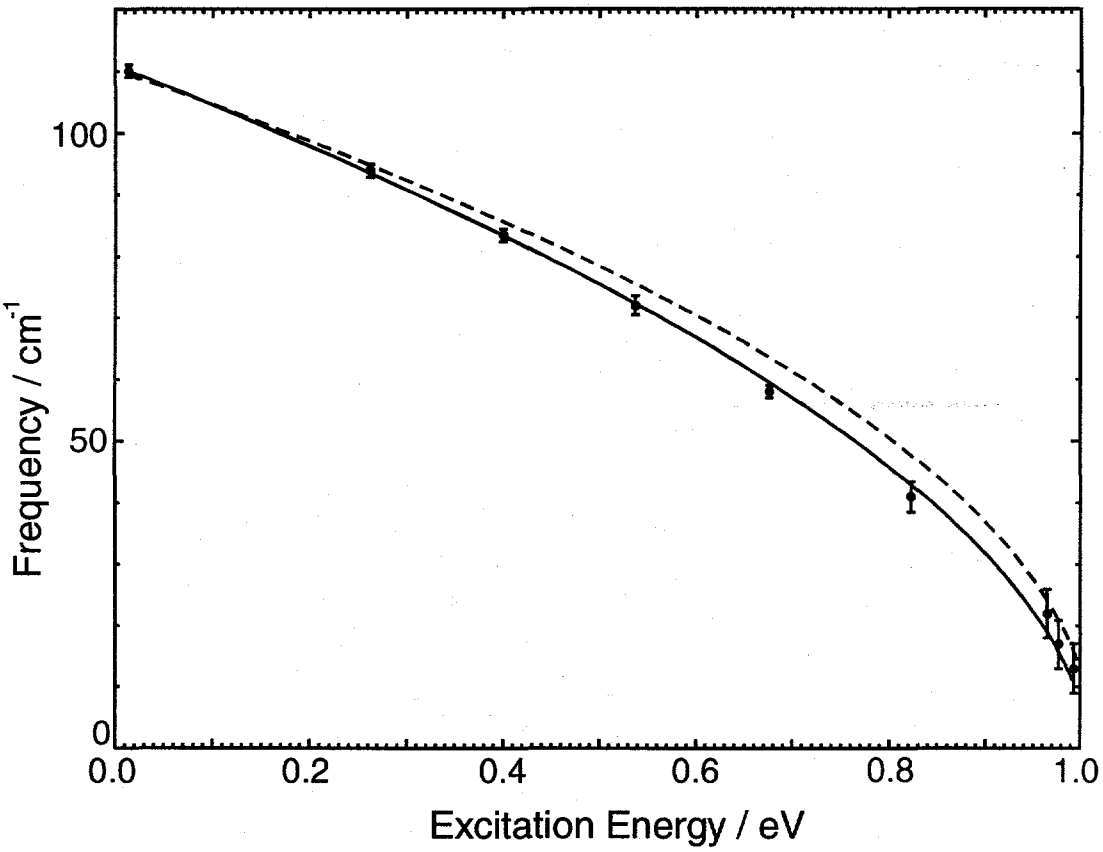

Figure 7. Comparison of experimental frequencies (circles) to those of the fit potential (solid) and previously determined Morse potential (dashed, Ref. 16).

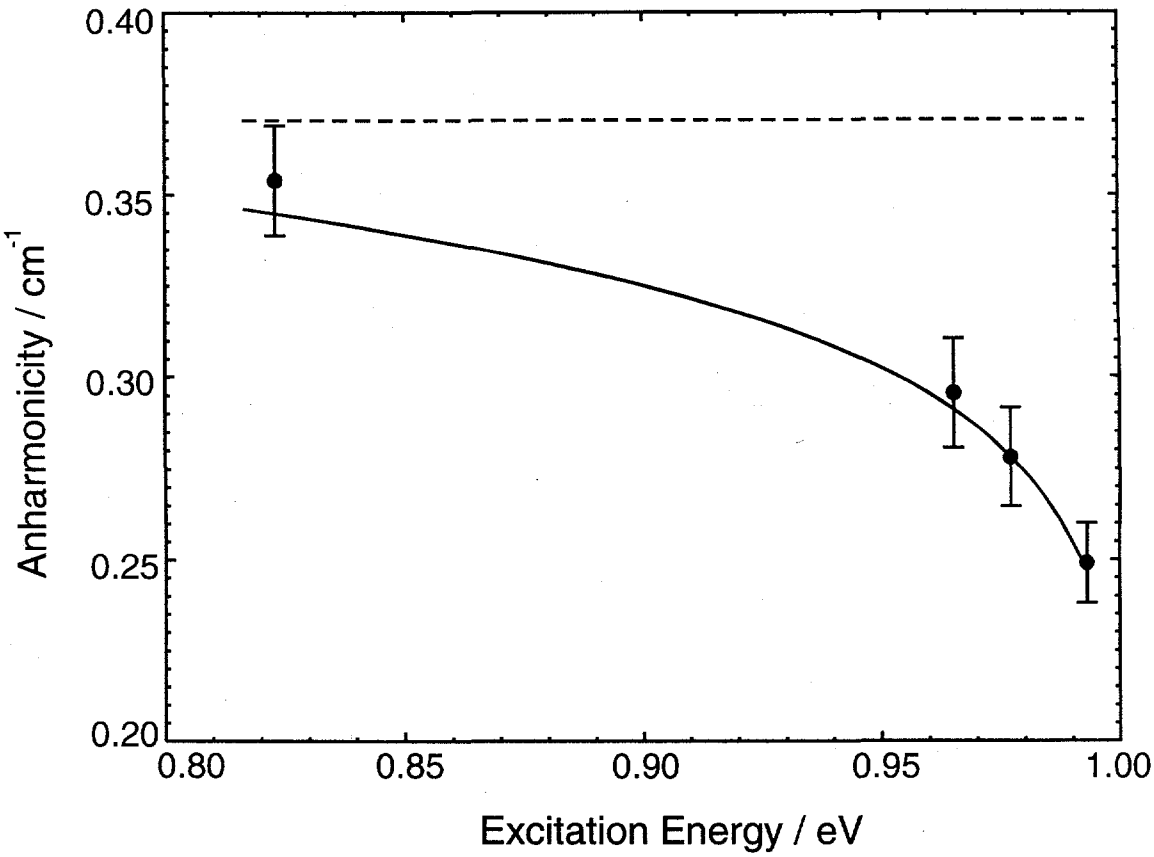

Figure 8. Comparison of the experimental anharmonicities (circles) to those of the fit potential (solid) and previously determined Morse potential (dashed, Ref. 16).

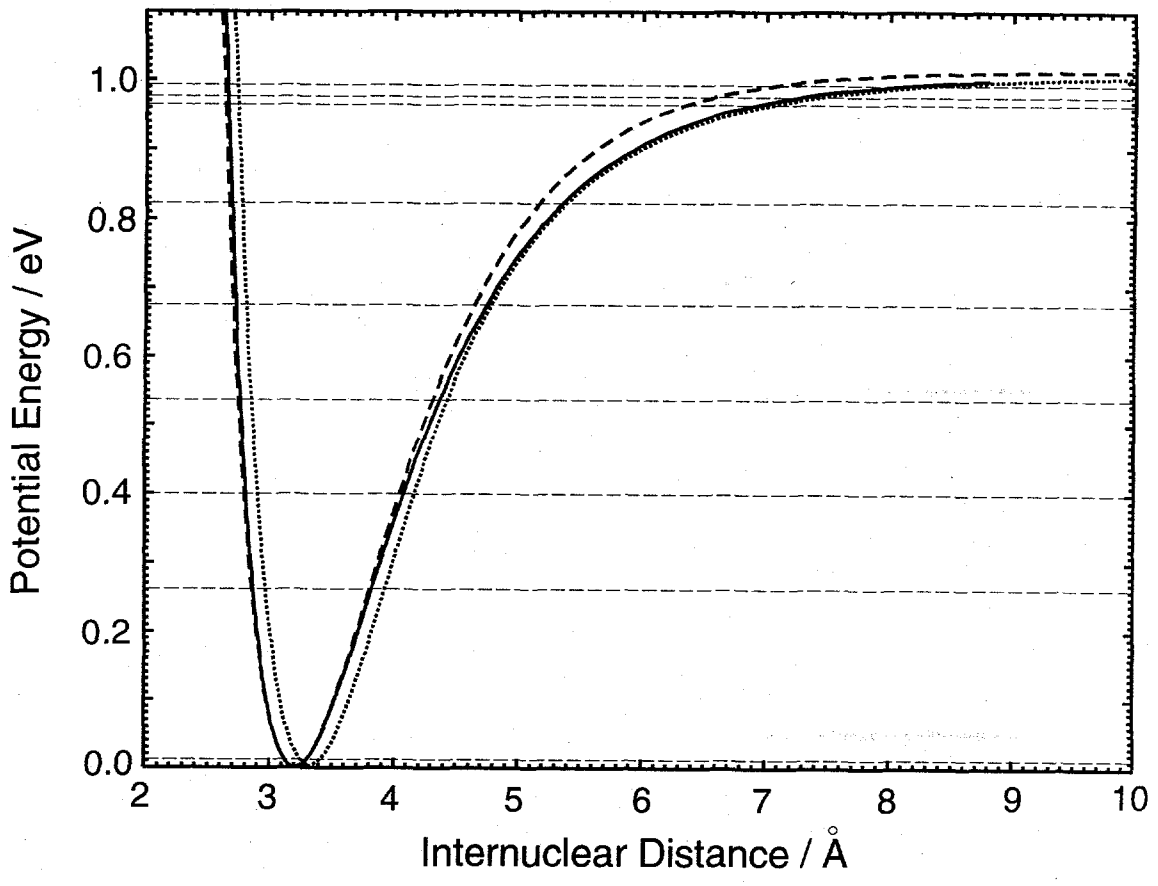

Figure 9. Comparison of the fit potential (solid) to the previously determined Morse potential (dashed, Ref. 16) and scaled *ab initio* potential (dotted, Refs. 14,15). The horizontal dotted lines are the excitation energies used to determine the fit potential (Table I).

It should be noted that rotational dynamics have not been included in the above calculations and discussion, even though Gruebele *et al.*[47,48] have shown that modeling the time-dependent rotational and vibrational wavepacket dynamics is equivalent to determining the potential using an RKR inversion technique with frequency resolved eigenstates. The angular distribution of the detached electrons does rotate with the molecular frame, but we are insensitive to this variation because we collect nearly all the photoelectrons in our apparatus. Also, in contrast to absorption experiments, the photodetachment probability is independent of molecular orientation.[49] Hence, we cannot monitor rotational dynamics, which limits our choices for analytical potentials to forms that have energy independent bond lengths.

4.3. Comparison with other potentials

In this section we compare our potential to the previous Morse[16] and scaled *ab initio* potentials.[14,15] For the Morse potential, the vibrational frequency and anharmonicities of the potential at the measured excitation energies were determined using the DVR code described above, and the results are compared to the values from experiment and our fit potential in Figs. 7 and 8. The potentials are shown in Fig. 9. The Morse potential correctly predicts the frequencies near the bottom of the well and again at the highest excitation energies, but the values lie outside the experimental bars for intermediate energies 0.400 – 0.823 eV (Fig. 7). Even though the frequencies are correctly predicted for the three highest excitation energies, the anharmonicities become exceedingly worse (Fig. 8), and indicates that the slope of the Morse potential in this energy range is too steep. Hence, we conclude that the Morse potential is a good

approximation below ~0.3 eV. Interestingly, Morse potentials are overly attractive at large internuclear distances for neutral molecules,[50] but in this case the Morse potential is not sufficiently attractive when compared to our potential. This is likely to be the effect of the $1/r^4$ charge-induced dipole potential inherent to negative ion systems (vs. $1/r^6$ for neutrals).

Comparison with the scaled *ab initio* potentials show the opposite trend. In Fig. 9, the *ab initio* potential agrees well with ours for energies above 0.7 eV and internuclear distances greater than 4.5 Å. At smaller radii the potential deviates from ours, primarily because the calculated equilibrium nuclear distance is too large. The agreement between our empirical and the scaled *ab initio* potential for radii above 4 Å is consistent with our work on the $I_2^-(\tilde{A}'\ ^2\Pi_{g,1/2})$ excited state surface where similar agreement at large internuclear distances was found.[17] This seems to indicate that the *ab initio* methods are exceedingly reliable at calculating potentials for large radii. It also strengthens the conclusions drawn from theoretical calculations studying the recombination and vibrational relaxation rates of photodissociated $I_2^-(Ar)_n$ and $I_2^-(CO_2)_n$ clusters,[14,15,51-53] since the *ab initio* potentials are very accurate at large internuclear distances where these processes are exceedingly sensitive to the potential surfaces.

4.4. Quantum mechanical simulations of the SEP process and FPE spectra

In the above sections, it was implicitly assumed that conservation of energy determines the mean of the vibrational distribution. Franck-Condon factors also affect the distribution, because the large bandwidths of the pump and dump lasers populate multiple vibrational states, which are not equally weighted. For example, at long delay

times the excited state wavepacket will not have overlap with low vibrational quanta, and hence skew the distribution in favor of higher vibrational levels. In order to understand better how the excitation energy and pump-dump delay time determines the ground state vibrational distribution, full quantum mechanical simulations of the SEP process are presented in this section. We also present simulations of the photoelectron spectra themselves for direct comparison with experiment.

Except for the additional of the dump pulse, the algorithm used in this section has been reported previously.[18,28] Our method is based on a wavepacket propagation scheme that numerically integrates the time-dependent Schrodinger equation:

$$i\hbar\frac{d}{dt}\begin{pmatrix}|\psi_1(t)\rangle\\|\psi_2(t)\rangle\end{pmatrix}=\begin{pmatrix}H_1 & -\mu\cdot E_1(t)-\mu\cdot E_2(t)\\-\mu\cdot E_1(t)-\mu\cdot E_2(t) & H_2\end{pmatrix}\begin{pmatrix}|\psi_1(t)\rangle\\|\psi_2(t)\rangle\end{pmatrix} \qquad (1)$$

Here H_1 and H_2 are the nuclear Hamiltonians for the $I_2^-(\tilde{X}\ ^2\Sigma_u^+)$ and $I_2^-(\tilde{A}'\ ^2\Pi_{g,1/2})$ states, respectively; μ is the transition dipole moment between the ground and excited states, assumed to be constant for all internuclear distances; and $E_1(t)$ and $E_2(t)$ are the time-dependent pump and dump laser pulses, respectively. The photoelectron spectrum can then be calculated from either anion surface using 1st order perturbation theory.

To begin the simulations, pulse widths, dipole moments, and potentials are needed. The pump and dump pulse widths have been set to 70 fs fwhm ($sech^2$). The transition dipole moment between the ground and excited states of I_2^- is not known. To account for this, we have scaled the pump pulse $\mu\cdot E_1(t)$ to deplete 42% of the ground υ=0 eigenstate in accordance with the experimental bleach of the probe-only features (Section

3, Fig. 2a). Since the pump and dump laser intensities are approximately equal, the dump pulse $\mu \cdot E_2(t)$ was set to the same value, although it is likely that μ depends on internuclear distance, and, hence, vibrational level. Calculation of H_n requires potential energy surfaces; for the excited state we used an empirical potential that we have previously developed,[17] and for the ground state, we use the potential obtained in Section 4.2.

With these parameters in place, the SEP signal was calculated for the experimental excitation energies from 0.262 to 0.993 eV. It was found that at all excitation energies population transfer is equally efficient, and that each excitation energy has an 80 fs FWHM range of pump-dump delays that gives good population transfer, albeit at increasingly longer delay times. Fig. 5 (dashed) plots the optimal delay time at each excitation energy with appropriate error bars. The optimal times fall within the experimental error bars, and for the most part linearly depend on the excitation energy. This is to be expected qualitatively; the optimal transfer point is at the internuclear distance where the dump pulse is in resonance with the energy difference between the ground and excited state potentials.[54] For increasingly higher vibrational excitation, longer wavelength dump pulses are needed, and hence, the resonance condition moves to larger internuclear distance. It should be noted that when a dissociative state is used for intermediate population transfer, the dump-transition always occurs before the turning point of the ground state potential, because the momentum built up on the excited state surface must be conserved upon transition to the ground state (Fig. 1). Moreover, it is the choice of a dissociative upper state that allows for efficient population transfer to all

vibrational levels, which is not the case for a bound upper potential. This is a particularly important advantage when a large range of excitation energies needs to be accessed.

Vibrational distributions for each excitation energy were also calculated by decomposing the ground state wavepackets into their vibrational eigenstates using the DVR code.[45] The results for an excitation energy of 0.965 eV at pump-dump delay times (Δt_1) of 37, 125, and 225 are show in Fig. 10. The optimal population transfer occurs at Δt_1=125 fs, and here the vibrational distribution is centered at the excitation energy. Many vibrational states are populated, and the distribution has a FWHM equal to the convolution of the pump and dump pulse widths, which are 0.019 eV FWHM. However, the mean energy of the vibrational distribution depends on the pump-dump delay time, Δt_1. Delay times earlier than the optimal time have similar distributions, albeit lower intensities, while larger than optimal delay times produce vibrational distributions shifted to higher energies. This is due to the evolving excited state wavepacket, for which the Franck-Condon overlap with low ground vibrational states diminishes with time. However, markedly long delay times away from optimum are needed to dramatically alter the vibrational distribution, so that under the conditions that our data were obtained, the assumption that the vibrational distribution is centered at the excitation energy is valid.

In the remainder of this section, we simulate the photoelectron spectrum using the potential obtained in Section 4.2 for direct comparison to experiment. This allows us to consider how the electron energy resolution, the temporal pulse widths, and the finite measurement time affect the spectra and Fourier transforms. To this end, we have calculated the photoelectron spectra at 0.823 eV excitation energy from 0 to 60 ps, and

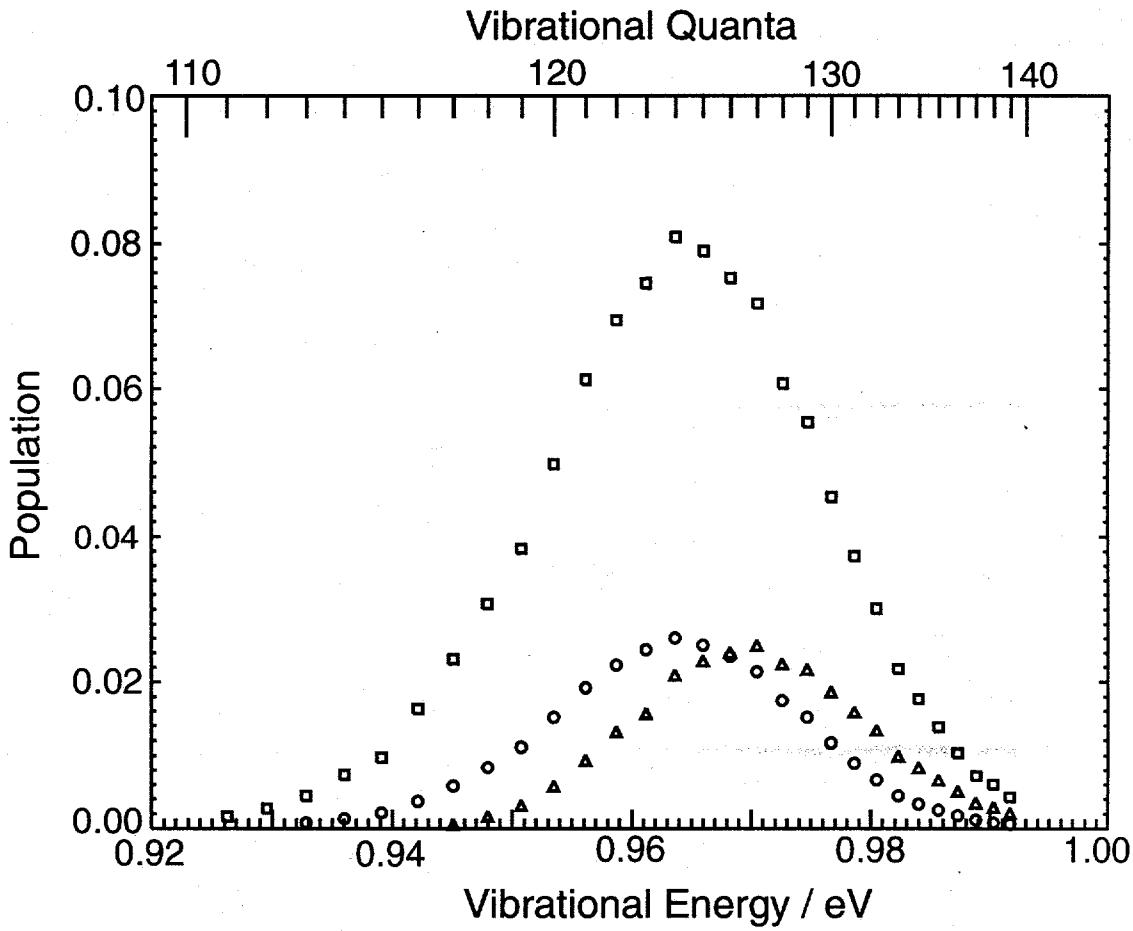

Figure 10. Simulated vibrational distribution for an excitation energy of 0.965 eV at 37 fs (circles), 125 fs (squares), and 225 fs (triangles).

convoluted the results with an empirically determined resolution function.[17] The time-dependent oscillations above 2.0 eV (dashed) are compared to experiment (solid) in Fig. 11, with their respective Fourier transforms in the insets.

Overall the agreement between the simulation and experiment is as predicted by the DVR analysis; the simulated frequency is shifted ~2 cm^{-1} to the blue (Fig. 11, inset), and the rephasing occurs at slightly longer times. On closer inspection, the first peak at Δt_2=800 fs agrees well with experiment, although subsequent peaks are not fit as well because of the slight frequency mismatch. This frequency mismatch is also apparent in the rephased oscillations around 45 ps. Evidently the error bars estimated from the FWHM of the Fourier transforms are generous, and the fit could be improved by reducing them in the X^2 fitting routine. On the other hand, the calculated anharmonicity is rather accurate since the simulated spectra rephase within 1 ps of the experimental measurement. This indicates that the calculated anharmonicity at this excitation energy is correct to within ~1/47 of the proper value. The largest discrepancy is that the oscillations are better defined in the simulations than experiment, which is presumably due to the ideal conditions in the simulations, e.g. no pulse chirping (from group velocity dispersion) and no noise. But even with this difference, the simulations confirm that our method of determining and fitting the frequencies and anharmonicities is a good procedure for obtaining the ground state potential.

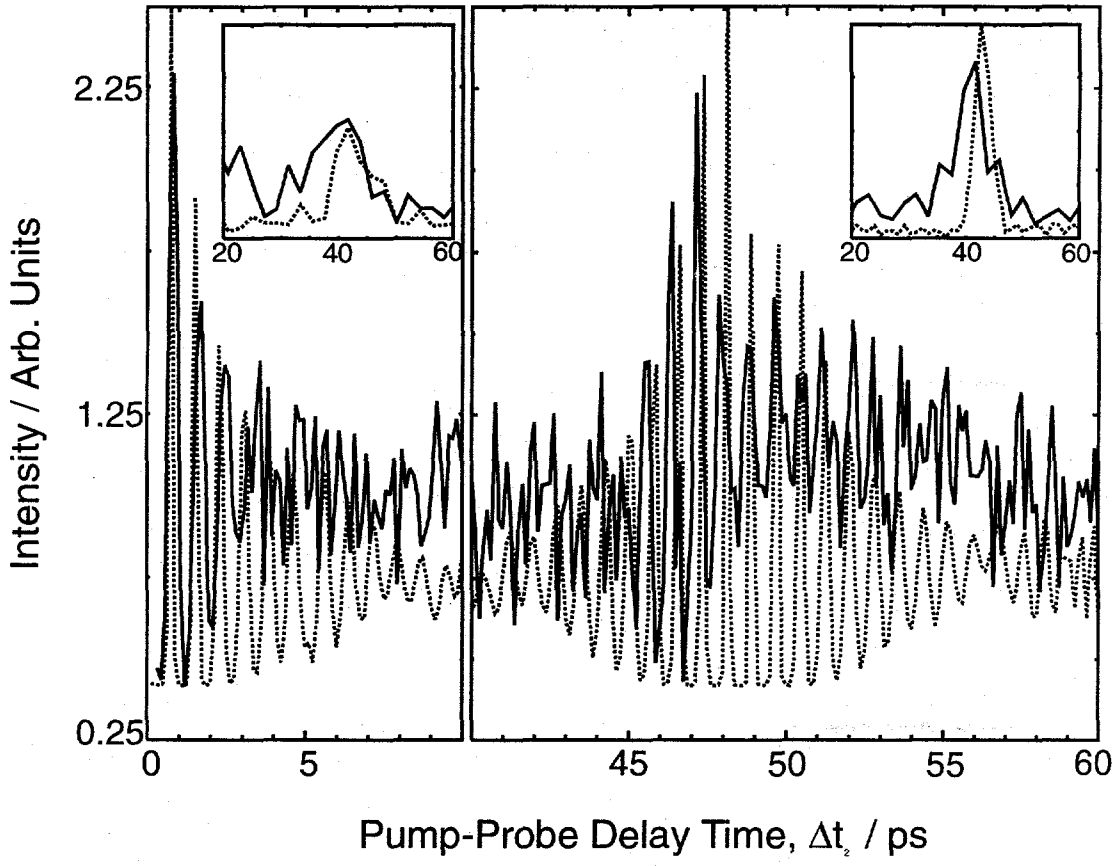

Figure 11. Experimental (solid) and simulated (dashed) slices above 2.0 eV eKE for the initial oscillations and recurrences at an excitation energy of 0.823 eV. The Fourier transforms of the slices are shown in the insets.

5. Conclusion

In this report we have applied femtosecond stimulated emission pumping to anions for the first time. By monitoring the resulting ground state wavepacket with FPES, we have demonstrated its utility in accessing a wide range of vibrational levels to allow the determination of an accurate ground state potential. Specifically, we measured the frequency and anharmonicity the of I_2^- ground state to within 2% of the dissociation limit and fit the results to a Morse potential with a β-parameter expanded in a Taylor series. Our results yield a potential that is significantly more attractive than the previously determined Morse potential at high vibrational energies. It was also shown that the use of a dissociative state for intermediate population transfer allows a wide range of ground state vibrational energies to be accessed with equal efficiency. Quantum mechanical simulations of the SEP technique provided insight into the effect of pump-probe delay time on the ground state vibrational distribution, and illustrated the accuracy of the fit potential. The results presented here suggest that the SEP-FPES technique will be useful in measuring the energy dependence of vibrational relaxation rates in cluster anions. Experiments in this direction are presently underway.

6. Acknowledgements

This research is supported by the National Science Foundation under Grant No. CHE-9710243 and from the Defense University Research Instrumentation Program under Grant No. F49620-95-0078. C.F. acknowledges post-doctoral support from the Deutsche Akademie der Naturforscher Leopoldina (BMBF-LPD 9801-6). A.V.D. is a National Science Foundation predoctoral fellow. M.E. and D.M.N. thank the France-Berkeley

Fund for financial support. The authors would also like to thank Steve Leone and David Tannor for helpful discussions, and Iddo Pinkas for a copy of Ref. 34 prior to publication.

7. References

[1] J. M. Papanikolas, J. R. Gord, N. E. Levinger, D. Ray, V. Vorsa, and W. C. Lineberger, J. Phys. Chem. **95,** 8028 (1991).

[2] J. M. Papanikolas, V. Vorsa, M. E. Nadal, P. J. Campagnola, H. K. Buchenau, and W. C. Lineberger, J. Chem. Phys. **99,** 8733 (1993).

[3] V. Vorsa, S. Nandi, P. J. Campagnola, M. Larsson, and W. C. Lineberger, J. Chem. Phys. **106,** 1402 (1997).

[4] A. Sanov, S. Nandi, and W. C. Lineberger, J. Chem. Phys. **108,** 5155 (1998).

[5] A. Sanov, T. Sanford, S. Nandi, and W. C. Lineberger, J. Chem. Phys. **111,** 664 (1999).

[6] B. J. Greenblatt, M. T. Zanni, and D. M. Neumark, Science **276,** 1675 (1997).

[7] M. T. Zanni, B. J. Greenblatt, and D. M. Neumark, J. Chem. Phys. **109,** 9648 (1998).

[8] B. J. Greenblatt, M. T. Zanni, and D. M. Neumark, J. Chem. Phys. **111,** 10566 (1999).

[9] B. J. Greenblatt, M. T. Zanni, and D. M. Neumark, J. Chem. Phys. , In Press (1999).

[10] A. E. Johnson, N. E. Levinger, and P. F. Barbara, J. Phys. Chem. **96,** 7841 (1992).

[11] J. C. Alfano, Y. Kimura, P. K. Walhout, and P. F. Barbara, Chem. Phys. **175,** 147 (1993).

[12] I. Benjamin, P. F. Barbara, B. J. Gertner, and J. T. Hynes, J. Phys. Chem. **99,** 7557 (1995).

[13] P. K. Walhout, J. C. Alfano, K. A. M. Thakur, and P. F. Barbara, J. Phys. Chem. **99,** 7568 (1995).

[14] J. Faeder, N. Delaney, P. E. Maslen, and R. Parson, Chem. Phys. Lett. **270,** 196 (1997).

[15] J. Faeder, N. Delaney, P. E. Maslen, and R. Parson, Chem. Phys. **239,** 525 (1999).

[16] M. T. Zanni, T. R. Taylor, B. J. Greenblatt, B. Soep, and D. M. Neumark, J. Chem. Phys. **107,** 7613 (1997).

[17] M. T. Zanni, V. S. Batista, B. J. Greenblatt, W. H. Miller, and D. M. Neumark, J. Chem. Phys. **110,** 3748 (1998).

[18] V. S. Batista, M. T. Zanni, B. J. Greenblatt, D. M. Neumark, and W. H. Miller, J. Chem. Phys. **110,** 3736 (1998).

[19] E. C. M. Chen and W. E. Wentworth, J. Phys. Chem. **89,** 4099 (1985).

[20] J. G. Dojahn, E. C. M. Chen, and W. E. Wentworth, J. Phys. Chem. **100,** 9649 (1996).

[21] E. C. M. Chen, J. G. Dojahn, and W. E. Wentworth, J. Phys. Chem. A **101,** 3088 (1997).

[22] P. W. Tasker, G. G. Balint-Kurti, and R. N. Dixon, Mol. Phys. **32,** 1651 (1976).

[23] G. A. Bowmaker, P. Schwerdfeger, and L. v. Szentpaly, J. Mol. Struct. THEOCHEM **53,** 87 (1989).

[24] D. Danovich, J. Hrusak, and S. Shaik, Chem. Phys. Lett. **233,** 249 (1995).

[25] P. E. Maslen, J. Faeder, and R. Parson, Chem. Phys. Lett. **263,** 63 (1996).

[26] C. Kittrell, E. Abramson, J. L. Kinsey, S. McDonald, D. E. Reisner, D. Katayama, and R. W. Field, J. Chem. Phys. **75,** 2056 (1981).

[27] M. Drabbels and A. M. Wodtke, J. Phys. Chem. A **103,** 7142 (1999).

[28] B. J. Greenblatt, M. T. Zanni, and D. M. Neumark, Chem. Phys. Lett. **258,** 523 (1996).

[29] M. Motzkus, S. Pedersen, and A. H. Zewail, J. Phys. Chem. **100,** 5620 (1996).

[30] M. Schmitt, G. Knopp, A. Materny, and W. Kiefer, Chem. Phys. Lett. **280,** 339 (1997).

[31] E. J. Brown, Q. Zhang, and M. Dantus, J. Chem. Phys. **110,** 5772 (1999).

[32] C. Hayden and D. W. Chandler, J. Chem. Phys **103,** 10465 (1995).

[33] M. Schmitt, G. Knopp, A. Materny, and W. Kiefer, Chem. Phys. Lett. **270,** 9 (1997).

[34] G. Knopp, I. Pinkas, and Y. Prior, J. Raman Spec. (1999). In Press

[35] B. J. Greenblatt, M. T. Zanni, and D. M. Neumark, Faraday Discuss. **108,** 101 (1998).

[36] W. C. Wiley and I. H. McLaren, Rev. Sci. Instrum. **26,** 1150 (1955).

[37] O. Cheshnovsky, S. H. Yang, C. L. Pettiette, M. J. Craycraft, and R. E. Smalley, Rev. Sci. Instrum. **58,** 2131 (1987).

[38] H. Handschuh, G. Gantefor, and W. Eberhardt, Rev. Sci. Instrum. **66,** 3838 (1995).

[39] L.-S. Wang, H.-S. Cheng, and J. Fan, J. Chem. Phys. **102,** 9480 (1995).

[40] M. D. Davidson, B. Broers, H. G. Muller, and H. B. v. L. v. d. Heuvell, J. Phys. B **25,** 3093 (1992).

[41] K. R. Asmis, T. R. Taylor, C. Xu, and D. M. Neumark, J. Chem. Phys. **109,** 4389 (1998).

[42] M. T. Zanni, B. J. Greenblatt, A. V. Davis, and D. M. Neumark, J. Chem. Phys. **111,** 2991 (1999).

[43] M. T. Zanni, B. J. Greenblatt, A. V. Davis, and D. M. Neumark, Laser Techniques for State-Selected and State-to-State Chemisry IV, Proc. SPIE **3271,** 196 (1998).

[44] W. N. Whitton and P. J. Kuntz, J. Chem. Phys. **64,** 3624 (1976).

[45] E. M. Greenawalt and A. S. Dickinson, J. Mol. Spectrosc. **30,** 427 (1969).

[46] W. H. Press, B. P. Flannery, S. A. Teukolsky, and W. T. Vetterling, *Numerical Recipes* (Cambridge University Press, Cambridge, 1989).

[47] M. Gruebele, G. Roberts, M. Dantus, R. M. Bowman, and A. H. Zewail, Chem. Phys. Lett. **166,** 459 (1990).

[48] M. Gruebele and A. H. Zewail, J. Chem. Phys. **98,** 883 (1993).

[49] E. P. Wigner, Phys. Rev. **73,** 1002 (1948).

[50] J. I. Steinfeld, J. S. Francisco, and W. L. Hase, *Chemical Kinetics and Dynamics* (Prentice Hall, New Jersey, 1989).

[51] J. Faeder and R. Parson, J. Chem. Phys. **108,** 3909 (1998).

[52] N. Delaney, J. Faeder, and R. Parson, J. Chem. Phys. **111,** 651 (1999).

[53] N. Delaney, J. Faeder, and R. Parson, J. Chem. Phys. **111,** 452 (1999).

[54] R. S. Mulliken, J. Chem. Phys. **55,** 309 (1971).

Chapter 6. Solvent effects on the vibrational frequency of I_2^- in size-selected $I_2^-(Ar)_n$ and $I_2^-(CO_2)_n$ clusters[†]

The vibrational frequency of the I_2^- chromophore in size selected $I_2^-(Ar)_n$ and $I_2^-(CO_2)_n$ clusters has been measured to wavenumber accuracy. The frequencies are determined by creating a coherent superposition of vibrational levels with a femtosecond laser pulse via a resonance impulsive stimulated Raman scattering process. The resulting wavepacket oscillations are detected with femtosecond photoelectron spectroscopy. Blue shifting of the frequency occurs upon solvation, with larger shifts observed for solvation with CO_2. The nature of the shifting is discussed and related to specific cluster geometries.

1. Introduction

Solvation plays a dramatic role in chemical physics, and its effect on the photodissociation dynamics, branching ratios, and product energy distributions has been explored in experiments with chromophores solvated in liquids,[1-5] solids,[6-10] and size-selected clusters.[11-14] Solvation not only has the ability to remove energy and redirect motion on potential surfaces, but can also modify the potentials themselves. One way to quantify this effect is to monitor the frequency shift of a chromophore as a function of cluster size, as has been done in high resolution studies of Ar_nHF.[15-18] Presumably, when enough solvent species are attached, the frequency will match that of the chromophore in a condensed phase environment.[19,20] However, in neutral species, it is difficult to determine unambiguously the number of solvent atoms for larger clusters. In studies of

[†] Originally published in J. Chem. Phys. **109**, 9648 (1998).

ion clusters, on the other hand, there is no ambiguity concerning the size of the clusters since they are readily mass-selected. In addition, the solvent-solute interactions are considerably stronger than in van der Waals clusters. In this paper we probe the effects of solvation on the ground electronic state of a diatomic anion by measuring the vibrational frequency of I_2^- in size-selected $I_2^-(Ar)_{n=6,12,18}$ and $I_2^-(CO_2)_{n=4,9}$ clusters.

This work represents a extension of earlier experiments in which the vibrational frequency of bare I_2^- was determined using resonance impulsive stimulated Raman scattering (RISRS) with femtosecond lasers.[21] We showed that by inducing coherent motion on the ground state of I_2^- with a femtosecond pump pulse and measuring the resulting oscillatory motion with femtosecond photoelectron spectroscopy (FPES), the ground state vibrational frequency can be obtained. This information was combined with results from conventional photoelectron spectroscopy to construct an accurate Morse potential for the ground state of I_2^-. In this report, we use this method to investigate I_2^- embedded in Ar and CO_2 clusters, and monitor the shift of vibrational frequency with wavenumber accuracy. Our results show that solvation generally results in a blue-shifting of the I_2^- vibrational frequency; the blue-shift increases with both the number of solvent species and the strength of the chromophore-solvent interaction. Comparison of the experimental shifts with calculated structures for these clusters suggests that the size of the shift is sensitive not only to the number of solvent species but also their configuration with respect to the I_2^- chromophore.

2. Experimental

The femtosecond photoelectron spectrometer has been described previously, and only a brief summary will be given here.[21,22] Argon carrier gas (seeded with 1.5% CO_2 when producing $I_2^-(CO_2)_n$ clusters) is passed over crystalline I_2 and supersonically expanded through a pulsed piezo electric valve operating at a repetition rate of 500 Hz. Anions are generated by crossing the expansion with a 1 keV electron beam and are mass-selected using a Wiley-McLaren time-of-flight mass spectrometer. After passing through several differentially pumped regions, the ions enter the detector chamber and are intercepted by the femtosecond pump and probe laser pulses at the focus of a "magnetic bottle" time-of-flight photoelectron spectrometer. Both laser pulses are generated using a commercial Ti:sapphire oscillator-regenerative amplifier laser system (CLARK-MXR). The pump pulse is centered at 780 nm with a fwhm duration of 75 fs ($sech^2$). A portion of the pump pulse is split off and frequency-tripled to give a probe pulse at 260 nm with a fwhm of 105 fs.

3. Results and Discussion

As has been described earlier,[21] the pump pulse is in resonance with the $I_2^-(\tilde{A}'\,^2\Pi_{g,1/2}) \leftarrow I_2^-(\tilde{X}\,^2\Sigma_u^+)$ transition. This transfers population from the $\tilde{X}$ state to the $\tilde{A}'$ excited electronic state. However, the pump pulse also creates a coherent superposition of vibrational states on the ground electronic state via a second order Raman process,[23-27] resulting in oscillatory wavepacket motion that is apparent in the time-resolved photoelectron spectra. Fig. 1 shows these oscillations for bare I_2^- and

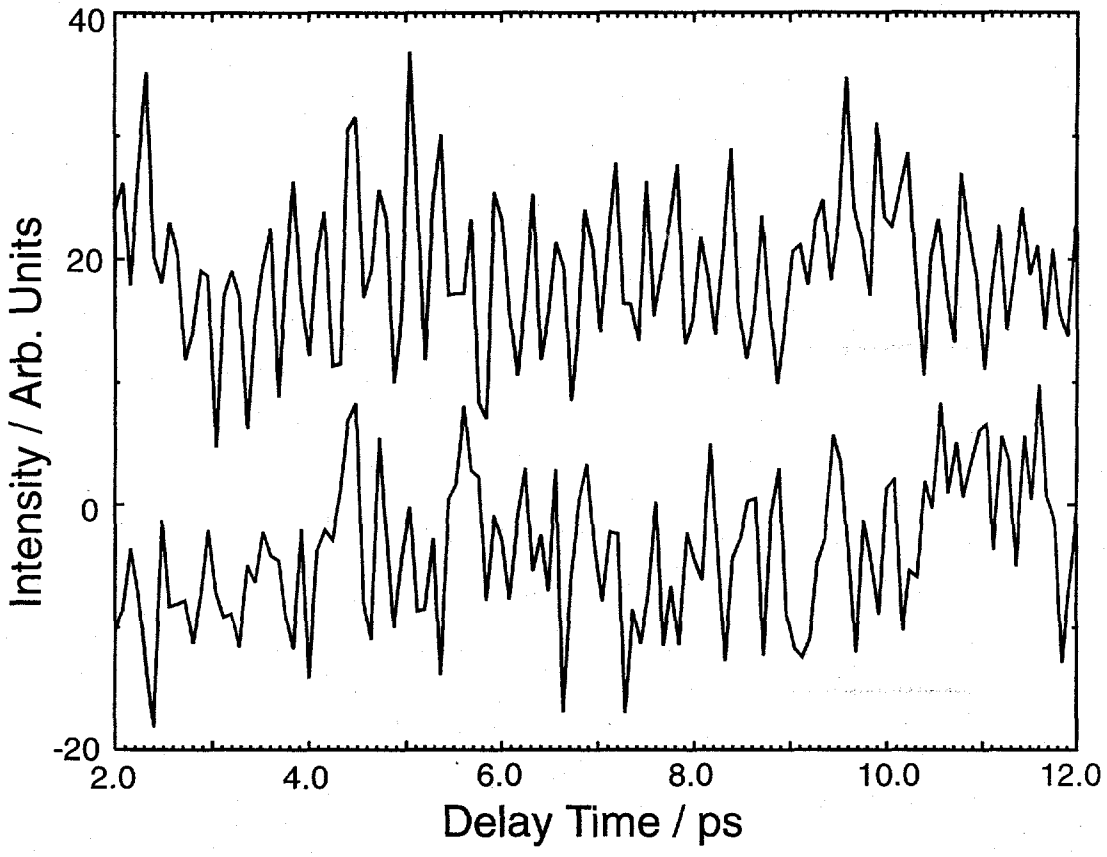

Figure 1. Photoelectron spectra as function of time for bare I_2^- (upper) and $I_2^-(CO_2)_9$ (lower). The spectra are shown at electron kinetic energies of 1.45 and 0.95 eV, respectively. The oscillations are caused by coherent wavepacket motion on the electronic ground state induced by the femtosecond pump pulse.

$I_2^-(CO_2)_9$ (upper and lower spectra, respectively) taken in 80 fs steps, at electron kinetic energies of 1.45 eV and 0.95 eV, respectively. In bare I_2^- the oscillations are clearly apparent with a period of approximately 300 fs. For $I_2^-(CO_2)_9$, the oscillations are less pronounced but still apparent, with a similar period of approximately 300 fs.

Vibrational frequencies are obtained by taking the Fourier transform of the photoelectron data at the electron energy where the oscillations are most evident. For all the clusters, spectra were taken at 80 fs steps out to time delays ranging from 11-17 ps. Shown in Fig. 2 is the Fourier transform from our previously reported experiment on bare I_2^-, yielding a frequency of 110.0±2.0 cm^{-1} (solid).[21] Also shown in Fig. 2 are the Fourier transforms obtained from $I_2^-(Ar)_6$, $I_2^-(Ar)_{12}$, and $I_2^-(Ar)_{18}$ clusters, indicating frequencies of 109.7±2.0, 111.4±1.7, and 112.7±1.5 cm^{-1}, respectively. Within our resolution, the $I_2^-(Ar)_6$ frequency is indistinguishable from that of bare I_2^-, while the $I_2^-(Ar)_{12}$ and $I_2^-(Ar)_{18}$ frequencies are progressively shifted to higher values. The Fourier transform of bare I_2^- is again shown in Fig. 3, along with the Fourier transforms obtained from $I_2^-(CO_2)_4$ and $I_2^-(CO_2)_9$. The two clusters show frequencies of 111.7±1.5 and 114.5±1.1 cm^{-1}, respectively. Both are blue-shifted with respect to bare I_2^-, and the degree of shifting is more pronounced than for the argon clusters, i.e. four CO_2 molecules produces the same blue shift as 12 Ar atoms. The larger effect of CO_2 is not surprising, given the considerably stronger binding energy of I_2^- to CO_2 *vs.* Ar; the dissociation energy of I_2^-Ar is 53 meV, whereas the average binding energy per CO_2 is 240 meV for $I_2^-(CO_2)_{n=10\text{-}22}$.[11,28]

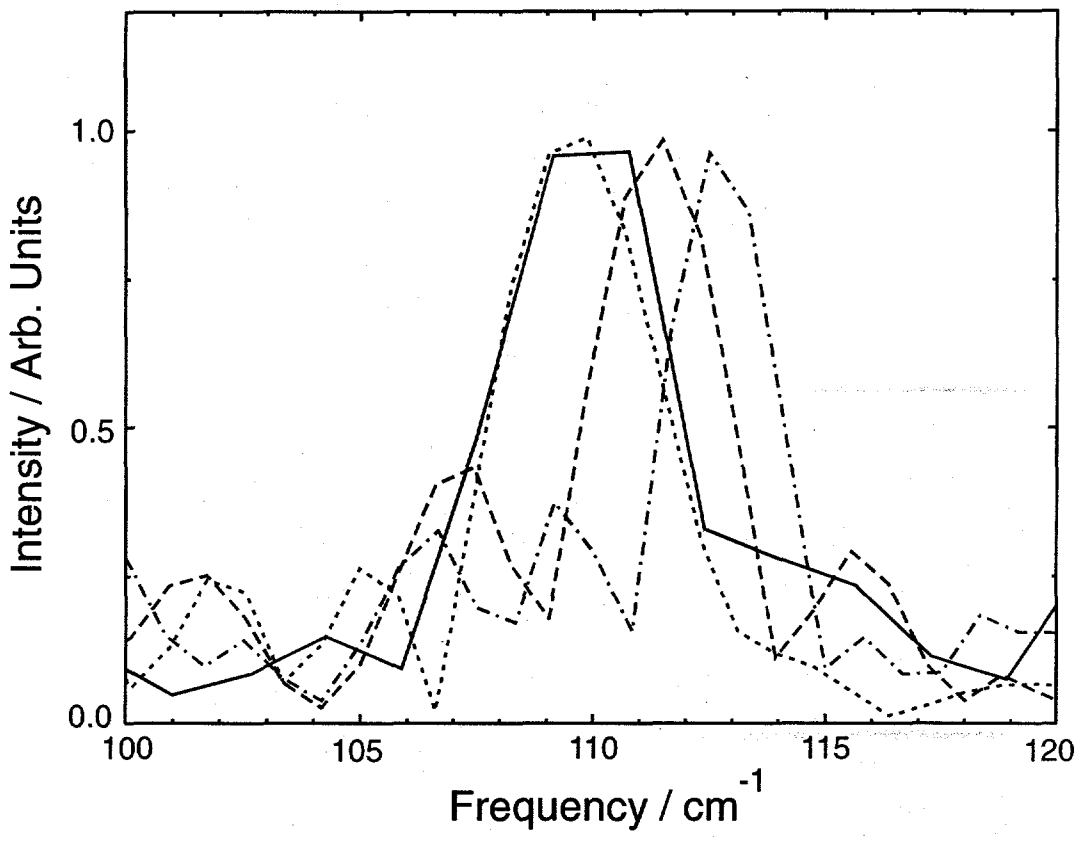

Figure 2. Fourier transforms of oscillatory photoelectron data yielding vibrational frequencies for $I_2^-(Ar)_n$: n=6 (dot), n=12 (dashed), and n=18 (dot-dashed), determined at electron kinetic energies of 1.38, 1.30, and 1.25 eV, respectively. The previously reported result for bare I_2^- is also shown (solid) for comparison.

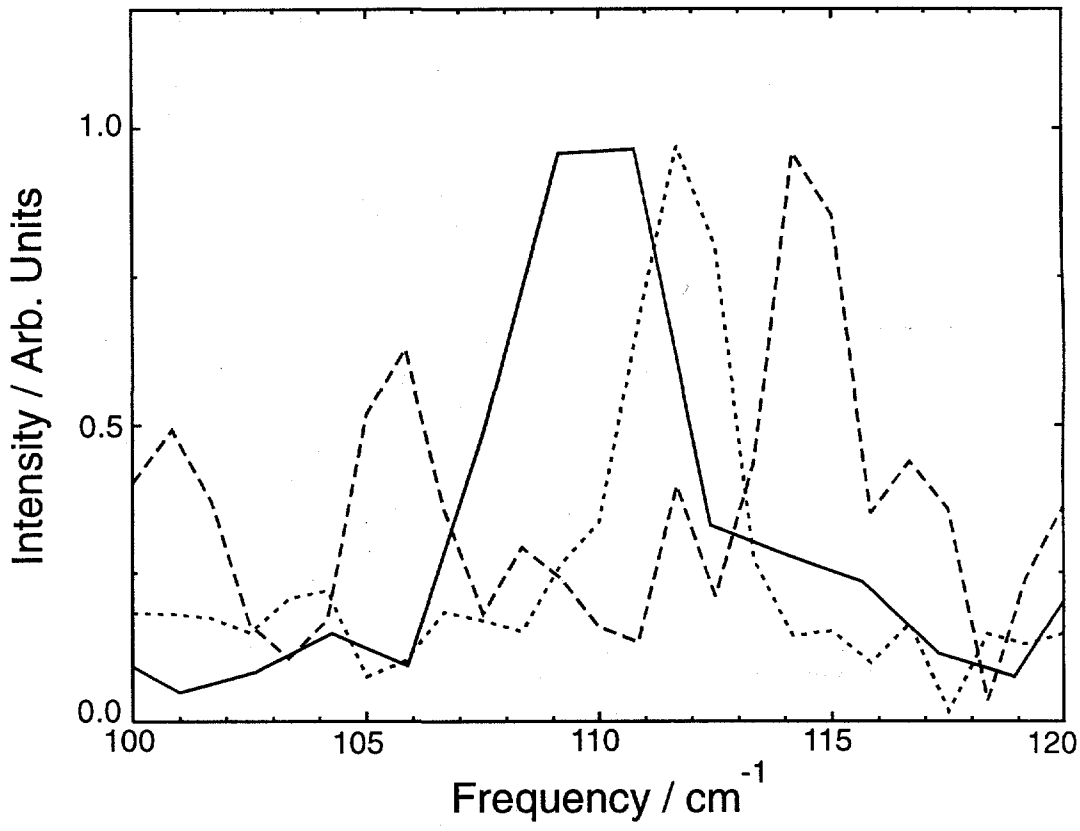

Figure 3. Fourier transforms of oscillatory photoelectron data yielding vibrational frequencies for $I_2^-(CO_2)_n$: n=4 (dot) and n=9 (dashed), determined at electron kinetic energies of 1.08 and 0.95 eV, respectively. The previously reported result for bare I_2^- is also shown (solid) for comparison.

The sign of the shift and its dependence on the number of solvent species is more intriguing. Blue-shifting of the I_2^- vibrational frequency can arise from electrostatic chromophore-solvent interactions, which can be visualized more easily by considering the calculated minimum energy structures[29-32] for the clusters shown in Fig. 4. In $I_2^-(Ar)_6$, the Ar atoms form a ring about the I_2^- bond.[31,32] $I_2^-(Ar)_{12}$ is a "half-solvated" species in which one I atom is surrounded by Ar atoms, while in $I_2^-(Ar)_{18}$ the solvent atoms form a nearly complete shell around the I_2^- (shell closure[33] is expected for n=20). As the I_2^- bond stretches during the course of a vibration, I atoms will collide with Ar atoms lying along or near the I_2^- internuclear axis; the I_2^- outer turning point is approximately 0.07 Å longer in the υ=1 level compared to the ground state. One might therefore expect this repulsive interaction to effectively steepen the potential at the outer turning point of the I_2^- vibration, resulting in bond compression and a higher vibrational frequency.

This picture is consistent with the trends in vibrational frequency. In $I_2^-(Ar)_6$, there are no Ar atoms along the internuclear axis, and no blue shift is observed. The structures in Fig. 4 show that the I atoms are progressively more confined along the internuclear axis for the n=12 and n=18 clusters, while the blue shifts are 1.4 and 2.7 cm^{-1}, respectively. Note that the blue shift in $I_2^-(Ar)_{18}$ is less than the ~5 cm^{-1} shift seen in an Ar matrix,[34] suggesting that the vibrational frequency in the clusters will continue to increase as a second solvent shell is added.

We therefore attribute the trends in vibrational frequency for $I_2^-(Ar)_n$ clusters to repulsive interactions between the chromophore and solvent. Although attractive anion-solvent interactions could also play a role, it is difficult to understand the absence of a blue-shift in $I_2^-(Ar)_6$ in terms of attractive forces alone. Moreover, in the larger clusters

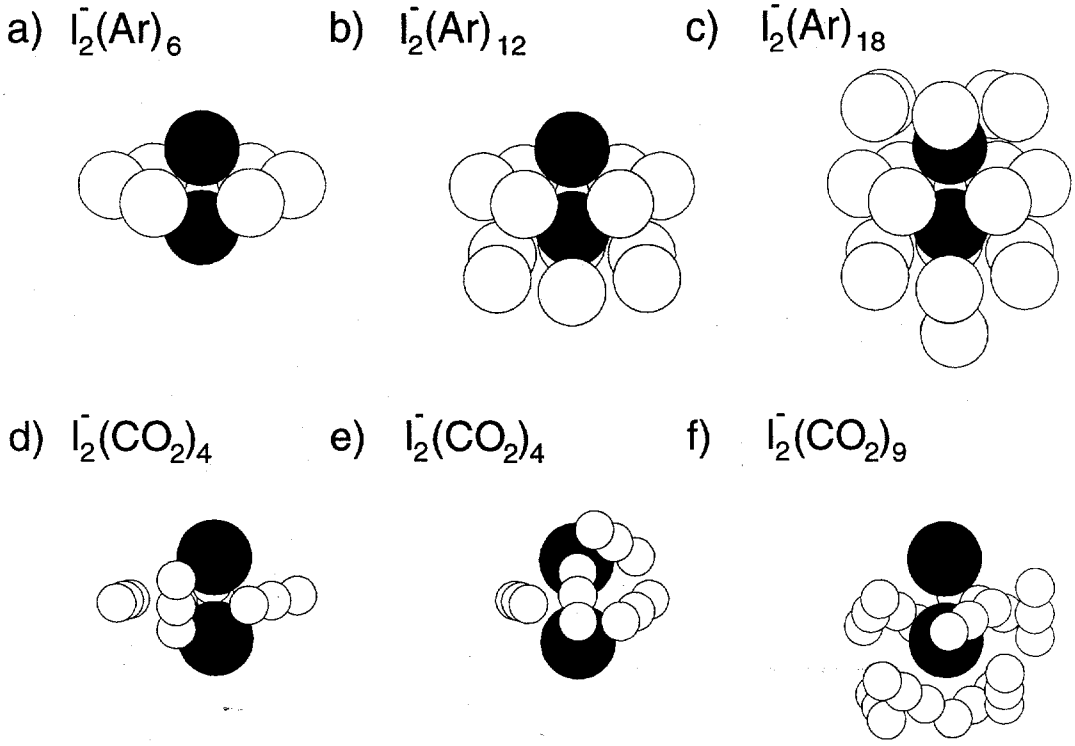

Figure 4. Minimum energy structures for $I_2^-(Ar)_n$ and $I_2^-(CO_2)_n$ clusters (Ref. 29-32) . For n=4, the ring and asymmetrical structures are both shown (d and e, respectively). The CO_2 molecules are reduced in size for clarity.

studied here, one might expect attractive anion-solvent forces to soften the I_2^- potential for $R>R_e$, resulting in a red-shifted vibrational frequency.[17,18]

The situation for $I_2^-(CO_2)_n$ clusters is more complex. Two calculated minimum energy structures for $I_2^-(CO_2)_4$ along with that for $I_2^-(CO_2)_9$ are shown in Fig. 4.[29,30,35] While the ring structure in Fig. 4d was originally calculated to be the ground state for $I_2^-(CO_2)_4$,[29] Parson and co-workers[35] find the asymmetric structure in Fig. 4e to be more stable by 30 meV. In $I_2^-(CO_2)_9$, one of the I atoms is completely solvated, as in the $I_2^-(Ar)_{12}$ structure, and one can explain the blue shift in terms of repulsive anion-solvent interactions as described above. It is more difficult to do this for either $I_2^-(CO_2)_4$ structure, particularly the ring. On the other hand, attractive interactions with the equatorial CO_2 molecules could be sufficiently strong to compress the I_2 bond, leading to a picture in which the blue shifts are due to a combination of attractive interactions with the equatorial CO_2 molecules and repulsive interactions with the axial CO_2 molecules.

Another possible origin for the blue shift is electron delocalization into the solvent species. The highest occupied molecular orbital in I_2^- is an anti-bonding σ_u^* orbital. Any electron delocalization would reduce the electron density in this orbital, thereby reducing the bond length and increasing the vibrational frequency. Electron delocalization in $I_2^-(Ar)_n$ clusters seems unlikely, but it is more difficult to rule out in the $I_2^-(CO_2)_n$ clusters, where the anion-neutral binding is stronger. Our previous study of the photoelectron spectra of $I^-(CO_2)_n$ showed that the anion-neutral interaction was strong enough to bend the CO_2 molecule by several degrees.[36] This could be explained solely by interaction of the I^- negative charge with the CO_2 quadrupole moment, without including any electron transfer. Since the $I_2^-\cdot CO_2$ binding energy is lower than that of I^-CO_2,[36,37] we expect minimal charge delocalization in $I_2^-(CO_2)_n$ clusters as well. Nonetheless, even

a small amount of delocalization could result in blue-shifts on the order of those seen here.

4. Conclusion

To summarize, we have demonstrated that our RISRS/FPES experiment yields relatively high resolution vibrational spectra on large, size-selected ion clusters. Specifically, we find that clustering of I_2^- with Ar and CO_2 results in a blue shift of the I_2^- frequency. The frequency shifts in $I_2^-(Ar)_n$ clusters are attributed to repulsive anion-solvent interactions with axial or near-axial Ar atoms. These interactions most likely play a role in $I_2^-(CO_2)_n$ clusters, but may be complemented by attractive interactions with equatorial solvent molecules and electron delocalization effects. These qualitative ideas can be explored more thoroughly with the aid of molecular dynamics simulations, and we hope the results presented here will stimulate such investigations. We plan to perform these experiments over a wider range of cluster sizes, and will vary both the anion and solvent species in order to gain a more complete picture of the trends in vibrational frequency with solvation.

5. Acknowledgments

This research is supported by the National Science Foundation under Grant No. CHE-9710243. Support from the Defense University Research Instrumentation Program under Grant No. F49620-95-1-0078 is also gratefully acknowledged. The authors would also like to thank Victor Batista, Marilyn Jacox, Jim Faeder, and Robert Parson for helpful suggestions.

6. References

[1] A. L. Harris, J. K. Brown, and C. B. Harris, Annu. Rev. Phys. Chem. **39,** 341 (1988).

[2] N. F. Scherer, L. D. Ziegler, and G. R. Fleming, J. Chem. Phys. **97,** 5544 (1992).

[3] U. Banin and S. Ruhman, J. Chem. Phys. **98,** 4391 (1993).

[4] N. Pugliano, D. K. Palit, A. Z. Szarka, and R. M. Hochstrasser, J. Chem. Phys. **99,** 7273 (1993).

[5] J. C. Alfano, Y. Kimura, P. K. Walhout, and P. F. Barbara, Chem. Phys. **175,** 147 (1993).

[6] V. E. Bondybey and C. Fletcher, J. Chem. Phys. **64,** 3615 (1976).

[7] R. Alimi, A. Brokman, and R. B. Gerber, J. Chem. Phys. **91,** 1611 (1989).

[8] R. Alimi, R. B. Gerber, J. G. McCaffrey, H. Kunz, and N. Schwentner, Phys. Rev. Lett. **69,** 856 (1992).

[9] J. G. McCaffrey, H. Kunz, and N. Schwentner, J. Chem. Phys. **96,** 155 (1992).

[10] M. Ovchinnikov and V. A. Apkarian, J. Chem. Phys. **108,** 2277 (1998).

[11] J. M. Papanikolas, J. R. Gord, N. E. Levinger, D. Ray, V. Vorsa, and W. C. Lineberger, J. Phys. Chem. **95,** 8028 (1991).

[12] Q. L. Liu, J. K. Wang, and A. H. Zewail, nature **364,** 427 (1993).

[13] J. K. Wang, Q. L. Liu, and A. H. Zewail, J. Phys. Chem. **99,** 11309 (1995).

[14] B. J. Greenblatt, M. T. Zanni, and D. M. Neumark, Science **276,** 1675 (1997).

[15] H. S. Gutowsky, T. D. Klots, C. Chuang, C. A. Schmuttenmaer, and T. Emilsson, J. Chem. Phys. **86,** 569 (1987).

[16] H. S. Gutowsky, C. Chuang, T. D. Klots, T. Emilsson, R. S. Ruoff, and K. R. Krause, J. Chem. Phys. **88,** 2919 (1988).

[17] D. J. Nesbitt, Chem. Rev. **88,** 843 (1988).

[18] D. T. Anderson, S. Davis, and D. J. Nesbitt, J. Chem. Phys. **107,** 1115 (1997).

[19] M. E. Jacox, Chem. Phys. **189,** 149 (1994).

[20] B. L. Grigorenko, A. V. Nemukhin, and V. A. Apkarian, J. Chem. Phys. **104,** 5510 (1996).

[21] M. T. Zanni, T. R. Taylor, B. J. Greenblatt, B. Soep, and D. M. Neumark, J. Chem. Phys. **107,** 7613 (1997).

[22] B. J. Greenblatt, M. T. Zanni, and D. M. Neumark, Faraday Discuss. **108,** 101 (1998).

[23] J. Chesnoy and A. Mokhtari, Phys. Rev. A **38,** 3566 (1988).

[24] B. Hartke, R. Kosloff, and S. Ruhman, Chem. Phys. Lett. **158,** 238 (1989).

[25] W. T. Pollard and R. A. Mathies, Ann. Rev. Phys. Chem. **43,** 497 (1992).

[26] U. Banin, A. Bartana, S. Ruhman, and R. Kosloff, J. Chem. Phys. **101,** 8461 (1994).

[27] D. M. Jonas, S. E. Bradforth, S. A. Passino, and G. R. Fleming, J. Phys. Chem. **99,** 2594 (1995).

[28] K. R. Asmis, T. R. Taylor, and D. M. Neumark, J. Chem. Phys. **109,** In Press (1998).

[29] F. G. Amar and L. Perera, Z. Phys. D **20,** 173 (1991).

[30] J. M. Papanikolas, P. E. Maslen, and R. Parson, J. Chem. Phys. **102,** 2452 (1995).

[31] J. Faeder, N. Delaney, P. E. Maslen, and R. Parson, Chem. Phys. Lett. **263,** 196 (1997).

[32] V. S. Batista and D. F. Coker, J. Chem. Phys. **106,** 7102 (1997).

[33] V. Vorsa, S. Nandi, P. J. Campagnola, M. Larsson, and W. C. Lineberger, J. Chem. Phys. **106,** 1402 (1997).

[34] W. F. Howard and L. Andrews, J. Am. Chem. Soc. **97,** 2956 (1975).

[35] J. Faeder, N. Delaney, and R. Parson, private communication .

[36] D. W. Arnold, S. E. Bradforth, E. H. Kim, and D. M. Neumark, J. Chem. Phys. **102,** 3510 (1995).

[37] V. Vorsa, Ph.D. Thesis, University of Colorado, Boulder, 1996.

Chapter 7. Time-resolved photodissociation dynamics of $I_2^-(Ar)_n$ clusters using anion femtosecond photoelectron spectroscopy[†]

Anion femtosecond photoelectron spectroscopy (FPES) is used to follow the dynamics of the $I_2^-(Ar)_6$ and $I_2^-(Ar)_{20}$ clusters subsequent to photodissociation of the I_2^- chromophore. The experiments show that photodissociation of the I_2^- moiety in $I_2^-(Ar)_6$ is complete by ~200 femtoseconds(fs), just as in bare I_2^-, but also that attractive interactions between the departing anion fragment and the solvent atoms persist for 1200 femtoseconds. Photodissociation of $I_2^-(Ar)_{20}$ results in caging of the I_2^- followed by recombination and vibrational relaxation on the excited $\tilde{A}\ ^2\Pi_{g,3/2}$ state and the ground $\tilde{X}\ ^2\Sigma_u^+$ states; these processes are complete in 35 picoseconds(ps) and 200 picoseconds, respectively.

1. Introduction

Our understanding of the potential energy surfaces governing the dynamics of elementary chemical reactions in the gas phase has grown significantly during the past 10 years, largely because of the development of new frequency and time-resolved experimental techniques(1, 2) combined with theoretical advances in quantum chemistry(3) and reaction dynamics(4). A very appealing new direction in this field is to investigate, in a systematic way, the effects of solvation on reaction dynamics. Studies of chemical reactions occurring within size-selected clusters provides an elegant means of achieving this goal, because one can monitor qualitative changes that occur as a function of cluster size and ultimately learn how the dynamics of an elementary unimolecular or bimolecular reaction evolve as one approaches a condensed phase environment.(5) It is particularly useful to perform such experiments on ionic clusters, for which size-selection is straightforward. We recently performed a time-resolved study of the photodissociation dynamics of the I_2^- anion using a new technique, anion femtosecond photoelectron

[†] Originally published in Science **276**, 1675 (1997).

spectroscopy (FPES)(6). We now apply this method to follow the dynamics that result from photodissociation of the I_2^- chromophore in the clusters $I_2^-(Ar)_6$ and $I_2^-(Ar)_{20}$. These experiments yield time-resolved measurements of the anion-solvent interactions subsequent to photodissociation and, in the case of $I_2^-(Ar)_{20}$, provide new insight into the caging and recombination dynamics of the I_2^- moiety.

Anion FPES is a pump-probe experiment that uses two femtosecond pulses, a pump pulse that photodissociates an anion (or anion chromophore in a cluster) and a probe pulse that ejects an electron from the dissociating species. By measuring the resulting PE spectrum at various delay times, the experiment yields "snapshots" of the dissociation dynamics, and in particular probes how the local environment of the excess electron evolves with time. This highly multiplexed experiment yields information on the entire photoexcited wavepacket at each delay time, in contrast to most pump-and-probe experiments in which signal is observed only if there is an absorption at the frequency of the probe pulse. Although FPES has also been applied to neutrals(7, 8, 9), the anion experiment is inherently mass-selective, making it especially useful in studies of size-selected clusters.

The present work builds on the experiments of Lineberger and co-workers (10, 11, 12), who performed one-photon photodissociation and time-resolved pump-and-probe experiments on size-selected $I_2^-(CO_2)_n$ and $I_2^-(Ar)_n$ cluster anions, and on the time-resolved studies of neutral $I_2(Ar)_n$ clusters by Zewail and co-workers (13). The one-photon cluster anion experiments yield the asymptotic daughter ion distributions as a function of initial cluster size, in particular the relative amounts of "caged" $I_2^-(Ar)_{m1<n}$ products, in which the I and I^- photofragments are trapped by the solvent atoms and eventually recombine, versus "uncaged" $I^-(Ar)_{m2<n}$ products in which trapping does not occur. Only uncaged products are observed from the photodissociation of $I_2^-(Ar)_6$, with ArI^- as the dominant product, indicating that there are not enough solvent atoms to trap the recoiling photofragments. In contrast, the solvent shell is approximately complete for $I_2^-(Ar)_{20}$ so that only caged products are seen. Moreover, photodissociation of $I_2^-(Ar)_{20}$ results in two distinct recombination channels formed with approximately equal yield: bare I_2^- and $I_2^-(Ar)_n$ with $\langle n \rangle = 11$. The time-resolved experiments on $I_2^-(Ar)_{20}$ yield a

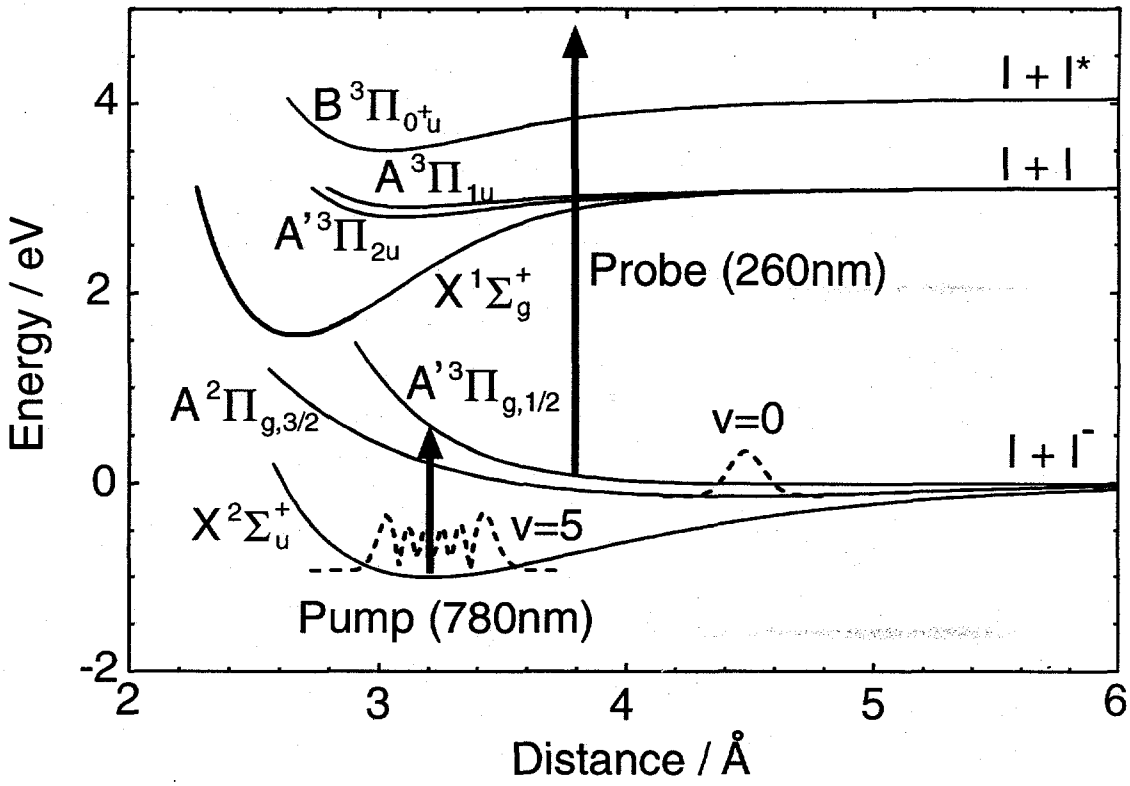

Figure 1. Potential energy curves for the low-lying electronic states of I_2^- and I_2. The curves for the I_2^- $\tilde{X}\ ^2\Sigma_u^+$ and $\tilde{A}'\ ^2\Pi_{g,1/2}$ states are taken from Refs. (15)and (14), respectively. For the $\tilde{X}$ state, D_e=1.01 eV and R_e=3.205 Å. The $\tilde{A}\ ^2\Pi_{g,3/2}$ state is described in the text. The v=0 and v=5 wavefunctions on the I_2^- $\tilde{X}$ and $\tilde{A}$ states are also shown (see text). The I_2 curves are from Ref. (16) and references therein.

time constant of 127 ps for recovery of the I_2^- absorption(12); this represents the overall time scale for recombination and relaxation of the I_2^- product. Our experiment provides a more complete picture of the dynamics following excitation of $I_2^-(Ar)_6$ and $I_2^-(Ar)_{20}$, and in particular clarifies the origin of the two product channels seen for $I_2^-(Ar)_{20}$.

2. Experimental

The FPES experiment is described in detail elsewhere(6). Briefly, a pulsed, mass-selected beam of cold cluster anions is intercepted by the pump and probe pulses at the focus of a "magnetic bottle" time-of-flight PE spectrometer. The two laser pulses are generated by a Ti:sapphire oscillator/regenerative amplifier system (Clark MXR) operating at a repetition rate of 500 Hz. The pump pulse at 780 nm and the probe pulse at 260 nm are 80 and 100 fs long, respectively. The high laser repetition rate combined with the high (>50%) collection efficiency of the magnetic bottle analyzer results in rapid data acquisition; each spectrum is typically obtained in 40 to 80 s for I_2^- and $I_2^-(Ar)_6$, and 10 to 15 minutes for $I_2^-(Ar)_{20}$. At the ion beam energy used in this work (1750 eV), the electron energy resolution of the spectrometer at 1 eV electron kinetic energy (eKE) is 0.25 eV for I_2^-, 0.18 eV for $I_2^-(Ar)_6$, and 0.12 eV for $I_2^-(Ar)_{20}$.

The relevant potential energy curves for I_2^- and I_2 are shown in Fig. 1(14, 15, 16). The pump pulse excites the $\tilde{A}'\ ^2\Pi_{g,1/2} \leftarrow \tilde{X}\ ^2\Sigma_u^+$ transition in I_2^-, creating a localized wavepacket on the repulsive excited state. The probe pulse detaches the dissociating ion to the various low-lying states of I_2 shown in Fig. 1. In the bare ion, rapid and direct dissociation to $I^- + I(^2P_{3/2})$ occurs. However, when the same I_2^- transition is excited in an $I_2^-(Ar)_n$ cluster, the recoiling fragments interact with the Ar atoms, and the FPES experiment provides a sensitive probe of these interactions.

3. Results

Fig. 2 shows selected PE spectra at various pump-probe delay times τ for I_2^-, $I_2^-(Ar)_6$ and $I_2^-(Ar)_{20}$. The spectra of I_2^- in Fig. 2a have been discussed in detail previously(6). Two peaks centered at eKE = 1.70 eV and 0.75 eV rise monotonically

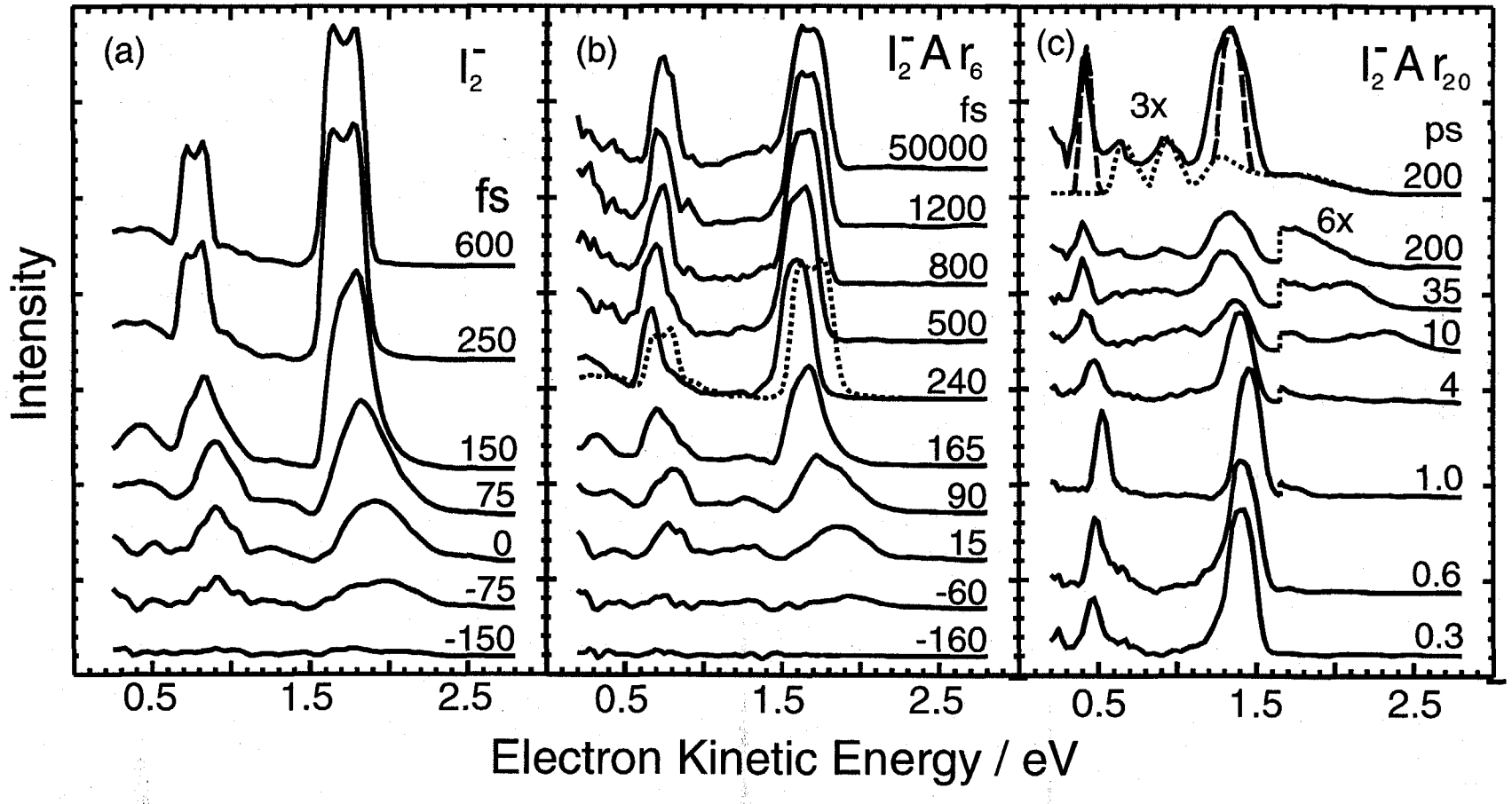

Figure 2. Anion femtosecond photoelectron spectra at various pump-probe delay times τ for (a) I_2^-, (b) $I_2^-(Ar)_6$, and (c) $I_2^-(Ar)_{20}$. In Fig. 2b, the I_2^- spectrum at 250 fs is superimposed on the $I_2^-(Ar)_6$ spectrum at 240 fs for comparison. In Fig 2c, the signal at eKE > 1.6 eV is magnified by a factor of 6 for $\tau \geq 1$ ps. A simulation of the $I_2^-(Ar)_{20}$ spectrum at 200 ps is superimposed on the experimental spectrum at the top of Fig. 2c. Contributions to the simulation from transitions originated from the I_2^- $^2\Pi_{3/2}$ state (···) and $^2\Pi_{1/2}$ state (---) are indicated.

with increasing delay; these correspond to photodetachment of the I^- photodissociation product to the $I(^2P_{3/2})$ and $I^*(^2P_{1/2})$ atomic states, respectively. In addition, there is a transient signal peaking at τ=50-100 fs on the high electron energy side of each product peak attributed to the dissociating ions. The product peaks dominate the spectra by 200 fs, and no further changes are observed at later times, indicating dissociation is complete.

The $I_2^-(Ar)_6$ spectra in Fig. 2b resemble the I_2^- spectra at first glance, particularly for τ<240 fs. By τ=240 fs, the spectra for $I_2^-(Ar)_6$ consist of two peaks clearly analogous to the atomic I←I^- transitions in the I_2^- spectra. However, these two "I^-" peaks occur at 0.12 lower eKE than for bare I^-. In addition, they gradually shift toward 0.10 eV higher eKE as τ increases from 240 to 1200 fs. The spectra do not change after τ=1200 fs.

The spectra for $I_2^-(Ar)_{20}$ in Fig. 2c show the same general trends up to τ=1 ps. Two new trends are seen at later times, however. First, as τ increases from 1 to 35 ps, the two "I^-" peaks apparently reverse direction and shift toward lower eKE by about 0.14 eV. Second, a new, broad feature at high electron energy (eKE>1.6 eV) appears at τ>4 ps. This feature shifts toward lower eKE until τ=200 ps, after which no further significant evolution occurs. Two small peaks between the two "I^-" peaks also grow in on this time scale.

4. Discussion

The $I_2^-(Ar)_6$ spectra indicate that the dynamics subsequent to photoexcitation can be divided into two time regimes. At early times ($\tau \leq 240$ fs), the I_2^- chromophore dissociates to I^- + I. The similarity between these spectra and those for I_2^- indicates that the primary bond-breaking dynamics are not affected by clustering, and that this process is complete by 240 fs. The interpretation of the spectra in the second time regime, from 240 to 1200 fs, is aided by our previous measurements of the electron affinities of $I(Ar)_n$ clusters, which show that each Ar atom increases the electron affinity by ~ 25 meV (17). The 0.12 eV energy offset in the "I^-" peaks at 240 fs relative to bare I^- is what would be expected for an I^- ion bound to 5 Ar atoms. As τ increases, the shifts of these peaks toward higher eKE indicate that the I^- is interacting with progressively fewer Ar atoms.

The spectrum at 1200 fs is that expected for ArI^-; this is consistent with the mass-resolved experiments(11) that show ArI^- to be the dominant product from $I_2^-(Ar)_6$ photodissociation. Thus, the evolution of the spectra from 240 to 1200 fs reflects the progressively weaker interactions between the solvent atoms and the I^- fragment, with formation of the asymptotic ArI^- product complete by 1200 fs.

One picture of the dynamics during the second time regime consistent with the spectra is that once the I_2^- chromophore is dissociated, the neutral I atom is ejected, leaving behind a vibrationally hot $I^-(Ar)_n$ cluster from which Ar atoms evaporate until the available energy is dissipated, with ArI^- as the stable product. This picture is suggested by molecular dynamics simulations carried out by Amar(18) on $Br_2^-(CO_2)_n$ clusters. However, recent molecular dynamics simulations by Faeder *et al.*(19, 20) suggest a somewhat different mechanism. Their calculations predict that the equilibrium geometry of $I_2^-(Ar)_6$ is an open, highly symmetric structure consisting of a ring of Ar atoms lying in the plane that bisects the I_2^- bond. When the I_2^- is dissociated, the I and I^- fragments separate sufficiently rapidly so that the Ar atoms do not cluster around the I^- fragment. Instead, the departing I^- fragment abstracts one of the solvent atoms, on average, as the cluster breaks up. The shifts in the PE spectrum during the second time regime are qualitatively consistent with this picture, in that as the I^- fragment leaves the cluster, its attractive interactions with the solvent atoms decrease and the electron affinity drops.

We next consider the $I_2^-(Ar)_{20}$ clusters, for which caging is complete(11). The overall appearance and evolution of these spectra from 300 fs to 1 ps is similar to that seen for $I_2^-(Ar)_6$, in that there are two "I^-" peaks that shift towards higher electron energy as τ increases. Thus, up to τ=1 ps, the cluster contains I and I^- fragments that are essentially independent of one another. The shifting of the peaks towards higher eKE can again be explained as a progressive weakening of the interactions between the I^- fragment and the solvent atoms. This is probably due to a combination of evaporation of solvent atoms induced by the recoil energy of the I and I^- fragments (~ 0.6 eV), and the rather large excursions that the I^- fragment makes within the cluster as the I and I^- photoproducts separate on the repulsive $\tilde{A}'\ ^2\Pi_{g,1/2}$ state. Molecular dynamics

simulations by Batista and Coker(21) predict the inter-iodine separation increases to 8-10 Å after 1 ps has elapsed, a distance comparable to the original size of the cluster, and it is likely that the strength of the solvent interactions with the I^- decreases while this occurs.

The evolution of the $I_2^-(Ar)_{20}$ spectra at later times can be explained as a result of recombination of the I and I^- on the two lowest potential energy curves in Fig. 1. The shifting of the two "I^-" peaks towards lower energy from τ=1 to 35 ps is consistent with recombination and vibrational relaxation on the $\tilde{A}\ ^2\Pi_{g,3/2}$ curve. Recent ab initio calculations predict that $R_e = 4.18$ Å and D_e=0.11 eV for this state(22). Fig. 1 shows that at such a large internuclear distance, photodetachment will access the neutral potential energy curves near their asymptotic energies. This will yield two peaks approximately separated by the I atom spin-orbit splitting, but shifted toward lower electron energy compared to bare I^- by the well depth (D_e) of the $\tilde{A}\ ^2\Pi_{g,3/2}$ state and the sum of the attractive interactions with the remaining Ar atoms. If we use an approximate binding energy of 73 meV/Ar (11), the total energy released by the recoiling photofragments and by vibrational relaxation of the I_2^- to the v=0 level of the *ab initio* $\tilde{A}\ ^2\Pi_{g,3/2}$ state is sufficient to evaporate 9 Ar atoms, so this excited state recombination mechanism is the likely origin of the $I_2^-(Ar)_{<n>=11}$ product seen by Lineberger and co-workers. From these considerations, it is reasonable to attribute the signal at eKE>1.6 eV to recombination on the $\tilde{X}\ ^2\Sigma_u^+$ state followed by vibrational relaxation. This can release enough energy to evaporate all of the Ar atoms, leaving $I_2^-(v=8)$ in the limit of zero photofragment KE.

In order to test these assignments, the spectrum at 200 ps was simulated assuming photodetachment to occur from $I_2^-(Ar)_{11}$ with the I_2^- chromophore in the v=0 level of the $\tilde{A}\ ^2\Pi_{g,3/2}$ state, and from $I_2^-(\tilde{X}\ ^2\Sigma_u^+)$ in a mixture of vibrational levels. The simulations involve calculating the Franck-Condon factors between the anion and neutral vibrational wave functions and scaling the results for different electronic transitions to best match the experimental intensities. For the $\tilde{A}\ ^2\Pi_{g,3/2}$ state, R_e and D_e were taken to be 4.5 Å and 0.16 eV, respectively, with both values differing somewhat from the ab initio values; these differences may reflect in part the influence of the remaining Ar atoms in the

cluster. Best results for the $\tilde{X}\ ^2\Sigma_u^+$ state were obtained using a vibrational distribution with <v>=5. The results, shown in Fig. 2c, reproduce the experimental spectrum quite well. The $I_2^-(\tilde{A}\ ^2\Pi_{g,3/2}, v=0)$ and $I_2^-(\tilde{X}\ ^2\Sigma_u^+, v=5)$ vibrational wave functions are superimposed on the appropriate potential energy curves in Fig. 1. Note that photodetachment from the inner turning point of the $I_2^-(\tilde{X}\ ^2\Sigma_u^+, v=5)$ wave function is responsible for the signal at eKE > 1.6 eV; the outer turning point contributes to the "I⁻" peak at 1.35 eV along with photodetachment from the $I_2^-(\tilde{A}\ ^2\Pi_{g,3/2})$ state.

The shifting of the signal at eKE > 1.6 eV toward lower energy from 10-200 ps is attributed to vibrational relaxation of the ground state I_2^- accompanied by evaporative cooling of the Ar atoms, that is a series of reactions of the type $I_2^-(v'')Ar_n \rightarrow I_2^-(v'<v'')Ar_{n-1}+Ar$. As the I_2^- vibrational quantum number decreases, the contribution to the PE spectrum from the inner turning point of the vibrational wavefunction shifts towards lower eKE. Although this is partially compensated by the lowering of the electron affinity as Ar atoms evaporate, our simulations of the PE spectra show a net shift of the signal in this region towards lower eKE as the cluster cools. By comparing these simulations with the experimental spectra, and starting with the I_2^- vibrational distribution at 200 ps, one can estimate the average number of Ar atoms <n> and I_2^- vibrational quantum number <v> for τ<200 ps. We find that <n>=2, <v>=17 at τ=35 ps, and <n>=4.5, <v>=32 at τ=10 ps. It therefore appears that 15 or 16 of the original 20 solvent atoms evaporate in the first 10 ps, and that the evaporation rate slows down markedly at later times.

5. Conclusions

Our spectra yield the following picture of the dynamics resulting from photoexcitation of $I_2^-(Ar)_{20}$. As with I_2^- and $I_2^-(Ar)_6$, dissociation of the I_2^- chromophore is complete by 300 fs. Between 300 fs and 1 ps, the interaction between the I and I⁻ atoms within the cluster is very weak. After 1 ps, the I and I⁻ atoms recombine on either of the two lower-lying attractive potential energy surfaces. Recombination on the

$\tilde{A}\ ^2\Pi_{g,3/2}$ state leads to $I_2^-(Ar)_{<n>=11}$ product in which the I_2^- is vibrationally cold, whereas recombination aon the $\tilde{X}\ ^2\Sigma_u^+$ state results in bare I_2^- with $<v>=5$. The first process is complete by 35 ps, whereas the second, involving considerably more energy flow between the I_2^- and the solvent atoms, is over after 200 ps. Although recombination on the $\tilde{A}\ ^2\Pi_{g,3/2}$ state was proposed as a possible mechanism in Lineberger's earlier study(11), our experiments provide conclusive spectroscopic evidence that this occurs.

6. Acknowledgements

This research is supported by the National Science Foundation under Grant No. CHE-9404735. Support from the Defense University Research Instrumentation Program under Grant No. F49620-95-1-0078 is also gratefully acknowledged. The authors thank J. Faeder, P. Maslen, V. Batista, and R. Parson for helpful discussions and for providing access to unpublished results. We are grateful to R. J. Le Roy for a copy of RKR1: A Computer Program for Implementing the First-Order RKR Method for Determining Diatom Potential Energy Curves from Spectroscopic Constants.

7. References

1. A. H. Zewail, *J. Phys. Chem.* **100**, 12701 (1996).
2. P. L. Houston, *J. Phys. Chem.* **100**, 12757 (1996).
3. M. H. Head-Gordon, *J. Phys. Chem.* **100**, 13213 (1996).
4. G. C. Schatz, *J. Phys. Chem.* **100**, 12839 (1996).
5. A. W. Castleman, K. H. Bowen, *J. Phys. Chem.* **100**, 12911 (1996).
6. B. J. Greenblatt, M. T. Zanni, D. M. Neumark, *Chem. Phys. Lett.* **258**, 523 (1996).
7. D. R. Cyr, C. C. Hayden, *J. Chem. Phys.* **104**, 771 (1996).
8. P. Ludowise, M. Blackwell, Y. Chen, *Chem. Phys. Lett.* **258**, 530 (1996).
9. A. Assion, M. Geisler, J. Helbing, V. Seyfried, T. Baumert, *Phys. Rev. A* **54**, R4605 (1996).
10. J. M. Papanikolas, et al., *J. Chem. Phys.* **99**, 8733 (1993).
11. V. Vorsa, P. J. Campagnola, S. Nandi, M. Larsson, W. C. Lineberger, *J. Chem. Phys.* **105**, 2298 (1996).

12. V. Vorsa, S. Nandi, P. J. Campagnola, M. Larsson, W. C. Lineberger, *J. Chem. Phys.* **106**, 1402 (1997).

13. Q. Liu, J.-K. Wang, A. H. Zewail, *Nature* **364**, 427 (1993).

14. E. C. M. Chen, W. E. Wentworth, *J. Phys. Chem.* **89**, 4099 (1985).

15. M. T. Zanni, T. Taylor, B. J. Greenblatt, D. M. Neumark, (unpublished results).

16. D. R. T. Appadoo, et al., *J. Chem. Phys.* **104**, 903 (1996).

17. I. Yourshaw, Y. X. Zhao, D. M. Neumark, *J. Chem. Phys.* **105**, 351 (1996).

18. L. Perera, F. G. Amar, *J. Chem. Phys.* **90**, 7354 (1989).

19. J. Faeder, N. Delaney, P. E. Maslen, R. Parson, *Chem. Phys. Lett.* (in press).

20. J. Faeder, R. Parson, (to be published).

21. V. S. Batista, D. F. Coker, *J. Chem. Phys.* (in press).

22. P. E. Maslen, J. Faeder, R. Parson, *Chem. Phys. Lett.* **263**, 63 (1997).

Chapter 8. Photodissociation of gas phase I_3^- using femtosecond photoelectron spectroscopy[†]

The photodissociation dynamics of gas phase I_3^- following 390 nm excitation are studied using femtosecond photoelectron spectroscopy. Both I^- and I_2^- photofragments are observed; the I_2^- exhibits coherent oscillations with a period of 550 fs corresponding to ~0.70 eV of vibrational excitation. The oscillations dephase by 4 ps and rephase at 45 and 90.5 ps on the anharmonic I_2^- potential. The gas phase frequency of ground state I_3^- is determined from oscillations in the photoelectron spectrum induced by resonance impulsive stimulated Raman scattering. The dynamics of this reaction are modeled using one- and two-dimensional wavepacket simulations from which we attribute the formation of I^- to three body dissociation along the symmetric stretching coordinate of the excited anion potential. The photodissociation dynamics of gas phase I_3^- differ considerably from those observed previously in solution both in terms of the I_2^- vibrational distribution and the production of I^-.

1. Introduction

Chemical reactions in the gas phase can now be probed by an impressive arsenal of frequency and time-resolved methods, leading to a detailed characterization of asymptotic product distributions and short-time transition state dynamics. It is of considerable interest to understand how the dynamics of even the simplest of chemical

---

[†] Originally published in *Laser Techniques for State-Selected and State-to-State Chemisry IV*, Proc. SPIE **3271**, 196 (1998) and J. Chem. Phys. **111**, 2991 (1999).

reactions is altered when the reaction is initiated in a liquid. The reaction coordinate near the transition state can be modified significantly for reactions in liquids,[1] and solvent friction near the transition state can also play an important role.[2] The rapid relaxation processes that occur in liquids have hindered the comparison of gas and liquid phase reaction dynamics. However, the development of ultrafast pump-probe laser techniques now enables one to initiate reactions and probe the products on a sub-100 fs time scale, thereby in principle yielding nearly nascent product distributions that can be compared to gas phase results.

Thus far, only one comparison of this type has been made for a reaction yielding molecular products, namely the photodissociation reaction $HgI_2 \rightarrow HgI + I$, which was studied in the gas phase and in ethanol by Zewail[3-6] and Hochstrasser,[7-10] respectively. During the last few years, a series of femtosecond time-resolved experiments on the photodissociation of I_3^- in ethanol solution have been performed in the laboratories of Ruhman[11-16] and, more recently, Vohringer,[17-19] that have yielded the vibrational distribution of the I_2^- photoproduct within a few hundred fs of the photodissociation pulse through the observation of vibrational coherences. However, until very recently,[20,21] no gas phase data were available for this reaction. In this paper, we report a gas phase photodissociation study of the I_3^- anion using femtosecond photoelectron spectroscopy (FPES) which allows a direct comparison with the liquid phase results.

The spectroscopy and dynamics of I_3^- have been studied extensively in solution. Its absorption spectrum consists of two broad bands centered at 360 and 290 nm.[22-28] The spectral assignment of these bands has been somewhat controversial,[23-25] although the solution phase work has shown that excitation into either band results in dissociation

to ground state I_2^- anions.[12,17] The resonance Raman spectrum of I_3^- reveals a long progression of the symmetric stretch,[26,27,29] indicating that at least the initial motion on the excited state is along this coordinate. However, some intensity in the antisymmetric stretch was also seen; this has been attributed to symmetry breaking of the linear triatomic by the solvent.[29,30]

In the work most relevant to that presented here, Banin *et al.*[12,13] performed femtosecond transient absorption spectroscopy measurements on I_3^- in ethanol, in which the anion was excited at 308 nm and the resulting time-dependent absorption was monitored at a series of wavelengths. They observed coherently vibrating I_2^- anions in their $\tilde{X}\,^2\Sigma_u^+$ state as early as 500 fs after the initial excitation. At this time the I_2^- products are in an average vibrational state of $\langle v \rangle = 12$, and the coherent motion is irreversibly lost within 4 ps due to interactions with the solvent molecules. Coherences due to ground state I_3^- were also observed with a frequency of 111 cm^{-1} and attributed to excitation via resonance impulsive stimulated Raman scattering (RISRS). No evidence for I^- production was seen, even though dissociation to $I^- + I_2$ is energetically favored with respect to $I_2^- + I$ by ~0.6 eV. More recently, Kuhne and Vohringer have performed similar experiments involving excitation of the lower band at 400 nm[17,18] and the blue edge of the upper band at 266 nm.[19] They also observed coherences due to vibrationally excited I_2^- products ($\langle v \rangle = 12$) and oscillating I_3^- parent molecules. In addition, their work at 266 nm showed indirect evidence for I^- photoproducts with a 20% yield.

Only a few studies of gas phase I_3^- have been performed. Do *et al.*[20] have measured the bond strength of ground state I_3^- through collision-induced dissociation in a tandem mass spectrometer, obtaining a value of 1.31±0.06 eV for dissociation to $I_2 + I^-$

products. This is 300 meV larger than previously reported.[31] Our group has reported a preliminary investigation of I_3^- photodissociation using FPES.[21] In addition, we have measured a high resolution (8-10 meV) photoelectron spectrum of I_3^-,[32] as well as the photofragment kinetic energy release from I_3^- photodissociation at a series of wavelengths. [33]

In this study, FPES was used to study the photodissociation dynamics of gas phase I_3^- following excitation of the lower absorption band at 390 nm, allowing a detailed comparison between the gas and condensed phase dynamics. In the FPES experiment, I_3^- is electronically excited with a femtosecond pump pulse. The resulting nonstationary state is photodetached by a femtosecond probe pulse and the photoelectron spectrum is measured. By performing this experiment at a series of pump-probe delay times one obtains a progression of snapshots detailing the dynamics induced by the pump pulse. As in the solution phase experiments, we observe coherently vibrating I_3^- anions caused by a RISRS process as well as coherent, vibrationally excited I_2^- photoproducts. The I_2^- vibrational distribution, however, is centered at significantly higher vibrational levels than in solution and exhibits rephasing dynamics. We also observe the formation of I^- product, which was not seen in the condensed phase studies at 308 and 400 nm.

2. Experimental

The FPES experiment consists of two major components: a negative ion photoelectron spectrometer with high collection efficiency and a high repetition rate femtosecond laser. Each has been described in detail elsewhere[34,35] and will only be briefly described below.

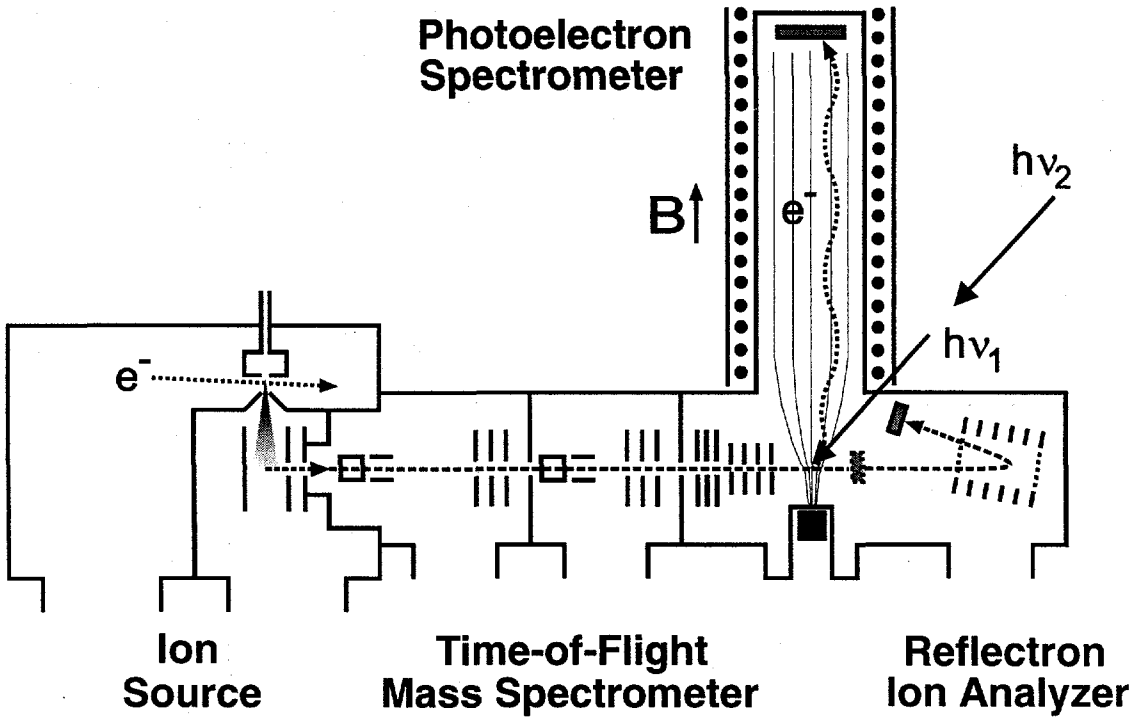

Figure 1. Schematic of apparatus showing ion source region, time-of-flight mass spectrometer, photofragment reflection assembly, and "magnetic bottle" photoelectron time-of-flight spectrometer.

The photoelectron spectrometer, Fig. 1, is designed to be compatible with the high laser repetition rate and the low photoelectron signal expected for a two-photon pump-probe experiment. Argon carrier gas (10 psig) is passed over crystalline I_2 and supersonically expanded through a pulsed piezo electric valve operating at a 500 Hz repetition rate. Anions are generated by a 1 keV electron beam which crosses the expansion just downstream of the nozzle, and are injected into a Wiley-McLaren time-of-flight mass spectrometer by applying pulsed extraction and acceleration fields perpendicular to the molecular beam axis. After passing through several differentially pumped regions, the ions enter the detector chamber and interact with the pump and probe pulses. The ions can either be monitored with a retractable, in-line microchannel plate detector or with a second, off-axis reflectron/microchannel plate assembly to record the photofragment mass spectrum. High electron collection efficiency is achieved with a "magnetic bottle" time-of-flight analyzer[36] whose energy resolution has been optimized using a pulsed decelerator[37,38] applied to the ions just prior to photodetachment. The instrument resolution is approximately 30 meV for an electron kinetic energy (eKE) of 0.8 eV and degrades as approximately $(eKE)^{1/2}$.

The magnetic bottle time-of-flight analyzer is calibrated by a quadratic fit to three peaks: two at 1.76 and 0.77 eV generated by photodetachment of I^- by 260 nm light (corresponding to the $I(^2P_{3/2})$ and $I^*(^2P_{1/2})$ states, respectively), and an additional peak at 0.12 eV from photodetachment of I^- to the $I(^2P_{3/2})$ state by 390 nm light. The calibration is more accurate for electron energies below 0.5 eV than in our previous report using a two-point linear fit.[21]

The pump and probe pulses are generated by respectively doubling and tripling the 780 nm output of a Clark-MXR regeneratively amplified Ti:Sapphire laser system. The energy of the resulting 260 nm (4.77 eV) probe pulse is 20 μJ and its duration is 130 fs FWHM ($sech^2$), the latter measured by difference frequency mixing with the fundamental light at 780 nm. The pulse energy of the pump pulse at 390 nm (3.18 eV) is typically 90 μJ; this pulse is characterized by difference frequency cross correlation with the previously determined probe pulse and has a FWHM of 100 fs. The relative delay between the pump and probe pulses is adjusted with a computer controlled translation stage, and the beams are collinearly recombined and gently focused prior to entering the vacuum chamber. The probe pulse alone has sufficient energy to detach I_3^-, producing a background signal observed in the experiment. By passing the pump beam through a 250 Hz chopper (New Focus, 3501), shot-to-shot background subtraction can be performed, and the electron signal during this time is integrated and used to normalize different scans.

The vacuum chamber window affects the individual pulse widths and the relative delay between the pump and probe pulses. Two-color above-threshold-detachment (ATD) [39] of I^- is used to characterize the pulses and determine the zero-of-time inside the chamber. The probe pulse alone produces a photoelectron spectrum with two peaks at 0.77 and 1.71 eV. When the pump and probe pulses are temporally overlapped, additional peaks are observed that correspond to shifting the I^- peaks by 3.18 eV toward higher eKE, i.e. the photon energy of the pump pulse. From the intensity of this two-color signal as a function of pump-probe delay, we determine the zero-delay time and the

cross-correlation of the pump and probe pulses inside the vacuum chamber. This yields a convoluted FWHM of 175 fs.

3. Results

In this section we present one-color photoelectron spectra of I_3^- taken separately with 390 and 260 nm light. We then present measurements of the photofragment yield upon dissociation with the 390 nm pump pulse, and the time-resolved FPES spectra taken with the combined pump and probe pulses.

3.1 One-color photoelectron spectra

Before considering the two-photon FPES spectra, the effect of the individual pump and probe pulses on the I_3^- anion needs to be determined. Shown in Fig. 2 (solid) is the one-color photoelectron spectrum of I_3^- taken at the probe wavelength, 260 nm (4.77 eV), and plotted as a function of electron kinetic energy (eKE). Two broad, featureless transitions are seen, centered at 0.52 and 0.25 eV. These peaks are assigned to transitions to the ground and first excited electronic states, respectively, of neutral I_3. From the peak centers one obtains the vertical detachment energy (VDE) from

$$\mathrm{VDE} = h\nu - \mathrm{eKE} \qquad (1)$$

This yields VDE's of 4.25 and 4.52 eV, for the small and large peaks, corresponding to the vertical transition energies from the anion to the two neutral electronic states. As discussed elsewhere, the peak at 0.52 eV exhibits vibrational structure at higher resolution and corresponds to a bound state of I_3.[32]

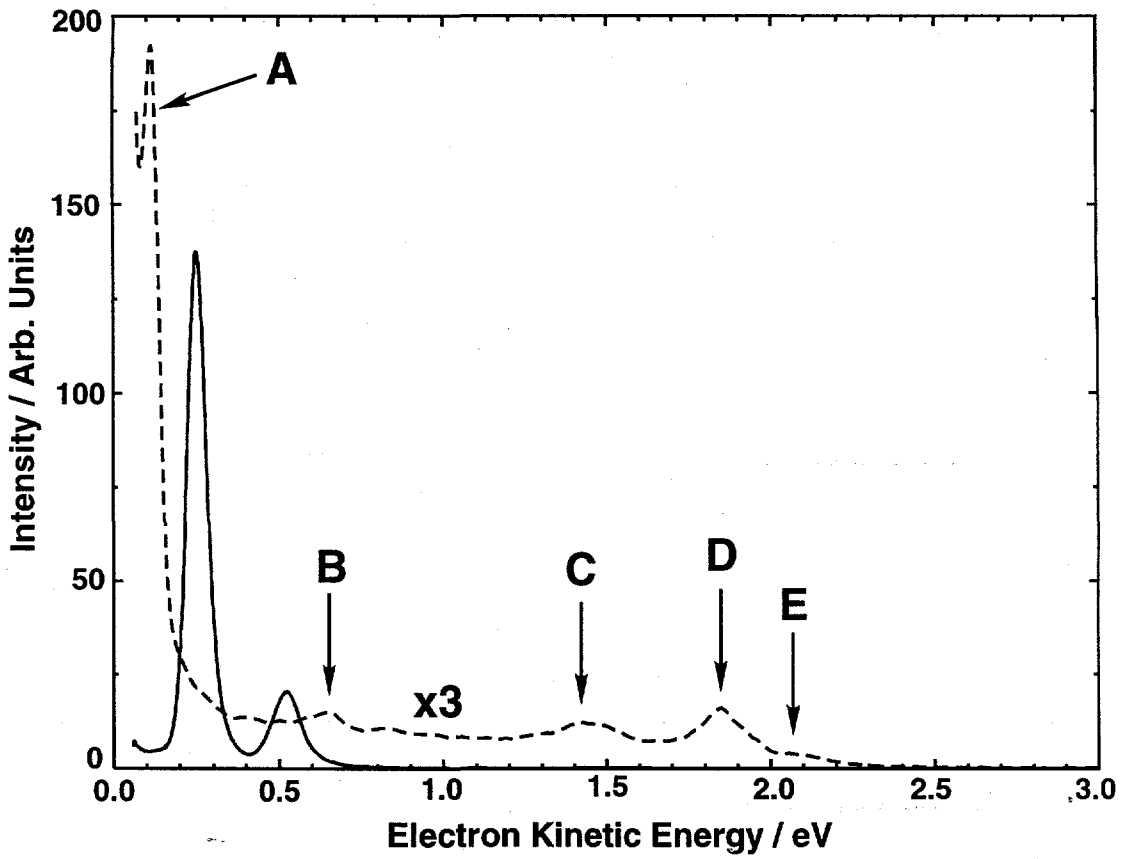

Figure 2. One-color photoelectron spectra of I_3^-. Results from detachment at 260 nm probe (4.77 eV, solid) and 390 nm (3.18 eV, dashed) photon energy are shown.

Also shown in Fig. 2 (dashed) is the photoelectron spectrum measured at the pump wavelength, 390 nm. This spectrum exhibits intensity up to eKE=2.3 eV with peaks centered at 0.12, 0.65, 1.45, 1.85, and 2.09 eV labeled A through E. The presence of features at higher eKE than in the 260 nm spectrum indicates that multiphoton processes are contributing to the 390 nm spectrum. Indeed, when $h\nu$ in Eq. (1) is taken as 6.36 eV (two 390 nm photons), the VDE's of peaks D and E match the VDE's of the two 260 nm bands. Peak A, the most prominent peak in the 390 nm spectrum, is due to photodetachment of I^- to the $I(^2P_{3/2})$ state by one photon of 390 nm light. This peak must also arise from a two-photon process in which one photon dissociates the I_3^- and the second photon detaches the I^- photofragment. Peaks B and C at 0.65 and 1.45 eV presumably arise from two-photon photodetachment to higher lying states of neutral I_3.

3.2 Photofragment Mass Spectroscopy

The photoelectron spectrum at 390 nm indicates that I^- is a photoproduct. To confirm this, the photofragment mass distribution resulting from excitation of I_3^- at 390 nm was determined using the reflectron assembly in our instrument (see Fig. 1). Equal yields of I^- and I_2^- were observed for pump powers ranging over an order of magnitude. Although the pump photon also detaches I^- products, as discussed in the preceding section, the relative yield between I^- and I_2^- does not seem to be affected. A more detailed power study was presented in our earlier report.[21]

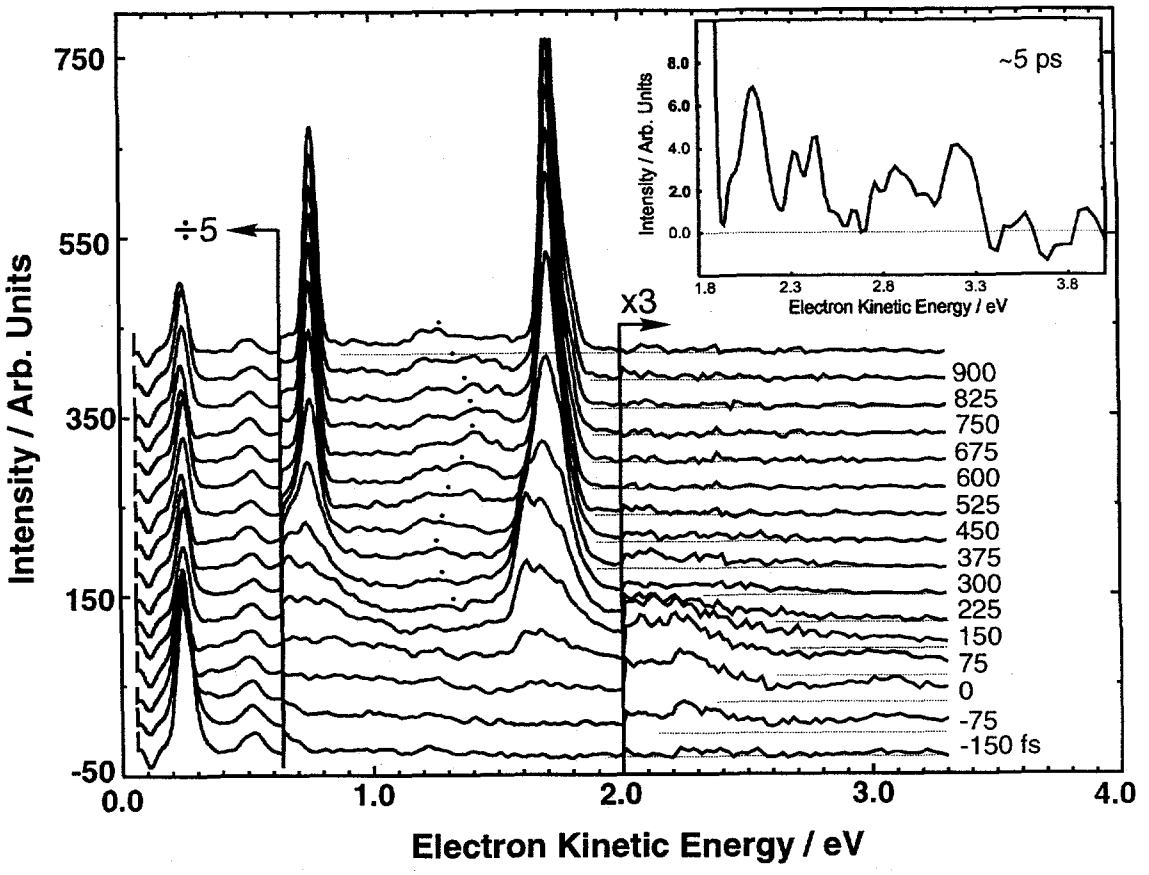

Figure 3. Experimental FPES spectra of I_3^- from –150 to 975 fs in 75 fs steps. Scaling factors for high and low energy ranges are shown, and a baseline for each delay time is marked with a dashed line. The approximate center of the broad feature between 0.8 and 1.6 eV is marked with a dot to show its time evolution. An expanded view of the high energy signal at ~5 ps is displayed in the inset.

3.3 Femtosecond Photoelectron Spectroscopy of I_3^- photodissociation

Fig. 3 shows successive time-resolved, two-photon photoelectron spectra for pump-probe delays of –150 to 975 fs in 75 fs increments. As discussed in Section 2, the background from the probe pulse (260 nm, Fig. 2) has been subtracted through the course of the experiment. Thus, at positive delay times, the background features from the probe pulse would normally be less than zero due to bleaching of the ground state. In Fig. 3, however, a constant fraction of background signal has been added back in to make the spectra positive at all delay times. Likewise, the signal arising from two-photon detachment by the pump pulse alone (390 nm, Fig. 2) has been subtracted to enhance the two-color features.

The spectra follow the same general trends we have observed before on other systems.[40,41] At –150 fs, when the probe pulse comes before the pump pulse, signal due to detachment of the I_3^- by the probe pulse is seen (260 nm, Fig. 2). As the delay time is increased, the pump and probe pulses begin to overlap, and the two I_3^- features decrease in intensity. This is accompanied by the appearance of electron signal at higher eKE, out to ~3.8 eV. Starting at 75 fs, this higher energy signal begins coalescing into two features that eventually become two tall, narrow peaks at 0.77 and 1.71 eV. The intensities of these peaks increase steadily up to about 600 fs, and are split by the spin-orbit splitting of atomic iodine. These features are due to the atomic $I(^2P_{3/2})\leftarrow I^-$ and $I^*(^2P_{1/2})\leftarrow I^-$ transitions, respectively, arising from detachment of I^- photoproduct. Additionally, first apparent at 150 fs, there is signal between 0.9 and 1.6 eV, and low intensity signal out to 3.2 eV; these features are present at the longest delay times probed in our experiments. The low intensity signal from 1.8 to 3.2 eV is displayed in the inset

of Fig. 3, taken at a delay time of ~5 ps. As discussed below, these features result from I_2^- photoproduct.

Overall, Fig. 3 demonstrates how FPES can provide a complete picture of a reaction occurring in real-time. By performing a single measurement (i.e. photoelectron spectroscopy) at each delay time, we observe depletion of I_3^- reactant and the accompanying evolution of the I^- and I_2^- products. We now consider these three aspects of the spectra in more detail.

3.3.1 I_3^- features

In addition to a steady drop in intensity of the two I_3^- features from –150 to 225 fs, close examination of the two bands at 0.25 and 0.52 eV reveals time-dependent oscillations. Figure 4 shows an enlarged view of the lower energy peak, the maximum of which oscillates between 0.24 and 0.25 eV with a 300 fs period. The total intensity of this band also depends on the position of the peak. The intensity is smaller when the peak is centered at low eKE and larger at high eKE; two examples are displayed in the inset of Fig. 4. The periodic nature of the oscillatory motion is seen more clearly in Fig. 5, which shows a cut through the photoelectron spectrum at 0.28 eV from 5 to 30 ps with a step size of 90 fs. This energy exhibits the largest oscillatory amplitude. The inset of Fig. 5 displays the Fourier transform of the time spectrum at 0.28 eV which is dominated by a single frequency at 112±1 cm^{-1}. No higher harmonics are observed.

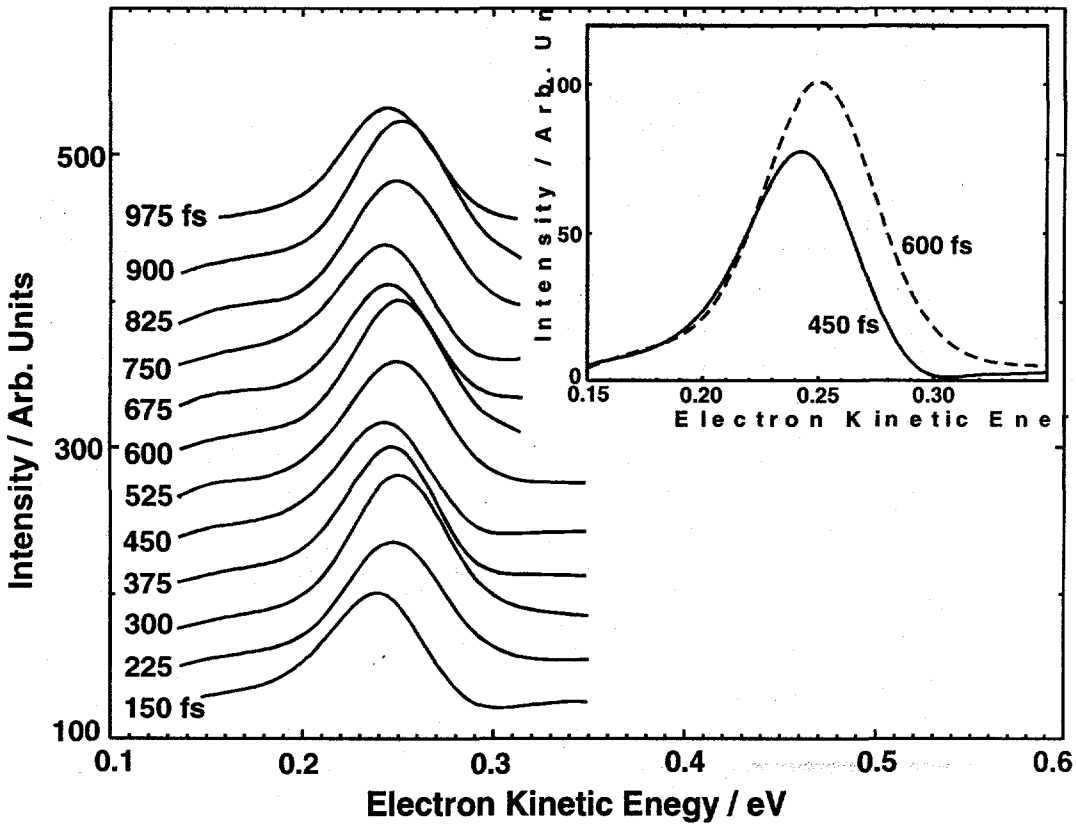

Figure 4. Expanded view of the I_3^- feature at 0.25 eV showing oscillatory motion. The inset overlays the spectra at 450 fs (solid) and 600 fs (dashed) to illustrate the intensity change associated with this oscillation.

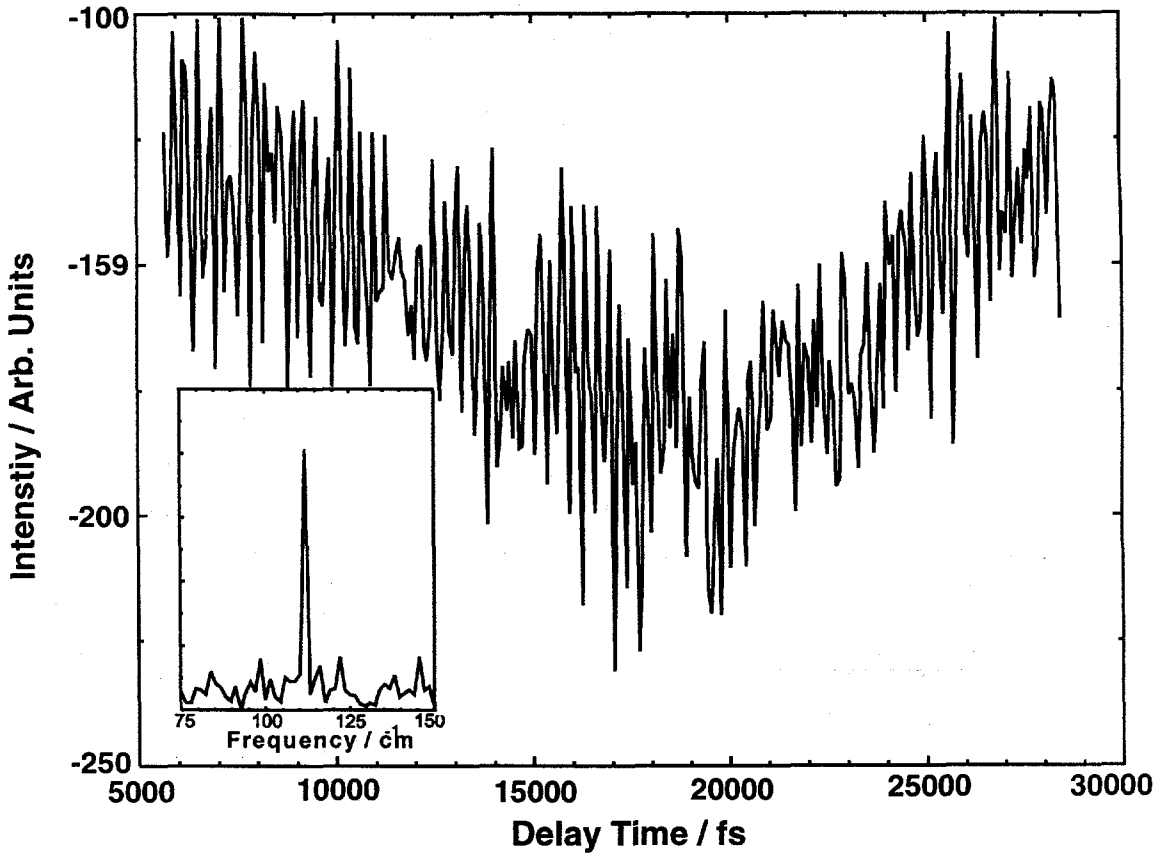

Figure 5. Intensity at 0.28 eV from 5 to 30 ps in 75 fs steps. The inset displays the Fourier transform of this signal which consists of one peak at 112±1 cm^{-1}.

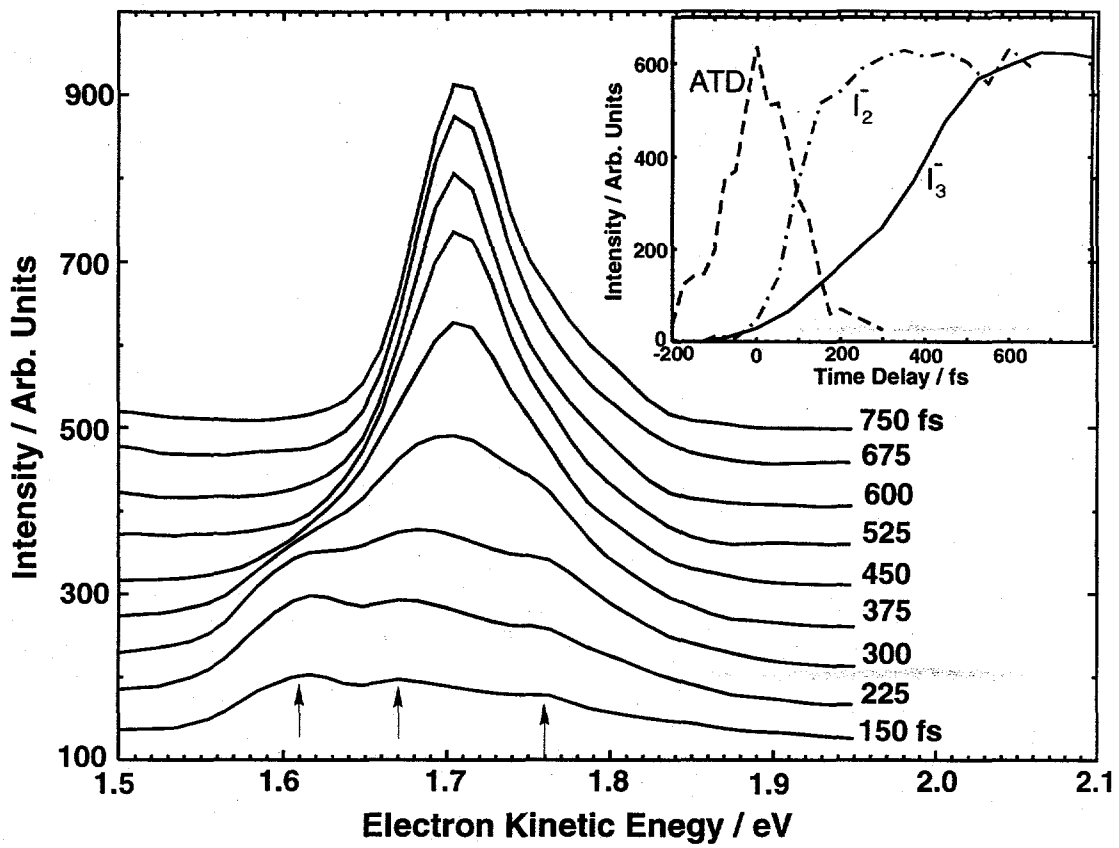

Figure 6. Expanded view of the atomic $I(^2P_{3/2})\leftarrow I^-$ feature at 1.7 eV. Arrows indicate small features that persist for early time delays. Note the dramatic decrease in width beginning at 300 fs. In the inset, the time-dependence of the signal at 1.70 eV is shown (solid). It reaches its half-maximum height by 350 fs. A similar cut for the 390 nm excitation of $I_2^-[I_2^-(^2\Sigma_g^+) \leftarrow I_2^-(\tilde{X}^2\Sigma_u^+; v=0)]$ is shown dot-dashed (see Section 4.2). The convoluted pump-probe width is also shown (dashed), as measured using above threshold detachment on I^-.

3.3.2 Atomic iodine features

Fig. 6 shows an expanded view of the atomic $I(^2P_{3/2})\leftarrow I^-$ feature, which evolves in two distinct steps. From 150-300 fs, a broad band is observed with downward sloping intensity from 1.55 to 1.8 eV that exhibits small features at 1.61, 1.67, and 1.76 eV, marked with arrows. Starting at 300 fs, the entire feature becomes progressively narrower. The shoulder at 1.61 eV drops in intensity and the distribution becomes peaked at 1.71 eV. This transformation continues until approximately 600 fs after which no additional changes are observed.

In the inset of Fig. 6 a cut through the photoelectron spectrum at 1.70 eV (solid) is displayed which provides a measure of I^- production as a function of time. The intensity reaches half of its maximum by 350 fs, although its full height is not reached until 600 fs. Hence, no more I^- is formed after 600 fs. Since the FWHM of the convoluted pump and probe pulses is 175 fs, the formation of I^- occurs long after interaction with the pump pulse has ceased. Similar behavior is seen for the $I^*(^2P_{1/2})\leftarrow I^-$ transition.

3.3.3 Intermediate Energies

The electron signal between 0.9 and 1.6 eV also exhibits oscillatory motion. Discernible beginning at 150 fs with a maximum near 1.4 eV, the intensity shifts to lower eKE and back again, completing a full oscillation by approximately 825 fs. In Fig. 3, a small dot marks the approximate center of intensity at each time delay to emphasize this behavior. The oscillatory motion is shown more clearly in Fig. 7 (solid) where slices at 1.29, 1.41, and 1.54 eV are observed with a period of approximately 550 fs (simulations are shown dashed and will be discussed in Section 4.4). The phase of the oscillations

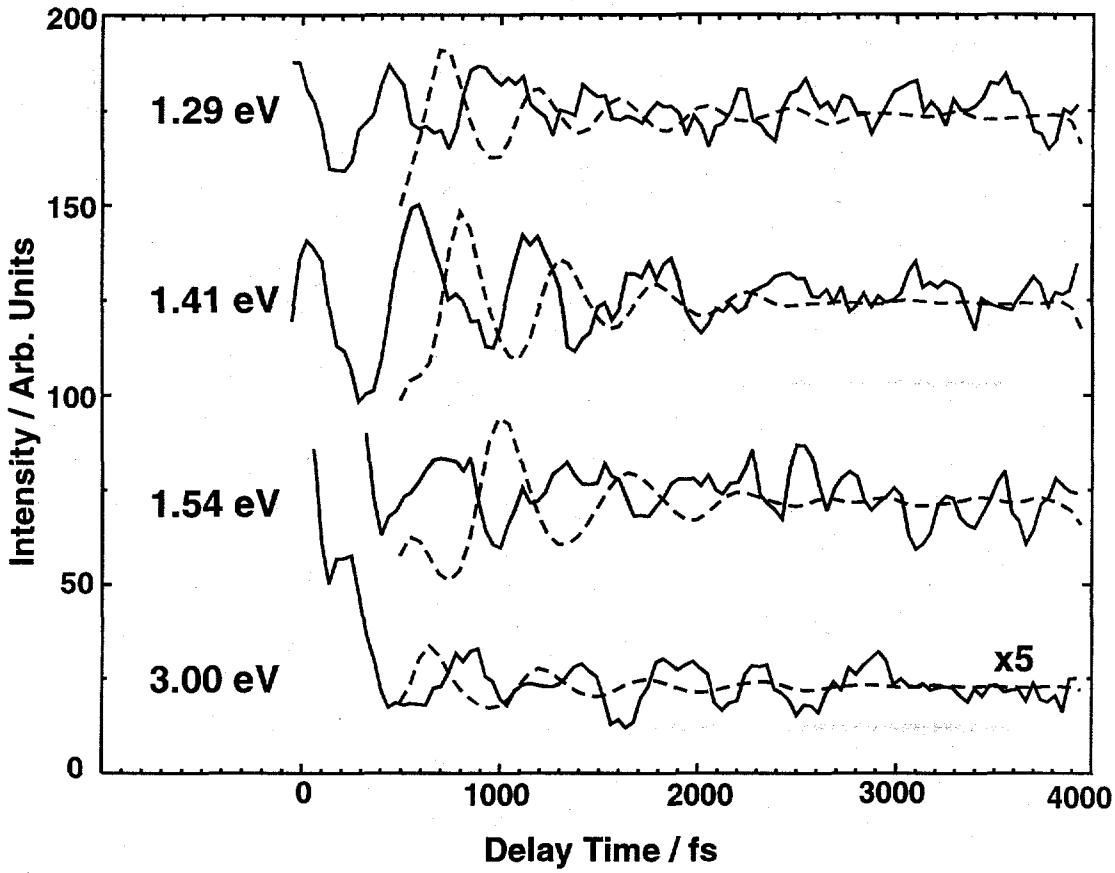

Figure 7. Time dependent signal at several values of eKE from 0 to 4000 fs illustrating the I_2^- product coherences (solid) with ~550 fs period. Simulations (Section IV. D) are also displayed (dashed).

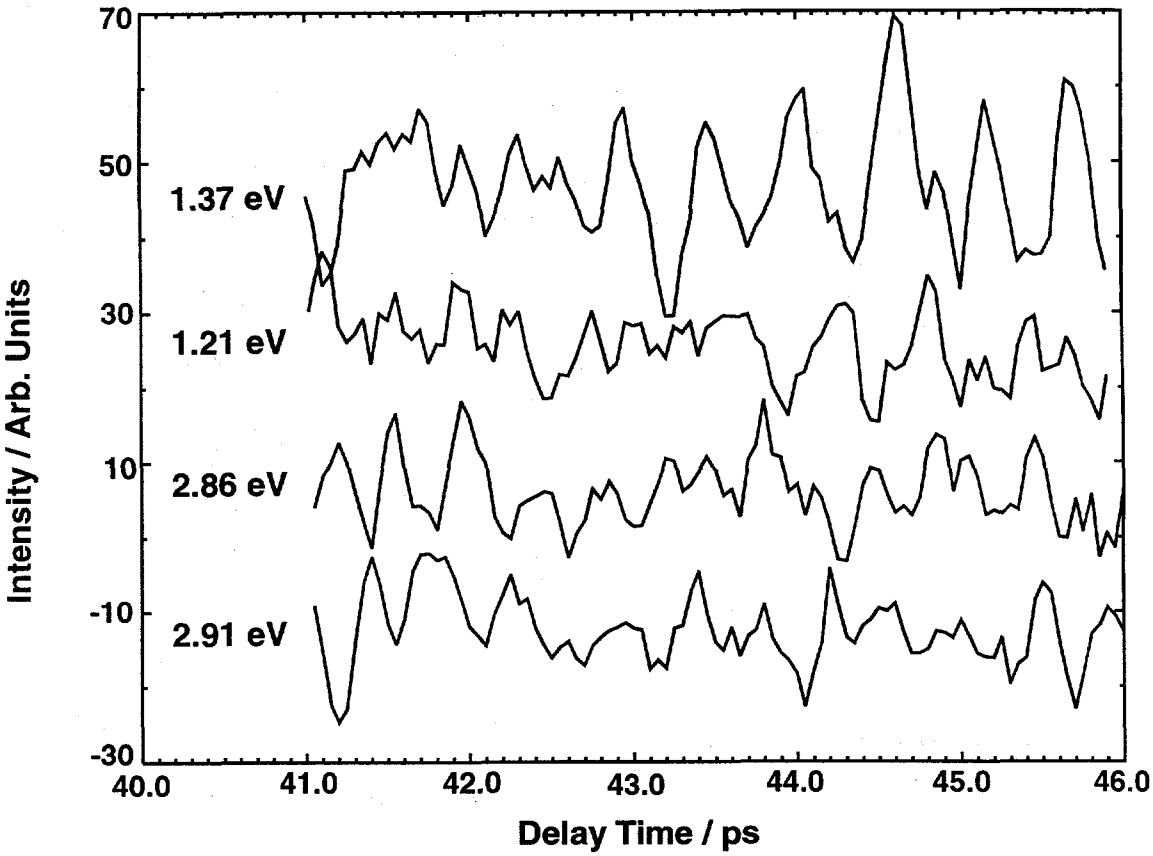

Figure 8. Time dependent signal at from 41 to 46 ps illustrating the I_2^- rephasing dynamics.

shifts with increasing energy until a 180° phase shift is observed between 1.29 and 1.54 eV. The amplitude of the oscillations also varies with energy and is largest at 1.41 eV. Note that at 1.41 eV, the amplitude of the second oscillation is larger than the first. Also shown in Fig. 7 is a slice at 3.00 eV that also exhibits oscillatory motion with the same frequency. These oscillations are of lower intensity and approximately 180° phase shifted from the oscillations appearing around 1.41 eV. At all electron energies the oscillations decay by 4 ps.

Oscillatory structure with the same period reappears at 45 and 90.5 ps. Figure 8 shows slices at 1.21, 1.37, 2.86, and 2.91 eV near 45 ps. At 1.21 and 1.37 eV, the oscillations are approximately 180° out-of-phase, and, likewise, the oscillations at 2.86 and 2.91 eV appear 180° out-of-phase, although they are centered at approximately 42 ps. At 90.5 ps, large oscillations are again observed (not shown).

4. Analysis and Discussion

In a similar fashion to Section 3, the analysis and discussion proceeds along three lines: analysis of the I_3^- bands at 0.31 and 0.55 eV, the origin of the atomic I^- features at 1.71 and 0.77 eV, and discussion of the nature of the oscillatory structure from 0.9 to 1.6 eV.

4.1 I_3^- coherences

In the FPES experiment, the pump pulse promotes I_3^- to the first excited state on which the reaction takes place. However, as was shown for I_2^-,[42] the pump pulse also creates a coherent superposition of vibrational levels on the ground state potential energy

surface of the anion that can be detected in the time-resolved photoelectron spectra. The process by which this occurs, resonance impulsive stimulated Raman scattering (RISRS), has been well documented in previous femtosecond absorption experiments, [43-47] including the studies of I_3^- in solution.[12,17,19]

In our FPES experiment, RISRS induced by the pump pulse results in modulation of the photoelectron spectrum of the I_3^- ground state. Thus, the oscillations superimposed on the peaks at 0.31 and 0.55 eV can be unambiguously assigned to coherent I_3^- vibrational motion induced by the pump pulse. This point is worth emphasizing; while the frequency associated with these oscillations, 112±1 cm^{-1}, is close to the I_2^- fundamental at 110 cm^{-1}, the photoelectron spectrum of I_2^- occurs at very different eKE values.

The 112 cm^{-1} frequency is assigned to the I_3^- symmetric stretch. This value lies only 1 cm^{-1} to the blue of the solution phase resonance Raman value.[27,48] However, in solution the RISRS oscillations associated with I_3^- decay in approximately 3 ps due to interactions with the solvent molecules. Such interactions are obviously absent in the gas phase and the oscillations are seen to persist indefinitely.

4.2 I^- Photofragments

Our finding of a 50% yield for I^- products based on reflectron measurements is of interest since the formation of atomic I^- was not observed in the solution phase work at 400 and 308 nm.[12,17] However, direct observation of I^- in solution is difficult, as it is a closed-shell species with no low-lying electronic states. In the solution phase studies by Vohringer[19] and Ruhman,[12] the amount of I^- production was indirectly determined at

delay times longer than 10 ps. These studies indicate that at 400 and 308 nm, 100% of the dissociated I_3^- has produced I_2^- products. At 266 nm, however, I_2^- is only produced in an 80% yield. The above studies are in stark contrast to the gas phase work.

It is possible that a multiphoton rather than a single photon process creates I^-. Specifically, vibrationally cold I_2^- in its electronic ground state has a large dissociative cross-section at 390 nm,[49,50] allowing for the possibility of a two-photon excitation to produce I^-:

$$I_3^- \xrightarrow{h\nu} I + I_2^-(^2\Sigma_u^+; v \approx 0) \xrightarrow{h\nu} I + I^- + I \qquad (2)$$

To determine the possible contribution of this process, we performed a power study varying the pump pulse intensity and monitoring the products with the 260 nm probe pulse set at long delay times. Shown in Fig. 9 is the amount of I^- produced over nearly two orders of magnitude in pump power (circles). The highest power corresponds to the conditions used in the experiment and the lowest power produces signal barely above the noise. The observed trend is linear (solid line) over the entire range of intensities, implying that single photon excitation of the I_3^- yields I^- products. It should also be noted that the pump pulse creates and then detaches a small amount of I^-, as was discussed in Section 3.1, in a second order process. This would have the effect of adding quadratic behavior to the power study, effectively decreasing the I^- intensity with increasing pump powers. No noticeable effect is seen, however.

To further preclude the possibility of a multiphoton process, an experiment probing the dynamics associated with the formation of I^- from 390 nm excitation of I_2^-

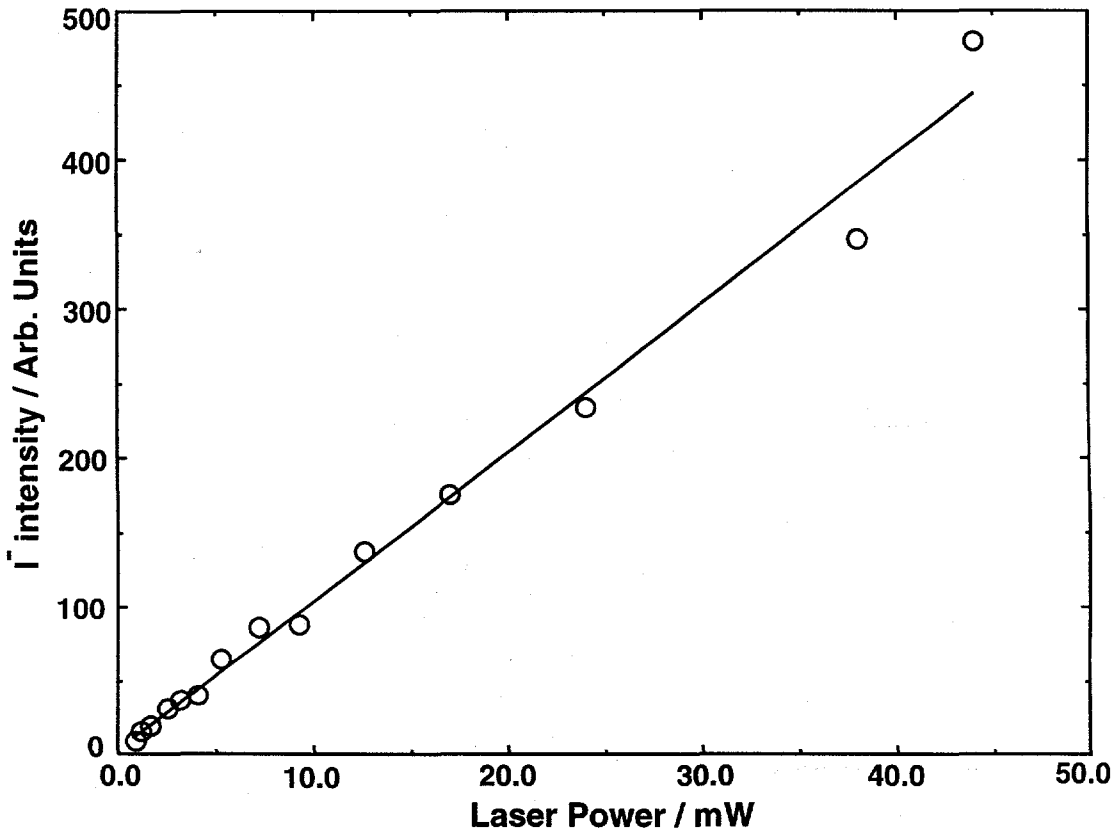

Figure 9. Power study monitoring I^- products versus pump laser power (circles). Linear fit is shown (solid).

was also performed. Shown in Fig. 6 (inset, dot-dashed) is the I^- intensity monitored at 1.7 eV from the $I_2^-(^2\Sigma_g^+) \leftarrow I_2^-(\tilde{X}^2\Sigma_u^+; v=0)$ excitation of I_2^-. It reaches its maximum by 400 fs, in contrast to 600 fs for I^- from I_3^- dissociation (Fig. 6 inset, solid), and displays a much sharper slope than for I_3^-. Although not shown, transient intensities for $I_2^-(^2\Sigma_g^+) \leftarrow I_2^-(\tilde{X}^2\Sigma_u^+)$ never pass below 1.7 eV, whereas in the 390 nm excitation of I_3^-, electron intensity moves to as low as 1.5 eV before peaking at 1.7 eV.

The dissimilarity between the formation of I^- from I_2^- versus I_3^-, as well as the linear trend in the power study makes the multiphoton production of I^- an unlikely process. The most likely reasons that Eq. 2 does not contribute significantly to I^- formation are because the majority of I_2^- products form after the FWHM of the pump pulse and the I_2^- is also highly vibrationally excited, reducing its absorption cross section at 390 nm (see below).

Production of I^- can occur by either a two- or three-body mechanism:

$$I_3^- \xrightarrow{h\nu} I^- + I_2 \qquad (3)$$

$$I_3^- \xrightarrow{h\nu} I^- + I + I \qquad (4)$$

The latter channel can be produced by a concerted three-body dissociation along the symmetric stretch of the potential, or, if the I_3^- first excited state correlates to a dissociative I_2^- potential (all of the excited states of I_2^- are dissociative or very weakly bound[41,51]), a sequential mechanism is also possible:

$$I_3^- \xrightarrow{h\nu} I + I_2^-(^2\Pi_{g,1/2}) \longrightarrow I + I^- + I \qquad (5)$$

Distinguishing among these possible routes of I^- formation is not straightforward. However, the qualitative features of the time-evolution of the $I(^2P_{3/2})\leftarrow I^-$ transition suggest a mechanism following Eq. 4. This will be addressed after a discussion of the oscillatory features at intermediate energies.

4.3 Vibrationally excited, coherent I_2^-

The photofragment mass spectra show that photolysis of I_3^- at 390 nm produces I_2^- in addition to I^-. The only features so far not accounted for in the photoelectron spectrum are the broad features between 0.9 and 1.6 eV and the low intensity signal up to 3.2 eV. Neither feature appears in the photoelectron spectrum of vibrationally cold I_2^-,[42] in which photodetachment to the I_2 ground state yields a single feature centered at 1.6 eV and no intensity above 1.9 eV as shown in Fig. 10. However, photoelectron signal from highly vibrationally excited I_2^- comes primarily from the inner and outer turning points of the anion wavefunction. Fig. 10 shows the $I_2^-(\upsilon=110)$ wavefunction and the simulated photoelectron spectrum from this level. The spectrum consists of two well-separated features that straddle the $I_2^-(\upsilon=0)$ photoelectron spectrum; detachment from the inner turning point of the $\upsilon=110$ wavefunction produces electrons up to 3.2 eV, while detachment from the outer turning point yields a more intense feature between 1.2 and 1.8 eV. Note that the most intense peak around 1.6 eV is from the outermost part of the anion wavefunction. At slightly smaller internuclear distances, the vertical detachment energy increases slightly due to the greater curvature of the anion potential. Hence,

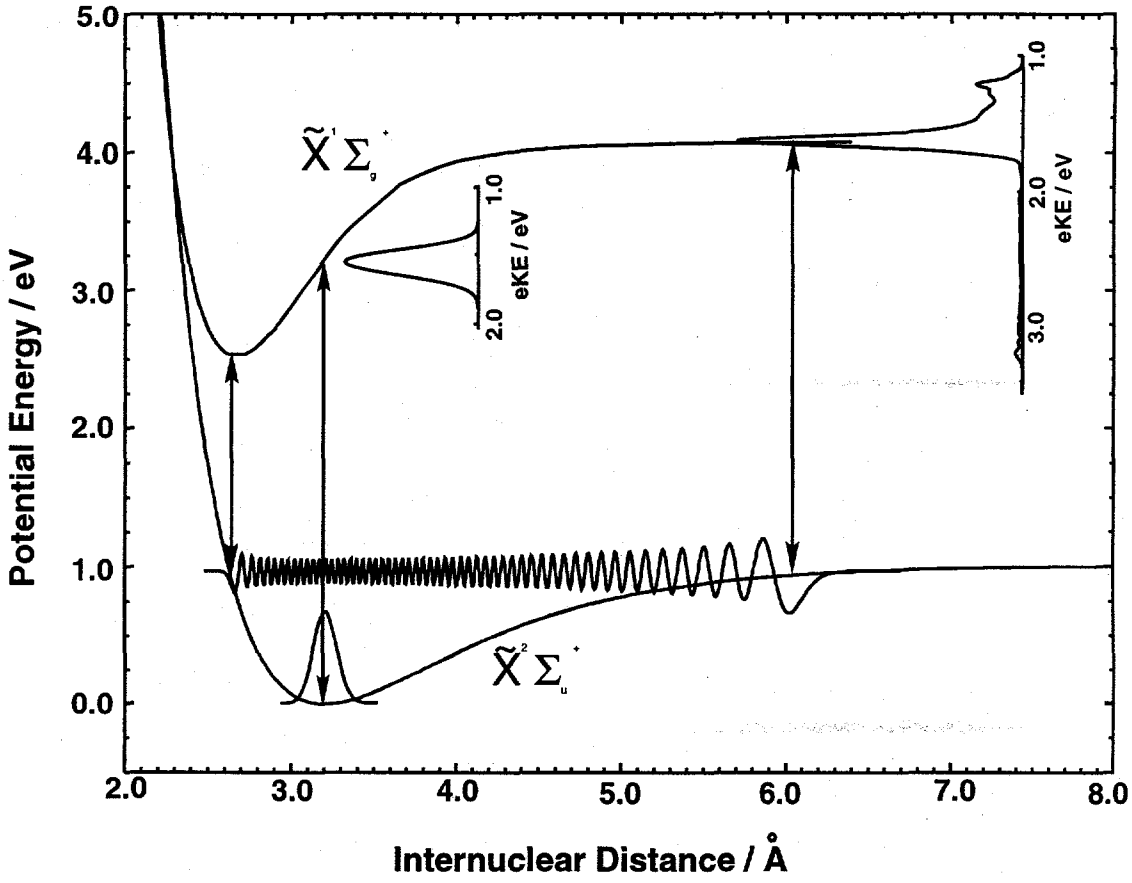

Figure 10. Wavefunctions for υ=0 and 110 on the I_2^- electronic ground state and their corresponding photoelectron spectra. The upper potential is the electronic ground state for I_2. Note that the inner turning point of the υ=110 eigenstate lies directly below the I_2 ground state, and the photoelectron spectrum reaches up to 3.2 eV.

photodetachment from the corresponding section of the anion wavefunction results in slower electrons.

We therefore attribute the remaining features in the experimental spectra to vibrationally excited I_2^-. The oscillations in these features shown in Figs. 7 and 8 must then be due to coherent vibrational motion of the I_2^- photoproduct. Both the maximum observed eKE and the frequency of the vibrational coherences can be used to characterize the I_2^- vibrational distribution.

The maximum vibrational energy of the I_2^- can be directly obtained from the maximum eKE based on the following considerations. The υ=0 wavefunction of I_2 has amplitude from 2.62 to 2.72 Å.[52] If the inner turning point of the I_2^- vibrational wavefunction lies in this range, it will detach directly to υ=0 of the I_2 ground state potential. Since the energy difference between υ=0 of I_2 and υ=0 of I_2^- is well known (EA = 2.52 eV),[42] the vibrational energy can be determined. Thus, for 3.2±0.1 eV electrons (Fig. 3, inset), the energy difference between the inner turning point of the I_2^- wavefunction and υ=0 of the neutral state potential is 1.57±0.1 eV, using Eq. 1. This gives 0.95±0.1 eV for the maximum vibrational energy. For the I_2^- Morse potential in Fig. 10, [42] photodetachment from all vibrational energy levels above 0.55 eV access the $I_2(\upsilon=0)$ state, so our result should be valid. We point out that this analysis directly yields the I_2^- vibrational energy; for the Morse potential in Fig. 10, the corresponding quantum number is 110, but the true quantum number is likely to differ because the Morse function is not very accurate so close to the dissociation limit.

The oscillatory I_2^- features also in Figs. 7 and 8 provide further information on the I_2^- vibrational distribution. Because the I_3^- dissociation is initiated with a laser pulse

shorter than a single period of product vibrational motion, the I_2^- photoproduct can be formed in a coherent superposition of vibrational levels spanning the nascent vibrational distribution. In the best case scenario, all of the frequencies associated with the product vibrational distribution will be in phase at short times and lead to large amplitude wavepacket oscillations which are detected in the FPES experiment. As time progresses the frequencies will dephase from one another due to the anharmonicity of the potential. However, because of the collisionless nature of the gas phase environment, pure dephasing will not play a role and the I_2^- products should rephase at a much later time. Using the I_2^- ground state frequency and anharmonicity (ω_e=110 cm^{-1} and $\omega_e x_e$=0.37 cm^{-1}),[42] the average vibrational state of the products can be determined along with the time at which rephasing might occur.

The 550 fs oscillations seen in the experiment correspond to an approximately 60 cm^{-1} energy difference which indicates a vibrational quantum number of υ=67, or 0.70 eV of vibrational energy. From the anharmonicity, a predicted rephasing time of τ=45 ps is calculated, in close agreement with experiment (Fig. 8). The number of states coherently populated, however, determines the dephasing time. If only three vibrational levels were populated, one would expect a dephasing time of $\tau/2$, which is much longer than the experimental dephasing time of ~4 ps. This indicates that a wide distribution of I_2^- states is populated. It is also consistent with a vibrational distribution having a maximum energy of 0.95 eV, as determined from the maximum eKE, and an average energy of 0.70 eV, as determined from the coherence frequency.

The accuracy of the average energy as determined from the coherence frequency is limited by the Morse potential. A better method of determining the vibrational energy

distribution is to measure the photofragment kinetic energy release from I_3^- photodissociation.[33] However, the coherences in this report can be directly compared to the solution experiments. In solution, I_2^- vibrational coherences were observed from photodissociated I_3^-,[12,17,19] with a period substantially shorter (350 fs) and the inferred average vibrational state ($\langle v \rangle = 12$) much lower than our results. This indicates that the "nascent" product distribution is quite different in solution than in the gas phase, a point discussed in Section 5.

Although the traces in Fig. 7 show intensity beginning at 0 fs, it is unclear at what point this signal should be attributed to I_2^- product. If we use as the criterion the start of the periodic oscillations, then the first maxima associated with I_2^- product are at 400 fs (1.29 eV), 550 fs (1.41 eV), 700 fs (1.54 eV), and 850 fs (3.00 eV). At 1.41 eV, there is an earlier, smaller maximum at 100 fs. Since product coherence is generally expected to decay with time, the lower intensity of the earlier maximum suggests it is due to transient I_3^- signal during the early stages of bond cleavage rather than I_2^-. It also seems unlikely that I_2^- products would appear within 100 fs, while I^- is not fully formed until 600 fs. Transient I_3^- signal is probably the origin of the shoulder at 200 fs in the 3.00 eV slice as well.

4.4 2-dimensional wavepacket simulations

4.4.1 Potential energy surfaces and wavepacket dynamics

In this section we characterize the I_3^- excited state potential energy surface on which dissociation occurs and investigate the mechanism responsible for the formation of atomic I^- products. In our previous report, 1-d wavepacket simulations using a Gaussian

distribution of I_2^- vibrational states were carried out to ascertain the distribution of excited vibrational levels,[21] a procedure that is approximate at best. To model the photodissociation process more realistically and determine the nature of the product coherences, we have performed 2-dimensional wavepacket simulations on a series of collinear London-Eyring-Polanyi-Sato (LEPS)[53] potential energy surfaces, and present the potential that best reproduces our I_2^- vibrational distribution. Although we do not model the full 2-d photoelectron spectrum, we can simulate the spectrum once I_2^- is formed by projecting the 2-d wavefunction onto the 1-d wavefunction for I_2^- vibration. This LEPS potential also predicts that a substantial amount of three-body dissociation will occur via. Eq. 4, which we are also able to simulate in 1-d and compare to the formation of the I^- feature at 1.7 eV.

This work was stimulated in part by the previous quantum simulations done by Banin *et al.*[13] in which a simple LEPS potential was used to model the excited potential energy surface. As in their work, our simulation was carried out using a method based on the wave packet propagation techniques of Kosloff and Kosloff.[54-56] It treats the dynamics along the two stretching coordinates exactly, and assumes that all nuclear motion takes place on a collinear potential energy surface.

Following Banin *et al.*,[13] we assume the ground state potential to be harmonic (Table I), the excited state potential to be a LEPS surface that correlates to ground state I_2^- products and an atomic iodine atom, and the pump pulse as being weak, coherent, and infinitely short. The iodine atomic product in their work, however, is assumed to be in its excited $^2P_{1/2}$ state since a pump frequency of 308 nm corresponds to excitation to the blue band in the I_3^- absorption spectrum. In our experiment, excitation at 390 nm corresponds

Table I. Parameters for the 1-d and 2-d potentials.

Ground state potential surface for I_3^-

$V_g(Q_1,Q_3) = \frac{1}{2}\mu_1\omega_1^2(Q_1-Q_{eq})^2 + \frac{1}{2}\mu_2\omega_2^2Q_3^2$

$Q_1 = r_{ab} + r_{bc} \quad Q_3 = r_{ab} - r_{bc}$

ω_1[a]=112 cm^{-1} ω_2[b]=145 cm^{-1} Q_{eq}=5.358 Å μ_1=63.5 amu μ_3=21.2 amu

Excited state potential surface for I_3^-

$$V_e(r_{ab},r_{bc},r_{ac}) = \Delta E_0 + Q_{ab} + Q_{bc} + Q_{ca} - (J_{ab}^2 + J_{bc}^2 + J_{ca}^2 - J_{ab}J_{bc} - J_{bc}J_{ca} - J_{ca}J_{ab})^{1/2}$$

$$Q_{\alpha\beta} = \frac{[(1+S_{\alpha\beta})^1E(r_{\alpha\beta}) + (1-S_{\alpha\beta})^3E(r_{\alpha\beta})]}{2(1+S_{\alpha\beta})} \qquad {}^1E(r_{\alpha\beta}) = D_{\alpha\beta}[1-e^{-\beta_{\alpha\beta}(r_{\alpha\beta}-r_{\alpha\beta}^{eq})}]^2 - D_{\alpha\beta}$$

$$J_{\alpha\beta} = \frac{[(1+S_{\alpha\beta})^1E(r_{\alpha\beta}) - (1-S_{\alpha\beta})^3E(r_{\alpha\beta})]}{2(1+S_{\alpha\beta})} \qquad {}^3E(r_{\alpha\beta}) = \{D_{\alpha\beta}[1+e^{-\beta_{\alpha\beta}(r_{\alpha\beta}-r_{\alpha\beta}^{eq})}]^2 - D_{\alpha\beta}\}/2$$

$r_{ab}^{eq} = r_{bc}^{eq}$ =3.205 Å $D_{ab} = D_{bc}$ =1.014 eV $\beta_{ab} = \beta_{bc}$ ==1.181 Å^{-1} S_{ab}=S_{bc}=0.50

r_{ca}^{eq} =2.983 Å D_{ca} =1.010 eV β_{ca} =1.000 Å^{-1} S_{ca}=0.00

ΔE_0=2.890 eV

1-dimensional potentials for the symmetric stretch of neutral I_3

$$\begin{aligned} V_n(\mathrm{r}) &= \Delta E_0 + 2D_e^n \exp[-\beta^n(r-r_e^n)] + D_e^n \exp[-2\beta^n(r-r_e^n)] \equiv v_1(r), && 0 < r \le 7 \text{ Å} \\ &= sf_1(r)v_1(r) + [1-sf_1(r)]v_2(r), && 7 \text{ Å} < r \le 11 \text{ Å} \\ &= \Delta E_0 + 2D_e \exp[-\beta(r-r_e)] + D_e \exp[-2\beta(r-r_e)] \equiv v_2(r), && 11 \text{ Å} < r \le r_\infty \end{aligned}$$

$$sf_n(r) = \frac{1}{2}\left(\cos\frac{\pi(r-r_n)}{r_{n+1}-r_n}+1\right)$$

r_e = 5.66 Å D_e = 1.47 eV β = 0.53 Å^{-1} ΔE_0 = 5.95 eV

V_1 : r_e^1= 5.10 Å D_e^1= 1.70 eV β^1= 0.38 Å^{-1}

V_2 : r_e^2= 5.66 Å D_e^2= 1.47 eV β^2= 0.45 Å^{-1}

V_3 : r_e^3= 6.10 Å D_e^3= 1.27 eV β^3= 0.52 Å^{-1}

[a]Symmetric stretch frequency taken from this report, Section 4.1.
[b]Antisymmetric stretch reported in Ref. 29.

to excitation into the lower I_3^- absorption band, which predominantly results in $I(^2P_{3/2})$ products.[33] This also means the energy available for bond dissociation differs between the two experiments. Banin *et al.* determined the available energy to be ~0.4 eV above the three-body dissociation limit of $I^- + I(^2P_{3/2}) + I^*(^2P_{1/2})$,[13] based on an approximate value of 1.0 eV for the bond strength of I_3^-.[31] Since publication of their work a gas phase bond strength of 1.31 ± 0.06 eV has been reported,[20] showing the amount of available energy is actually much smaller. Using similar energetic arguments, the new I_3^- bond strength, and the more recent bond strength for I_2^-,[42] ~0.3 eV of energy is estimated to be available for product dissociation at 390 nm to $I^- + I(^2P_{3/2}) + I(^2P_{3/2})$. With this in mind, the ground state geometry is adjusted so that a vertical transition to the excited state lies 0.3 eV above the three-body asymptote.

In an effort to understand the features required to produce vibrationally excited I_2^- products, we first ran simulations, using the methods described below, on the original Banin *et al.* excited state potential with the I_3^- ground state geometry adjusted so that the vertical transition energy was at 0.3 eV above the three-body asymptote. We found that this surface yielded considerably less I_2^- vibrational excitation than was observed experimentally, and no I^- was produced. We then adjusted the Sato parameters on the excited state surface to achieve better agreement with experiment. The original potential had a barrier of ~300 meV along the minimum energy path for the symmetric exchange reaction $I + I_2^- \rightarrow I_2^- + I$. Lowering the barrier resulted in more I_2^- vibrational excitation, but not until the barrier was eliminated in favor of a shallow well did the I_2^- vibrational distribution peak at vibrational energies comparable to our experiment. This modification also produced more I^- via three-body dissociation, as shown below.

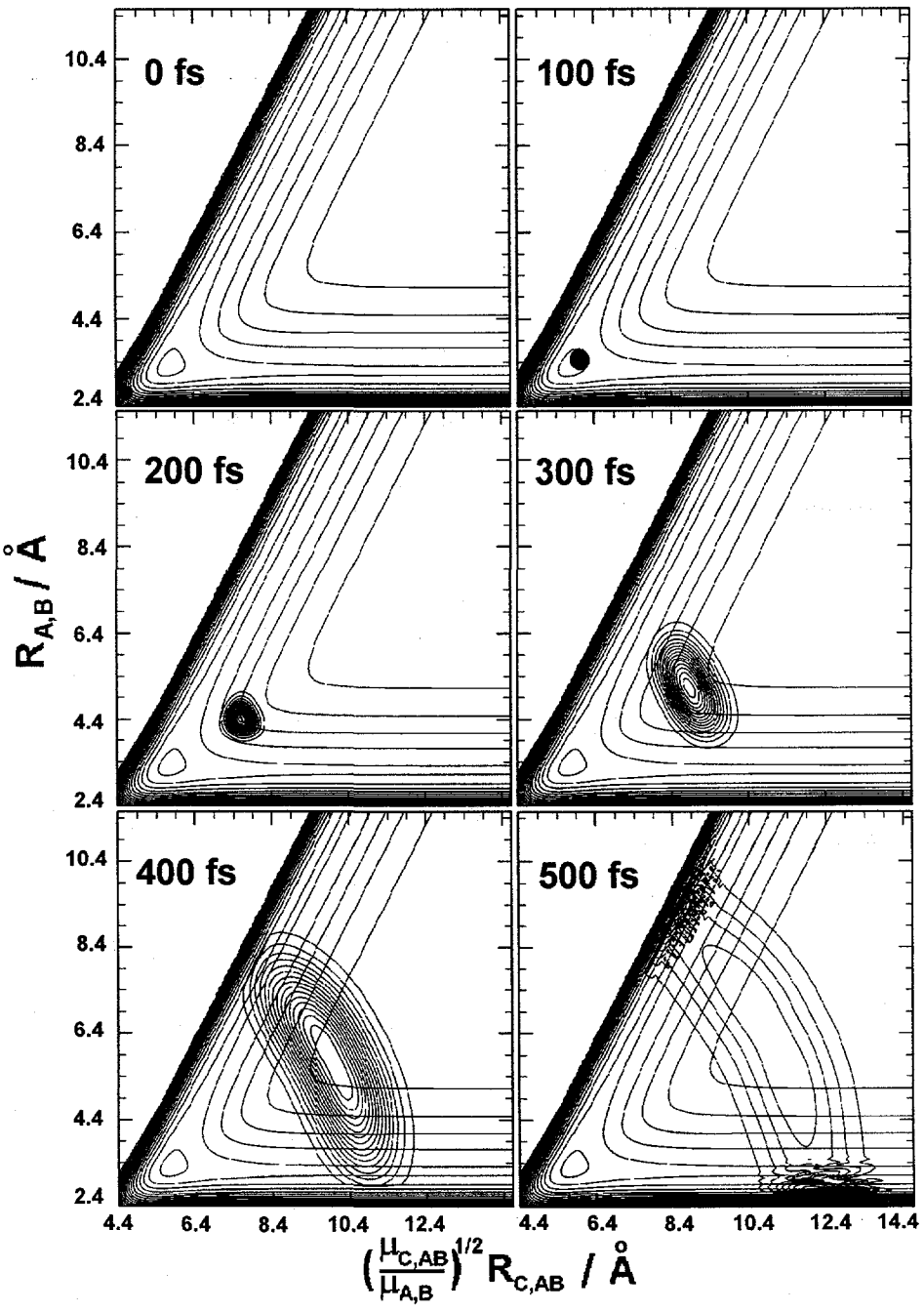

Figure 11. Snapshots of the evolving wavepacket on the 2-d LEPS potential for the excited state of I_3^- from Table I. The potential is shown in mass-weighted coordinates for the linear I_A-I_B-I_C molecule. $R_{C,AB}$ is the distance between I_C and the center-of-mass of the I_2^- fragment (I_A-I_B), and $R_{A,B}$ is the I_2^- bond length. Contours for the potential are in ~200 meV steps and contours for the wavepacket represent a 10% change in $|\Psi|^2$. At 500 fs, significant intensity remains along the symmetric stretching coordinate.

The final potential is shown in Fig. 11, along with snapshots of the wavepacket evolving in 100 fs intervals, starting from its initial placement vertically above the ground state minimum. The potential is presented in mass weighted coordinates for the linear I_A-I_B-I_C molecule with the x-axis representing the distance from I_C to the center-of-mass of the departing I_2^- (I_A-I_B) product. The y-axis corresponds to the I_2^- bond length $R_{A,B}$. The parameters for the potentials are listed in Table I.

The initial motion is primarily along the symmetric stretch coordinate of the potential, consistent with the resonance Raman work.[29,30] Once the wavepacket passes through the potential well (~100 fs) it begins spreading along the antisymmetric stretching coordinate. This broadening continues until the wavepacket boundaries reach the repulsive walls in the I_2^- product valleys at around 400 fs. By this time, the wavepacket spans the entire potential but still has significant intensity along the symmetric stretching coordinate, in contrast to the surface of Banin *et al.*[13] By 500 fs the wavepacket is entirely out of the transition state region, and continues to expand as the products move apart. The simulations in Fig. 11 show similar features to those by Banin *et al.*, but the wavepacket progresses further along the symmetric stretch coordinate before spreading on our surface, a direct consequence of the shallow well in the transition state region which accelerates the wavepacket along the symmetric stretch coordinate.

By 500 fs, the portion of the wavepacket residing in the upper and lower I_2^- valleys will form $I + I_2^-$ and $I_2^- + I$ products, respectively, while the remaining portion of the wavepacket will form $I^- + I + I$ via. Eq. 4. Assuming that there is equal probability for dissociating to $I + I_2^-$ or $I_2^- + I$ products, and that the dividing line between lower valley products and three-body dissociation products occurs at $R_{A,B}$=5.5 Å, integration

of the lower valley gives a 27% probability for three-body dissociation at 500 fs. To insure that further motion did not significantly decrease the three-body yield, the wavepacket was allowed to evolve for an additional 150 fs, and the three-body dissociation probability was again determined to be 27%.

4.4.2 I_2^- vibrational distribution and dynamics

At times ≥500 fs, the wavepacket has essentially reached the asymptotic region of the potential energy surface, so that slices through the upper and lower valleys perpendicular to the minimum energy path yield the Morse function for the I_2^- ground state. In the lower valley, the wavepacket can therefore be decomposed into vibrational and translational eigenstates according to Eq. 6:

$$\Psi(x,y) = \sum_{n,i} c_{n,i}\phi_n(x)\chi_i(y) \qquad (6)$$

where $\chi_i(y)$ are the Morse oscillator wavefunctions for the I_2^- ground state, and $\phi_n(x)$ are 1-d free particle waves.[57] In this basis x and y are perpendicular and parallel, respectively, to the minimum energy path. Only intensity at internuclear distances smaller than $R_{A,B}$=5.5 Å is decomposed in this manner since the basis only applies to those products correlating to I_2^- + I. Using the determined coefficients, the vibrational energy distribution is determined by first squaring and then summing (over n) the coefficients along the translational coordinate, and the results are plotted in Fig. 12. The maximum occurs at υ=65 with a FWHM of 50 vibrational states. It is also asymmetric,

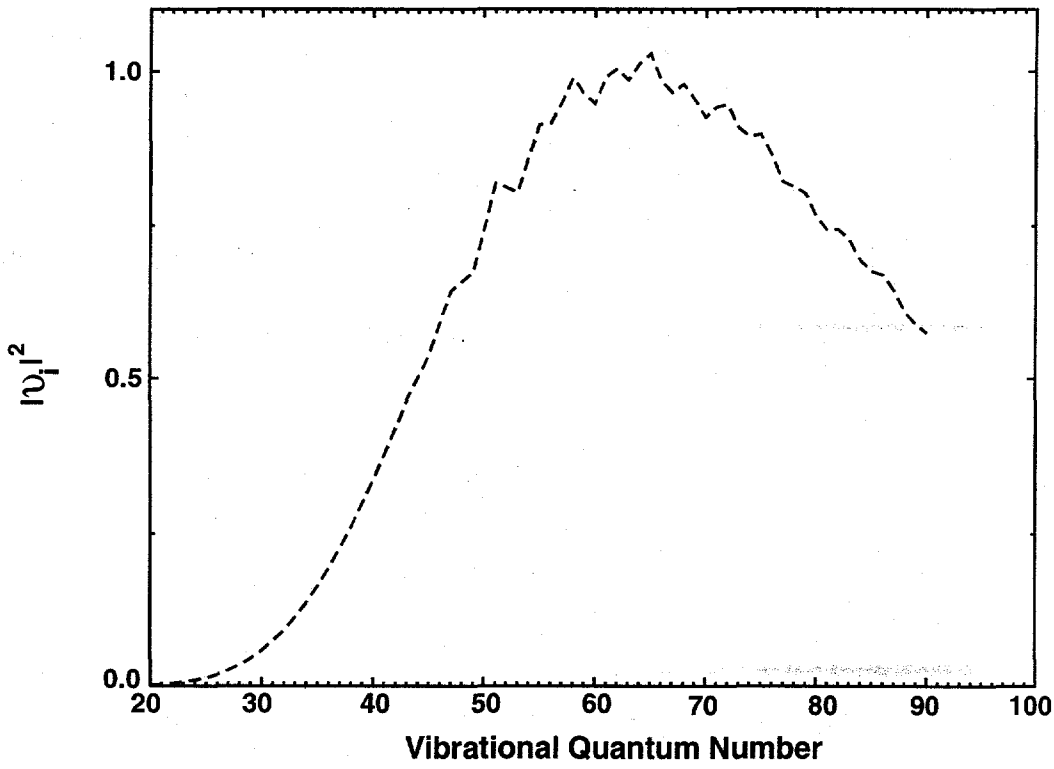

Figure 12. Vibrational energy distribution (Eq. 6) for the 2-d wavepacket at 500 fs.

with a tail that reaches to at least υ=120, in agreement with our analysis in the previous section.

At early delay times, 2-d calculations are required to simulate the photoelectron spectrum arising from detachment of dissociating I_3^-. However, at delay times longer than 500 fs, the portion of the photoelectron spectra due to detachment of I_2^- in the lower valley only depends on the y-axis motion of the wavepacket. This allows the spectra to be simulated using our previously developed 1-d simulation code.[58] Using the above coefficients, a time-dependent 1-d wavefunction was generated using the wavefunction at 500 fs as a starting point. Photoelectron spectra were then calculated from 500 to 4000 fs for detachment to the $\tilde{X}\ ^1\Sigma_g^+$, $\tilde{A}'^3\Pi_{2u}$, and $\tilde{A}^3\Pi_{1u}$ states of neutral I_2.[52,59,60] The results were convoluted to match our energy resolution and energy slices were taken for comparison with experiment (Fig. 7, dashed).

In agreement with experiment, the simulations produce 550 fs oscillations that rapidly dephase by 4 ps and reflect the same energy dependent phase shift. The first maximum is due to reflection at the inner turning point and occurs at 650 fs at eKE = 3.00 eV. Reflection from the outer turning point is observed 275 fs later in the slice at 1.54 eV. Results at 1.29 and 1.41 eV reflect wavepacket motion in between these two limits (see Fig. 10 and Section 3.3)

However, the maxima in the simulated energy slices fall directly between the maxima in the experimental slices. For example, at 1.29 eV, the first two experimental maxima occur at 400 and 1000 fs, while the first simulated maximum is at 700 fs. As mentioned above, this simulated maximum is associated with wavepacket amplitude near the outer turning point of the I_2^- potential. In a 2-d simulation of the photoelectron

spectrum, we would expect an earlier maximum at 1.29 eV around 200-300 fs associated with wavepacket bifurcation into the product valleys, because the wavepacket motion along the symmetric stretch coordinate slows down significantly in the region where bifurcation begins (see Fig. 11). It is therefore reasonable to assign the first two experimental maxima at 400 fs and 1000 fs to wavepacket bifurcation and the first bond compression of the newly formed I_2^-. Hence, although there is significant agreement between the experimental and simulated energy slices, it appears that the maxima in the simulated energy slices occur too early.

4.4.3 I^- channel

We can also explore production of I^- on this surface. If I^- production occurs via concerted three-body dissociation, detachment of the wavepacket along the symmetric stretching coordinate of I_3^- should give rise to the atomic I^- features in Figs. 3 & 6. It should therefore be possible to reproduce the main trends in the I^- features by performing 1-d simulations of wavepacket motion along the symmetric stretch coordinate of the potential in Fig. 11.

Shown in Fig. 13 are cuts along the symmetric stretching coordinate of the ground and excited state I_3^- potentials. Potentials for I_3 are also needed. These are represented by Morse-Morse-switching-function potentials (Table I) with vertical electron affinities of 4.25, 4.52, and 3.32 eV that match those measured for the ground and first two excited states of neutral I_3 (Section 3.1). Using the same initial wavefunction in the 1-d simulation as was used along the symmetric stretch coordinate of the 2-d simulations, the wavepacket is coupled to the excited anion state by a pump pulse where it is propagated,

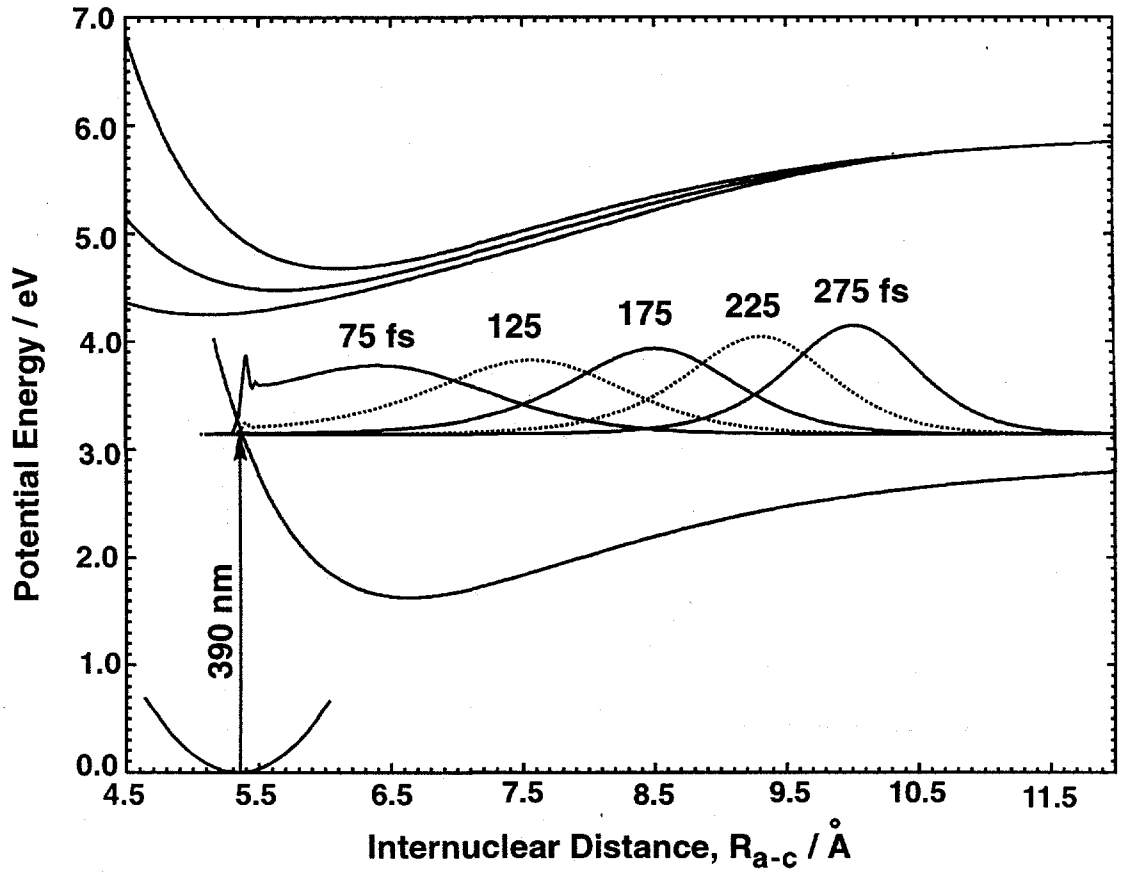

Figure 13. 1-d potentials representing the symmetric stretching coordinate for the I_3^- anion ground, excited, and lowest 3 neutral I_3 states. Parameters are given in Table I. Wavepackets created by the 1-d simulation described in Section IV. D are also displayed.

the time-dependent photoelectron spectrum is calculated using a technique described previously,[58] and the results are convoluted with an instrument response function. To more realistically model the spectra the pump pulse was given a FWHM of 90 fs. Fig. 14 shows the calculated photoelectron spectra at delay times of 75, 125, 175, 225, and 275 fs, and the wavepackets that correspond to these delay times are shown in Fig. 13.

In the simulated spectra, formation of the I^- feature at 1.7 eV occurs in two steps, in agreement with experiment (Figs. 3 & 6). At 75 and 125 fs a broad distribution of energies is formed ranging from 1.55 to 1.80 eV with three features at 1.61, 1.67, and 1.76 eV. At these times the wavepacket resides primarily at internuclear distances near the potential minimum along the symmetric stretch coordinate (see Fig. 13), and the three small features arise from detachment to the three neutral states. At 175 fs the simulated spectrum has leveled and begun to narrow, at which time the wavepacket is approximately half-way out of the potential minimum. At this internuclear distance (~8.5 Å), the anion and neutral potentials are nearly parallel. By 275 fs the wavepacket has largely left the potential minimum and the photoelectron spectrum is dominated by a single atomic peak at 1.7 eV. Thus, the two-step trend in the photoelectron spectrum corresponds to the wavepacket traversing the potential minimum along the symmetric stretching coordinate of the 2-d potential energy surface, and the narrowing of the $I(^2P_{3/2})\leftarrow I^-$ feature is the consequence of the wavepacket climbing out of the potential well and leaving the transition state region, by which point the three I_3 surfaces have almost converged. Therefore, in the simulations, bond cleavage to $I^- + I + I$ occurs between 175 and 275 fs when the $I(^2P_{3/2})\leftarrow I^-$ feature narrows in width.

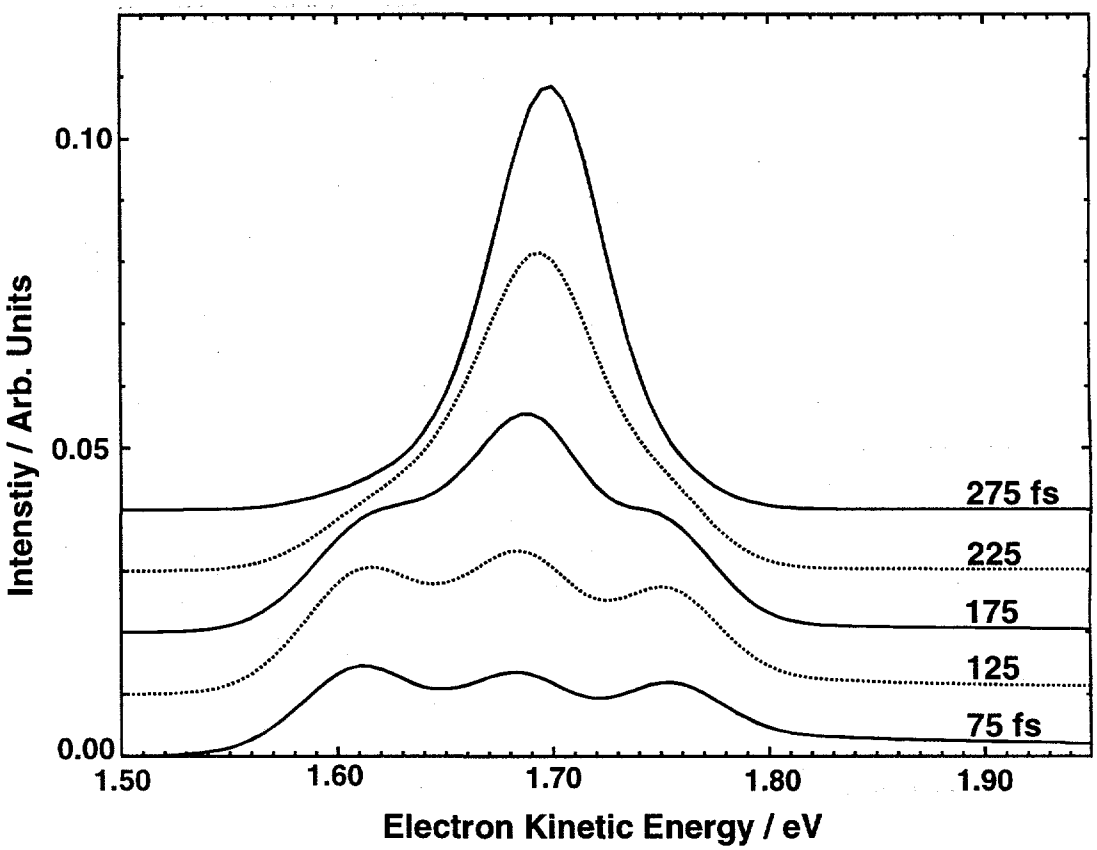

Figure 14. Simulated 1-d FPES of the atomic $I(^2P_{3/2})\leftarrow I^-$ feature at 1.7 eV. The three peaks at 75 fs arise from detachment to the three neutral states and the transformation from a broad spectrum to the atomic feature occurs starting around 175 fs.

The qualitative agreement between the simulation and experiment leads us to believe that I^- is being formed by three-body dissociation via Eq. 4. However, the narrowing of the $I(^2P_{3/2})\leftarrow I^-$ feature at 1.7 eV experimentally occurs at 300 fs, not at 175 fs as in the simulation, and suggests that the simulated wavepacket leaves the transition state region too quickly. This is consistent with our conclusions modeling the I_2^- coherences; the simulated I^- and I_2^- products form too quickly with this LEPS potential. A surface with a potential well that extends to larger internuclear distances may decrease the discrepancy in both cases, or the slope of the excited state potential in the Franck-Condon region may be too steep, imparting too much momentum to the wavepacket. We also must consider the limitations inherent in explaining the dynamics with a collinear rather than 3-dimensional potential energy surface. In any case, comparison of the simulations to experiment indicates that the bond cleavage to $I^- + I + I$ occurs between 300 and 600 fs.

5. Discussion and comparison of gas and solution phase dynamics

There are significant differences between the gas phase and solution photodissociation dynamics of I_3^-. In the I_3^-/EtOH experiments involving excitation to the lower electronic state, oscillations from I_2^- products are first resolved at approximately 500 fs with a frequency of 103 cm^{-1}.[17] This corresponds to $\langle v \rangle = 12$ (0.13 eV),[42] a considerably colder population than seen in the gas phase. In addition, no I^- product was seen in the solution experiments at 400 nm, in contrast to the significant amount of I^- seen in the gas phase. Based on the simulations in the previous section, we understand what type of early time (<500 fs) dynamics lead to the observed gas phase results. We now consider how these dynamics are modified in solution.

Four effects unique to the experiments in solution are (1) symmetry breaking of the I_3^- due to its interaction with the polar solvent, (2) solvent friction effects on the dissociation dynamics in the transition state region, (3) vibrational relaxation of the I_2^- products, and (4) solvent induced dephasing. It is useful to distinguish these effects by the time interval over which they are important. Symmetry-breaking, in which the $D_{\infty h}$ symmetry of the anion is lowered to $C_{\infty v}$, represents an initial-state effect whereby the anion is distorted before any laser fields are applied. Solvent friction in the transition state region is relevant to the time interval just after excitation, when the dissociating wavepacket is in transit between the Franck-Condon region and the I_2^- product valleys. Finally, solvent induced dephasing occurs throughout the reaction while vibrational relaxation is relevant once the I_2^- products are formed.

The observation by Myers and co-workers[29,30] of anti-symmetric stretch excitation in the resonance Raman spectrum of I_3^-/EtOH provides strong evidence for symmetry-breaking. In addition, Geshgoren et al.[15] performed femtosecond dissociation experiments on I_3^- in CH_3CN, a less polar solvent than ethanol, and found that the I_2^- product coherences were less pronounced. This was attributed to a more rapid and coherent entry into the I_2^- product valley induced by broken symmetry of the I_3^- anion in the more polar solvent. This interpretation is consistent with the wavepacket simulations in Fig. 11; if the initial wavepacket did not lie along the symmetric stretch coordinate, one would expect less motion along the symmetric stretch coordinate and earlier localization in one of the product valleys. As a result, the I_2^- vibrational population would be colder and less I^- would be produced, consistent with the differences between the gas phase and solution experiments. Symmetry breaking of I_3^- has also been modeled

theoretically[63,64] and similar effects on the I_2^- vibrational distribution are expected in the photodissociation of I_3^- with antisymmetric stretch excitation.[57]

Solvent friction effects can also play a role consistent with the differences in the gas phase and solution experiments. Suppose that in solution the initial wavepacket in Fig. 11 does lie along the symmetric stretch coordinate. One would then expect interactions with the solvent to impede the motion of the wavepacket along this coordinate, leading to a bifurcation of the wavepacket at smaller internuclear distances than in the absence of solvent. This, like symmetry breaking, would result in a colder I_2^- distribution and reduced I^- formation.

Vibrational relaxation of the I_2^- products may account for some of the discrepancy between the gas phase and solution experiments. The relaxation rate of I_2^- is known to be strongly vibrational state dependent. In the I_3^-/EtOH experiments, an estimated 0.17 eV of vibrational energy is lost within 7 ps although 0.13 eV of this energy is dissipated during the first 1.5 ps.[17] In experiments monitoring the recombination of photodissociated I_2^- in ethanol, ~0.75 eV of vibrational energy is dissipated in the first 0.3 ps while the remaining 0.25 eV of vibrational energy takes ~10 ps to dissipate.[61,62] Hence, extremely fast relaxation rates for vibrational levels above υ=30 are expected,[62] and relaxation of these highly excited levels may have already occurred by 500 fs, the earliest time at which clear I_2^- coherences are seen in solution. Solvent induced dephasing accounts for a portion of the coherence loss of I_3^- in solution although this does not affect the vibrational distribution.[13,17]

It is likely that symmetry breaking as well as solvent friction and vibrational relaxation effects contribute to the differences between the I_3^- experiments. We note that

similar but smaller differences are seen in HgI_2 photodissociation in the gas phase and in solution. The gas phase reaction produces coherent HgI in approximately $\langle v \rangle = 29$ (0.31 eV of vibrational energy).[4] In EtOH solution, one finds $\langle v \rangle = 15$ for HgI at 500 fs, corresponding to 0.21 eV of vibrational energy.[7] Symmetry-breaking is unlikely to occur in HgI_2 because of its weaker interaction with the solvent molecules, so in this case solvent friction and vibrational relaxation are the likely causes of the lower vibrational energy at the earliest observation times.

A possible means of gaining further insight into differences between the I_3^- experiments is to perform experiments on clustered I_3^-. For example, in the binary cluster I_3^-(EtOH), the interaction between the I_3^- and EtOH could easily be strong enough to induce distortion in the I_3^-, but the presence of only a single "solvent" molecule is unlikely to perturb the outgoing I_2^- photoproduct significantly. Hence, a significantly colder I_2^- vibrational distribution in this case would point to symmetry-breaking as the primary culprit. Experiments of this type will be carried out in the near future in our laboratory.

Regardless of the origin of the differences between the gas phase and solution experiments, the results presented here emphasize the importance of studying reactions in both environments. The scope and significance of the solvent effects in I_3^- photodissociation cannot be appreciated without comparison to the gas phase results. By the time I_2^- photoproducts can be unambiguously identified in solution, they are already significantly colder than the gas phase photoproducts. The potential energy surface constructed in this work, although approximate, provides a foundation for a better understanding of the reaction dynamics in solution.

6. Conclusions

We report the first study on the gas phase photodissociation dynamics of I_3^-. The experimental method, femtosecond photoelectron spectroscopy, allows us to simultaneously observe depletion of the I_3^- reactant and formation of the ionic photoproducts I_2^- and I^-. We find that I^- and I_2^- are produced in approximately equal yield, in contrast to photodissociation experiments at a similar wavelength in solution where only I_2^- was observed.

The femtosecond photoelectron spectra reveal vibrational coherences in the I_3^- reactant induced by resonant impulsive stimulated Raman scattering (RISRS), from which we obtain a symmetric stretch frequency of 112 cm^{-1} for the I_3^- ground state. Starting around 400 fs, coherent nuclear motion of the I_2^- products is also observed which exhibits rapid dephasing due to the anharmonicity of the potential followed by rephasing at much longer times. The oscillation period of these coherences yield an average $\langle v \rangle = 67$, a much higher result than obtained in ethanol solution ($\langle v \rangle = 12$).

Two-dimensional wavepacket simulations on a collinear I_3^- excited state surface yielded further insight into the dissociation dynamics. A surface was constructed that yielded the appropriate I_2^- vibrational distribution and also resulted in significant I^- production. Comparison of simulations with the time-dependence of the I^- photoelectron signal indicates the I^- is produced by concerted three-body dissociation. The excited state surface is clearly approximate as both channels are produced too quickly in the simulations, but should serve a useful starting point for future analysis of this system.

Comparison of the gas phase and solution dynamics indicates that the differences are most likely to arise from symmetry breaking effects of the solvent on the I_3^-

chromophore and to solvent effects in the first several hundred femtoseconds after photodissociation. In comparison with the HgI_2 system, I_3^- photodissociation provides a more extreme example of the solvent's ability to alter chemical dynamics. Future work will focus on experiments monitoring the product yield and degree of coherence on the stepwise solvation of I_3^- in size-selected clusters. This should yield information on the solvent role in symmetry breaking and energy partitioning.

7. Acknowledgments

This research was supported by the National Science Foundation under Grant No. CHE-9710243. Support from the Defense University Research Instrumentation Program under Grant No. F49620-95-1-0078 is also gratefully acknowledged. This research used resources of the National Energy Research Scientific Computing Center, which is supported by the Office of Energy Research of the U.S. Department of Energy under Contract No. DE-AC03-76SF00098. The authors would like to thank Anne Myers, Sandy Ruhman, Ronnie Kosloff, Uri Banin and Robin Hochstrasser for helpful and stimulating conversations concerning this project.

8. References

[1] M. L. Chabinyc, S. L. Craig, C. K. Regan, and J. I. Brauman, Science **279,** 1882 (1998).

[2] M. Volk, S. Gnanakaran, E. Gooding, Y. Kholodenko, N. Pugliano, and R. M. Hochstrasser, J. Phys. Chem. A **101,** 638 (1997).

[3] R. M. Bowman, M. Dantus, and A. H. Zewail, Chem. Phys. Lett. **156,** 131 (1989).

[4] M. Dantus, R. M. Bowman, M. Gruebele, and A. H. Zewail, J. Chem. Phys. **91,** 7437 (1989).

[5] M. Dantus, R. M. Bowman, J. S. Baskin, and A. H. Zewail, Chem. Phys. Lett. **159,** 406 (1989).

[6] M. Gruebele, G. Roberts, and A. H. Zewail, Phil. Trans. R. Society Of Lond. A **332,** 223 (1990).

[7] N. Pugliano, D. K. Palit, A. Z. Szarka, and R. M. Hochstrasser, J. Chem. Phys. **99,** 7273 (1993).

[8] N. Pugliano, A. Z. Szarka, S. Gnanakaran, M. Triechel, and R. M. Hochstrasser, J. Chem. Phys. **103,** 6498 (1995).

[9] N. Pugliano, A. A. Szarka, and R. M. Hochstrasser, J. Chem. Phys. **104,** 5962 (1996).

[10] S. Gnanakaran, M. Lim, N. Pugliano, M. Volk, and R. M. Hochstrasser, J. Phys.: Condens. Matter **8,** 9201 (1996).

[11] U. Banin, A. Waldman, and S. Ruhman, J. Chem. Phys. **96,** 2416 (1992).

[12] U. Banin and S. Ruhman, J. Chem. Phys. **98,** 4391 (1993).

[13] U. Banin, R. Kosloff, and S. Ruhman, Israel J. Of Chem. **33,** 141 (1993).

[14] U. Banin, R. Kosloff, and S. Ruhman, Chem. Phys. **183,** 289 (1994).

[15] E. Gershgoren, E. Gordon, and S. Ruhman, J. Chem. Phys. **106,** 4806 (1997).

[16] E. Gershgoren, U. Banin, and S. Ruhman, J. Phys. Chem. A **102,** 9 (1998).

[17] T. Kühne and P. Vöhringer, J. Chem. Phys. **105,** 10788 (1996).

[18] T. Kühne and P. Vöhringer, J. Phys. Chem. A **102,** 4177 (1998).

[19] T. Kühne, R. Küster, and P. Vöhringer, Chem. Phys. **233,** 161 (1998).

[20] K. Do, T. P. Klein, C. A. Pommerening, and L. S. Sunderlin, J. Am. Soc. Mass Spectrom. **8,** 688 (1997).

[21] M. T. Zanni, B. J. Greenblatt, A. V. Davis, and D. M. Neumark, Laser Techniques for State-Selected and State-to-State Chemisry IV, Proc. SPIE **3271** (1998).

[22] R. E. Buckles, J. P. Yuk, and A. I. Popov, J. Am. Chem. Soc. **74,** 4379 (1952).

[23] W. Gabes and D. J. Stufkens, Spectrochim. Acta **30A,** 1835 (1974).

[24] M. Mizuno, J. Tanaka, and I. Harada, J. Phys. Chem. **85,** 1789 (1981).

[25] T. Okada and J. Hata, J. Mol. Phys. **43,** 1151 (1981).

[26] K. Kaya, N. Mikami, Y. Udagawa, and T. Ito, Chem. Phys. Lett. **16,** 151 (1972).

[27] W. Kiefer and H. J. Bernstein, Chem. Phys. Lett. **16,** 5 (1972).

[28] H. Isci and W. R. Mason, Inorg. Chem. **24,** 271 (1985).

[29] A. E. Johnson and A. B. Myers, J. Chem. Phys. **102,** 3519 (1995).

[30] A. E. Johnson and A. B. Myers, J. Phys. Chem. **100,** 7778 (1996).

[31] L. E. Topol, Inorg. Chem. **10,** 736 (1971).

[32] T. R. Taylor, K. Asmis, M. T. Zanni, and D. M. Neumark, in preparation .

[33] H. Choi, R. T. Bise, A. A. Hoops, and D. M. Neumark, In preparation .

[34] B. J. Greenblatt, M. T. Zanni, and D. M. Neumark, Chem. Phys. Lett. **258,** 523 (1996).

[35] B. J. Greenblatt, M. T. Zanni, and D. M. Neumark, Faraday Discuss. **108,** 101 (1998).

[36] O. Cheshnovsky, S. H. Yang, C. L. Pettiette, M. J. Craycraft, and R. E. Smalley, Rev. Sci. Instrum. **58,** 2131 (1987).

[37] H. Handschuh, G. Gantefor, and W. Eberhardt, Rev. Sci. Instrum. **66,** 3838 (1995).

[38] L.-S. Wang, H.-S. Cheng, and J. Fan, J. Chem. Phys. **102,** 9480 (1995).

[39] M. D. Davidson, B. Broers, H. G. Muller, and H. B. v. L. v. d. Heuvell, J. Phys. B **25,** 3093 (1992).

[40] B. J. Greenblatt, M. T. Zanni, and D. M. Neumark, Science **276,** 1675 (1997).

[41] M. T. Zanni, V. S. Batista, B. J. Greenblatt, W. H. Miller, and D. M. Neumark, J. Chem. Phys. **110,** 3748 (1998).

[42] M. T. Zanni, T. R. Taylor, B. J. Greenblatt, B. Soep, and D. M. Neumark, J. Chem. Phys. **107,** 7613 (1997).

[43] A. Mokhtari and J. Chesnoy, Europhys. Lett. **5,** 523 (1988).

[44] J. Chesnoy and A. Mokhtari, Phys. Rev. A **38,** 3566 (1988).

[45] S. L. Dexheimer, Q. Wang, L. A. Peteanu, W. T. Pollard, R. A. Mathies, and C. V. Shank, Chem. Phys. Lett. **188,** 61 (1992).

[46] W. T. Pollard and R. A. Mathies, Ann. Rev. Phys. Chem. **43,** 497 (1992).

[47] U. Banin, A. Bartana, S. Ruhman, and R. Kosloff, J. Chem. Phys. **101,** 8461 (1994).

[48] W. Gabes and H. Gerding, J. Mol. Struct. **14** (1972).

[49] C. J. Delbecq, W. Hayes, and P. H. Yuster, Phys. Rev. **121,** 1043 (1961).

[50] T. Shida, Y. Takahashi, and H. Hatano, Chem. Phys. Lett. **33,** 491 (1975).

[51] E. C. M. Chen and W. E. Wentworth, J. Phys. Chem. **89,** 4099 (1985).

[52] F. Martin, R. Bacis, S. Churassy, and J. Verges, J. Mol. Spectrosc. **116,** 71 (1986).

[53] S. Sato, J. Chem. Phys. **23,** 592 (1955).

[54] R. Kosloff and D. Kosloff, J. Chem. Phys. **79,** 1823 (1983).

[55] D. Kosloff and R. Kosloff, J. Comput. Phys. **52,** 35 (1988).

[56] S. E. Bradforth, A. Weaver, D. W. Arnold, R. B. Metz, and D. M. Neumark, J. Chem. Phys. **92,** 7205 (1990).

[57] G. Ashkenazi, R. Kosloff, S. Ruhman, and H. Tal-Ezer, J. Chem. Phys. **103,** 10005 (1995).

[58] V. S. Batista, M. T. Zanni, B. J. Greenblatt, D. M. Neumark, and W. H. Miller, J. Chem. Phys. **110,** 3736 (1998).

[59] D. R. T. Appadoo, R. J. Leroy, P. F. Bernath, S. Gerstenkorn, P. Luc, J. Verges, J. Sinzelle, J. Chevillard, and Y. Daignaux, J. Chem. Phys. **104,** 903 (1996).

[60] X. N. Zheng, S. L. Fei, M. C. Heaven, and J. Tellinghuisen, J. Chem. Phys. **96,** 4877 (1992).

[61] D. A. V. Kliner, J. C. Alfano, and P. F. Barbara, J. Chem. Phys. **98,** 5375 (1993).

[62] P. K. Walhout, J. C. Alfano, K. A. M. Thakur, and P. F. Barbara, J. Phys. Chem. **99,** 7568 (1995).

[63] H. Sato, F. Hirata, and A. B. Myers, J. Phys. Chem. A **102,** 2065 (1998).

[64] R. M. Lynden-Bell, R. Kosloff, S. Ruhman, D. Danovich, and J. Vala, J. Chem. Phys. **109,** 9928 (1998).

Chapter 9. Electron Solvation in Finite Systems: Femtosecond Dynamics of Iodide·(Water)$_n$ Anion Clusters[†]

Electron solvation dynamics in photoexcited anion clusters $I^-\cdot(D_2O)_{n=4-6}$ and $I^-(H_2O)_{4-6}$ were probed by using femtosecond photoelectron spectroscopy (FPES). An ultrafast pump pulse excites the anion to the cluster analog of the charge-transfer-to-solvent state seen for I^- in aqueous solution. Evolution of this state is monitored by time-resolved photoelectron spectroscopy using an ultrafast probe pulse. The excited n=4 clusters showed simple population decay, but in the n=5 and 6 clusters the solvent molecules rearranged to stabilize and localize the excess electron, showing characteristics associated with electron solvation dynamics in bulk water. Comparison of the FPES of $I^-(D_2O)_n$ with $I^-(H_2O)_n$ indicates more rapid solvation in the H_2O clusters.

1. Introduction

A free electron can be trapped by solvent reorientation in polar solvents such as ammonia(*1*) or water.(*2*) These "solvated" electrons play an important role in condensed phase chemistry, including radiation chemistry, electron transfer, and charge-induced reactivity. A microscopic understanding of the electron-solvent and solvent-solvent interactions that govern electron solvation is a therefore a fundamental and challenging problem. These considerations have motivated femtosecond time-resolved studies that

---

[†] Originally published in Science, **284**, 635 (1999), and Ultrafast Phenomena XI, edited by T. Elsaesser *et al.*, Springer Series Chem. Phys. **63**, 474 (1999).

have demonstrated rich and complex dynamics after electronic excitation of electrons in water.(*3*,*4*)

To gain a complementary perspective on this problem, we have studied solvated electron dynamics in finite clusters and compared these results with our understanding of bulk solvation phenomena. We used two-photon anion femtosecond (10^{-15} s) photoelectron spectroscopy(*5*,*6*) (FPES) to study electron solvation dynamics in mass-selected anion clusters $I^-(D_2O)_n$ and $I^-(H_2O)_n$ in order to address the following questions:

- 1) What is a minimum solvent cluster size needed to "solvate" an electron?
- 2) What is a typical time scale for solvent reorientation in a cluster?
- 3) What type of solvent motion is involved in electron solvation dynamics?

Aqueous solutions of I^- exhibit broad electronic bands in the ultraviolet (UV) corresponding to electron ejection from the I^- into the solvent,(*7*) known as "charge-transfer-to-solvent" (CTTS) states. Excitation of these states represents an elegant means of generating solvated electrons, as was first demonstrated by Jortner.(*8*) The dynamics of these states have been investigated by Eisenthal,(*9*) Gaudeul,(*10*) and Bradforth,(*11*) and their co-workers, all of whom excited the CTTS states to inject an electron into the water and then followed the subsequent electron solvation dynamics by femtosecond absorption spectroscopy. These experimental studies along with simulations by Sheu and Rossky(*12*) and Staib and Borgis(*13*) show that excitation of the lowest energy CTTS band results in the generation of fully solvated electrons on a 200 fs time scale.(*11*) Once

generated, these electrons thermalize with the solvent molecules, and some are then lost through geminate recombination with the neutral halogen atom over a time scale of tens of picoseconds.

The issue of how the CTTS bands manifest themselves in finite clusters was first addressed in experiments by Johnson and co-workers(*14*) in which a diffuse absorption band was seen just above the detachment threshold for $I^-(H_2O)_n$ clusters (n=1-4). As the number of water molecules increases, this band shifts to the blue, and appears to converge toward the lower energy CTTS band in aqueous solution. These cluster analogs to the CTTS band most likely correspond to excitation of the electron from an orbital localized on the I^- into a more delocalized state supported by the network of water molecules in the cluster.

The work reported here builds on these spectroscopic measurements in that we use FPES to perform time-resolved measurements of the microscopic electron solvation dynamics subsequent to excitation of the CTTS cluster analog bands. In these experiments, mass-selected clusters $I^-(H_2O)_n$ are electronically excited with an ultraviolet (UV) pump laser pulse (263 nm, 4.71 eV) of ~100 fs duration. The upper state evolves for a fixed time interval and is then photodetached by a probe laser pulse (790 nm, 1.57 eV) of similar duration. The resulting photoelectron (PE) spectrum provides a "snapshot" of the upper state. Measurement of the photoelectron spectrum at a series of pump-probe delay times thus provides a detailed probe of the electron and solvent dynamics in the electronically excited state. The overall experiment is described in detail elsewhere.(*5,15,16*)

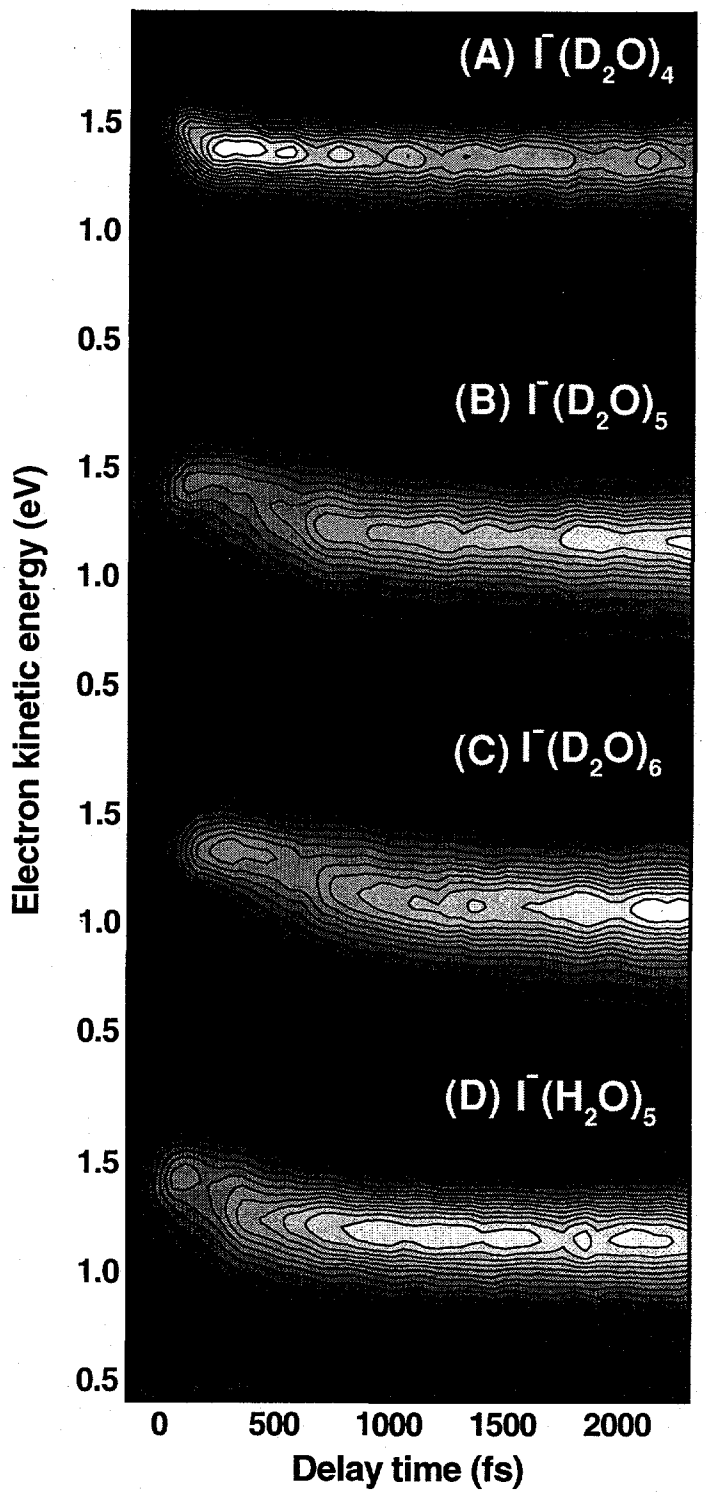

Figure 1. Femtosecond photoelectron spectra of (A to C) $I^-\cdot(D_2O)_n$ n=4 to 6 and (D) $I^-\cdot(H_2O)_5$ plotted as two-dimensional contour plots of electron KE versus pump-probe delay time.

2. Results

Results are presented for $I^-(D_2O)_n$ and $I^-(H_2O)_n$, (n=4-6). Our results suggest that for all the clusters, the electron is photoexcited into a dipole-bound state supported by the network of water molecules. In the n=4 cluster, this state decays rapidly by vibrational autodetachment. However, the n=5 and 6 clusters undergo solvent rearrangement that stabilizes the excess electron. These systems are therefore the smallest in which the cluster analog of electron solvation occurs.

FPE spectra for $I^-(D_2O)_{4-6}$ are shown in Fig. 1A to 1C; those for $I^-(H_2O)_5$ are shown in Fig. 1D. Each plot shows a two-dimensional contour plot of photoelectron intensity versus electron kinetic energy (eKE) and pump-probe delay. Fig. 2 shows the average eKE as a function of time for these clusters as well as $I^-(H_2O)_4$ and $I^-(H_2O)_6$.

In the FPES of $I^-\cdot(D_2O)_4$ (Fig. 1A), the intensity rises to a maximum during the first 200 fs, and during this time the average eKE decreases by about 0.07 eV. By 200 fs, the spectrum is centered at 1.38 eV with a full-width at half maximum (FWHM) of 0.28 eV. At longer times, the spectrum shifts slightly toward lower eKE (0.04 eV by 1 ps), but the major time-dependent effect observed is decay of the integrated intensity, dropping by about 20% over 2.3 ps.

The FPE spectra of the larger clusters are more complex. The eKE's stay constant for several hundred femtoseconds and then undergo significant shifts to lower eKE. In addition the intensity of the electron signal varies non-monotonically with time. For $I^-\cdot(D_2O)_5$ (Fig. 2B), starting from 200 fs, the average eKE decreases from 1.38 to 1.17 eV with a time constant of 390 fs. The contour plot shows the maximum electron intensity

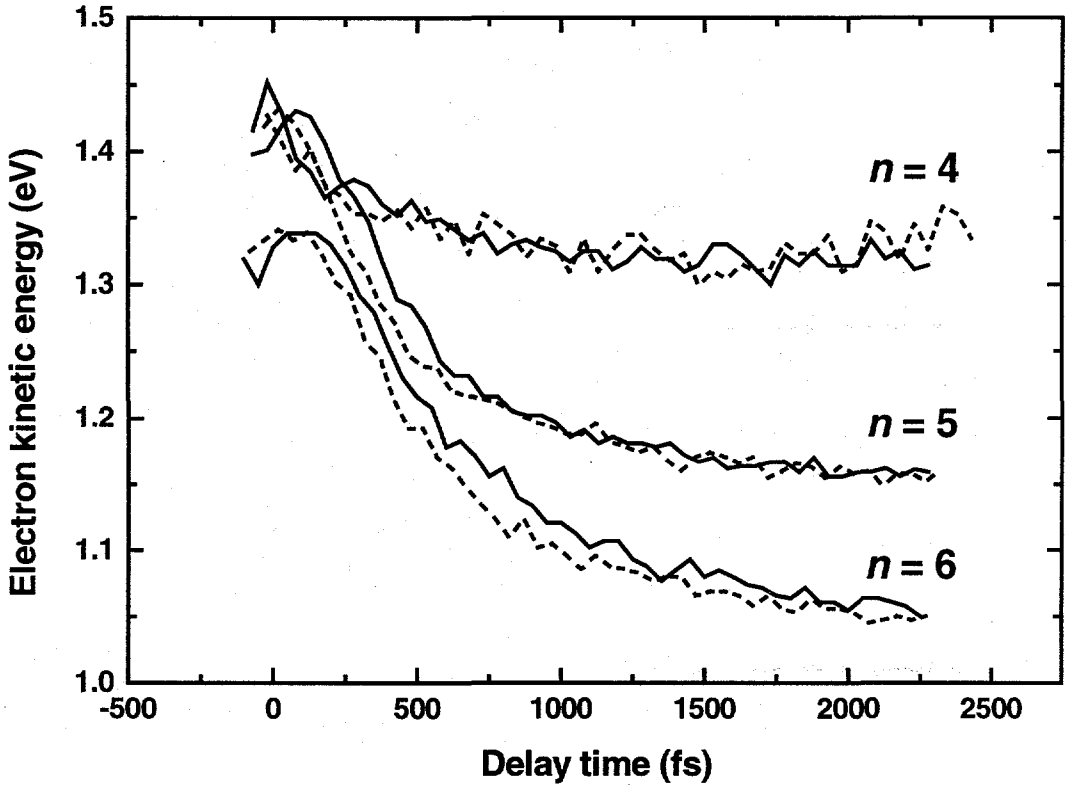

Figure 2. Plot of average electron KE as function of delay time for clusters shown in Fig. 1 as well as $\Gamma(H_2O)_{4,6}$.

remaining constant until ~400 fs, after which it increases, reaching an absolute maximum by 2300 fs. (At much longer pump-probe delays, the signal then decays again with a time constant of about 37±1 ps.) The shift in eKE is accompanied by an increase in the overall width of the spectrum, from 0.27 eV at 180 fs to 0.345 eV at 800 fs. Similar trends are seen for $\Gamma(D_2O)_6$. The main differences are that the shift toward lower eKE (from 1.33 to 1.05 eV) is slower, with a time constant of 560 fs. The contour plot in Fig. 1 shows a slight dip in maximum intensity around 500 fs before rising at longer times. The signal ultimately decays with a time constant of 96±3 ps.

Comparison of $\Gamma(D_2O)_n$ and $\Gamma(H_2O)_n$ results in Figs. 1 and 2 reveals the effects of isotopic substitution. The $\Gamma(H_2O)_n$ clusters are all shifted by 20 meV toward higher eKE, a shift attributed due to zero point energy effects. We find virtually no difference in the time-evolution of the n=4 clusters. For n=5 and n=6, the shift toward lower electron energy begins about 100 fs earlier in the H_2O clusters. The time constant for this shift is the same for the n=5 clusters, but is about 17% lower for $\Gamma(H_2O)_6$ (470 fs) than for $\Gamma(D_2O)_6$.

3. Discussion

The most significant feature of these results is the marked change in the time-evolution of the spectra in going from the n=4 to n=5 clusters. The results suggest that simple population decay of an excited state occurs for n=4, whereas for n≥4 a severe reorganization within the cluster must take place. The initial excitation and subsequent dynamics responsible for these effects are considered below.

Ground state structures for $X^-(H_2O)_{n\geq 4}$ clusters have been calculated by Jortner and co-workers, (*17*) Perera and Berkowitz,(*18*) and Xantheas.(*19*) These structures all show the halide bound to a water cluster, with the water molecules oriented so as to maximize their interaction with each other and the halide anion. For example, in the solvent network for $I^-(H_2O)_4$, each water molecule donates one hydrogen to form a hydrogen bond with another water molecule, and simultaneously offers the other dangling hydrogen to the anion, to form a "ring" of water molecules each with an H atom pointing toward the halide. As more waters are added, the I^- is predicted to remain on the "surface" of the water cluster, although this point is somewhat controversial based on comparison with PE spectra of $I^-(H_2O)_n$ clusters obtained by Cheshnovsky and co-workers.(*17,20*)

Johnson and co-workers have pointed out that the orientation of the water molecules induced by the halide results in a high dipole moment, estimated at μ=4.4 D for the water network in $I^-(H_2O)_4$, for example.(*14*) The significance of this is that neutral molecules with a dipole moment larger than ≈2 D can bind an electron in a "dipole-bound" state,(*21*) the negative ion analog of a Rydberg state in which the orbital for the excess electron is exceptionally diffuse. It is therefore reasonable to assign the upper state initially generated by the pump pulse to a short-lived state of the form $I(^2P_{3/2})\cdot(H_2O)_n^-$, in which the electron is transferred from the halide to a dipole-bound state of the solvent network.

The FPE spectra for $I^-(D_2O)_4$ and $I^-(H_2O)_4$ indicate that the initially excited electronic state undergoes population decay with no other dynamics occurring. The pump

photon energy, 4.71 eV, lies well above the adiabatic detachment energy of $I^-(D_2O)_4$, 4.36 eV,(*22*) so decay of the excited state by electron emission is certainly energetically accessible. Moreover, the PE spectrum is centered at 1.38 eV, whereas the probe photon energy is 1.57 eV, so the vertical detachment energy for the excited state is 0.19 eV. Excitation at the pump wavelength thus results in an excited electronic state with ~0.45 eV of vibrational energy. We attribute the decay of this state to vibrational autodetachment to form $I(^2P_{3/2})\cdot(D_2O)_4 + e^-$.

The time-evolution of the FPES spectra for n=5 and 6 clusters shows that complex dynamics occur after initial photoexcitation into the dipole-bound state. The lowering of the mean electron energy by ~0.3 eV during the first picosecond implies that the excess electron is stabilized by solvent motion on this time scale. Moreover, the non-monotonic variation of integrated electron intensity suggests that the nature of the orbital in which the excess electron resides changes significantly over the time scale of this intensity variation. Overall, we attribute these trends to solvent isomerization from the initial, dipole-bound state to a second, more stable conformer with the character of a "partially solvated electron."

Figure 3 presents a qualitative potential energy surface diagram consistent with our results for the n=5 and 6 clusters. The dipole-bound state discussed above is resonantly excited by the pump pulse at 263 nm (violet arrow) and subsequent dynamics are probed by photodetachment with the time-delayed probe pulse at 790 nm (red arrow). As shown by Bowen and co-workers,(*23*) photodetachment of a dipole-bound state

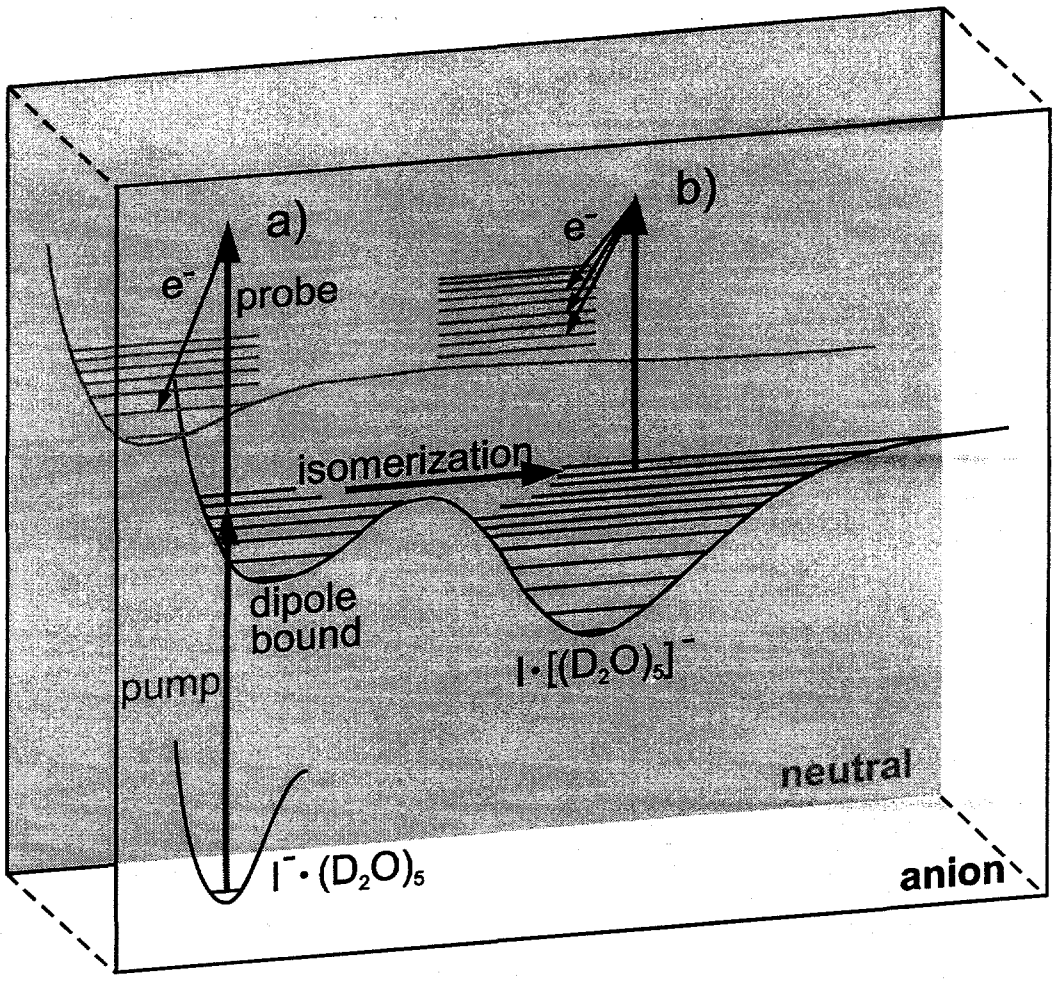

Figure 3. Excitation scheme of resonant UV-IR two-photon photodetachment via dipole bound states. Front plane: anion states. Rear gray plane: neutral states. (A) Pump-probe excitation via dipole bound states (B) Isomerization to a lower energetic conformer. The electronic energy converted into vibration is no longer fully available for the photodetachment resulting in a red shift of photoelectron energy.

results in minimal Franck-Condon activity, consistent with the narrow width of the PE spectrum at short delay times. If isomerization (blue arrow) into a lower energy cluster conformer then occurs, electronic energy is converted into vibrational energy. For a cluster of this size, this vibrational energy should be dispersed over many vibrational modes. The relatively small broadening accompanying the electron energy shift indicates only slightly more Franck-Condon activity in the partially solvated state than in the initially excited state. Thus, the excess vibrational energy of this state largely remains as vibrational energy upon photodetachment, so the 0.3 eV shift of the eKE is approximately equal to the difference in the vertical detachment energies of the conformers.

The time-dependent intensities for the n=5 and 6 clusters (Fig. 1) cannot be attributed to the population of excited state anions, as this must decline monotonically once the pump pulse terminates. Instead, it appears that the dynamics associated with stabilization of the excess electron also result in an increased photodetachment cross section. This result is consistent with isomerization from a dipole-bound state, in which the electron cloud is exceedingly diffuse, to a conformer in which the excess electron is more solvated and hence more localized. Two isomers are known to exist for $(H_2O)_6^-$, and the photodetachment cross section for the more weakly bound isomer (with respect to electron detachment) is considerably less than for the more strongly bound isomer.(*24*) Note that the vertical detachment energies for these isomers (0.2 and 0.5 eV) are quite close to those for the two excited $I^-(H_2O)_6$ species in our experiment.

We next consider isotopic effects. The earlier onset (by 100 fs) of the shift in electron energy for $I^-(H_2O)_5$ and $I^-(H_2O)_6$ compared to the analogous D_2O clusters

indicates that isomerization begins earlier in the H_2O clusters, and suggests that librational-rotational motion of the solvent molecules plays an important role in stabilizing the excess electron. A large isotope effect attributed to librational solvent motion has also been seen at very early times (30 to 80 fs) in bulk hydrated electron studies.(*4*)

Fig. 4 presents a qualitative picture of the isomerization and electronic localization dynamics consistent with our experimental results. At short delay times the geometry of the initially excited state (4B), should resemble that of the ground state (Fig. 4A), (*17*) and the excess electron in Fig. 4B is bound by the dipole moment of the solvent network. However, Kim and co-workers(*25*) calculate that the lowest energy structure for $(H_2O)_6^-$ is quite different from the solvent network in Fig. 4B; they find instead a "half-cage" structure in which the excess electron is considerably more localized. Their calculation is the basis for the structure in Fig. 4C, which has a different hydrogen bonding network than that in Fig. 4C.

One must realize the approximate nature of Fig. 4. First, because of the finite (and unknown) cluster temperature, it is possible that fluctional as well as rigid structures play a role in the dynamics. For example, recent infrared spectroscopy experiments on $I^-(H_2O)_2$ suggest that the inter-water hydrogen bond is disrupted at finite temperatures.(*26*) In addition, many low-lying isomers are expected for $(H_2O)_6^-$,(*25*) including a linear structure that appears to be consistent with its infrared spectrum.(*27*) Finally, perturbations and dynamics associated with the neutral I atom have not been considered.

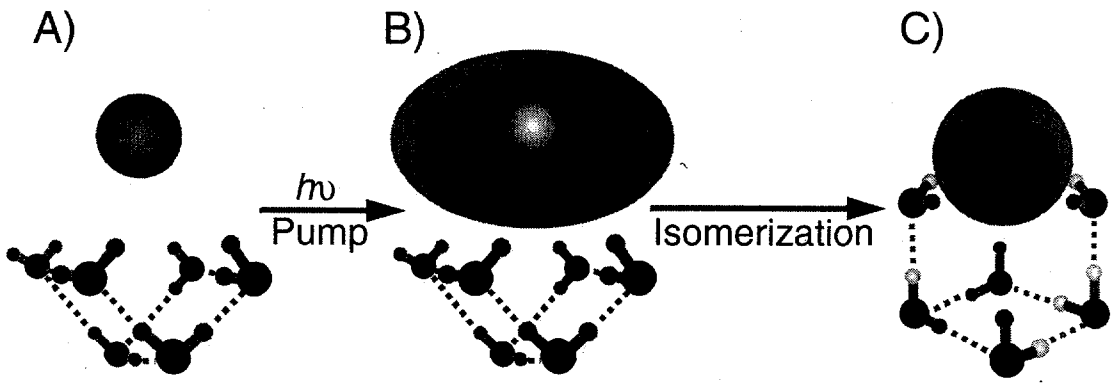

Figure 4. Candidate structures for (A) ground state, (B) dipole-bound excited state, and (C) partially-solvated state of $I^-(H_2O)_6$. A and B are based on the anion ground state calculated in (*17*), and C is based on the lowest energy calculated structure for $H_2O_6^-$ (*25*).

4. Conclusion

We close by comparing our results to Bradforth's experiments(*11*) on CTTS excitation of I^- in liquid water, since these are the liquid-phase experiments most analogous to ours. In his experiments, transient absorption at 800 nm was monitored after excitation at 255 nm. Bradforth observes a short-lived (~50 fs) transient assigned to the initially excited CTTS state, followed by an increasing absorption with a rise time of 200 fs associated with formation of the solvated electron; this then decays biexponentially with time constants of 9 and 60 ps. This interpretation suggests several parallels with the n=5 and 6 FPES results presented here, namely that the CTTS state in the bulk is analogous to the short-lived dipole-bound state seen in our experiments, and that the bulk solvation on a 200 fs time scale corresponds to the isomerization and solvation dynamics seen in our experiments. There are, however, important differences. Simulations of CTTS excitation shows that solvation is accompanied by the electron moving away from the halogen species,(*12,13*) a reasonable result for an infinite number of water molecules but one which may not occur in a small cluster. Also, in liquid water, the longer time decay of the solvated electron signal occurs by recombination with neutral I atoms. While this may be responsible for the long-time decay in the clusters, a likelier mechanism is thermionic emission, a process which generally does not occur in liquids.

5. References

1 W. Weyl, Poyg. Ann. **123,** 350 (1864).

2 E.J. Hart and J.W. Boag, J. Am. Chem. Soc. **84**, 4090 (1962).

3 M. Wiesenfeld and E.P. Ippen, Chem. Phys. Lett. **73**, 47 (1980); A. Migus, Y. Gauduel, J.L. Martin, A. Antonetti, Phys. Rev. Lett. **58,** 1559 (1987).

4 C. Silva, P.K. Walhout, K. Yokoyama, P.F. Barbara, Phys. Rev. Lett. **80,** 1086 (1998).

5 B.J. Greenblatt, M.T. Zanni, D.M. Neumark, Chem. Phys. Lett. **258**, 523 (1996)

6 B. J. Greenblatt, M. T. Zanni, D. M. Neumark, Science **276**, 1675 (1997).

7 J. Franck and G. Scheibe, Z. Phys. Chem. A **139**, 22 (1928).

8 J. Jortner, M. Ottolenghi, G. Stein, J. Phys. Chem. **68**, 247 (1964).

9 F. H. Long, X. Shi, H. Lu, K. B. Eisenthal, J. Phys. Chem. **98**, 7252 (1994).

10 Y. Gaudeul, H. Gelabert, M. Ashokkumar, Chem. Phys. **197**, 167 (1995).

11 J. A. Kloepfer, V. H. Vilchiz, V. A. Lenchenkov, S. E. Bradforth, Chem. Phys. Lett. **298**, 120 (1998).

12 W.-S. Sheu and P. J. Rossky, Chem. Phys. Lett. **213**, 233 (1993).

13 A. Staib and D. Borgis, J. Chem. Phys. **104**, 9027 (1996).

14 D. Serxner, C.E. Dessent, M.A. Johnson, J. Chem. Phys. **105**, 7231 (1996).

15 B.J. Greenblatt, M.T. Zanni, D.M. Neumark, Disc. Faraday Soc. **108**, 101 (1997).

16 Briefly, a pulsed beam of cold $I^-(D_2O)_n$ anion clusters is formed by crossing an electron beam with a pulsed supersonic expansion of a gas mixture of about 5% CH_3I, 2% D_2O (or H_2O) in 1 bar N_2 into a vacuum chamber. The resulting anions are mass selected by time-of-flight and interact with the pump and probe laser pulses at the focus of a "magnetic bottle" TOF photoelectron spectrometer. The pump and probe laser pulses were generated by a Ti:sapphire oscillator-regenerative amplifier system (Clark MXR) running at a repetition rate of 500 Hz.

17 J. E. Combariza, N. R. Kestner, J. Jortner, J. Chem. Phys. **100**, 2851 (1994); Chem. Phys. Lett. **221**, 156 (1994).

18 L. Perera and M. Berkowitz, J. Chem. Phys. **100**, 3085 (1994).

19 S. S. Xantheas, J. Phys. Chem. **100**, 9703 (1996).

20 G. Markovich, S. Pollack, R. Giniger, O. Cheshnovsky, J. Chem. Phys. **101**, 9344 (1994).

21 O. H. Crawford, Mol. Phys. **20**, 585 (1971).

22 T. R. Taylor, H. Gomez, and D. M. Neumark, to be published.

23 J.V. Coe et al., J. Chem. Phys. **92**, 3980 (1990); J. H. Hendricks et al., in "Structure and Dynamics of Clusters", T. Kondow, K. Kaya, and A. Terasaki, Eds., Unversal Academy Press, Tokyo, 1996, pp. 321-328.

24 C.G. Bailey and M.A. Johnson, Chem. Phys. Lett. **265**, 185 (1997).

25 S. Lee, J. Kim, S. J. Lee, K. S. Kim, Phys. Rev. Lett. **79**, 2038 (1997).

26 P. Ayotte et al., Chem. Phys. **239**, 485 (1998).

27 P. Ayotte et al., J. Chem. Phys. **110**, (in press).

28 Supported by the Air Force Office of Scientific Research under F49620-97-0018. R.W. acknowledges funding by the Deutsche Forschungsgemeinschaft. C.F. acknowledges post-doctoral support from the Deutsche Akademie der Naturforscher Leopoldina (BMBF-LPD 9801-6). L.L acknowledges financial support by E.W. Schlag.

Chapter 10. Dynamics of the charge-transfer-to-solvent states in $I^-(Xe)_n$ clusters

We have used femtosecond photoelectron spectroscopy to monitor the dynamics associated with the charge-transfer-to-solvent (CTTS) states in $I^-(Xe)_n$ clusters. We find that the lifetime for the $^2P_{1/2}$ CTTS state increases approximately linearly with cluster size, e.g. 550±50, 700±50, and 1550±200 fs for clusters n=11, 20, and 38, respectively. These states are determined to decay by spin-orbit autodetachment. In contrast, the $^2P_{3/2}$ CTTS state has a lifetime greater than 225 ps for even the smallest cluster studied, n=6. No evidence for solvent reorganization is observed in the photoelectron spectra..

1. Introduction

Anions solvated in polar solutions generally exhibit distinct bands in the ultraviolet known as charge-transfer-to-solvent bands (CTTS).[1,2] These states involve electron detachment from the solute anion to nearby solvent molecules and serve as precursor states to fully solvated electrons. In recent years there has been considerable experimental and theoretical interest in the complex dynamics associated with CTTS excitation, particularly for halide ions in methanol and H_2O.[3-8] In order to gain a complementary perspective on this problem, and as part of a broader effort to understand how effects associated with electron solvation are manifested in systems of finite size, the spectroscopy and solvation dynamics associated with the CTTS bands have been investigated in finite clusters. For example, Johnson has located the cluster analog of the lower $^2P_{3/2}$ CTTS band in $I^-(H_2O)_n$ clusters,[9] and we have used anion femtosecond photoelectron spectroscopy (FPES)[10] to probe the dynamics associated with this band in

$I^-(H_2O)_n$ clusters.[11,12] The FPE spectra showed clear evidence for nuclear rearrangement and electron solvation within the cluster for n≥5. One might expect dramatic differences in the nature of the excited state if a nonpolar solvent such as Xe is used instead of H_2O. Efforts in this direction have been initiated in experiments by Cheshnovsky and coworkers,[13,14] who located CTTS bands in $I^-(Xe)_n$. In this paper, anion FPE spectra of $I^-(Xe)_n$ clusters are reported that indeed exhibit significantly different dynamics than the spectra of $I^-(H_2O)_n$ clusters.

As shown by Cheshnovsky and coworkers,[13,14] the excitation spectra of size-selected $I^-(Xe)_n$ (n=1-54) clusters exhibit two CTTS bands beginning with n=4. These bands are associated with the creation of a neutral I atom core in its $^2P_{3/2}$ ground or $^2P_{1/2}$ spin-orbit excited states, and a weakly bound electron that is stabilized by the cluster polarizability, e.g. $[I(^2P_{1/2})Xe_n]^-$. The bands become more prominent with increasing n, and are found to be quite narrow, e.g. 0.04 and 0.02 eV FWHM for the $^2P_{3/2}$ and $^2P_{1/2}$ CTTS states of n=12. The $^2P_{3/2}$ CTTS band is broader than the $^2P_{1/2}$ because its degeneracy is broken by the anisotropic interaction of the $I(^2P_{3/2})$ core with the surrounding solvent atoms.[15,16] A comparison of Cheshnovsky's results with the threshold photodetachment studies of Lenzer et al.,[15,16] in which the electron affinities of $I^-(Xe)_n$ clusters (n=1-14) were measured, indicates that the two CTTS bands lie just below the detachment thresholds for $I(^2P_{3/2})Xe_n$ and $I(^2P_{1/2})Xe_n$.

The stability of the CTTS states is intimately related to electron solvation in bulk and clustered xenon; bulk xenon stabilizes electrons by 0.58 eV, even though a single xenon atom does not bind an electron.[17] Experimental work on Xe_n^- clusters has shown that the minimum cluster size needed to bind an electron is n=6,[18,19] while diffusion

Monte Carlo simulations show that electron binding in Xe_n^- clusters arises from attractive, narrow electron "channels" that exist between the Xe atoms and a broad stabilizing potential around the cluster itself.[20,21] Although calculations have not been performed on the CTTS states in $I^-(Xe)_n$ clusters, qualitative comparisons can still be drawn between these states and Xe_n^- clusters, as will be discussed below.

The FPES experiment[10,22] involves exciting the $I^-(Xe)_n$ cluster with a femtosecond pump pulse at the resonant wavelength measured by Cheshnovsky and coworkers.[14] The photoelectron spectrum of the excess electron is then measured at a series of delay times by photodetachment with a femtosecond probe pulse. At each delay time, the photoelectron spectrum represents a complete "snapshot" of the evolving state. The time-evolution of the intensity and shape of the photoelectron spectrum probe the population change of the excited state and any solvent rearrangement within this state, thereby providing a detailed picture of the excited state dynamics.

2. Experimental

In our experiments, $I^-(Xe)_n$ clusters are formed in a pulsed, supersonic expansion of about 5% CH_3I and 10% Xe in Ar carrier gas (2 bar total pressure) that is crossed with a 1 keV electron beam and size-selected by injection into a Wiley-McLaren time-of-flight mass spectrometer. After passing through several differentially pumped chambers, the anions are intercepted by the pump and probe pulses at the focus of a magnetic bottle photoelectron spectrometer. In these experiments the electron energy resolution is 150 meV at 1.5 eV electron kinetic energy (eKE) for $I^-(Xe)_6$, and scales as $n^{-1/2}$. The pump and probe pulses are generated with a Clark-MXR regeneratively amplified Ti:Sapphire

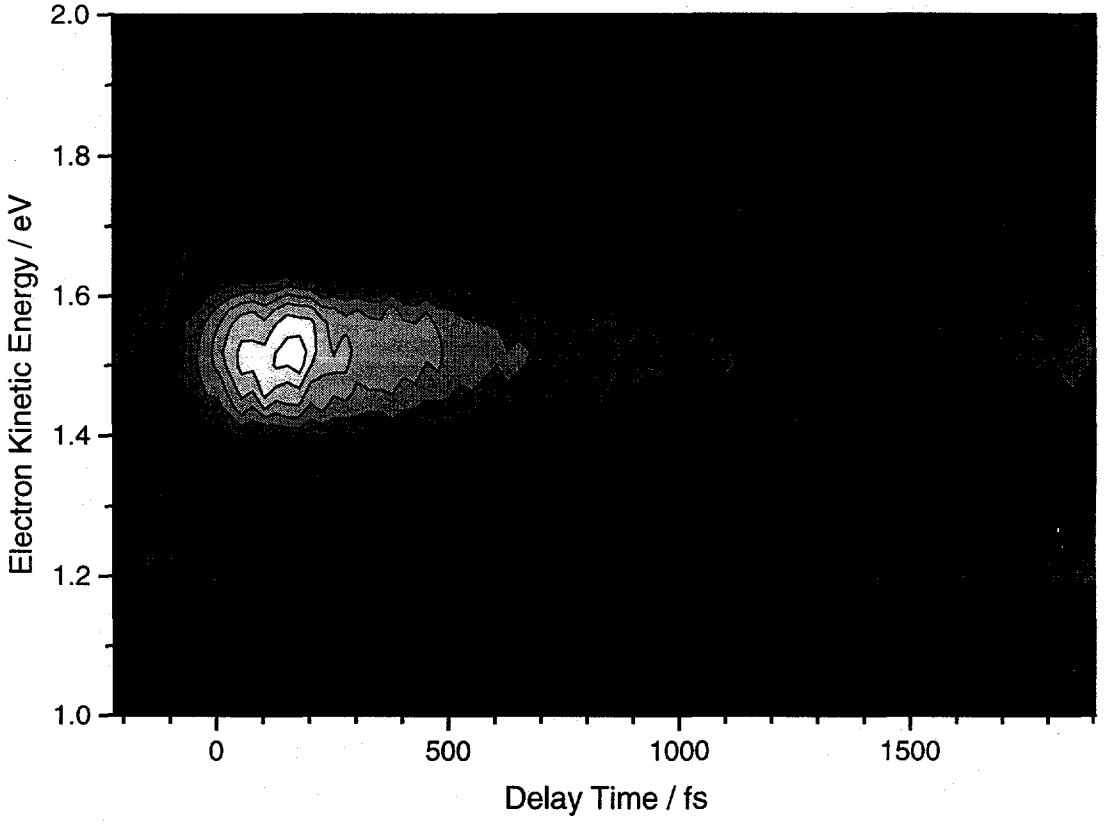

Figure 1. Contour plot of FPE spectra for the $^2P_{1/2}$ state of $I^-(Xe)_{11}$ excited at 272 nm. The spectra are presented as a contour plot of the photoelectron intensity versus eKE, electron binding energy (eBE), and pump-probe delay.

laser system that generates pulses near 800 nm (1.56 eV), 1 mJ, and 80 fs ($sech^2$) FWHM. About 200 μJ of this is used as the probe pulse, while the rest generates a tunable UV pump pulse by one of two methods. In the experiments pumping the $^2P_{1/2}$ CTTS state, the fundamental light is tuned between 825 and 790 nm, depending on the cluster size, and frequency tripled to produce 12 μJ of UV in the range 275 to 263 nm (4.51 to 4.71 eV) with a FWHM of 110 fs. For the experiments on the $^2P_{3/2}$ CTTS state, the fundamental pumps a Light Conversion optical parametric amplifier (TOPAS) whose output is quadrupled, resulting in 4 μJ of UV in the range 369 to 344 nm (3.36 to 3.60 eV) with a FWHM of 110 fs. For each of the clusters studied, the pump pulse is set to within 20 meV of the vertical detachment energy measured by Cheshnovsky and coworkers.[14]

3. Results

FPE spectra are shown in Fig. 1 for excitation of the $^2P_{1/2}$ state of $I^-(Xe)_{11}$ excited at 272 nm. The spectra are presented as a contour plot of the photoelectron intensity versus eKE, electron binding energy ($eBE=h\nu_{probe}-eKE$), and pump-probe delay. The FPE spectra of $I^-(Xe)_{11}$ in Fig. 1 are typical for all clusters measured; the intensity rises to a maximum during the first 200 fs and then decays to the baseline by ~2 ps with no shift in electron kinetic energy. The vertical detachment energy (VDE), which we determine by finding the average electron binding energy at a particular delay time, is 0.007±0.08 eV for this cluster and shows no time dependence.

Experiments on the $^2P_{1/2}$ CTTS states of larger clusters yield similar FPE spectra with no time-dependence in the VDE. However, the VDE does increase with cluster size

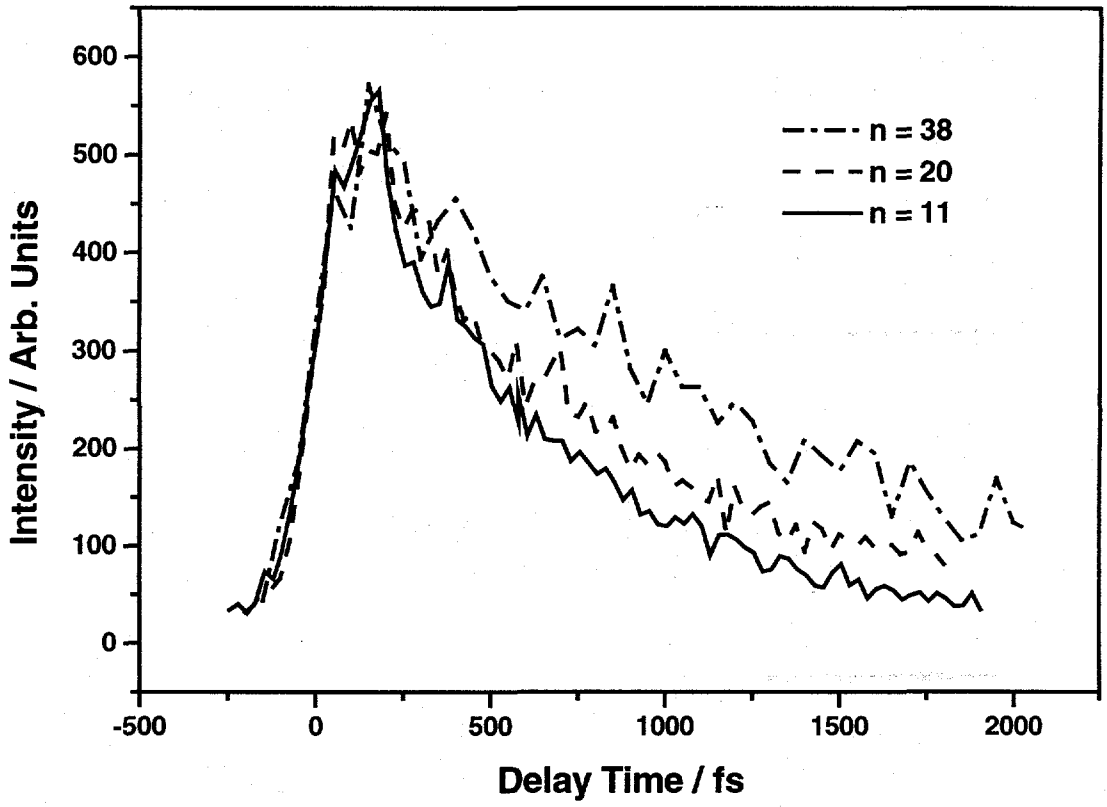

Figure 2. Integrated intensity of the $^2P_{1/2}$ CTTS state FPE spectra as a function of time for $I^-(Xe)_{11}$, $I^-(Xe)_{20}$, and $I^-(Xe)_{38}$.

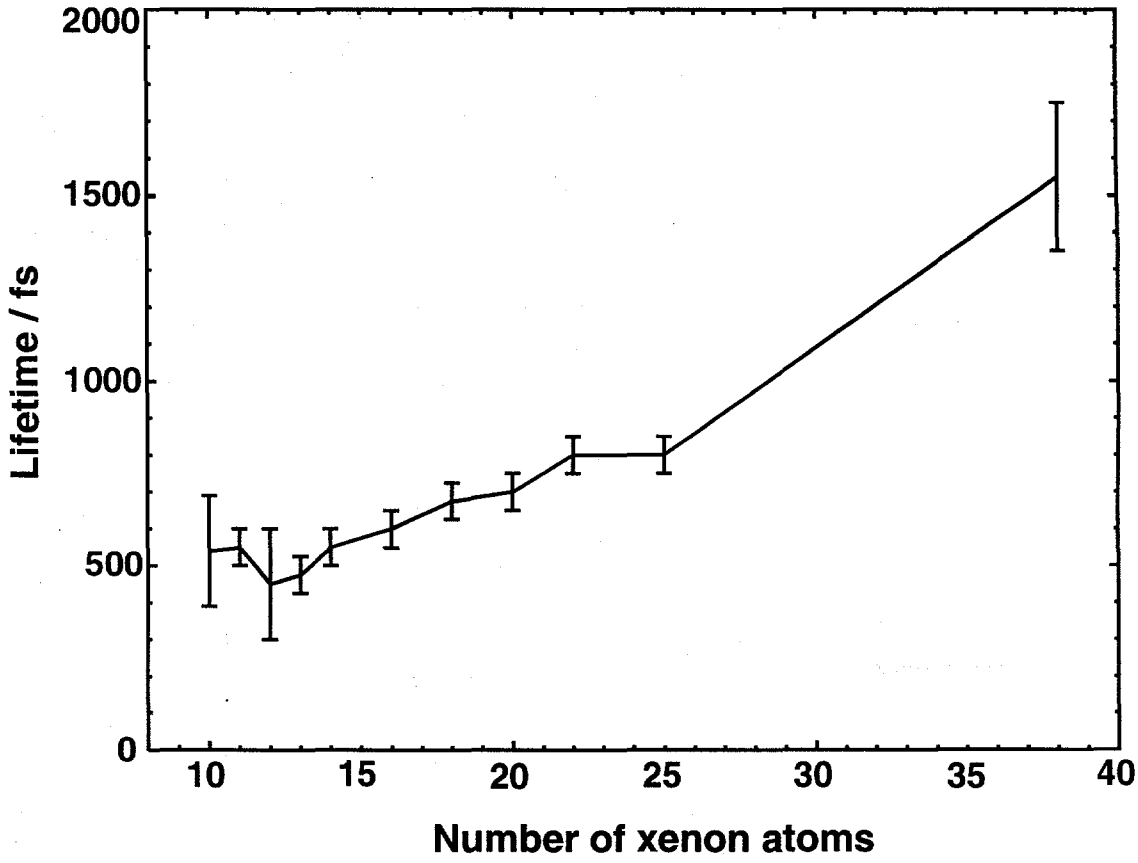

Figure 3. Lifetimes of $^2P_{1/2}$ CTTS state as determined from fitting the lifetime data (Fig. 2) to a single exponential decay convoluted with an instrument response function.

and is found to be 0.048±0.07 and 0.096±0.07 eV for n = 20 and 38, respectively. These spectra were taken with at pump wavelengths of 269 and 265 nm. In addition, the lifetime of the CTTS state increases. Fig. 2 shows integrated intensities of the FPE spectra vs. time for the n=11, 20, and 38 clusters. These decay with time constants of 550±50, 700±50, and 1550±200 fs, respectively, as determined from a single exponential fit to the data, convoluted with an instrument response function. Fig. 3 plots the lifetimes of the $^2P_{1/2}$ CTTS states for all the clusters measured, and an approximately linear dependence on the cluster size is found. Markedly different dynamics are found for the $^2P_{3/2}$ CTTS states, which show no decay for even the smallest cluster studied (n=6) up to the longest times measured (>225 ps), as illustrated in Fig. 4.

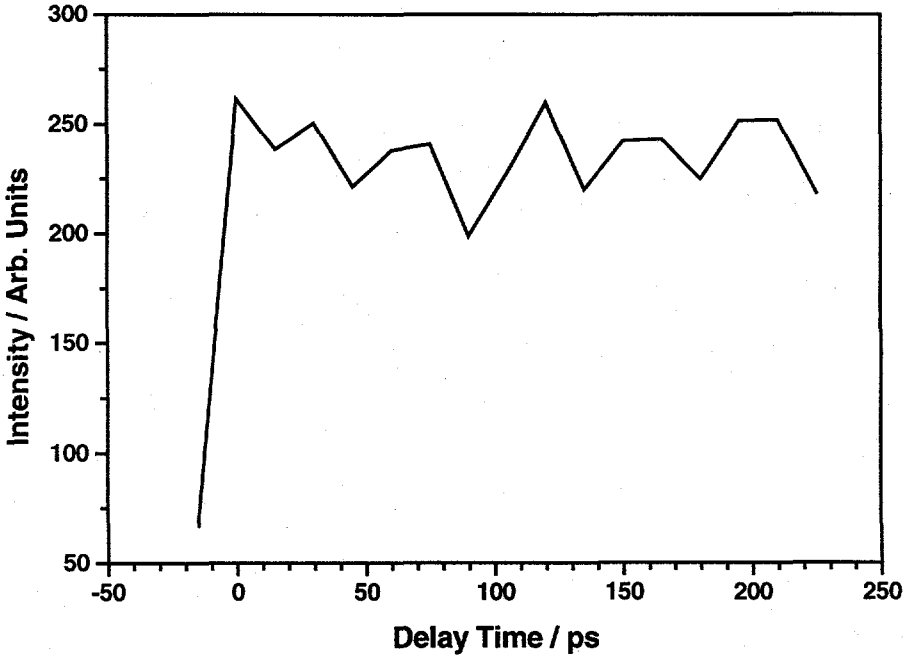

Figure 4. Integrated intensity of the $^2P_{3/2}$ CTTS state FPE spectra for $I^-(Xe)_6$.

4. Discussion

The difference in lifetimes for the $^2P_{1/2}$ and $^2P_{3/2}$ CTTS states implies that the higher energy state decays by spin-orbit induced autodetachment, i.e.

$$[I(^2P_{1/2})Xe_n]^- \rightarrow I(^2P_{3/2})Xe_n + e^- \qquad (1)$$

No such decay pathway exists for the $^2P_{3/2}$ CTTS state, consistent with its long lifetime. In fact, the experiments by Cheshnovsky and coworkers[13,14] and Lenzer *et al.*[15,16] suggest that the $^2P_{3/2}$ CTTS state is bound with respect to electron detachment. Vibrational to electron energy transfer could also result in electron detachment if the anion cluster temperature is high or if there is a large amount of vibrational energy in the excited state. However, this energy transfer mechanism would presumably affect both clusters equally. Since we observe no such decay for the $^2P_{3/2}$ state on the time scale of our experiment, this process must be considerably slower than spin-orbit autodetachment (from the $^2P_{1/2}$ state) in these clusters.

The time-independent vertical detachment energies are in sharp contrast to the FPE spectra of $I^-(H_2O)_n$ ($n \geq 5$) clusters.[12] For those species, the electron kinetic energy drops by ~0.3 eV within the first ps. This shift was attributed to stabilization of the excess electron via solvent reorganization, i.e. electron solvation. This reorganization occurs because the geometry of the H_2O molecules in the ground state of $I^-(H_2O)_n$ clusters is not the most favorable for minimizing the energy of the excess electron in the excited state. Similar but less pronounced solvation dynamics were seen in $I^-(NH_3)_n$ clusters.[23] Although our resolution is 180 meV for $I^-(Xe)_{11}$, we have shown in previous studies that we are sensitive to *changes* in electron affinity on the order of 10 meV.[24]

The absence of any shifts indicates that only minimal solvent reorganization takes place subsequent to excitation of the CTTS bands.

The absence of solvent reorganization is consistent with the frequency domain spectroscopy of these clusters. Our ZEKE/threshold photodetachment spectra of $I^-(Xe)_n$ clusters and the accompanying molecular dynamics calculations show that in the lowest energy geometry, Xe atoms surround the I^- to the greatest extent possible, and that I^- clearly lies inside a cluster of Xe atoms for $n \geq 11$.[16] The narrow CTTS bands seen by Cheshnovsky and coworkers indicate that similar structures hold for the excited states.[14] Excitation of these states will therefore access at least a local minimum on the excited state surface, in which case no solvent reorganization should occur.

The lack of cluster rearrangement can be understood in the context of calculations on Xe_n^- clusters. The work by Martyna and Berne shows that Xe_n^- clusters are essentially neutral Xe_n clusters surrounded by a very diffuse electron cloud that is considerably larger than the nuclear core of the cluster.[20,21] For Xe_{13}^-, the electron probability distribution peaks ~2 Å outside and extends ~36 Å beyond the nuclear core. Because the excess electron is bound solely by the polarizability of the cluster atoms, and the polarizability of iodine and xenon are very similar ($\alpha_I = 30.05\ a_0^3$; $\alpha_{Xe} = 27.16\, a_0^3$), the wavefunction for the excess electron should resemble that of the CTTS states in $[I(Xe)_n]^-$ clusters. The essential feature in both cases is that the excess electron does not perturb the nuclear cluster geometry, because the binding energy of the electron per atom is small and the electron is spatially diffuse. Under such circumstances, it is unlikely that nuclear rearrangement could produce an overall lower energy structure in which the excess electron is more solvated (and more localized). This situation differs markedly

from $I^-(H_2O)_n$ clusters, in which stronger interactions between the excess electron and solvent molecules drive the solvation dynamics in the excited state.[12]

Finally, we consider the size-dependence of the autodetachment rate from the $^2P_{1/2}$ excited states. As shown in Fig. 3, the upper state lifetime increases with the number of Xe atoms. The mechanism given by Eq. (1) requires an interaction between the excess electron and the $I(^2P_{1/2})$ core in order to induce a spin-flip of the unpaired electron on the I atom. Thus, the increase in lifetime of the $^2P_{1/2}$ CTTS state with cluster size presumably reflects a reduction in this interaction. A simple explanation of this trend would be that the I atom, which sits at the center of the cluster, is more effectively shielded from the diffuse electron cloud by Xe atoms in the larger clusters, resulting in a lower excess electron probability density at the I atom.

The calculations by Martyna and Berne[20,21] on Xe_n^- suggest the situation is more complex. They find that as *n* increases, the electron cloud becomes less diffuse and the probability of finding the excess electron close to a Xe atom increases, as reflected in their calculated electron-Xe pair correlation function. However, the pair correlation function is averaged over all Xe atoms. The electron density may actually decrease around the innermost Xe atom because the interior electron-Xe channels narrow with cluster size. Since the I atom in $I^-(Xe)_n$ clusters is structurally analogous to the innermost Xe atom in Xe_n^- clusters, it is possible that the electron probability density around the I atom decreases with increasing cluster size, even though the excess electron cloud is less diffuse in the upper state for the larger clusters. In any case, it appears that the degree of electron-iodine interaction is a subtle effect, and calculations specifically on $I^-(Xe)_n$ CTTS states are needed.

5. Conclusion

In conclusion, we have measured the dynamics and lifetimes associated with the $^2P_{1/2}$ and $^2P_{3/2}$ CTTS states in size-selected $I^-(Xe)_n$ clusters. We suggest that the increasing lifetime of the $^2P_{1/2}$ CTTS state with cluster size is due to the electron-iodine interaction decreasing, resulting in less probable spin-orbit autoionization. Solvent rearrangement is not observed, probably because excitation of the $I^-(Xe)_n$ cluster directly accesses the origin of the CTTS state. In this case, the iodine remains at the center of the cluster and the electron does not access states exclusively solvated by xenon atoms. Higher resolution experiments and theoretical calculations are needed to test these hypotheses.

6. Acknowledgments

This research was supported by the National Science Foundation under Grant No. CHE-9710243 and from the Defense University Research Instrumentation Program under Grant No. F49620-95-0078. C.F. acknowledges post-doctoral support from the Deutsche Akademie der Naturforscher Leopoldina (BMBF-LPD 9801-6). The authors would also like to thank Ori Chesnovsky for helpful discussions, and M.T.Z. thanks Niels Damrauer for help fitting the CTTS lifetimes.

7. References

[1] E. Rabinowitch, Rev. Mod. Phys. **14,** 112 (1942).

[2] M. Blandamer and M. Fox, Chem. Rev. **70,** 59 (1970).

[3] J. Jortner, M. Ottolenghi, and G. Stein, J. Phys. Chem. **68,** 247 (1964).

[4] F. H. Long, X. Shi, H. Lu, and K. B. Eisenthal, J. Phys. Chem. **98,** 7252 (1994).

[5] Y. Gaudeul, H. Gelabert, and M. Ashokkumar, Chem. Phys. **197,** 167 (1995).

[6] J. A. Kloepfer, V. H. Vilchiz, V. A. Lenchenkov, and S. E. Bradforth, Chem. Phys. Lett. **298,** 120 (1998).

[7] W.-S. Sheu and P. J. Rossky, J. Phys. Chem. **100,** 1295 (1996).

[8] A. Staib and D. Borgis, J. Chem. Phys. **104,** 9027 (1996).

[9] D. Serxner, C. E. H. Dessent, and M. A. Johnson, J. Chem. Phys. **105,** 7231 (1996).

[10] B. J. Greenblatt, M. T. Zanni, and D. M. Neumark, Chem. Phys. Lett. **258,** 523 (1996).

[11] M. T. Zanni, L. Lehr, B. J. Greenblatt, R. Weinkauf, and D. M. Neumark, in *Ultrafast Phenomena XI*, Vol. 63, edited by T. Elsaesser et al. (Springer Series Chem. Phys., 1999), p. 474.

[12] L. Lehr, M. T. Zanni, C. Frischkorn, R. Weinkauf, and D. M. Neumark, Science **284,** 635 (1999).

[13] I. Becker, G. Markovich, and O. Cheshnovsky, Phys. Rev. Lett. **79,** 3391 (1997).

[14] I. Becker and O. Cheshnovsky, J. Chem. Phys. **110,** 6288 (1999).

[15] T. Lenzer, M. R. Furlanetto, K. R. Asmis, and D. M. Neumark, J. Chem. Phys. **109,** 10754 (1998).

[16] T. Lenzer, M. R. Furlanetto, N. L. Pivonka, and D. M. Neumark, J. Chem. Phys. **110,** 6714 (1999).

[17] R. Reininger, U. Asaf, and I. T. Steinberger, Chem. Phys. Lett. **90,** 287 (1982).

[18] H. Haberland, C. Ludewigt, H.-G. Schindler, and D. R. Worsnop, J. Chem. Phys. **81,** 3742 (1984).

[19] H. Haberland, T. Kolar, and T. Reiners, Phys. Rev. Lett. **63,** 1219 (1989).

[20] G. J. Martyna and B. J. Berne, J. Chem. Phys. **88,** 4516 (1988).

[21] G. J. Martyna and B. J. Berne, J. Chem. Phys. **90,** 3744 (1989).

[22] B. J. Greenblatt, M. T. Zanni, and D. M. Neumark, Science **276,** 1675 (1997).

[23] C. Frischkorn, M. T. Zanni, A. V. Davis, and D. M. Neumark, Faraday Discuss. , In press (1999).

[24] M. T. Zanni, V. S. Batista, B. J. Greenblatt, W. H. Miller, and D. M. Neumark, J. Chem. Phys. **110,** 3748 (1998).

Appendix 1. Program for iteratively determining the beta-parameters of a modified Morse potential using experimental frequencies and anharmonicities

In Chapter 5, femtosecond stimulated emission pumping was used to determine the frequency and anharmonicity of the $I_2^-(\tilde{X}\ ^2\Sigma_u^+)$ state potential as a function of excitation energy. In order to fit the data points to a modified Morse potential, an algorithm was developed to iteratively modify the β-parameters and determine the best fit potential by minimizing X^2. This is accomplished using a downhill simplex method in multidimensions (Numerical Recipes, Chapt. 10.4). A least squares fitting routine was not used because of the difficulty of determining the 1st derivative of the β-parameters with respect to the X^2 value. For details on the potential form and data points, see Chapter 5.

Specifically, the routine works as follows. `step6.f` allows the user to set the range of β-parameters being used in the potential, e.g. β_0 to β_4, β_1 to β_8, etc., using the variables `nbmin` and `nbmax`. Up to β_8 is allowed. The simplex method requires initial data points, one more than the number of β-parameters being fit. These are input using the data commands in `step6.f`. The program than calls `mtz8.f` one time for each initial point to determine its value of X^2. Having done this, the iterative routine `amoeb4.f` is called. This routine iteratively alters the β-parameters, and calls `mtz8.f` to determine whether X^2 is improved. When either the maximum number of iterations is reached or the minimum X^2 is found (as set by `itmax` and `ftol` in `step6.f`), the subroutine returns to `step6.f`. `step6.f` then makes a final call to `mtz8.f`, this time ordering `mtz8.f` to write the potential to a file.

The heart of the program lies in `mtz8.f`, which is essentially Ivan Yourshaw's DVR code stripped down to a subroutine package that can be called easily and quickly. The experimental excitation energies, frequencies, and anharmonicities, along with their standard deviations, are input in the code using data statements. `mtz8.f` calculates the eigenstates for the modified Morse potential as determined from the β-parameters using a Morse oscillator DVR code (for details, see Yourshaw's thesis). Using the experimental excitation energies, the frequency and anharmonicity of the nearest eigenstates is found, and X^2 calculated.

`step6.f` has been written to run on aether. It can be compiled with the following command:

```
make -f makestep6
```

where makestep6 is the following file:

```
dvrmo3: step6.o mtz8.o amoeb4.o gammln.o rsb.o rs.o matrix.o
      f77 -O -o step6 step6.o  mtz8.o amoeb4.o gammln.o rsb.o
rs.o matrix.o -C

step6.o: step6.f
mtz8.o: mtz8.f
amoeb4.o: amoeb4.f
gammln.o: gammln.f
rsb.o: rsb.f
rs.o: rs.f
matrix.o: matrix.f
```

Only the files `step6.f`, `amoeb4.f`, and `mtz8.f` are included in the appendix. `gammln.f` can be found in Numerical Recipes, and `matrix.f`, `rs.f`, and `rsb.f` can be found in Yourshaw's thesis.

program step6

```
c This program will iteratively determine the beta-parameters
c for a modified morse potential given an input of frequencies
c and anharmonicities.

c The frequencies and anharmonicities are input in the
c subroutine mtz8

C Up to eight beta-parameters can be used. Set nbmin and
c nbmax for the range being used. e.g. nbmin=2,nbmax=5, using
c beta-parameters b1 through b4.

      parameter (nbmin = 1, nbmax = 5)
      parameter (ndim = nbmax - nbmin + 1)
      parameter (mp = ndim + 1)
      parameter (np = 9)
      implicit double precision(b-h,q-z)
      integer nbmin, nbmax
      dimension y(mp),b2(mp,np)
      common / mtz2var / beta2(0:8)

c Note: to convert b2 values to beta parameters (beta2), subtract one.
      data b2(1,1), b2(1,2), b2(1,3), b2(1,4) /
     :   1.1885,-6.8105e-2,1.3059e-2,-2.9576e-3  /
      data b2(1,5), b2(1,6), b2(1,7), b2(1,8), b2(1,9) /
     : 1.9413e-4,0.000000, 0.000000, 0.0000  , 0.00  /

      data b2(2,1), b2(2,2), b2(2,3), b2(2,4) /
     :   1.1886 ,0.0173215,-0.0625, 0.012562  /
      data b2(2,5), b2(2,6), b2(2,7), b2(2,8), b2(2,9) /
     :  3.978e-6 , 8.21e-7,-9.1e-7,-5.74e-8, -.1e-8/

      data b2(3,1), b2(3,2), b2(3,3), b2(3,4) /
     :   1.1884  , 0.0180000, 3.63e-3  ,-1.63e-3/
      data b2(3,5), b2(3,6), b2(3,7), b2(3,8), b2(3,9) /
     : 2.39e-3   , 8.695e-6 ,-3.16e-5,-2.88e-6,.1e-8 /

      data b2(4,1), b2(4,2), b2(4,3), b2(4,4) /
     :   1.1885  ,0.0170, -9.8e-3   , 8.0789e-3   /
      data b2(4,5), b2(4,6), b2(4,7), b2(4,8), b2(4,9) /
     : -7.4e-4    , 1.07e-5 , -5.5e-6  , 1.3e-6  ,1.e-8/

      data b2(5,1), b2(5,2), b2(5,3), b2(5,4) /
     :   1.1886  , -0.045   , 0.01 , -0.0030 /
      data b2(5,5), b2(5,6), b2(5,7), b2(5,8), b2(5,9) /
     :  -0.000310, 0.000010, 0.00005, 1.e-7  , 1.e-8/

c     data b2(6,1), b2(6,2), b2(6,3), b2(6,4) /
c     :   1.1885  , 0.01732, -0.06250 , 2.584e-3  /
c     data b2(6,5), b2(6,6), b2(6,7), b2(6,8), b2(6,9) /
c     :   -2.7e-3 , 1.36e-4  , 7.97e-5 , 5.14e-6,-.1e-8/

c     data b2(7,1), b2(7,2), b2(7,3), b2(7,4) /
c     :.  1.1884  , 0.01732, -0.06250 , 0.012562  /
c     data b2(7,5), b2(7,6), b2(7,7), b2(7,8), b2(7,9) /
c     :   0.000000, 0.0000000,  0.00000, 0.00   , .1e-8/

c     data b2(8,1), b2(8,2), b2(8,3), b2(8,4) /
c     :   1.1885  ,-6.5e-2 ,9.9e-3   , -1.9e-3   /
c     data b2(8,5), b2(8,6), b2(8,7), b2(8,8), b2(8,9) /
c     :   6.9e-5  , 2.64e-7  , 6.2e-7  , 0.01e-4   , 2.e-8/

c     data b2(9,1), b2(9,2), b2(9,3), b2(9,4) /
c     :   1.1880  , 0.01732, -0.06250 , 0.012562  /
c     data b2(9,5), b2(9,6), b2(9,7), b2(9,8), b2(9,9) /
c     :   0.000100, 0.0000010,  0.00010, 0.01e-4   , -1.e-8/

c     data b2(10,1), b2(10,2), b2(10,3), b2(10,4) /
c     :   1.1880  , 0.01732, -0.06250 , 0.012562  /
c     data b2(10,5), b2(10,6), b2(10,7), b2(10,8), b2(10,9) /
c     :   0.000100, 0.0000010,  0.00010, 0.01e-4   ,1.e-8 /

c determine chi2 for each guess.  Any beta parameters not being
```

```
c  used need to be set to some value.
      do j = 1,mp
       do i = 1,np
         beta2(i-1) = b2(j,i)
       enddo
c       beta2(0) = 1.1885
c       beta2(1) = -6.13e-2
c       beta2(2) = 2.71e-3
c       beta2(3) = 0.0
c       beta2(4) = 0.0
       beta2(5) = 0.00
       beta2(6) = 0.00
       beta2(7) = 0.00
       beta2(8) = 0.00
       call mtz8(0,y(j))
       write(*,*) 'y = ', j, y(j)
      enddo

c  call amoeba4 which does the iterative process.
c  itmax is the maximum number of iterations to perform for the fit
c  ftol sets the chi2 tolerance; program stops when chi2 is less than
c   this number
      open(38,file='step6.beta')
      write(*,*) 'calling amoeba4'

      itmax = 600
      ftol = 0.00005
      call amoeb4(b2,y,mp,np,ndim,ftol,itmax,iter,nbmin,nbmax)
      write(*,*) iter

c  for the best data point, calls mtz8, but this time mtz8 writes
c  the potential to a file.
      ylow = 1000.
      do j = 1,5
       if (y(j).lt.ylow) then
         ylow = y(j)
         jlow = j
       endif
      enddo

      call mtz8(1,y(jlow))
      close(38)

      end
```

```
      subroutine amoeb4(p,Y,mp,np,ndim,FTOL,itmax,ITER,nbmin,nbmax)

      PARAMETER (NMAX=20,ALPHA=1.0,BETA=0.5,GAMMA=2.0)
      double precision
     ftol,p(mp,np),Y(mp),PR(NMAX),PRR(NMAX),PBAR(NMAX)
      double precision ypr,yprr,beta2
      integer nbmin, nbmax
      common / mtz2var / beta2(0:8)

c  taken from numberical recipes.
c  step-wise iteration of beta-parameters, and calls mtz8

      write(*,*) nbmin, nbmax
      MPTS=NDIM+1
      ITER=0
1     ILO=1
      IF(Y(1).GT.Y(2))THEN
       IHI=1
       INHI=2
      ELSE
       IHI=2
       INHI=1
      ENDIF
      DO 11 I=1,MPTS
       IF(Y(I).LT.Y(ILO)) ILO=I
       IF(Y(I).GT.Y(IHI))THEN
        INHI=IHI
        IHI=I
       ELSE IF(Y(I).GT.Y(INHI))THEN
        IF(I.NE.IHI) INHI=I
       ENDIF
11    CONTINUE
      RTOL=2.*ABS(Y(IHI)-Y(ILO))/(ABS(Y(IHI))+ABS(Y(ILO)))
      IF(RTOL.LT.FTOL) then
       write(*,*) 'tolerance found'
       RETURN
      endif
      IF(ITER.EQ.ITMAX) then
       write(*,*) 'Amoeba exceeding maximum iterations.'
       return
      endif
      ITER=ITER+1
c     DO 12 J=1,NDIM
      DO 12 J=nbmin,nbmax
       PBAR(J)=0.
12    CONTINUE
      DO 14 I=1,MPTS
       IF(I.NE.IHI)THEN
c        DO 13 J=1,NDIM
        DO 13 J=nbmin,nbmax
         PBAR(J)=PBAR(J)+P(I,J)
13       CONTINUE
       ENDIF
14    CONTINUE
c     DO 15 J=1,NDIM
      DO 15 J=nbmin,nbmax
       PBAR(J)=PBAR(J)/NDIM
       PR(J)=(1.+ALPHA)*PBAR(J)-ALPHA*P(IHI,J)
       beta2(J-1) = PR(J)
15    CONTINUE
c     YPR=FUNK(PR)
      call mtz8(0,YPR)
      IF(YPR.LE.Y(ILO))THEN
c       DO 16 J=1,NDIM
       DO 16 J=nbmin,nbmax
        PRR(J)=GAMMA*PR(J)+(1.-GAMMA)*PBAR(J)
        beta2(J-1) = PRR(J)
16      CONTINUE
c       YPRR=FUNK(PRR)
       call mtz8(0,YPRR)
       IF(YPRR.LT.Y(ILO))THEN
c        DO 17 J=1,NDIM
        DO 17 J=nbmin,nbmax
         P(IHI,J)=PRR(J)
```

```
17      CONTINUE
        Y(IHI)=YPRR
       ELSE
c       DO 18 J=1,NDIM
        DO 18 J=nbmin,nbmax
         P(IHI,J)=PR(J)
18      CONTINUE
        Y(IHI)=YPR
       ENDIF
      ELSE IF(YPR.GE.Y(INHI))THEN
       IF(YPR.LT.Y(IHI))THEN
c       DO 19 J=1,NDIM
        DO 19 J=nbmin,nbmax
         P(IHI,J)=PR(J)
19      CONTINUE
        Y(IHI)=YPR
       ENDIF
c      DO 21 J=1,NDIM
       DO 21 J=nbmin,nbmax
        PRR(J)=BETA*P(IHI,J)+(1.-BETA)*PBAR(J)
        beta2(J-1) = PRR(J)
21     CONTINUE
c      YPRR=FUNK(PRR)
       call mtz8(0,YPRR)
       IF(YPRR.LT.Y(IHI))THEN
c       DO 22 J=1,NDIM
        DO 22 J=nbmin,nbmax
         P(IHI,J)=PRR(J)
22      CONTINUE
        Y(IHI)=YPRR
       ELSE
        DO 24 I=1,MPTS
         IF(I.NE.ILO)THEN
c          DO 23 J=1,NDIM
           DO 23 J=nbmin,nbmax
            PR(J)=0.5*(P(I,J)+P(ILO,J))
            P(I,J)=PR(J)
            beta2(J-1) = PR(J)
23          CONTINUE
c           Y(I)=FUNK(PR)
           call mtz8(0,Y(I))
          ENDIF
24       CONTINUE
        ENDIF
       ELSE
c       DO 25 J=1,NDIM
        DO 25 J=nbmin,nbmax
         P(IHI,J)=PR(J)
25      CONTINUE
        Y(IHI)=YPR
       ENDIF
       GO TO 1
       END
```

```
      subroutine mtz8(nwrite,csq)

c  this program determines chi2 for the beta parameters determines
c  in amoeba4. The data points used in the fit are listed in the
c  data commands below. The eigenstates of the potential are determined
c  using ivans morse oscillator DVR code.

      implicit double precision(b-h,q-z)
      parameter(ndim=500)
      parameter(nfreq=9)
      parameter(ndwexe = 4)
      integer nmax,numvib,nwrite
      double precision norm(ndim+1),u(ndim+1,ndim+1),eigval(ndim+1),
     &  eigvec(ndim+1,ndim+1),fv1(ndim+1),fv2(ndim+1),r(ndim+1),
     &  diagv(ndim+1),eigmdvr(ndim+1,ndim+1),ham(ndim+1,ndim+1),
     &  adiagv(ndim+1),
     &  apeigval(ndim+1),
     &  apeigvec(ndim+1,ndim+1),fcf(ndim+1,ndim+1),totfcf(ndim+1),
     &  bv3(ndim+1),rexp(ndim+1),cm(ndim+1)
      double precision eval(10),csq,freq(nfreq),sig(nfreq),
     &  tfreq(nfreq), dwexe(ndwexe), dsig(ndwexe), twexe(ndwexe)

      character*30 fn,feig,fvsticks,fbv,wavefile
      double precision rmu,anbasis(3),neubasis(3),
     &  anpot(10),neupot(10),potfile
      integer npot(2)
      common / mtz2var / beta2(0:8)

      parameter(evtocm=8065.541)

c  Input data points and standard deviations, and
c  excitation energies.

      data freq(1), freq(2), freq(3), freq(4) /
     :     110. ,  94. ,  83.5 ,  72.    /
      data freq(5), freq(6), freq(7), freq(8), freq(9) /
     :     58. ,  41. ,  22. , 17.  , 13.  /

      data dwexe(1), dwexe(2), dwexe(3), dwexe(4) /
     :     0.708 , 0.591  , 0.556  , 0.498  /

      data dsig(1) , dsig(2) , dsig(3) , dsig(4)  /
     :     0.015 , 0.03   , 0.03   , 0.025  /

      data sig(1) , sig(2) , sig(3) , sig(4) /
     :     2.  ,  1.  ,  1. , 1.5  /
      data sig(5) , sig(6) , sig(7) , sig(8), sig(9) /
     :     1.  , 2.5  ,  4.  , 4.  , 4.  /

      data eval(1), eval(2), eval(3), eval(4) /
     :     0.014 , 0.262  , 0.400 , 0.537  /
      data eval(5), eval(6), eval(7), eval(8), eval(9) /
     :     0.676 , 0.823 , 0.965 , 0.977 , 0.993  /

c  Parameters for Ivan's code.  neubasis is the re,de, and t value.
c  see his code for explanation.
      amass1 = 126.9045
      amass2 = amass1
      rmu = amass1*amass2/(amass1 + amass2)
      anpot(1) = 1.014
      neubasis(1) = 2.805
      neubasis(2) = 1.1820
      neubasis(3) = 248.2

c     do i = 0,4
c      write(*,*) 'beta = ',i,beta2(i)
c     enddo

      nmax = 240              ! number of basis functions to use in
      nmax=nmax-1             ! fit.  can't exceed neubasis(3)

      nanshow = 140           ! number of anion states to calc.
      nanshow=nanshow-1
```

```
      re=neubasis(1)
      beta=neubasis(2)
      t=neubasis(3)
      depthm=(2.09008e-3)*((beta*t)**2)/rmu

      call umat(nmax,t,ndim,norm,u)

      call rsb(ndim+1,nmax+1,2,u,eigval,1,eigvec,fv1,fv2,ierr)
      if (ierr.ne.0) then
        write(*,*)'*** ierr=',ierr,' from rsb'
      endif

      call rcalc(nmax,ndim,re,t,beta,eigval,r)

c     open(8,file='potlA.out')
c345  format(2x,'r(i)',5x,'anion',4x,'neutral')
c     write(*,*) '**********************nmax = ',nmax
c     write(*,*) 'depthneu = ',depthneu
c     write(*,*) 'anpot(1) = ',anpot(1)
c     write(*,*)
c     do 400 i=0,nmax
c       potenA = potfile(r(i+1))
c       write(8,*) r(i+1),potenA
c400  continue
c     close(8)
c350  format(f8.4,1x,f8.6,1x,f8.6)

      call morseig(ndim,nmax,rmu,neubasis,eigvec,eigmdvr)

      call diffpot(ndim,nmax,rmu,neubasis,1,npot(1),anpot,
     &           r,adiagv,depthan)

      call hcalc(ndim,nmax,eigmdvr,adiagv,ham)
      call rs(ndim+1,nmax+1,ham,apeigval,1,apeigvec,fv1,fv2,
     &       ierr)

c     write(*,*)
c     write(*,*) ' Anion vibrational eigenvalues '
c     write(*,*) ' '
c     write(*,245)
c245  format(15x, 'Total', 6x, 'Spacing')
c250  format(1x,'v = ',i3,4x,f9.5,4x,f8.2)
c     write(*,*) ' '
c     depthm=((beta*t/21.87343)**2)/rmu

      nf = 0
      nwexe = 0
      temp2=0.
      csq = 0.
      do 800 i=0,nanshow
        tempev=(apeigval(i+1)) - anpot(1)
        temp=(apeigval(i+1))*8065.541
        temp3ev=(apeigval(i+2)) - anpot(1)
        temp3=(apeigval(i+2))*8065.541
        do 811 j=1,nfreq
          if ((temp3ev.gt.eval(j)).and.(tempev.lt.eval(j))) then
            nf = nf + 1
            tfreq(nf) = temp3 - temp
            if (nf-(nfreq-ndwexe).eq.(nwexe+1)) then
              temp0 = (apeigval(i))*8065.541
              temp4 = (apeigval(i+3))*8065.541
              temp01 = (temp - temp0)
              temp13 = (temp3 - temp1)
              temp34 = (temp4 - temp3)
              nwexe = nwexe + 1
              twexe(nwexe) = ((temp01-temp13) + (temp13-temp34))/2.
            endif
            goto 32
          endif
811     enddo
32      temp2=temp
800   continue
```

```
      if (nf.ne.nfreq) then
       csq = 10000.0
       write(*,*) 'attention: csq = 1000.0'
       write(38,*) csq, beta2(0), beta2(1), beta2(2), beta2(3),
     &      beta2(4), beta2(5), beta2(6), beta2(7), beta2(8)
       write(*,*) csq, beta2(0), beta2(1), beta2(2), beta2(3),
     &      beta2(4), beta2(5), beta2(6), beta2(7), beta2(8)
       return
      elseif (nwexe.ne. ndwexe) then
       write(*,*) 'attention: nwexe .ne. 4'
       return
      endif
53    format(f7.5,2x,f7.5,2x,f7.5,2x,f7.5,2x,f7.5,2x,f7.5,2x,f7.2,
     & 2x,f7.2)

      csq = 0.0
      do i = 1,nf
c       if (i.ne.6) then
c        weight = 1.0          ! tried biasing the weights
c       else
c        weight = 90.0
c       endif
c       csq = csq + weight*(freq(i)-tfreq(i))**2/sig(i)**2
       csq = csq + (freq(i)-tfreq(i))**2/sig(i)**2
      enddo
      do i = 1,nwexe
c       if (i.eq.1) then
c        weight = 70.0
c       elseif ((i.eq.3).or.(i.eq.4)) then
c        weight = 70.0
c       else
c        weight = 1.0
c       endif
c       csq = csq + weight*(dwexe(i)-twexe(i))**2/dsig(i)**2
       csq = csq + (dwexe(i)-twexe(i))**2/dsig(i)**2
      enddo
```



```
c write chi2 and beta parameters to file.
      write(38,*) csq, beta2(0), beta2(1), beta2(2), beta2(3),
     &      beta2(4), beta2(5), beta2(6), beta2(7), beta2(8)
      write(*,*) csq, beta2(0), beta2(1), beta2(2), beta2(3),
     &      beta2(4), beta2(5), beta2(6), beta2(7), beta2(8)

c if it is last iteration, write the potential to a file, etc.
      if (nwrite.eq.1) then
       open(31,file='freq.out')
       open(32,file='wexe.out')
       do i = 1,nf
        write(31,*) eval(i), tfreq(i)
       enddo
       do i = 1,nwexe
        write(32,*) eval(i+5), twexe(i)
       enddo
       close(31)
       close(32)
       open(8,file='potlA.out')
       do i=0,nmax
        potenA = potfile(r(i+1))
        write(8,*) r(i+1),potenA
       enddo
       close(8)
       open(8,file='levels.out')
       temp2 = 0.
       write(*,*)
       write(*,*) ' Anion vibrational eigenvalues '
       write(*,*) ' '
       write(*,245)
       write(8,245)
245    format(15x, 'Total', 6x, 'Spacing')
250    format(1x,'v = ',i3,4x,f10.7,4x,f8.4)
       write(*,*) ' '
       do i = 0,nanshow
        tempev = (apeigval(i+1)) - anpot(1)
        temp = (apeigval(i+1))*8065.541
```

```
c        write(*,250) i,tempev,temp-temp2
         write(8,250) i,tempev,temp-temp2
         temp2 = temp
       enddo
     endif

c    if (nwrite.eq.2) then
c      temp2 = 0.
c      write(*,*)
c      write(*,*) ' Anion vibrational eigenvalues '
c      write(*,*) ' '
c      write(*,245)
c245   format(15x, 'Total', 6x, 'Spacing')
c250   format(1x,'v = ',i3,4x,f10.7,4x,f8.4)
c      write(*,*) ' '
c      do i = 0,nanshow
c        tempev = (apeigval(i+1)) - anpot(1)
c        temp = (apeigval(i+1))*8065.541
c        write(*,250) i,tempev,temp-temp2
c        temp2 = temp
c      enddo
c    endif

     return
     end

*=======================================================
     subroutine normcalc(nmax,t,beta,ndim,norm)
*=======================================================
*
* Generates normalization factors for Morse eigenfunctions
* defined by Whittaker functions.
*
* Input: nmax,    largest n value to calculate, starting
*                 starting from n=0
*
*          t,     = sqrt(2*redmass*De)/(hbar*beta) = 2k
*
*          beta,  parm of Morse function in angstrom-1
*
*          ndim, dimension of norm vector (assumed first
*                element is 0)
*
* Output: norm contains natural logs of normalization factors
*
* Uses:  gammln.f
*
     implicit double precision(b-h,q-z)
     double precision t,beta,norm(ndim+1)
     double precision gammln

     write(*,*)'normcalc'

     do 100 n=0,nmax
       norm(n+1)=gammln(dble(n+1))+gammln(2*t-2*n)
    &      +gammln(2*t-2*n-1)-gammln(2*t-n)-log(beta)
100  continue
     return
     end

*=======================================================
     subroutine umat(nmax,t,ndim,norm,u)
*=======================================================
*
* Set up diagonal and diag-1 of u(z) matrix elements, in
* form suitable for input to rsb diagonalization routine
*
* Input:  nmax, largest n value to calc.
*           t,        for Morse
*           ndim   dimension of norm vector
*           norm  vector containing ln(norm). constants
*
* Output: u   contains diag-1 in first column,
*                diag in 2nd, first row index is 1.
```

```
*
      implicit double precision(b-h,q-z)
      double precision t,norm(ndim+1),u(ndim+1,ndim+1)

      write(*,*) 'umat'

*  Diag-1 elements

      u(1,1)=0.
      do 100 i=1,nmax
*
*       Old way, from normalization consts
*
c       u(i+1,1)=exp((norm(i+1)-norm(i))/2)
*
*       New way, by cancelling gammas
*
        u(i+1,1)=sqrt(i*(2*t-i)/((2*t-2*i+1)*(2*t-2*i)**2
     &                  *(2*t-2*i-1)))
  100 continue

*  Diagonal elements

      do 200 i=0,nmax
        u(i+1,2)=t/(2*(t-i)*(t-i-1))
  200 continue

      return
      end

*=======================================================
      subroutine rcalc(nmax,ndim,re,t,beta,udiag,r)
*=======================================================
*
*  Calculate points R(i) from diagonalized u(R) matrix
*  elements.
*
*  Input:  udiag,  vector with eigenvalues of u(R)
*          nmax,   maximum n value (=# of evals -1)
*          ndim    dimension of udiag vector
*          re,     bond length of Morse
*          t,      for Morse
*          beta,   for Morse
*
*  Output: r,      contains R(i)'s (in Angstroms if beta
*                  is in angst-1)
*
      implicit double precision(b-h,q-z)
      double precision udiag(ndim),r(ndim),re,t
      integer nmax,ndim

      write(*,*)'rcalc'

      do 100 i=0,nmax
        r(i+1)=re+log(2*t*udiag(i+1))/beta
  100 continue
      return
      end


*=======================================================
      subroutine diffpot(ndim,nmax,rmass,basis,numb,npot,parms,
     &                   r,diagv,depthp)
*=======================================================
*
*  Calculate difference potential matrix  (delt-V = V - Vref)
*  in dvr by quadrature at points R(i), and transform to Morse fbr.
*  Zero energy is bottom of potential wells.
*
*  Inputs:      ndim
*               nmax
*          rmass                Reduced mass (amu)
*               basis(re,beta,t) Morse parms
*          numb                 1 for anion, 2 for neutral
```

```
*           npot                    type of potential
*                   parms()                 potential paramaters
*                   r()                     quadrature points
*
* Output:           diagv()         diff. potl. elements in dvr basis
*                   deltav()  difference potl matrix in Morse basis
*                   depthp          well depth of poten (needed for Aqui poten)
*
      implicit double precision(b-h,q-z)
      parameter(evtocm=8065.541)

      integer ndim,nmax,numb,npot
      double precision basis(3),parms(10),
     &    r(ndim+1),diagv(ndim+1)
      double precision poten,morse,potfile

      write(*,*) 'diffpot'

      re=basis(1)
      beta=basis(2)
      t=basis(3)
      depthm=(2.09008e-3)*((beta*t)**2)/rmass
      depthp=parms(1)
*
* Fill diagonal delta-v with dvr matrix elements
*

      do 100 i=1,nmax+1
      diagv(i)=potfile(r(i))+depthp
     &        -morse(depthm,re,beta,r(i))-depthm

100   continue

      return
      end
```



```
*=============================================================
      subroutine morseig(ndim,nmax,rmass,basis,tmat,eigmdvr)
*=============================================================
*
* Calculates eigenvalues of the morse potential
*
* Inputs:           ndim
*                   nmax
*                   rmass
*                   basis(re,beta,t)
*                   tmat()              Transformation matrix
*
* Output:           eigmdver()          Matrix with Morse eigenvalues
*                     in eV referred to asymptote,
*                                       transformed to dvr basis.
*
      implicit double precision(a-h,o-z)
      parameter(c1=0.0457176,c2=2.09010e-3)

      integer ndim,nmax
      double precision basis(3),eigmdvr(ndim+1,ndim+1),
     &            tmat(ndim+1,ndim+1)
      double precision eigm(300)

      write(*,*) 'morseig'

      re=basis(1)
      beta=basis(2)
      t=basis(3)
      depthm=(2.09008e-3)*((beta*t)**2)/rmass

      do 100 n=0,nmax
        eigm(n+1)=(-5.22519e-4)*beta*beta*((t*2-1-2*n)**2)
     &            /rmass+depthm
100   continue

*
```

```
*  Transform E0(dvr) = T(transpose)*E0(fbr)*T
*
      do 400 n=1,nmax+1
       do 300 m=1,n
        temp=0.
        do 200 j=1,nmax+1
         temp=temp+tmat(j,n)*tmat(j,m)*eigm(j)
200      continue
        eigmdvr(n,m)=temp
300    continue
400   continue

      return
      end


*=============================================================
      subroutine hcalc(ndim,nmax,eigmdvr,diagv,ham)
*=============================================================
*
*  Calculate total hamiltonian in the dvr basis by adding Morse
*  eigenvalue (K) matrix to the potential difference matrix
*
*  Input: ndim
*                 nmax
*                 eigmdvr()       Morse eigenvalues transformed to dvr
*                 diagv()         potl difference matrix in dvr
*
*  Output:        ham()           Total ham matrix(lower half)
*
      implicit double precision(a-h,o-z)
      integer ndim,nmax
      double precision eigmdvr(ndim+1,ndim+1),diagv(ndim+1),
     &           ham(ndim+1,ndim+1)

      write(*,*)'hcalc'
      do 100 i=1,nmax+1
       do 200 j=1,i-1
        ham(i,j)=eigmdvr(i,j)
200    continue
100   continue
      do 300 i=1,nmax+1
       ham(i,i)=eigmdvr(i,i)+diagv(i)
300   continue
      return
      end



*-------------------------------
      double precision function morse(depth,rmin,beta,rt)
*-------------------------------

      implicit double precision (a-h,o-z)

      xt = rt/rmin
      morse = depth*(exp(2.*beta*rmin*(1.-xt))-2.*exp(
     &       beta*rmin*(1.-xt)))
      return
      end

*-----------------------------------------------------------------
      double precision function potfile(rt)
*-----------------------------------------------------------------

      implicit double precision (a-z)
      common / mtz2var / beta2(0:8)

c calculates the potential using input beta-parameters.
c re and de are fixed from previous study.

      re = 3.205
      de = 1.014
```

```
      btot = beta2(0)+beta2(1)*(rt-re)+beta2(2)*(rt-re)**2
     &       +beta2(3)*(rt-re)**3+beta2(4)*(rt-re)**4
     &       +beta2(5)*(rt-re)**5+beta2(6)*(rt-re)**6
     &       +beta2(7)*(rt-re)**7 + beta2(8)*(rt-re)**8
      potfile = de*(1-dexp(-btot*(rt-re)))**2

      return
      end
```

Appendix 2. Publications from graduate school

B. J. Greenblatt, M. T. Zanni, and D. M. Neumark, "Photodissociation dynamics of the I_2^- anion using femtosecond photoelectron spectroscopy," Chem. Phys. Lett. **258**, 523 (1996).

B. J. Greenblatt,* M. T. Zanni,* and D. M. Neumark, "Photodissociation of $I_2^-(Ar)_n$ clusters studied with anion femtosecond photoelectron spectroscopy," Science **276**, 1675 (1997).
**equal authors*

M. T. Zanni, T. R. Taylor, B. J. Greenblatt, B. Soep, and D. M. Neumark, "Characterization of the I_2^- anion ground state using conventional and femtosecond photoelectron spectroscopy," J. Chem. Phys. **107**, 7613 (1997).

B. J. Greenblatt, M. T. Zanni, and D. M. Neumark, "Time-resolved studies of dynamics in molecular and cluster anions," Faraday Discuss. **108**, 101 (1997).

M. T. Zanni, B. J. Greenblatt, A. V. Davis, and D. M. Neumark, "Photodissociation dynamics of I_3^- using femtosecond photoelectron spectroscopy," *Laser Techniques for State-Selected and State-to-State Chemisry IV*, Proc. SPIE **3271**, 196 (1998).

M. T. Zanni, B. J. Greenblatt, and D. M. Neumark, "Solvent effects on the vibrational frequency of I_2^- in size-selected $I_2^-(Ar)_n$ and $I_2^-(CO_2)_n$ clusters," J. Chem. Phys. **109**, 9648 (1998).

M. T. Zanni, L. Lehr, B. J. Greenblatt, R. Weinkauf, and D. M. Neumark, "Dynamics of charge-transfer-to-solvent precursor states in $I^-(D_2O)_n$ clusters," *Ultrafast Phenomena XI*, edited by T. Elsaesser *et al.*, Springer Series Chem. Phys. **63**, 474 (1999).

V. S. Batista, M. T. Zanni, B. J. Greenblatt, D. M. Neumark, and W. H. Miller, "Femtosecond photoelectron spectroscopy of the I_2^- anion: a semiclassical molecular dynamics simulation method," J. Chem. Phys. **110**, 3736 (1999).

M. T. Zanni, V. S. Batista, B. J. Greenblatt, W. H. Miller, and D. M. Neumark, "Femtosecond photoelectron spectroscopy of the I_2^- anion: characterization of the $\tilde{A}'\,^2\Pi_{g,1/2}$ excited state," J. Chem. Phys. **110**, 3748 (1999).

L. Lehr,* M. T. Zanni,* C. Frischkorn, R. Weinkauf, and D. M. Neumark, "Electron solvation dynamics in finite systems: A femtosecond study of iodide·(water)$_n$ anion clusters," Science **284**, 635 (1999).
**equal authors*

T. R. Taylor, K. R. Asmis, M. T. Zanni, and D. M. Neumark, "Characterization of the I_3 radical by anion photoelectron spectroscopy," J. Chem. Phys. **110**, 7607 (1999).

M. T. Zanni, B. J. Greenblatt, A. V. Davis, and D. M. Neumark, "Photodissociation of gas phase I_3^- using femtosecond photoelectron spectroscopy," J. Chem. Phys. **111**, 2991 (1999).

B. J. Greenblatt, M. T. Zanni, and D. M. Neumark, "Femtosecond photoelectron spectroscopy of $I_2^-(Ar)_n$ photodissociation dynamics (n = 6,9,12,16,20)," J. Chem. Phys. **111**, 10566 (1999).

B. J. Greenblatt, M. T. Zanni, and D. M. Neumark, "Femtosecond photoelectron spectroscopy of $I_2^-(CO_2)_n$ photodissociation dynamics (n = 4,6,9,12,14,16)," J. Chem. Phys. (in press).

M. T. Zanni, C. Frischkorn, A. V. Davis, and D. M. Neumark, "Dynamics of the charge-transfer-to-solvent states in $I^-(Xe)_n$ clusters," J. Phys. Chem. A (submitted).

M. T. Zanni, A. V. Davis, C. Frischkorn, Mohammed Elhanine, and Daniel M. Neumark, "Femtosecond stimulated emission pumping: characterization of the I_2^- ground state," J. Chem. Phys. (submitted).

C. Frischkorn, M. T. Zanni, A. V. Davis, and Daniel M. Neumark, "Electron solvation dynamics in $I^-(NH_3)_n$ clusters," Faraday Discuss. (in press).

A. V. Davis, M. T. Zanni, C. Frischkorn, Daniel M. Neumark, "Time-resolved dynamics of charge transfer to solvent states in solvated iodide clusters," J. Elec. Spec. Related Phenomena (in press).